



A University of Sussex PhD thesis

Available online via Sussex Research Online:

<http://sro.sussex.ac.uk/>

This thesis is protected by copyright which belongs to the author.

This thesis cannot be reproduced or quoted extensively from without first obtaining permission in writing from the Author

The content must not be changed in any way or sold commercially in any format or medium without the formal permission of the Author

When referring to this work, full bibliographic details including the author, title, awarding institution and date of the thesis must be given

Please visit Sussex Research Online for more information and further details

The XMM Cluster Survey: A New Cluster Catalogue and Applications.

Philip Rooney

Submitted for the degree of Doctor of Philosophy

University of Sussex

September 2015

Declaration

I hereby declare that this thesis has not been and will not be submitted in whole or in part to another University for the award of any other degree.

Signature:

Philip Rooney

UNIVERSITY OF SUSSEX

PHILIP ROONEY, DOCTOR OF PHILOSOPHY

THE XMM CLUSTER SURVEY: A NEW CLUSTER CATALOGUE AND APPLICATIONS.

In this thesis, we present the XMM Cluster Survey Second Data Release (XCS-DR2) and use it to test possible spectroscopic biases, fit scaling relations, and find massive, relaxed galaxy clusters. XCS finds clusters in the XMM public archive. The new cluster candidate list includes 15,642 objects found in the 688 square degrees of sky suitable for cluster detection.

XCS-DR2 is the largest X-ray selected cluster catalogue to date. It contains 7,129 unique preliminary cluster identifications and 1,177 unique firm cluster identifications. Where redshifts were available, a spectral fitting was made leading to 4,987 unique cluster temperature and luminosity measurements. XCS-DR2 is more than an order of magnitude larger than XCS-DR1.

As XCS-DR2 is a catalogue of homogeneously processed galaxy clusters, it is an ideal dataset to test possible spectroscopic biases during X-ray spectral fitting. This thesis answers seven questions related to the combining and fitting of multi-observational data and the instrumental calibration of XMM. Notably we present strong evidence that spectral selection must take place before any final X-ray spectral fitting takes place.

XCS-DR1 clusters have been used to fit a luminosity-temperature scaling relation. This thesis presents new spectral fitting pipelines, so the previous scaling relations work was revisited to ascertain how the results have changed. Additionally, by using the latest SPT cluster catalogue, a scaling relation was fit between the X-ray and the SunyaevZel'dovich

effect properties of XCS-DR2 clusters.

Massive, relaxed galaxy clusters have been used to fit cosmological parameters through measurements of their baryon fractions. XCS-DR2 contains 342 clusters observed on-axis with temperature, $T_X \geq 4.5$ keV. A morphological analysis of these clusters shows that 20 of them appear to be relaxed. When added to the latest analysis, a subsample of six relaxed clusters, can improve Ω_M and w estimates by 18% and 12% respectively.

Contents

1	Introduction	30
1.1	The XMM-Newton Satellite Observatory	30
1.1.1	Instrument Setup	31
1.1.2	The XMM Science Archive	33
1.1.3	Specialist Astronomy Software	34
1.1.4	Features to account for when analysing XMM data	35
1.2	Cluster Surveys	37
1.2.1	Detection Methods	37
1.2.2	XMM Cluster Survey	38
1.2.3	Other X-ray Cluster Surveys	42
1.2.4	Optical and Microwave Cluster Surveys	45
1.3	Concepts in Cluster Astrophysics	47
1.3.1	Basic Concepts in Cosmology	47
1.3.2	The Relationship Between Cluster Mass and Temperature	50
1.3.3	The Relationship Between Cluster Mass and Radius	51
1.3.4	X-ray Emission Mechanisms	52

1.3.5	X-ray Surface Brightness Profiles	54
1.3.6	The relationship between X-ray Luminosity and X-ray Temperature	55
1.3.7	The relationship between X-ray observables and the Sunyaev-Zel'dovich Effect	56
1.3.8	Cool-Core Galaxy Clusters	57
1.4	Concepts in Cluster Cosmology	58
1.4.1	The f_{gas} Test	59
1.4.2	The Cluster Number Count test	61
1.5	Thesis Overview	62
2	Generation of a New XCS Master Source List	84
2.1	Overview	84
2.2	Acquiring XMM Data	86
2.3	The XCS Event List Cleaning and Image-Making Pipeline (XIP)	86
2.3.1	Creating Event Lists	86
2.3.2	XMM Mosaic Event Lists	87
2.3.3	Out of Time Events	87
2.4	Data Cleaning	88
2.5	Single Camera Image Generation	89
2.6	Merged Image Generation	89
2.6.1	XIP Batch Processing	90
2.7	Source Detection	91

2.7.1	Mis-targeted Observations	93
2.7.2	XAPA Batch Processing	94
2.8	Results	94
2.8.1	Area Covered	94
2.8.2	Source Detection	95
2.8.3	Comparison With XCS-DR1	95
2.8.4	Comparison With XCLASS	96
2.8.5	Contamination from non-cluster sources	97
2.9	Conclusions and Future work	98
2.9.1	Conclusions	98
2.9.2	Work Required Before Publishing in a Paper	98
2.9.3	Future Work for XCS-DR3	98
3	Generation of a New XCS Cluster Sample	115
3.1	Overview	115
3.2	Preliminary Cluster Confirmation using GMPHoRCC	116
3.2.1	The GMPHoRCC Algorithm	116
3.2.2	GMPHoRCC applied to XCS-DR2 Clusters Candidates	117
3.3	Preliminary cluster confirmation using NED	118
3.4	Candidate confirmation using well understood cluster samples	118
3.5	Candidate Confirmation using DES-SV data	119
3.6	X-ray Post Processing	120

3.6.1	Temperature Measurement Methodology for DR2	120
3.6.2	Luminosity Measurement Methodology for DR2	122
3.7	The XCS-DR2 Cluster Catalogue	123
3.8	Conclusions and Future Work	124
3.8.1	Conclusions	124
3.8.2	Work Required Before Publishing in a Paper	125
3.8.3	Future Work for XCS-DR3	125
4	Application of XCS-DR2: An investigation of bias in the spectroscopic analysis of clusters	142
4.1	Overview	142
4.2	Test 1: Is it beneficial to combine data from different observations?	143
4.3	Test 2: What is the best way to combine data from different observations?	144
4.4	Test 3: Do offsets in detector calibration impact fitted cluster temperatures?	146
4.5	Test 4: Does time variation in detector calibration impact fitted cluster temperatures?	146
4.6	Test 5: Does the detected position on the field of view impact fitted cluster temperatures?	147
4.7	Test 6: Does the type of filter used during an observation impact fitted cluster temperatures?	148
4.8	Test 7: How does core excision impact fitted cluster temperatures?	149
4.9	Conclusions and Future Work	150
4.9.1	Conclusions	150
4.9.2	Work Required Before Publishing in a Paper	150

4.9.3	Future Work for XCS-DR3	151
5	Application of XCS-DR2: X-ray Cluster Scaling Relations	164
5.1	Overview	164
5.2	The XCS-DR1 $L_X - T_X$ scaling relation	165
5.2.1	Pre-Hilton 2012 Luminosity-Temperature Scaling Relations	166
5.2.2	Data Inputs	167
5.2.3	Fitting Method	167
5.2.4	Results	168
5.2.5	H12 Discussion	170
5.2.6	New Scaling Relation Results Since Hilton et al (2012)	170
5.3	The XCS-DR1 $L_X - T_X$ scaling relation revisited	171
5.3.1	Data inputs and fitting method	171
5.3.2	Results	171
5.4	A new measurement of X-ray to SZ scaling relations	172
5.4.1	Previous measurements	172
5.4.2	Data inputs and fitting method	173
5.4.3	Results	174
5.5	Conclusions and Future Work	175
5.5.1	Conclusions	175
5.5.2	Work Required Before Publishing in a Paper	175
6	Application of XCS-DR2: Selection of clusters for the f_{gas} cosmology	

test	185
6.1 Overview	185
6.2 The CARGC morphology test and its application to Chandra data	186
6.2.1 Principles of the CARGC Cosmology Test	186
6.2.2 Principles of the CARGC Morphology Test	187
6.2.3 Practicalities of the CARGC Morphology Test	188
6.3 The CARGC morphology test applied to XMM data	192
6.3.1 Choice of pixel size and detector	192
6.3.2 Accounting for the Effective Area	192
6.3.3 Masking point sources	193
6.3.4 Gridding Over the Core Radius	193
6.4 Searching for relaxed XCS-DR2 clusters	193
6.4.1 Selection of clusters for the morphology test	193
6.4.2 Results	194
6.5 Chandra Cycle 17 proposal	195
6.6 Conclusions and Future Work	196
6.6.1 Conclusions	196
6.6.2 Future Work	196
7 Conclusions	206
7.1 Future Work	208
Bibliography	211

List of Figures

- 1.1 The original orbit of XMM. Since then corrections and perturbations have slightly altered this to apogee 118,000 km and perigee 8,000 km. (Figure courtesy of Dornier Satellitensysteme GmbH, 2001) 63
- 1.2 XMM-Newton layout. (Figure courtesy of the XMM-Newton SOC VILSPA, 2001) 63
- 1.3 XMM mirror module. 58 Wolter I mirrors can be seen in nested arrangement. (Figure courtesy of Dornier Satellitensysteme GmbH, 2001) 64
- 1.4 Left: The CCDs of one of the MOS cameras. Right: The CCDs of the PN camera. (Figures courtesy of XMM-Newton SOC VILSPA, 2001) 64
- 1.5 The light path to the reflection grating spectrometer can be seen. A reflection grating plate passes 40% of the light headed towards the reflection grating spectrometer at a secondary focus (Figure courtesy of XMM-Newton SOC VILSPA, 2001). 64
- 1.6 Example auxiliary response file. Red Line is PN ARF; Dark Blue Line is MOS 1 ARF; Light Blue Line is MOS 2 ARF. The PN ARF is larger as some of the light headed towards the MOS detectors is diverted to the reflection grating spectrometer. 65
- 1.7 The on-axis pn encircled energy as a function of angular radius. (Figures courtesy of XMM-Newton SOC VILSPA, 2001) 66

1.8	XMM PSF for 1keV photons. Left Column MOS1; Centre Column MOS2; Right Column PN. Top to bottom shows PSF at increasing off axis angle (arcminutes): 0, 2.5, 5, 7.5, 10. Images created using SAS task <code>psfgen</code> using the ellbeta model.	67
1.9	Left: An XMM MOS1 image in Full Image Mode; Right: An XMM MOS1 image in Small Image Mode 1	68
1.10	Left: An XMM MOS1 image in Small Image Mode 2; Right: An XMM MOS1 image in Small Image Mode 3	69
1.11	Left: An XMM PN image in Full Image Mode 1; Right: An XMM PN image in Large Image Mode 1	70
1.12	An XMM PN image in Small Window Mode 1	71
1.13	Abell 1689 taken with the Hubble Space Telescope. A galaxy cluster may contain tens, hundreds or even thousands of individual galaxies. Image credits: ESA / LFI and HFI Consortia (Planck image); MPI (ROSAT image); NASA/ESA/DSS2 (visible image). Acknowledgement: Davide De Martin (ESA/Hubble	72
1.14	Merged X-ray and optical image of XMMXCSJ003346.3-431729.3. Galaxy data from the DES survey. X-ray data taken by XMM-Newton; soft X-rays (0.50-2.00keV) shown in blue, hard X-rays (2.00-10.00keV) shown in red. Contours show increasing X-ray surface brightness. The image is taken from Miller, Rooney et al. 2015 (in prep).	73
1.15	The Coma cluster observed at microwave and X-ray frequencies. The colours show the Planck satellite image of the Sunyaev-Zel'dovich Effect, and the white contours show the X-ray signal measured by the ROSAT satellite. Image credits: ESA / LFI and HFI Consortia (Planck image); MPI (ROSAT image); NASA/ESA/DSS2 (visible image). Acknowledgement: Davide De Martin (ESA/Hubble)	74

- 1.16 Hubble Space Telescope images of merging clusters 1E0657-558 ($z = 0.30$) and MACSJ0025.4-1222 ($z = 0.54$). X-ray emission measured with Chandra overlaid in pink and gravitational lensing reconstruction in blue. The X-ray peaks tracing the collisional gas is offset from the dark matter and collisionless galaxies. This has the implication that dark matter also behaves as a collisionless fluid. Image credits: Left: X-ray: NASA/CXC/CfA/M. Markevitch et al.; Optical: NASA/STScI; Magellan/U. Arizona/D. Clowe et al. Right: NASA, ESA, CXC, M. Bradac (University of California, Santa Barbara), and S. Allen (Stanford University). 74
- 1.17 Wide angle tailed radio galaxy at the centre of the rich Abell cluster of galaxies A2634. It is thought that the high ambient density and modest speeds of the host galaxy with respect to the intra-cluster medium produce the bends. Credit: F. N. Owen 75
- 1.18 Composite Herschel (far-IR), VLT (optical) and Subaru (near-IR) image of XDCPJ0044.0-2033, a massive galaxy cluster at $z = 1.6$. Infrared emission within a 2 arcminute by 2 arcminute region centred on the galaxy cluster XDCPJ0044.0-2033. The image is constructed from K (red), J (green) and I (blue) band images. The red glow at shows far-infrared emission from galaxies located in the cluster's core. Credit: ESA/Herschel/J. Santos et al. 2015; NAOJ/Subaru; ESA/VLT/Hawk-I 75
- 1.19 Cosmological parameter fit when uncertainty in either temperature (left) or redshift (right) exist and are accounted for. 76
- 1.20 Cosmological parameter fit when uncertainty in either temperature (left) or redshift (right) exist but are not accounted for. 76
- 1.21 Cosmological parameter fit when there are unaccounted for uncertainties with both temperature and redshift. 76

1.22	Figure 15 from Sahlen et al (2009). Expected 68 and 95 per cent parameter constraints for XCS500. Where inappropriate cluster scaling relation assumptions are made the fiducial model is not well fit. Top: Different models and fitting methods used. Middle: Confidence regions in Ω_m integrated over σ_8 . Bottom Left: Confidence regions for σ_8 and Ω_m . Bottom Right: Confidence regions in σ_8 integrated over Ω_m	77
1.23	Thermal bremsstrahlung radiation for a cluster with temperature 1 keV (top) and 10 keV (below). Images made using MEKAL model with XSPEC.	78
1.24	Scaling relations Mass and temperature (left) and gas mass (right). (Vikhlinin et al., 2009a)	79
1.25	Scaling relation between cluster mass and the combination between gas mass and temperature (Vikhlinin et al., 2009a).	79
1.26	Scaling relation between cluster mass and luminosity (Maughan, 2007)	80
1.27	(Figure taken from Vikhlinin, 2005) An X-ray temperature profile of Abell 262	81
1.28	(Figure taken from M14) The ratio of gas mass and total gravitational mass in a galaxy cluster as a function of redshift for two different assumed cosmological models. Left: an open cosmology. Right: a flat cosmology.	82
1.29	(Figure taken from Mantz et al. (2014b)) Cosmological results from f_{gas} test.	82
1.30	The sensitivity of the cluster mass function to cosmological models (Borgani, 2008)	83
1.31	(Figure taken from (Vikhlinin et al., 2009b)) A comparison of the observed cluster mass function (data points), at two different redshifts, with theoretical predictions. Right: a flat cosmology. Left: an open cosmology.	83
2.1	An example of an XMM mosaic mode observation, Top: mosaiced images; Bottom: mosaiced exposure maps (ObsID: 067300010, PI: Megan Urry, Total Exposure: 113 ks, Target name: <i>Stripe 82 X-1</i>).	99

- 2.2 An example of a sub-observation from the mosaic observation shown in Figure 2.1. Left: The XIP produced merged (PN, MOS1, MOS2) image. Right: The XIP produced merged (PN, MOS1, MOS2) exposure map. . . . 100
- 2.3 Example of an observation that has been effected by out of time events (ObsID: 0600540601). Top Left: Original XIP PN image. Top Right: The modelled out of time events. Bottom: The PN image after the modelled out of time events have been subtracted. 100
- 2.4 Examples of observations with different noise levels, before and after cleaning. Top row: XIP PN image of ObsID:0554700101 before and after cleaning; Bottom row: XIP PN image of ObsID:0147610101 before and after cleaning. Note that the corner of detectors are cut off in the cleaned image as they are not exposed to the sky. 101
- 2.5 The XMM light curves for ObsID:0600540601. The left-hand plots refer to soft photon (0.1-1.0 keV) data, and the right-hand to hard photon (12-15 keV) data. The top row shows the light curve, in 50 second time bins. The bottom row shows the distribution of counts. Iterative three sigma clipping has been used to select good time intervals (blue points). 102
- 2.6 As Figure 2.5, but for ObsID:0111260501. In this case the three sigma clipping has not worked so well. (Note that the initial peak in the counts histogram reflects the fact that the filter was closed due to high background for substantial periods of the observation - hence no photons were collected during these periods.) 103
- 2.7 Example of a XIP PN image for ObsID:0724770501. On the left is the image and the on the right is an exposure map. The exposure map shows the effective exposure level of the observation at different points on the detector. Effective exposure is highest in the centre and then drops off due to vignetting. The dark lines represent chip gaps and bad columns. 103
- 2.8 As Figure 2.7, but for the MOS1 image for ObsID:0724770501. The unusual shape is a result of the fact that two MOS1 CCDs have been damaged by micrometeorite strikes (see § 1.1.4). 104

2.9	As Figure 2.7, but for the MOS2 image for ObsID:0724770501.	104
2.10	Example of a XIP merged (PN+MOS1+MOS2) image of ObsID:0724770501. This has been generated by scaling the MOS1 and MOS2 images & exposure maps (Figures 2.8 and 2.9 to the sensitivity of the PN (Figure 2.7).	104
2.11	Locations of the 8,598 ObsIDs processed by XIP for XCS-DR2 (Aitoff projection in Ecliptic coordinates). The size of the dots does not represent the field of view of the EPIC camera (they are larger than the FOV). Clumps of dots indicate where surveys have taken place (including those in mosaic mode).	105
2.12	Left: The distribution of total PN observation exposure times (grey) and of clean exposure times (blue) for the 8,598 ObsIDs processed by XIP. Right: Total number of observations with clean exposure times for MOS1 (blue), MOS2 (green) and PN (red) detectors.	106
2.13	(Figure taken from LD11) A cartoon to demonstrate the decision tree used by XAPA to merge (or otherwise) sources detected at different wavelet scales. Left: An extended source and point source contaminant. Right: A 1-d slice of the source detected at five scales. The vertical bars denote the width of the source at each scale. The ellipses fit to the point source do not overlap with the centroid of the largest scale, so the point source and extended source are both detected.	106
2.14	Examples of individual XAPA sources classified as extended (left), PSF-like (middle), and point-like (right). These are $3' \times 3'$ cutouts from the XIP merged image of the respective ObsID.	107
2.15	Examples of XAPA outputs for ObsID:0057560301 (left) and ObsID:0723800901 (right). The XAPA source ellipses have been overlaid on the XIP merged images. Point sources are shown by red ellipses, extended sources by green ellipses and PSF sources by magenta ellipses. Note that the target of ObsID:072380090 was Abell cluster A4059 (this is the bright extended source in the middle).	108

2.16	An example of an observation (ObsID:0554770101) that was mis-targeted during some of observation. Left: The exposure map with regular scaling. Right: The exposure map scaled to show very low exposure regions.	108
2.17	Left: Area of sky covered as a function of cleaned exposure time; Right: Cumulative plot of area of sky as function of exposure time. (These areas include the Galactic plane and Magellanic clouds.) (Image courtesy of Harry Wilcox.)	109
2.18	Left: Area of sky as a function of minimum flux; Right: Cumulative plot of area of sky as function of minimum.	109
2.19	Left: Point source flux limit versus exposure time; Right: Point source flux limit versus total number of sources found by XAPA. (Image courtesy of Harry Wilcox.)	109
2.20	Examples of XCS ³⁰⁰ candidates from the XCS-DR1 sample (shown with white circles) that were not detected by XAPA during the XCS-DR2 run. Case I: Despite the XIP images looking ‘normal’, XAPA has failed to complete successfully, so no sources have been recorded in XCS-DR2 for these ObsIds.	110
2.21	As Figure 2.20. Case II: These sources are not visible by eye in the XCS-DR2 XIP images, despite having typical exposure times and background levels (hence the XCS-DR1 sources were likely ‘phantoms’).	110
2.22	As Figure 2.20. Case III: The DR1 source lies outside the XIP merged image, because different combinations of images were used. In the left image, the PN is missing. In the right image, MOS2 is missing.	111
2.23	As Figure 2.20. Case IV: There is an obvious extended source at the XCS-DR1 location. We do not know why these sources were not re-directed in XCS-DR2.	111
2.24	Example of an XCLASS candidate (shown with white circles) that was not detected by XAPA during the XCS-DR2 run. Case I: XClass source 1856 has been merged by XAPA with a nearby extended object.	112

2.25	As Figure 2.24. Case II: There is an obvious extended source at the XClass source 417 location. We do not know why these sources were not re-directed in XCS-DR2.	112
2.26	As Figure 2.24. Case III: There is an obvious extended source at the XClass source 228 location. We do not know why these sources were not re-directed in XCS-DR2.	113
2.27	Top Left: The percentage of all sources classified as extended - including PSF flag - as a function of off-axis angle. Top Right: The percentage of all sources classified as extended - excluding PSF flag - as a function of off-axis angle. Bottom Left: The percentage of all sources both classified as extended and including PSF flag - as a function of off-axis angle. Bottom Right: The percentage of all extended sources classified with a PSF flag - as a function of off-axis angle.	114
3.1	Where NED records at least two redshifts for a given XCS-DR2 cluster, the difference between between those records is as shown.	126
3.2	Redshift distributions for XCS-DR2 clusters. Redshifts were derived using the GMPHoRCC technique applied to photometric data from SDSS (top), CFHTLS (middle), and ATLAS (bottom)	127
3.3	Redshift distributions for XCS-DR1 (top) and RedMaPPer (bottom) XCS-DR2 sub-samples.	128
3.4	Redshift distributions for SPT (top) and Planck (bottom) XCS-DR2 sub-samples.	129

- 3.5 (Figures and caption wording taken from Miller, Rooney et al. in prep.) Four main regions of the footprint containing both Dark Energy Survey (DES) and the *XMM* data used in this analysis. In all panels, dark grey regions have DES g, r, i, z data as well as *XMM* coverage and define the regions used to identify and characterize the optical/X-ray cluster sample. Black regions denote other *XMM* pointings or mosaics that are without DES optical overlap. Medium-shaded gray regions denote the rest of the DES data within the “SVA” sample. Light-shaded gray regions denote other areas of the DES which have some data, but which are not included in the primary DES sample (denoted “SVAext” in the text). The **top left** panel highlights the largest contiguous region as well as the Bullet Cluster off to the right. The **top right** and **bottom left** panels show the regions with the largest contiguous X-ray coverage and include the two XXL areas (upper right is the BCS and lower left is the CFHTLS W1 region). The **lower right** highlights one of the supernovae fields. 130
- 3.6 (Figures and caption wording taken from M12.) The first four clusters classified as *gold* in *Zoo*^{DR7}. False colour-composite images are 3×3 arcmin with X-ray contours overlaid in blue. Corresponding X-ray images are shown below each optical image (lighter regions show areas of increased X-ray flux). The shape of the XAPA-detected extended (point) source ellipses are highlighted in green (red). From left to right, the clusters are: XMMXCS J001737.4–005235.4 at $z = 0.21$; XMMXCS J010858.7+132557.7 at $z = 0.15$; XMMXCS J083454.8+553420.9 at $z = 0.24$; and XMMXCS J092018.9+370617.7 at $z = 0.21$ 131

3.7	(Figure and caption wording taken from M12.) A selection of XCS sources classified as <i>other</i> in <i>Zoo</i> ^{DR7} . None of these objects are included in XCS-DR1. False colour-composite images are 3×3 arcmin with X-ray contours overlaid in blue. Corresponding X-ray images are shown below each optical image (lighter regions show areas of increased X-ray flux). The shape of the XAPA-detected extended (point) source ellipse is highlighted in green (red). Reasons for a classification as <i>other</i> include artifacts at the edge of ObsID masks (far left); extended X-ray sources not associated with a galaxy cluster, such as a low-redshift galaxy (middle); cases where neighbouring X-ray point sources have been blended by XAPA into an erroneous extended source (mid right); and finally, cases of point sources misclassified as extended (because the point spread function model at the edge of the XMM field-of-view is inadequate;bottom).	132
3.8	Examples of XCS-DR2 cluster candidates identified as either <i>clusters</i> (top and middle) or <i>other</i> (bottom).	133
3.9	(Figure from Miller, Rooney et al. in prep) The statistical error on the DES-SV photometric redshifts of XCS-DR2 clusters.	134
3.10	Redshift distribution of the XCS-DR2 clusters confirmed using DES-SV and XCS-Zoo.	135
3.11	The difference in measured redshift between that catalogued by RedMaPPer and by other samples. In 719 of 915 comparisons (79%), the difference was <10%.	135
3.12	A comparison of the X-ray temperatures measured using the XCS-DR2 methodology and the XCS-DR1 (as described in LD11) methodology.	136
3.13	A comparison of the errors on the X-ray temperatures measured using the XCS-DR2 methodology and the XCS-DR1 (as described in LD11) methodology.	136

- 3.14 A comparison of the XAPA defined source ellipse and the R_{500} aperture (calculated using the redshift, $z=0.0844$, temperature, $T_X = 4.44$ and Equation 3.2) for XCS-DR2 cluster, XMMXCSJ032835.6-554243.2. R_{500} is shown in green and the XAPA source ellipse is shown in yellow 137
- 3.15 The ratio in aperture size between R_{500} and the major-axis of the XAPA source ellipse. The analysis uses 660 clusters (duplicates removed) from SPT, Planck, RedMaPPer and XCS DR1 with relative temperature errors of $\leq 15\%$ 138
- 3.16 A comparison of the bolometric luminosities measured using the XCS-DR2 methodology and the XCS-DR1 (as described in LD11) methodology. 139
- 3.17 Top: Redshift distribution of all confirmed XCS-DR2 galaxy clusters. Middle: T_X distribution of all confirmed XCS-DR2 galaxy clusters. Bottom: L_X distribution of all confirmed XCS-DR2 galaxy clusters. 139
- 3.18 Temperature distributions for various cluster XCS-DR2 sub-samples. Top Left: SPT. Top Right: Planck. Middle Left: DES-SV. Middle Right: GMPhoRCC_{SDSS}. Bottom Left: GMPhoRCC_{ATLAS}. Bottom Right: GMPhoRCC_{CFHTLS}. 140
- 3.19 XCS-DR2 cluster luminosities as a function of redshift. Colours represent different normalised exposure time ranges (blue $< 50,000$ s, red $> 200,000$ s). Note that by ‘normalised’ we mean Mos 1 + Mos 2 + $3.5 \times$ PN, this roughly corrects for the extra sensitivity of the PN instrument. 141
- 3.20 The distribution of XCS-DR2 cluster luminosities in different redshift bins. Top: $z < 0.4$. Middle: $0.4 < z < 0.8$. Bottom: $z > 0.8$ 141
- 4.1 (Figure and caption wording taken from LD11.) Fractional temperature uncertainty as a function of the number of soft-band counts as a result of fitting simulated $z = 0.5$ MEKAL spectra with different temperatures, going from cool to hot clusters. The red, orange, yellow, green and blue points represent spectra of 1.5, 2, 3, 5 and 8 keV, respectively. 152

- 4.2 (Figure and caption wording taken from LD11.) The XCS-determined X-ray temperatures (and uncertainty) as a function of the number of counts in the fitted spectrum. Each colour represents a cluster that was detected with more than 5000 counts. For details of the four clusters used in this plot, see Table C1. The respective exposures were then subdivided to generate lower count spectra. Note that the higher temperature systems do not yield fits at the low-count end. The 1σ error bars come from the XSPEC fitting software. 153
- 4.3 A comparison of the number of total spectra available for a given cluster compared to the number used in the XCS-DR2 joint spectral fitting (each dot represents a different cluster). 154
- 4.4 A comparison of the total counts used to fit cluster temperatures in XCS-DR1 compared to XCS-DR2, for the clusters in common between the two samples. 155
- 4.5 An example of a joint XSPEC fit to seven spectra extracted from multiple observations of cluster XMMXCSJ234444.0-424314.2. Each colour indicates a different spectrum. Top Left: The individual spectra with the best fit model curves overlaid (solid line). Top Right: The best fit model spectrum (including energy regions not included in the observed spectrum). The low energy feature is due to the galactic absorption model. Middle left: Residuals between data and model. Bottom Left: Ratio of data to model. Bottom Right: The solid line shows the best fit model integrated through the instrument response, the data point shows the number of background counts at each energy. 156
- 4.6 As counts increase signal to noise improves. The relative error falls with increasing counts and signal to noise. Grey points show clusters fit with 3 or less spectra - these were usually spectra from MOS1, MOS2 and PN detectors from a single observation and are shown to be the default result. Red points show clusters fit with between 4 and 10 spectra. Blue points show clusters fit with more than 10 spectra. 157

4.7	A comparison between the best fit T_X value recorded from composite spectra that met the XCS-DR2 criteria (Method 3) and other spectral selection methods (see text for details).	158
4.8	Temperature differences measured when comparing spectra accumulated in different XMM detectors. Only cases where both T_X values were recorded with relative errors of 15% or less are shown. Blue points indicate both detectors measurements were from the same observation (i.e. ObsID record), grey indicates the comparison is between detectors from different observations.	159
4.9	Difference in temperature measurements when two or more observations of the same cluster have been made at different times. Only cases where both T_X values were recorded with relative errors of 15% or less are shown.	159
4.10	(Figure and [adapted] caption wording taken from LD11.) Comparison of XCS-determined X-ray temperatures when the cluster is observed off-axis (y-axis) or on-axis (x-axis). The solid line shows the one-to-one relationship. The error bars are 1σ . Both x- and y-errors come from XSPEC.	160
4.11	Difference in temperature measurements of clusters that have been observed at different off-axis angles. Only cases where both T_X values were recorded with relative errors of 15% or less are shown.	161
4.12	Difference in temperature measurements of clusters that have been observed through different filters. Only cases where both T_X values were recorded with relative errors of 15% or less are shown.	162
4.13	Difference in temperature measurements of Planck-XCS clusters with and without core excision before spectral fitting. Only cases where both T_X values were recorded with relative errors of 15% or less are shown.	163
4.14	Luminosity vs temperature plot for all core excised (red) and non-core excised (blue) Planck clusters.	163

- 5.1 (Figure and caption wording taken from H12). The $L_X - T_X$ relation for the 211 XCS-DR1 clusters with spectroscopic redshifts. The dashed line is the best-fitting four parameter model (Equation 1), determined using the orthogonal fitting method. The luminosities have been scaled to take into account the evolution in the normalisation as a function of redshift inferred from the best-fitting model parameters, as well as the $E^{-1}(z)$ evolution expected in the self-similar case. 176
- 5.2 (Figure and caption wording taken from H12). Evolution of the normalisation of the $L_X - T_X$ relation relative to the self-similar case [$E(z)$], as inferred from the best-fitting four parameter model (Equation 5.1), using the orthogonal fitting method. The shaded area shows the marginalised 68 per cent confidence region on the evolution derived using MCMC. The dot-dashed line shows the track for no redshift evolution in the normalisation of the relation. The black diamonds show individual XCS clusters (error bars are omitted for clarity). 177
- 5.3 (Figure and caption wording taken from H12). One and two dimensional marginalised distributions (contours mark 68 and 95 per cent confidence limits) for each combination of parameters in the four parameter evolving $L_X - T_X$ relation model (Equation 5.1), as determined using the orthogonal fitting method. Note that the luminosities have been scaled by $E^{-1}(z)$, and so $C = 0$ corresponds to the case of self-similar evolution. 178

5.4 (Figure and and caption wording taken from H12) Evolution of the normalisation of the $L_X - T_X$ relation as measured from XCS-DR1, compared with numerical simulations. The solid thin red line is the best-fit obtained from XCS-DR1 using the orthogonal method, while the black diamonds show the corresponding median values for the clusters in each redshift bin (horizontal error bars indicate the redshift range of each bin, while vertical error bars indicate the 1s uncertainty in the median, estimated using bootstrap resampling). The dotted thin red line similarly represents the best-fit for XCS-DR1 obtained using the bisector method, with the slope fixed at the $z = 0$ value (2.81, see Table 3), and the open circles indicate the median values for clusters in redshift bins for this set of best-fit $L_X - T_X$ relation parameters. This latter fit is consistent with no evolution (dot-dashed line). The shaded regions mark the marginalised 68 per cent confidence regions. While the amount of evolution inferred from the XCS sample depends on the fitting technique used, there is no such dependence for the simulated data (see Table 4), and so we only show the results of the fits to the simulations using the orthogonal method. The XCS data favour negative evolution with respect to self-similar ($E(z)$; horizontal dotted line), and are clearly better described by the CLEF or MG1-PC models, rather than the models which implement AGN and supernovae feedback using a semi-analytic prescription (MG1-FO and MG2-FO). 179

5.5 Top: as Figure 5.1, but using the XCS-DR2 derived parameters for the clusters. Bottom: as Figure 5.2, but using the XCS-DR2 derived parameters for the clusters. 180

5.6 Similar to Figure 5.5, but for the SPT determined Y_{SZ} value as a function of T_X value. 181

5.7 Similar to Figure 5.6, but for the SPT determined Y_{SZ} value as a function of L_X value. 182

5.8 Similar to Figure 5.6, but a lower L_X threshold has been applied. 183

5.9 Similar to Figure 5.7, but a lower L_X threshold has been applied. 184

- 6.1 (Figures taken from M14) Chandra images clusters that have been run through the CARGC morphology test. Left: Abell 1835 (classified as relaxed). Right: Abell 2163 (classified as non-relaxed). Crosses show the global centres. Blue ellipses show the five fitted isophote levels. In the morphology test, the ‘alignment metric’ reflects how close the centres of these ellipses lie to one another, while the ‘symmetry metric’ reflects how well they agree with the global centre. 197
- 6.2 (Figure taken from M14) Surface brightness profiles for Abell 1835 and Abell 2163 (Chandra images shown in Figure 6.1), scaled according to Equation 6.3. Dashed lines correspond to the brightness levels defined in Equation 6.4 (the lowest level corresponds to $j = 0$). In the morphology test, the ‘peakiness metric’ depends on the average surface brightness in a circular aperture whose radius is given by the intersection of the observed profile with the highest level ($j = 5$). 197
- 6.3 (Figure taken from M14) Results of the CARGC morphology test for all three metrics (peakiness, symmetry and alignment). Dashed lines show threshold cuts. Clusters that passed all three thresholds shown with blue points (the remainder are shown in red). 198
- 6.4 Comparison between SPA results found with Chandra and XMM. Clusters which passed morphology test shown in blue, those that failed shown in red. 198
- 6.5 An XMM MOS image of an XCS-DR2 with two different pixel scales. Top: 4.35'' pixel scale (as used in XIP. Bottom: 1.1'' pixel scale (as used for the morphology test). 199
- 6.6 Preparation of an XMM MOS image for the morphology test. Top: MOS image of ObsID:0111000101. Middle: MOS image with XAPA source regions overlaid. Bottom: MOS image with adjusted source regions overlaid (areas inside these regions are masked during the morphology test). Note that the central cluster is not inside a ellipse (otherwise it would be itself masked during the test). 200

6.7	Morphology tests of a single cluster using two different core radius values as inputs. Top set (bottom left): the β -model fit (dashed line) lines up well with the surface brightness profile (blue points). Bottom set (bottom left): the β -model fit (dashed line) does not line up well with the surface brightness profile (blue points). Both sets (other figures): top left: the XMM image, top centre: the cluster region with mask applied and isophotes colour coded, top right: the cluster region with fitted isophote ellipses overlaid	201
6.8	Distributions of temperature (top) and redshift (bottom) for the 342 XCS-DR2 clusters that were subjected to the morphology test.	202
6.9	Morphology test results for 97 XCS-DR2 clusters. Objects that passed (failed) the morphology test are shown with blue (red) dots.	202
6.10	Examples of XCS-DR2 clusters classified as relaxed using the CARGC morphology test. Left: Isophote levels. Centre: Ellipses fit to isophote levels. Right: Surface brightness profile fitting.	203
6.11	As Figure 6.10, but non-relaxed XCS-DR2 clusters.	204
6.12	Comparison between the morphology metric values results found using Chandra (CARGC team analysis) and using XMM (our analysis) for 12 clusters in common between the sample. Clusters that passed (failed) the morphology test shown in blue (red).	204

- 6.13 (Wording taken from the Chandra proposal) Left: Distribution of 2 of the 3 morphology statistics measured by M15 for clusters in the Chandra archive (relaxed clusters as blue circles and unrelaxed clusters as red crosses). Dashed lines indicate cuts used in the determination of relaxation. Our targets are shown as filled, black circles. We expect the XMM PSF to reduce the peakiness measurement somewhat; even without correcting for this effect, our targets pass the same morphological cuts as the Chandra-relaxed sample. Right: Constraints on flat constant- w models, showing the improvement over M14. The “Proposal” constraints are projections based on adding the 6 targets of this proposal, as well as Perseus (approved in AO16), to the M14 sample. Compared to the M14 uncertainties, the Ω_m constraint is improved by almost 20% by this proposal, while the w constraint is improved by $\sim 11\%$ by adding Perseus and an additional $\sim 11\%$ from this proposal. The “Whitepaper” contours are projections for an additional 44 clusters beyond this proposal (Allen et al., 2013), plus Perseus (which was not included in the original white paper). 205

List of Tables

3.1	Detection grades of confirmed GMPHoRCC galaxy clusters.	118
3.2	For each sub-sample of clusters used during XCS-DR2 cluster candidate confirmation, the number of clusters for which redshift information is available, the number of those for which acceptable T_X and L_X fits were derived, and the percentage of redshifts for which the difference was $\delta < 10\%$ when compared to a measurements from another sub-sample. (The number of clusters in the redshift comparison is given in parentheses).	124
5.1	Priors used when fitting XCS-DR1 luminosity-temperature relation.	167
5.2	XCS-DR2 luminosity-temperature scaling relation fit without evolution . . .	171
5.3	Priors used when fitting $Y_{SZ} - L_X$ scaling relation.	174
5.4	Priors used when fitting $Y_{SZ} - T_X$ scaling relation.	174
6.1	Threshold cuts for s,p,a parameters.	191
6.2	XCS-DR2 clusters included in a Cycle 17 Chandra Proposal	195

Chapter 1

Introduction

Galaxy clusters are the most massive gravitationally collapsed objects in the universe. They range in size between $10^{13.5}$ and 10^{15} solar masses. They are both the largest dynamically relaxed objects and the smallest objects large enough to contain a fair sample of the materials of the universe (Sarazin, 1986). The tight connection between their observed properties and underlying physical and cosmological principles make them ideal laboratories for a variety of scientific studies. The first step in the exploitation of clusters for science is access to large, well understood cluster samples.

Subsequent chapters in this thesis describes the development of a new cluster sample. In this chapter we review the properties of galaxy clusters and the processes that underpin them. Section 1.1 introduces the XMM-Newton satellite observatory, the data from which is at the core of this thesis. Section 1.2 reviews previous surveys for clusters of galaxies, based both on X-ray selection and selection at other wavelengths (optical and microwave). Section 1.3 introduces some of the underlying theory that motivate the study of clusters of galaxies. Section 1.4 describes how cosmology is measured using galaxy clusters. Section 1.5 previews the remaining chapters in this thesis.

1.1 The XMM-Newton Satellite Observatory

This section introduces the X-ray Multi-Mirror Telescope (known as XMM-Newton). Section 1.1.1 discusses the XMM instrument setup including the satellites orbit and hardware. Section 1.1.2 describes the XMM science archive, and in Section 1.1.3 the software available to process XMM data. In Section 1.1.4 some of the nuances and details of typical XMM data processing issues are discussed.

1.1.1 Instrument Setup

Launch and Orbit

Weighing 3.8 tonnes, with a length of 10 meters and span of 16 metres, XMM-Newton is the largest European Space Agency (ESA) satellite to date. XMM-Newton was designed to collect high energy astronomical data to probe a wide variety of phenomena, from black holes to clusters of galaxies. XMM launched on 10th December 1999 as part of the Horizon 2000 Science Programme. Since then it has completed almost 3,000 revolutions of the earth, and led to more than 4,000 refereed papers.

XMM has an extremely elliptical orbit with an apogee height of 108,000 km and perigee of 12,200km (see Figure 1.1). This value changes gradually over time due to small perturbations in the orbit. The orbit was corrected in 2003 to ensure that the satellite is always in contact with one of the three ground-based stations.

Spacecraft

XMM has several instruments working at the same time. A three-axis stabilisation system delivers a pointing accuracy of one arcsecond and allows the user to choose the most suitable angle to observe a source. The satellite contains mirror modules that focus X-rays along the telescope tube to a focal plane carrying scientific instruments. It also houses propulsion and electronics modules. The scientific payload includes an optical monitor, three X-ray detectors and reflection grating spectrometers (see Figure 1.2).

Mirrors

X-rays focus onto the chips via 58 nested Wolter I mirrors (see Figure 1.3). The mirrors ability to focus X-rays varies as a function of energy and position in the field of view. The total on-axis effective area for each telescope is approximately 1550 cm^2 at 1.5keV giving a combined collecting area of 4650 cm^2 . In comparison Chandra (Section 1.2.3) has an effective area of 800 cm^2 and ROSAT (Section 1.2.3) had an effective area of 94.5 cm^2 .

European Photon Imaging Camera (EPIC)

XMM has three X-ray imaging detectors, two use MOS CCDs while the other uses PN CCDs (see Figure 1.4). The PN detector has a superior energy resolution while MOS

chips have a better spatial resolution and PSF. MOS chips are rotated by 90 degrees to one another, and all three fields of views overlap. The combined field of view has a radius of 16 arcminutes.

XMM CCDs are sensitive to the energy of incoming photons, allowing users to produce spectra of detected sources. The energy resolution the CCDs is better at lower energies. Currently, in 2015, MOS (PN) chips have a FWHM energy resolution of 70 eV (100 eV) at 1keV and 150 eV (170 eV) at 5 keV. The PN detector's energy resolution degrades by 2.5 eV per year. After launching XMM, the MOS chips showed an initial deterioration in spectral resolution of 10%. By decreasing the operational temperature of the instruments, the original performance was restored.

The XMM PN detector is composed of four quadrants, each with three CCDs with 200x64 pixels. PN CCDs have a 4.1x4.1 arcsecond pixel size. The MOS detector is made up of seven CCDs each with 600x600 pixels. MOS CCDs have a 1.1x1.1 arcsecond pixel size.

Filters

The EPIC CCDs are sensitive to UV, optical and IR light. Photons from bright optical sources can contaminate the X-ray signal. A contaminated X-ray signal can increase the image's noise levels, alter the normalisation of the energy scale, lower detection efficiency and alter charge transfers across the CCD. Therefore filters are used to block optical and near infra-red light.

The thick filter is used if there are bright sources that would worsen the calibration of the detectors. The medium filter is used to avoid contamination from point sources. The thin filter is used when there are only faint optical sources in the field of view. The thick filter leads to a smaller effective area between 0-1.3 keV.

Reflection Grating Spectrometer

Approximately 40% of the light passing through the XMM MOS mirror modules is dispersed to the reflection grating spectrometers (see Figure 1.5). The reflection grating spectrometer has a high spectral resolution in the temperature range 0.33-2.5 keV, with peak effective area at 0.83 keV of 150 cm² (Brinkman et al., 1998). The reflection grating spectrometer is not used by XCS so will not be discussed further.

Optical Monitor

The optical monitor detects photons in the optical and ultraviolet range of electromagnetic spectrum and is co-aligned with the EPIC detectors ([Mason et al., 2001](#)). The optical monitor is not used by XCS so will not be discussed further.

1.1.2 The XMM Science Archive

The XMM Science Archive (XSA) contains all public XMM data and includes XMM Observation Data Files (ODFs), Slew Data Files (SDFs), and Processing Pipeline System (PPS) products. It also includes data from the XMM-Newton Serendipitous Source Catalogue, the XMM-Newton OM Serendipitous Ultra-violet Source Survey (SUSS) Catalogue, and the Slew Survey source catalogue.

XMM instruments are always operational. While XMM is slewing into position from one observation to another, it is taking data. This information is all saved in the XMM Slew Survey. Slew data is available for download in SDF files for analysis. The Slew Survey Source Catalogue contains objects found in slew data.

Pre-processed (cleaned event lists, images, exposure maps) data are available in PPS files. PPS data were used to create the XMM-Newton Serendipitous Source Catalogue ([Rosen et al., 2015](#); [Watson et al., 2009, 2001](#)). The XMM the OM Serendipitous Ultra-violet Source Survey Catalogue contains all sources found using the optical monitor ([Page et al., 2012](#)).

XMM pointed observation data are available in their rawest available form in ODF files. XCS currently only makes use of the ODF files.

1.1.3 Specialist Astronomy Software

XMM SAS is a suite of tools designed to process XMM data. It contains programs for many tasks such as finding the suitable calibration files for an observation, creating event lists, extracting images/ spectra and many others. Some tasks can be used interactively through GUIs while others can be accessed from the command line, allowing automated data analysis pipelines.

Many SAS ([Gabriel et al., 2004](#)) tasks make use of the X-ray software HEASOFT ([Blackburn, 1995](#)). HEASOFT is a range of packages that enable the manipulation of X-ray data. It includes mission dependent packages and flexible programs that are applicable to all X-ray data. Subpackages include: CALTOOLS (calibration tasks); FIMAGE (image manipulation tasks); and XRONOS (timing analysis tasks).

A heavily used part of the HEASOFT suite by XCS, is XSPEC ([Arnaud, 1996](#)). XSPEC is a command line based X-ray spectral fitting package. It uses spectral data, background data, auxiliary response files and redistribution matrix files, created for a source, to fit an X-ray spectral model.

Fitting a spectrum to the detected X-ray photons in the instrument channels is non-trivial. The inverse of the spectral response cannot be convolved with detected photons to recover a spectrum. Instead, a model spectrum must be convolved with the spectral response and compared to the number of detected photons in each energy bin. A fit statistic is used to check if it is a good match (e.g the Cash statistic ([Cash, 1979](#))). Model parameters are varied to find the best fitting spectra. To find a confidence interval, parameters are varied again to find a range of values before a critically poor fit value is determined.

DS9 and TOPCAT ([Taylor, 2005](#)) are general purpose astronomical packages. DS9 is a FITS image viewer that also allows region files to be created and overlaid. TOPCAT is a program that allows for manipulation of tables, with emphasis on applications to astronomy. TOPCAT allows for easy cross-matching between large datasets.

1.1.4 Features to account for when analysing XMM data

XMM Background

The XMM background is complex and multi-sourced (Snowden et al., 2004; Collier et al., 2004; Kuntz & Snowden, 2001; Hickox & Markevitch, 2007). The instrument suffers from detector noise and interactions between high-energy particles and the satellite architecture. There is a background component caused by soft protons funnelled onto the detector by the mirrors. Other sources of background include stellar winds, reflections of photons from outside the field of view, and the galactic disc. The background can be modelled and included in fittings or approximated and subtracted from source data.

Instrumental Calibration

XMM is a complicated instrument that has been operating in a hostile environment for almost 16 years. The science team that control XMM constantly monitor the health of the instrumentation and how it changes over time. They produce frequent calibration updates. Updates account for new instrumental understanding that will affect old data, and any changes to the instrumentation that will affect new data. These calibrations concern a range of issues including degradation in charge transfer efficiency, effective area, hot pixels, hot columns and changes in the instrument's gain. On two occasions, micrometeorite strikes have occurred which as well as destroying CCDs (see Figure 1.10) required extensive follow-up tests.

XMM calibrations account for many of the features listed in Section 1.4. Calibration takes into account all aspects of the satellites health including PSF, effective area, vignetting and spectral resolution.

Effective Area

Effective area describes the total area of the focusing mirrors capable of focusing photons of a given energy to a particular point on a detector (see Figure 1.6). The effective area is useful, for example, in accounting for differences between MOS detectors, where around half of photons divert to the reflection grating spectrometer, and the PN detectors. Auxiliary response files (ARF) contain the effective area. ARF files are generated using the SAS task `arfgen`.

Response Files

The redistribution matrix file (RMF) captures the instrument's spectral resolution as a function of energy. In the case of the MOS detector, this is created using calibration data which accounts for spatial dependence. The PN RMF file does not account for spatial dependence. Currently, bad pixels are not taken into consideration. RMF files are generated using the SAS task `rmfgen`.

Point Spread Function (PSF)

The point spread function (PSF) is complicated; it is simplest at low energies and in the centre of the FOV, where it is approximately circular with an FWHM of 4.5 arcseconds. Towards the edge of the FOV the FWHM gets progressively larger and the shape becomes more elliptical and finally bow tie shaped (Read et al., 2011) (see Figures 1.7 and 1.8).

There are currently five PSF models available. Two are two-dimensional models: `medium mode` and `ellbeta`. `Medium mode` is a set of 66 images taking into account six off-axis angles and eleven energies. `Ellbeta` is a 2D parameterization of the three XMM-Newton detectors accounting for the individual detector, energy, off-axis angle and azimuthal angle (see Figure 1.8). Three PSF models are one dimensional. `Low mode` is no longer recommended for use. `High mode` is a Gaussian parametrization of the `medium mode` images. The `extended mode` uses a King profile taking into account energy, off-axis angle and detector.

Pointing Modes

XMM has a wide variety of applications, so is equipped to carry out observations with different settings. These can involve altering the readout times of its CCDs, choosing a suitable pointing, and specifying which parts of the detector will be read out (see Figure 1.9, 1.10, 1.11, 1.12).

In full frame modes, all CCDs are read out. In partial window modes, the central CCD of the MOS chip is not used or partially read out while the PN chips are half read out, or only half of a single chip is used. In timing mode, imaging is collapsed into one dimension to allow quicker read out. In the mosaic mode, an individual pointing is made and then the satellite moves into a new position to take another pointing. The process repeats until it has built up an image of a larger contiguous field in the sky.

1.2 Cluster Surveys

There are numerous surveys of galaxy clusters. In this section we will discuss how several of these were performed. Particular emphasis is paid to the subject of this thesis, the XMM Cluster Survey. We note that only surveys that aim to find clusters (both new discoveries and re-discoveries) are discussed below. Surveys that follow-up existing catalogues (e.g. [Mantz et al., 2014b](#)) are not discussed here.

1.2.1 Detection Methods

One of the key advantages of clusters over other probes of astrophysics and cosmology is the fact that they can be detected and studied at a variety of wavelengths. For the purposes of *cluster discovery*, the optical plus near infra-red, X-ray, and microwave bands are the most important, because these give access to the features of: galaxy over density ([Figure 1.13](#)); X-ray emission from the inter-galaxy gas ([Figure 1.14](#)); and the shadowing effect of that gas (known as the ICM, for intra-cluster medium) on the Cosmic Microwave Background ([Figure 1.15](#)). The ICM is composed of a hot ($10^7 - 10^8$ K) X-ray bright ($10^{43} - 10^{46}$ erg s⁻¹) ionised plasma. This intracluster gas is the dominant reservoir of baryons in the cluster. The ICM accounts for 15% of the total mass needed to keep the system gravitationally bound. Dark matter explains the difference. Dark matter was first postulated in the 1930's following observations of the galaxy velocity distribution in the Coma cluster ([Zwicky, 1933](#)). The exact nature of Dark matter is still an outstanding question in astrophysics today.

Galaxy clusters were first noticed as overdensities of 'nebulae' on the sky ([Messier, 1784](#); [Herschel, 1811](#)). Since then a plethora of optical cluster catalogues have been produced, with the most famous being the Abell catalogues ([Abell, 1958](#); [Abell et al., 1989](#)). The first generation of X-ray detectors mounted on rockets, balloons, and the first X-ray satellite Uhuru ([Giacconi et al., 1971](#)) found X-ray emission originating from the ICM of nearby galaxy clusters Virgo and Coma. Microwave detections of clusters came much later. The observational signal, the so-called Sunyaev-Zel'dovich effect was predicted in the early 1970's ([Sunyaev & Zeldovich, 1972](#)), but not measured until the 1980's ([Birkinshaw et al., 1984](#)).

For the purposes of *cluster studies*, the combination of wavelengths can be important: [Figure 1.16](#) shows merging clusters where the X-ray gas has disassociated from the galaxy

population, and where weak lensing studies (based on optical observations) demonstrate that the dark matter is following the galaxies not the gas. Other examples are shown in Figures 1.17 and 1.18, where far-infrared images have been used to highlight star formation in a very distant cluster and radio interferometry has been used to investigate how relativistic charged particles interact with the ICM. We do not discuss studies of individual clusters further in this thesis, because our focus is on discovery and on statistical analysis of the population as a whole.

1.2.2 XMM Cluster Survey

Motivation and Goals

The XMM Cluster Survey (XCS) (Romer et al., 2001) is a survey of clusters, both serendipitous and targeted, found in the XMM archive. The primary goal of XCS is to constrain cosmological parameters using clusters and their properties. Secondary goals include; fitting scaling relations; understanding the astrophysical processes governing clusters; and studies of the evolution of galaxies in clusters.

Early predictions for XCS envisioned a cluster survey of 8,000 galaxy clusters, 750 of which would be at $z > 1$. The eventual XMM catalogue with measurements of luminosity and temperature would be more than an order of magnitude better than the state of the art results at the time. This survey would then be used to place constraints on Ω_M and Ω_Λ (for definitions see SecIntro:Sec:ClusTheory).

The number of clusters detected and predicted selection function were used to forecast possible cosmological results using Markov Chain Monte Carlo methods (Sahlén et al., 2009). Predicted constraints of 0.05 were found on Ω_M and Ω_Λ . Predicted constraints on σ_8 were found to be 0.05.

Particular attention was paid to incorporating the following nuisance parameters: scatter in scaling relations; the survey simulated selection function; and redshift errors (including catastrophic errors). Importantly, it was shown that scaling relation systematics can lead to a $2\text{-}\sigma$ difference between the measured and fiducial model (see Figure 1.21,1.22).

Publications

A Serendipitous Galaxy Cluster Survey with XMM: Expected Catalogue Properties and Scientific Applications (Romer et al., 2001)

An outline of how the new XMM satellite will serendipitously discover a large catalogue of galaxy clusters that can be used to fit cosmology. The paper predicted the properties of sets of clusters, detected by the EPIC PN detector, with a given simulated cluster population.

Apparent and actual galaxy cluster temperature (Liddle et al., 2001)

This study concentrates on how apparent temperatures, combined with other X-ray information, can constrain cluster redshifts. A cosmological fit can be made on Ω_m and σ_8 , but to break the degeneracy between the two, redshifts are needed.

The XMM Cluster Survey: A Massive Galaxy Cluster at $z=1.45$ (Stanford et al., 2006)

Six galaxies within XMMXCS J2215.9-1738 were used to fit a redshift, $z = 1.457$. The cluster had the highest measured temperature for a cluster at $z \geq 1$. An X-ray temperature of 7.4 keV was fit, however this may be reduced to 6.5 keV if a suspected contaminating emission is present.

The XMM Cluster Survey: The Dynamical State of XMMXCS J2215.91738 at $z=1.457$ (Hilton et al., 2007)

The number of galaxies used to measure a redshift for XMMXCS J2215.9-1738 was increased from 6 to 17. A line of sight velocity was measured, $580 \pm 140 \text{ km s}^{-1}$. The cluster is shown to be under luminous - this could be due to a recent merger, although no strong supporting evidence exists.

Early assembly of the most massive galaxies (Collins et al., 2009)

The stellar masses of brightest central galaxies in five high redshift clusters ($1.2 \leq z \leq 1.5$) are calculated. Their evolution are investigated and compared to a low redshift cluster sample. The stellar masses are not significantly different implying that brightest central galaxies were already assembled nine billion years ago.

The XMM Cluster Survey: Galaxy Morphologies and the Color-Magnitude Relation in XMMXCS J2215.91738 at $z=1.46$ (Hilton et al., 2009)

A study of the morphological properties of galaxies in XMMXCS J2215.91738. The proportion of galaxy types is found to be similar to clusters at redshift $z = 1$. The colour

magnitude relation is similar to Coma, but with a much larger scatter.

The XMM Cluster Survey: Forecasting cosmological and cluster scaling-relation parameter constraints (Sahlén et al., 2009)

The predicted number of clusters in 500 square degrees of sky, in bins of mass and redshift are used forecast cosmological constraints. It is shown that making wrong assumptions when including scaling relations can lead to measurements more than $2\text{-}\sigma$ different to the fiducial model (See Figures 1.21,1.22).

The XMM Cluster Survey: The Build Up of Stellar Mass in Brightest Cluster Galaxies at High Redshift (Stott et al., 2010)

Twenty clusters at redshift, $z \geq 0.8$ are examined. Analysis on the sample shows that average stellar mass in the brightest central galaxy has remained constant since $z = 1.5$. The result implies that dry merging has little effect on stellar mass build up.

The XMM Cluster Survey: Active Galactic Nuclei and Starburst Galaxies in XMMXCS J2215.91738 at $z=1.46$ (Hilton et al., 2010)

Chandra and Spitzer data were used to find previously undetected point sources in XMMXCS J2215.91738. A joint analysis of XMM and Chandra data is performed finding a new best fit X-ray temperature of 4.1 keV. The cluster is now less significantly under-luminous.

The XMM Cluster Survey: X-ray analysis methodology (Lloyd-Davies et al., 2011)

The X-ray XCS event list cleaning, image reduction, source detection, and spectra fitting pipelines are described. The X-ray source properties of sources in 5,776 observations are presented. There are 3,675 extended sources with more than 50 counts - these are galaxy cluster candidates (the new X-ray analysis methodologies are presented in Chapter 2).

The XMM Cluster Survey: Predicted overlap with the Planck Cluster Catalogue (Viana et al., 2012)

A list of clusters in XCS likely to be detected by Planck. Three such clusters are already present in the Planck Early Sunyaev-Zel'dovich (ESZ) catalogue. Their properties are characterised and the work takes into account effects such as the XCS selection function.

The XMM Cluster Survey: The interplay between the brightest cluster galaxy and the intra-cluster medium via AGN feedback (Stott et al., 2012)

The relationship between intracluster medium, brightest central galaxy, and its black hole is investigated. Systems with AGN are found to be dominated by radiative feedback below 2 keV and by gas cooling above this temperature. Scaling relations are steepest where BCGs are located at the peak of X-ray emission, but are more self similar when BCGs are smaller or offset from the X-ray peak.

The XMM Cluster Survey: The Stellar Mass Assembly of Fossil Galaxies ([Harrison et al., 2012](#))

A sample of 17 fossil groups are found from the magnitude difference between the brightest and fourth brightest galaxies. Fossil galaxies are found to have as much as 85% of the total optical luminosity within $0.5 R_{500}$.

The XMM Cluster Survey: Optical analysis methodology and the first data release ([Mehrtens et al., 2012](#))

A public release of a catalogue of galaxy clusters detected by XCS containing 503 (256 new to the literature) optically confirmed objects. Of these 463 have a redshift and 401 have spectrally measured temperatures and luminosities (a new catalogue of galaxy clusters is presented in Chapter 3).

The XMM Cluster Survey: Evidence for energy injection at high redshift from evolution of the X-ray luminosity-temperature relation ([Hilton et al., 2012](#))

A luminosity-temperature scaling relation for the 211 clusters in XCS-DR1 with spectroscopically measured redshifts. The normalization shows strong negative evolution with redshift which is interpreted as evidence that the majority of excess entropy is injected into the cluster at high redshift (an updated scaling relation is presented in Chapter 5).

The XMM Cluster Survey: testing chameleon gravity using the profiles of clusters ([Wilcox et al., 2015](#))

Chameleon gravity models are tested using XCS galaxy clusters. A chameleon fifth force would exert an influence over the hot gas of a cluster but not its weak lensing signal. General relativity is sufficient to explain their stacked X-ray and weak lensing profiles.

Selection Function

To avoid overrepresented clusters in a catalogue biasing any scientific applications it is important to quantify and correct for selection effects. X-ray selected cluster samples find

clusters based on their surface brightness, with brighter clusters detected more often than less luminous clusters.

X-ray selection functions can be calculated analytically or numerically. An analytical selection function places fake cluster models (covering a relevant parameter space, such as counts and core radius) into real world observations, whereas a numeric selection function are fit with simulations of the X-ray sky, modified to match the properties of an X-ray satellite. The selection function is then the probability that sources are found as a function of their properties. (The XCS selection function is described in greater details in [Sahlén et al. \(2009\)](#); ? and [Lloyd-Davies et al. \(2011\)](#))

1.2.3 Other X-ray Cluster Surveys

Pre ROSAT

The Einstein Observatory, launched into orbit in 1978, was the first NASA X-ray imaging telescope designed to observe objects outside of our solar system. The Einstein Observatory had a 40 arcsecond angular resolution and was sensitive in the 0.2-3.5 keV band, with effective area peaking at 20 cm² at 0.25 keV.

The Einstein-Observatory Extended Medium-Sensitivity Survey (EMSS) ([Gioia et al., 1990](#); [Henry et al., 1992](#); [Gioia & Luppino, 1994](#))

Clusters had been previously detected in the X-ray band, but EMSS was first to demonstrate the ability to serendipitously detect them, in large numbers, in X-ray surveys. A total of 93 clusters were found in 778 square degrees of sky. EMSS made a preliminary detection of evolution in the X-ray properties of clusters.

ROSAT

The ROentgen SATellite (ROSAT) was launched on June 1, 1990. ROSAT imager had a 38 arcminute square field of view with 2 arcsecond spatial resolution. The instrument was sensitive in the 0.1-2.5 keV and had an 80 cm² effective area at 1 keV.

MAssive Cluster Survey(MACS) ([Ebeling et al., 2001](#); [LaRoque et al., 2003](#); [Allen et al., 2004](#); [Hsu et al., 2013](#))

The MAssive Cluster Survey (MACS) is aimed at finding very luminous clusters at redshift, $z \geq 0.3$. The sample applied hardness and flux cuts to 5,000 X-ray sources in the

ROSAT survey area of 22,735 square degrees. It has found 124 galaxy clusters increasing the known sample of high redshift objects by 20 times.

REFLEX (Collins et al., 2000; Böhringer et al., 2001a; Boehringer et al., 2001b; Schuecker et al., 2001; Böhringer et al., 2002; Schuecker et al., 2002, 2003; Böhringer et al., 2004; Guzzo et al., 2009)

The ROSAT-ESO-Flux-Limited-X-ray (REFLEX) cluster survey was carried out using data taken by the ROSAT satellite. REFLEX found 452 galaxy clusters and have redshifts for all but three of them. REFLEX used this catalogue to find two point correlation functions between galaxy clusters, the density fluctuation power spectrum, the X-Ray luminosity function and constrain cosmological parameters.

400d (Burenin et al., 2007; Voevodkin et al., 2010; Israel et al., 2010, 2012, 2014; Vikhlinin et al., 2009a,b)

The 400d cluster survey found 242 galaxy clusters using 400 square degrees of pointed ROSAT observations. The Chandra Cluster Cosmology follow up program observed a complete sample of 41 of the cluster found by the 400d survey in conjunction with 49 low redshift clusters from the ROSAT All Sky Survey. These clusters were used to fit cosmology using cluster number counts.

BCS (Ebeling et al., 1997, 1998; Crawford et al., 1999; Ebeling et al., 2000)

The ROSAT Brightest Cluster Sample was the largest cluster survey while ROSAT was still operational. The BCS contained the 201 galaxy clusters in the northern sky outside the galactic plane ($|b| \geq 20$ degrees) with fluxes $4.4 \times 10^{-12} \text{ ergs cm}^{-2} \text{ s}^{-1}$.

ROSAT Deep Cluster Survey (Rosati et al., 1998; Borgani et al., 1999, 2001)

The ROSAT Deep Cluster Survey found 103 galaxy clusters in the deepest 50 square degrees covered by ROSAT, including four clusters at redshift, $z \geq 0.9$. The sample was used to measure Ω_m and investigate the cluster luminosity function.

The Bright Serendipitous High-redshift Archival ROSAT Galaxy Cluster Survey (Bright SHARC) (Nichol et al., 1999; Adami et al., 2000; Romer et al., 2000)

Bright SHARC used the 460 pointed ROSAT observations with greater than 10ks exposure time to find galaxy clusters. The survey confirmed and measured redshifts for 37 galaxy clusters. A selection function was calculated and the cluster luminosity function fit.

Chandra

Chandra is a NASA X-ray mission launched on July 23, 1999. Chandra has 0.492 pixel size. Chandra has several instruments but the High Resolution Camera I has the largest field of view (a 30 arcminute square). The Advanced CCD Image Spectrometer (ACIS) is made up of ten 1024x1024 CCD chips. ACIS chips are arranged into a 2x2 and a 1x6 CCD array, the later of which can be used for imaging or as a grating readout. Chandra's effective area peaks at 600 cm² at 1.5 keV.

Ultra-deep catalog of X-ray groups in the Extended Chandra Deep Field South ([Finoguenov et al., 2015](#))

Using deep X-ray observations taken by XMM and Chandra, extended sources are found with fluxes down to 2×10^{-16} ergs s⁻¹ cm⁻². In a 0.3 square degree field, 46 galaxy groups are found.

Chandra Multi-wavelength Project - Serendipitous Galaxy Cluster Survey ([Barkhouse et al., 2006](#))

The Chandra Multi-wavelength Project - Serendipitous Galaxy Cluster Survey compares X-ray and optical cluster detection methods in Chandra observations totalling 130 square degrees. They find 115 optically detected clusters, of which 28 were also detected in X-ray images. The non-detected clusters were significantly poorer systems.

XMM-Newton

The X-ray Multi-Mirror Mission (XMM-Newton) was launched on December 10, 1999. XMM-Newton is sensitive in the 0.1-15 keV energy range. It has a 33x33 arcminute² field of view. XMM-Newton contains three imaging detectors; PN, MOS1 and MOS2. The PN detector has the largest effective area; 1,227 cm² (XMM is reviewed in greater detail in Section 1.1).

XMM-LSS ([Pierre et al., 2006](#); [Bremer et al., 2006](#); [Pacaud et al., 2007](#); [Adami et al., 2011](#))

XMM LSS has produced catalogue papers, investigated cluster spatial distributions, investigated AGN within galaxy clusters, classified point sources, looked at the angular correlation function of point sources and found lensing candidates. They have found more than 30 galaxy clusters.

XXL (Pierre et al., 2011; Mantz et al., 2014a)

The XXL cluster survey uses two 25 deg² regions of the sky, split into ten kilosecond XMM pointings. The survey has so far used more than 6Ms of time, and is the largest XMM project to date. The primary goal of the project is to fit the dark energy equation of state.

XXL has produced papers looking at high redshift SZ detected clusters and best practice in cosmological analysis with galaxy cluster surveys. XXL will release a series of papers including a cluster catalogue, scaling relations and cosmology.

XCLASS (Clerc et al., 2012b,a)

The XCLASS survey found 850 clusters using 2774 high-galactic observations from the XMM archive. These clusters have been used a count rate to hardness ratio to fit cosmological parameters.

The XMM-Newton Distant Cluster Project (Mullis et al., 2005; Fassbender et al., 2008; Rosati et al., 2009; Santos et al., 2009; Schwöpe et al., 2010; Fassbender et al., 2011a,b; Šuhada et al., 2011)

The XMM-Newton Distant Cluster Project (XDCCP) find high redshift galaxy clusters in the XMM archive. XDCCP have detected 47 galaxy clusters with spectroscopic redshifts greater than 0.8.

Swift

Swift is a gamma ray mission including an X-ray detector launched on November 20, 2004. It has an energy range between 0.2-10 keV with an effective area of 220 cm² at 1.5 keV. Swift has a 23.6 × 23.6 arcminute field of view.

Swift X-ray Cluster Survey (Tundo et al., 2012; Tozzi et al., 2014; Liu et al., 2015)

The Swift X-ray Cluster Survey (SXCS) are attempting to understand global cluster populations using serendipitously detected clusters in the Swift data archive. They have attempted to understand their selection function. SXCS have detected 263 galaxy clusters, of which 126 are new. SXCS have measured redshift information for 158 clusters.

1.2.4 Optical and Microwave Cluster Surveys

The Abell Cluster Catalogues (Abell, 1958; Abell et al., 1989)

The first systematically produced catalogue of clusters was created by George Abell in

1958. This catalogue contained 2,712 clusters visually identified in the northern sky using red Palomar Sky Survey 103a-E plates (Abell, 1959). Cluster candidates were confirmed if they had at least 30 bright galaxies within a $1.72/z$ arcminutes radius circle, and were at a nominal redshift of $0.02 \leq z \leq 0.2$

This catalogue was updated to include clusters in the southern sky in 1989. An additional 1,361 clusters were found in the deep IIIa-J plates produced for the Southern Sky Survey (SSS) (Schuster, 1980) giving a total catalogue size of 4,703 clusters.

The MaxBCG Cluster Catalogue (Hansen et al., 2005; Koester et al., 2007a,b; Rozo et al., 2007; Johnston et al., 2007a,b; Rykoff et al., 2008b,a; Hansen et al., 2009; Becker et al., 2007; Sheldon et al., 2009a; Rozo et al., 2009a,b, 2010; Tinker et al., 2012; Sheldon et al., 2009a)

The MaxBCG cluster finding algorithm finds galaxy clusters by searching for red-sequence galaxies and a bright central galaxy in the SDSS regions. The MaxBCG cluster finder identified 13,823 galaxy clusters.

The MaxBCG cluster catalogue has been used to fit cosmology using cluster abundances and the mass-to-number ratio of galaxy clusters. Masses for MaxBCG clusters have been found using weak lensing. There has been work to calibrate the optical-X-ray mass proxy scaling relations. The properties of the MaxBCG galaxies have been investigated, as well as their velocity dispersions.

Percolation Galaxy Groups and Clusters Catalogue (Berlind et al., 2006)

The Percolation Galaxy Groups and Clusters method searched for over-densities of galaxies in a volume limited samples of SDSS galaxies, at $z \leq 0.1$ using a redshift-space friends-of-friends algorithm. The optimal linking left were found using mock catalogues of galaxies where it is known if more than one galaxy inhabits a single dark matter halo. The Percolation Galaxy Groups and Clusters catalogue contains 57,138 clusters.

The Planck Cluster Sample (Planck Collaboration et al., 2011a,b,c,d,e,f, 2013a,b, 2014a,b,c, 2015a,b)

Planck is an all sky CMB mission that detects galaxy clusters using the Sunyaev-Zel'dovich effect. The Planck cluster catalogue contains 1,203 confirmed galaxy clusters. The catalogue is estimated to be 83% pure. The Planck team fit cosmological parameters with clusters and primary fluctuations in the CMB. Currently there is tension in σ_8 measure-

ments made with the two methods. (The overlap between XCS-DR2 and Planck are given in Chapter 3)

The South Pole Telescope Cluster Sample (Reichardt et al., 2013; Benson et al., 2013; Vanderlinde et al., 2010; Williamson et al., 2011; Bleem et al., 2015; Liu et al., 2015)

The South Pole Telescope has produced a galaxy cluster catalogue covering 2,500 square degrees of sky that contains 677 confirmed clusters. These clusters have been used to constrain the richness mass relation. The baryonic contents and AGN cavities of these clusters have been used to probe baryonic physics. (The overlap between XCS-DR2 and SPT are given in Chapter 3)

The RedMaPPer Cluster Samples (Rykoff et al., 2014; Rozo & Rykoff, 2014; Rozo et al., 2015b,a)

Redmapper is a red-sequence cluster detection algorithm. Redmapper uses an adaptable pipeline that self-trains its red-sequence model with spectroscopic data and can then be applied to large photometric surveys. The algorithm has been run on the SDSS regions and found 25,000 clusters, and is in the process of being run on the DES regions. (The overlap between XCS-DR2 and RedMaPPer are given in Chapter 3)

1.3 Concepts in Cluster Astrophysics

Clusters of galaxies are complex astrophysical laboratories. The interplay between their various components, such as between active galactic nuclei at the core of the brightest cluster galaxy and the hot ionised plasma that fills the space between the galaxies, leads to a wealth of observational phenomena and theoretical challenges. Some of these phenomena and challenges are described in other parts of this thesis, but for now let us consider a “cartoon” version of clusters, i.e. perfectly spherical, completely isolated, objects. The properties of these “cartoon” clusters would be governed by gravity alone and not affected by complex astrophysics.

However, before we discuss clusters, it is prudent to review some very basic concepts in modern cosmology to give context to what follows.

1.3.1 Basic Concepts in Cosmology

The simplest cosmological models assume that gravity is the only force that influences the dynamics of cosmic expansion. This model allows for three possible universes; open, flat or closed. An open universe has negative curvature and does not contain enough matter to halt the cosmic expansion and will have a critical density, $< \rho_c$. Contributions to the density are often expressed in terms of this value. A flat universe has no curvature and will eventually stop expanding but will not collapse. A closed universe is positively curved and will eventually collapse back in on itself.

The density of a universal component can be expressed:

$$\Omega_i = \frac{\rho_i}{\rho_c} \tag{1.1}$$

where i is the component of interest. The symbol Ω_M is used to express the contribution from non-relativistic matter (both baryonic and dark), Ω_R for that of relativistic particles (radiation and neutrinos). Evidence from the CMB implies that the universe is flat (e.g. [Larson et al., 2011](#); [Dunkley et al., 2011](#); [de Bernardis et al., 2002](#)), thus implying that $\Omega_{total} = 1$. Evidence from various observations, including the gas fraction of massive galaxy clusters and the large scale distribution of galaxies, suggests that the density of matter is $\Omega_M \simeq 0.3$, and the density of radiation is negligible today (although was the

dominant component in the early universe). Therefore, there is a gap of $\Omega_{unknown} \simeq 0.7$ to be filled to ensure $\Omega_{total} = 1$

Recent observations of supernovae have suggested that the expansion of the universe is currently accelerating. This in turn implies the existence of a peculiar phenomenon (particle, field, phase transition etc.) that has an effective negative pressure. One such phenomenon would be a cosmological constant (Λ) that is contributing sufficient energy density to make up the difference required for a flat universe ($\Omega_\Lambda \simeq 0.7$). The existence of this constant is not contrary to fundamental physics, but the measured value is vastly different than that predicted - the so-called 'Cosmological Constant Problem'. An alternative model, dark energy, is one where the negative pressure phenomenon does not have a constant energy density, but one that varies with time. Dark energy can be treated like a fluid with an equation of state:

$$p_\Lambda = w\rho_\Lambda, \quad (1.2)$$

where any value of $w < -1/3$ will lead to an accelerated expansion and in the special case of $w = -1$ the fluid behaves like a cosmological constant.

Some other definitions useful for this thesis include:

Proper Distance The proper distance, $d(t)$ grows over time with the expansion of the universe. The co-moving distance χ is measured while accounting for cosmic expansion. It is defined so that two objects moving away from one another due to the expansion of the universe remain a constant comoving distance apart. χ can be defined as:

$$d(t) = a(t)\chi, \quad (1.3)$$

where a is the scale parameter of the universe and is defined to be unity today, i.e. $a_0 = 1$.

The Hubble Parameter The Hubble parameter is defined in terms of the time differential of a :

$$H(t) = \frac{\dot{a}}{a}. \quad (1.4)$$

This parameter changes with time

$$H(z) = H_0 E(z), \quad (1.5)$$

where H_0 is the value today (measured to be $\simeq 70 \text{ km s}^{-1} \text{ Mpc}^{-1}$) and $E(z)$ depends on the underlying cosmology, e.g. in a flat universe with a cosmological constant:

$$E(z) = \sqrt{\Omega_M(1+z)^3 + \Omega_\Lambda}. \quad (1.6)$$

We can define the critical density in terms of $H(z)$ as follows with reference to the Friedman equation:

$$\rho_c = \frac{3H^2}{8\pi G}. \quad (1.7)$$

Cosmological Redshift A photon emitted at t_e and received at t_0 will be stretched by the expansion of the universe. This is known as redshifting and is defined as:

$$1+z = \frac{\lambda_0}{\lambda_e} = \frac{a_0}{a_e} \quad (1.8)$$

Redshift can also be expressed in terms of a

$$a = \frac{1}{1+z} \quad (1.9)$$

The Hubble parameter can be written:

$$H(z) = H_0 E(z) \quad (1.10)$$

Luminosity and Angular Diameter Distance The luminosity distance, d_L , to a source can be calculated from the measured flux F if its intrinsic luminosity L is known:

$$d_L = \left(\frac{L}{4\pi F} \right)^{1/2} \quad (1.11)$$

The angular diameter distance, d_A , to a source can be calculated from the measured projected size if its intrinsic size is known. It is related to d_L as follows:

$$d_A = d_L / (1 + z)^2 \quad (1.12)$$

Both d_L and d_A depend on the underlying cosmology. The exact dependencies are complex and require numerical integration, but in a flat universe, at low z , d_L can be approximated as follows:

$$d_L \simeq \frac{c}{H_0} z \quad (1.13)$$

Comoving Volume The co-moving volume is found by integrating [1.12](#) over redshift and the solid angle.

$$dV_x(z) = \frac{c}{H_0} \frac{(1+z)^2 d_A^2}{E(z)} d\Omega dz \quad (1.14)$$

1.3.2 The Relationship Between Cluster Mass and Temperature

Let us first consider a cluster that contains only dark matter particles (i.e. devoid of stars or ICM), we can derive an exact relationship between the total mass of the “cluster” and the temperature of the dark matter particles, as shown below.

In an isolated cluster, the kinetic energy, K , is related to potential energy, U , by the Virial relation:

$$2K + U = 0 \quad (1.15)$$

The potential energy of the cluster is given by:

$$U \propto \frac{GM_{\Delta}^2}{R_{\Delta}} \quad (1.16)$$

where M_{Δ} is the mass within R_{Δ} , and Δ is the over density factor compared to the critical density (ρ_c):

$$M_{\Delta} = 4\pi R_{\Delta}^3 \rho_c. \quad (1.17)$$

Assuming the dark matter particles behave like a monatomic gas, the kinetic energy per particle is proportional to temperature. The total kinetic energy summed over all the particles will be proportional to the cluster mass, so

$$M_{\Delta} T \propto \frac{GM_{\Delta}^2}{R_{\Delta}}. \quad (1.18)$$

Combining these two equations and re-arranging leads to

$$M_{\Delta} \propto T^{3/2} \rho^{-1/2}. \quad (1.19)$$

Using Equation 1.7 and re-arranging leads to

$$\begin{aligned} M_{\Delta} &\propto T^{3/2} E(z)^{-1} \\ &\propto T^{3/2} E(z)^{-1}. \end{aligned} \quad (1.20)$$

1.3.3 The Relationship Between Cluster Mass and Radius

The relationship between “cluster” mass and radius for collision-less, i.e. pressure-less, dark matter in spherical halos that develop gravitationally in an expanding universe is not trivial to determine analytically. However it has been predicted to high accuracy using numerical simulations and is usually expressed in terms of the following, so-called NFW, parameterisation (Navarro et al., 1996):

$$\rho(r) = \frac{\rho_0}{\frac{r}{R_s} \left(1 + \frac{r}{R_s}\right)^2}. \quad (1.21)$$

where r is the radius and R_s is a scale radius.

1.3.4 X-ray Emission Mechanisms

Our cartoon cluster resides in an expanding Universe that originated in a hot big bang. A natural consequence of the big bang model is baryogenesis, i.e. the formation of light elements a few minutes after the big bang. Therefore, let us now consider that our “cartoon” cluster contains, in addition to dark matter, baryons. In a real cluster, those baryons would be distributed between the diffuse intracluster medium and condensed structures, such as stars in galaxies. Moreover, in addition to the light elements created in baryogenesis, there is by now a rich assortment of heavier elements produced via fusion in stars diffused through the ICM. Typically the heavy (heavier than Helium) element abundance in clusters is roughly one third of that found in the Sun ($0.3Z_\odot$).

Consider a gas atom entering a cluster for the first time. It will be drawn towards the centre of the gravitational well. In the process, its potential energy is converted into thermal energy by adiabatic compression and shocks. Heating continues until it reaches thermal equilibrium at the virial temperature (see above), and because the virial temperature is high, all but the heaviest elements are fully ionised:

$$T \propto \frac{GM\mu m_H}{3k_B R} \quad (1.22)$$

G is the gravitational constant. M is the total cluster mass, μm_H is the mean gas mass per particle, and k_B is the Boltzmann constant. R is the cluster radius. The ionised particle can lose thermal energy (and fall even closer to the cluster core) through radiation. In clusters, the dominant radiation mechanism is due to thermal bremsstrahlung and line emission. The equation for thermal bremsstrahlung is:

$$\epsilon_\nu^{ff} = \frac{2^5 \pi e^6}{3m_e c^3} \frac{2\pi}{3m_e k}^{1/2} n_e T^{1/2} \exp(-h\nu/kT) \sum_i Z_i^2 n_i g_{ff}(Z_i, T, \nu) \quad (1.23)$$

where ϵ_ν^{ff} is energy emitted per unit time, frequency and volume, and $g_{ff}(Z_i, T, \nu)$ is the

Gaunt factor, this slowly varies over T and ν and corrects for quantum effects and distant collision events. The sum is over all ions in the ICM but dominated by hydrogen and helium.

Bremsstrahlung continuum emission dominates for virial temperatures of $T > 3 \times 10^7$ keV, but for lower temperatures, line emission becomes increasingly important, for example the $F_e K_\alpha$ complex at around 6.7 keV (see Figure 1.23).

Most X-ray lines are excited by collisions with electrons. The equation for line emission is given by:

$$\int \epsilon_\nu^{line} d\nu = n(X^i) n_e \frac{h^3 \nu \Omega(T) B}{4 \omega_{gs}(X_i)} \left[\frac{2}{\pi^3 m_e^3 k T} \right]^{1/2} e^{-\Delta E/kT} \quad (1.24)$$

Where $h\nu$ is the energy of transition. ΔE is the difference in excitation energy between the excited state and the ground state. B is the branching ratio of the line and Ω is the collisional strength (not the density parameter). $\omega_{gs}(X_i)$ is the statistical weight of the energy levels of the ion.

The intracluster medium is in collisional ionization equilibrium, meaning the ionization fractions depend on electron temperatures. The density of an ion is proportional to the proton density and element abundance. It is clear from this and Equation 1.24 that all X-ray emission is proportional to the density of protons and electrons. Luminosity is defined:

$$L_\nu = \Lambda_\nu(T, Z) \int n_e n_p dV \quad (1.25)$$

and X-ray surface brightness by:

$$I_\nu = \Lambda_\nu(T, Z) \int n_e n_p dl \quad (1.26)$$

The first equation is integrated over the volume and the second along the line of sight. It is useful to note that both thermal bremsstrahlung and line emissivity are proportional to gas density, so their ratio is independent of gas density. By using one of these mechanisms to fit a temperature, their ratio can be used to estimate the abundance of heavy elements

(For a more in depth discussion of equations 1.23-1.26 the reader is referred to (Sarazin, 1986)). Λ_ν is the cooling function. The cooling function calculates the emitted energy per volume for a plasma given its temperature and emissivity

Other useful measures of the intracluster medium include entropy, S , and the combination of temperature and gas mass, Y_X . Entropy is defined as:

$$S = \frac{k_B T_{gas}}{(n_e)^{2/3}} \quad (1.27)$$

and is related to thermodynamic entropy, s , by Voit (2005):

$$s = k_B S + constant. \quad (1.28)$$

Y_X is a low scatter mass proxy defined as:

$$Y_X = M_{gas} T_X \quad (1.29)$$

where M_{gas} is measured within a fixed overdensity, usually R_{500} .

1.3.5 X-ray Surface Brightness Profiles

Assuming that a cluster is virialised, then the ionised gas density follows the so-called β -profile distribution:

$$\rho_{gas} = \rho_0 (1 + r/r_c^2)^{-3\beta/2}, \quad (1.30)$$

Where ρ is density, ρ_0 is the density at the centre of the distribution, r is radius and r_c is core radius (Cavaliere & Fusco-Femiano, 1976; Cavaliere et al., 1979). This profile is similar to that predicted for the density of stars in a spherically symmetric, isolated, isothermal globular cluster (King, 1962).

1.3.6 The relationship between X-ray Luminosity and X-ray Temperature

In a simple model of cluster formation, all energy is from gravitational collapse. This model leads to power law scaling relations between observables and their underlying mass. Galaxy clusters are then expected to be "self-similar". High mass cluster properties appear as scaled up versions of low mass clusters. Weak self-similarity also takes into account a scaling by the critical density. Any observed differences from these assumptions may point to interesting physical processes. (see Figures 1.25, 1.26 and 1.27)

The luminosity-temperature relation is the longest studied X-ray scaling relationship (e.g. (Mitchell et al., 1977; Edge & Stewart, 1991; Allen et al., 2001; Hilton et al., 2012; Maughan et al., 2012)).

The bolometric luminosity of a cluster is given by:

$$L_x = \int \epsilon(T, n) dV \quad (1.31)$$

If particles only interact collisionally:

$$\begin{aligned} \epsilon(T, n) &= n_i n_e \Lambda(T, Z) \\ &\propto n_i n_e \Lambda_0 T^{1/2} \end{aligned} \quad (1.32)$$

when a cluster is isothermal with $T \gg 10^7 K$. Then:

$$L_x = \Lambda_0 T^{1/2} \int n_i n_e dV \quad (1.33)$$

Using $n_e, n_i \propto \rho$ we find

$$L_x \propto \rho^2 T^{1/2} R^3 \quad (1.34)$$

Substituting Eq. 1.7 and simplifying:

$$L_x \propto \rho T^{1/2} M \quad (1.35)$$

Substitute Eq. 1.3 into 1.16 to give:

$$\begin{aligned} L_x &\propto \Delta\rho_c T^{1/2} M \\ &\propto E(z)^2 T^{1/2} M \end{aligned} \tag{1.36}$$

And finally substituting Eq 1.17 gives:

$$L_x \propto E(z) T^2 \tag{1.37}$$

i.e. clusters with the same temperature are more luminous at higher redshift.

1.3.7 The relationship between X-ray observables and the Sunyaev-Zel'dovich Effect

Photons from the cosmic microwave background can inverse-Compton scatter off the free electrons in the intracluster medium. This induces a frequency-dependent distortion of the cosmic microwave background in the direction of the cluster. The Compton y parameter is the integral of electron pressure along the line of sight and can be written:

$$y = \int_{\hat{n}} \frac{kT_e}{m_e c^2} n_e \sigma_T dl \tag{1.38}$$

where \hat{n} is the direction of the cluster and σ_T is Thompson cross section.

The total SZ flux in a cylinder is then given by:

$$Y_{SZ} = \int_{\Omega} d\Omega y \tag{1.39}$$

where Ω is the solid angle.

Y_{sz} can be expressed in terms of the mass and temperature of the cluster by noting that Equation 1.29 and 1.39 can be expressed as:

$$\begin{aligned}
Y_{sz} &\propto \int M_{gas} T dV \\
&= f_{gas} M_{total} T
\end{aligned}
\tag{1.40}$$

Assuming the simplest model of self similar collapse we would expect the fraction of gas, f_{gas} to be constant (see Section 1.4.1). Inserting Equation 1.19 rearranged as a function of T_x gives:

$$Y_{sz} \propto M^{5/3} E^{2/3} \tag{1.41}$$

Similarly inserting this into eq. 1.27 gives:

$$L_X \propto M^{4/3} E^{7/3} \tag{1.42}$$

Rearranging eq 1.29 and eq. 1.30 for M we find:

$$\begin{aligned}
M &\propto (Y_{sz} E^{-2/3})^{3/5} \\
M &\propto (L_X E^{-7/3})^{3/4} \\
(Y_{sz} E^{-2/3})^{3/5} &\propto (L_X E^{-7/3})^{3/4}
\end{aligned}
\tag{1.43}$$

The scaling between mass and temperature is given in Equation 1.19 giving the result:

$$(Y_{sz} E^{-2/3})^{3/5} \propto (T_x E^{-2/3})^{3/2} \tag{1.44}$$

1.3.8 Cool-Core Galaxy Clusters

Early X-ray observations of galaxy clusters found bright central regions of clusters (Cowie & Binney, 1977; Fabian & Nulsen, 1977). This motivated scientists to create a cooling-flow model of galaxy cluster formation. The cooling-flow model predicts that gas preferentially settles at the centre of a galaxy cluster. The denser gas in the cluster core has more particle-particle interactions than in the cluster outskirts. Particle-particle interactions

produce a photon allowing the gas to lose energy and become cooler. The pressure of the cooler gas is not sufficient to overcome gravitational collapse and so the core contracts. Gas from the outskirts streams in to replace the cool gas leading to a process of runaway cooling. A prediction of the cooling flow model is that the gas in the centre of a galaxy cluster should cool below X-ray emission but there should be increased luminosity around the core.

Later observations of galaxy clusters, using the superior energy and spatial resolution of XMM and Chandra, found that the cooling-flow model is a poor fit to real data (Peterson et al., 2001). When left to relax, galaxy clusters have a differential gas cooling time between the core and outskirts of a galaxy cluster. However, the gas is not able to cool until it is no longer X-ray emitting. Galaxy clusters must have a mechanism to inject energy into the gas that prevents a runaway cooling process. There are a number of possible mechanisms that could inject this energy, notably AGN feedback and supernova (Mathews et al., 2006).

The new model of galaxy cluster cooling is called the cool-core model. The term cool-core is applied variably. All cool-core models assume an excess of cool gas in the cluster core relative to the cluster outskirts, but how much cool gas and how cool that gas has to be to classify a cluster as having a cool-core varies between studies. There are a number of ways of identifying cool-core galaxy clusters in observations including a sharp temperature drop (see Figure 1.27) and corresponding luminosity peak in cluster centres, and measuring central cooling times.

1.4 Concepts in Cluster Cosmology

Galaxy clusters are vast concentrations of baryons and dark matter pulled together by gravity. They are the largest objects in the universe, and they continue to evolve today. They can be used to constrain parameters in the cosmological model by comparing observations (of their: internal structure; distribution across the sky; redshift evolution etc.) to predictions from theory and simulations (e.g Vikhlinin et al. (2009b); Mantz et al. (2010); Rozo et al. (2010); Sehgal et al. (2011); Benson et al. (2013)). Doing this can place powerful constraints on dark energy, dark matter, gravity, neutrinos and inflation (e.g Mantz et al. (2014b); Rapetti et al. (2010); Hoyle et al. (2011)). There are two main cosmology tests one can perform with clusters: the ‘ f_{gas} test’, which uses measurements of the baryonic

mass fraction of relaxed clusters as a function of redshift (§ 1.4.2), and the ‘cluster number counts test’, which uses measurements of volume density of clusters as a function of both redshift and mass (§ 1.4.1).

1.4.1 The f_{gas} Test

Clusters are ‘cosmic buckets’ large enough to scoop up a representative volume of the universe. The ratio of ICM mass to total cluster mass should then be the same as the ratio between the cosmic baryon density and total matter density of the universe (the ICM contains the majority of baryons in the cluster), i.e.

$$\begin{aligned} f_{gas} &= \frac{M_{gas}}{M_{total}} \\ \Rightarrow f_{gas} &= \frac{\Omega_b}{\Omega_m} \end{aligned} \tag{1.45}$$

Consider a spherical region of a cluster with angular radius θ . The physical radius of this region is:

$$R = \theta d_A \tag{1.46}$$

and its volume is:

$$V = \frac{4\pi}{3}(\theta d_A)^3 \tag{1.47}$$

so that its gas mass can be expressed as:

$$\begin{aligned} M_{gas} &= \rho_{gas} V \\ &= \frac{4\pi}{3} \rho_{gas} (\theta d_A)^3 \end{aligned} \tag{1.48}$$

The gas density is related to X-ray luminosity by:

$$L_X \propto \int n_p n_e dV \propto \rho_{gas}^2 V \tag{1.49}$$

and luminosity to flux, F , by:

$$L_X = 4\pi F d_l^2 \quad (1.50)$$

where d_L is the luminosity distance to the cluster. Rearranging gives:

$$\begin{aligned} \rho_{gas} &\propto \left(\frac{L}{V}\right)^{1/2} \\ &\propto \left(\frac{F d_l^2}{\theta^3 d_A^3}\right)^{1/2} \end{aligned} \quad (1.51)$$

so that the gas mass is dependent on distance by:

$$M_{gas} \propto (F\theta^3)^{1/2} d_L d_A^{3/2} \quad (1.52)$$

The total mass is dependent upon

$$M_{tot} \propto d_A, \quad (1.53)$$

so that the gas fraction is a function of:

$$f_{gas} \propto d_L d_A^{1/2}. \quad (1.54)$$

As shown by recent hydrodynamical simulations ([Planelles et al., 2013](#); [Battaglia et al., 2013](#)), f_{gas} should be the same at all redshifts after an early period of initial cluster formation. Since we can directly measure F , θ , and f_{gas} from observations, we can indirectly measure $d_L d_A^{1/2}$ by forcing f_{gas} to be constant with redshift. As stated previously, d_L and d_A are dependent on the underlying cosmological model, hence the f_{gas} test allows us to measure cosmological parameters. Figure 1.28 shows how f_{gas} changes with redshift for two very different cosmological models: the model that shows no redshift evolution is preferred over that which is not ([Mantz et al., 2014b](#)), M14 hereafter. In practice, a whole

range of models are tested so that confidence intervals can be defined. In Figure 1.29 the M14 cosmology results are shown. These were based on observations of 40 galaxy clusters observed with Chandra. The fitted parameters were constrained to be: $h^{\frac{3}{2}}\Omega_b/\Omega_M$ (0.089 ± 0.012), Ω_M (0.27 ± 0.04), Ω_Λ ($0.65 + 0.17/ - 0.22$) and w (0.98 ± 0.26). This level of accuracy is competitive with, and in some cases better than, the best alternative measurements (CMB, BAO and SNIa). (See Chapter 6 for a further discussion of the f_{gas} test)

1.4.2 The Cluster Number Count test

The mass function of clusters is a description of the number of clusters with a given mass in a unit of co-moving volume. The mass function can be predicted analytically (Press & Schechter, 1974), which has the advantage that it is possible to make predictions for a wide variety of possible cosmological models efficiently. However, the predictions are not very accurate, due to the non-linear nature of halo formation. Therefore, it is more common nowadays to use a mass function estimated from n-body simulations, e.g. (Tinker et al., 2008). The disadvantage of the n-body approach is that each simulation takes months of super computing time to complete, and so only a limited number of input cosmological models can be used, e.g. Figure 1.30. The best model is chosen by comparing the observed number of clusters in a given survey to the predicted mass functions. For example, the Chandra Cluster Cosmology Project used a catalogue of 36 clusters from the 400 square degree survey and 49 bright clusters from the ROSAT all sky survey to measure cosmological parameters (Vikhlinin et al., 2009b). This study found that a dark energy component to the universe is required with 5σ significance. The survey constrained the equation of state for dark energy, w_0 (-1.14 ± 0.21) $\Omega_M h$ (0.184 ± 0.037) and σ_8 (Figure 1.31).

There are many complications associated with the number count test, not least because the survey volume needs to be accurately defined as function of cluster mass and redshift, i.e. the integral of

$$dV_\chi(z) = \frac{c}{H_0} \frac{(1+z)^2 d_A^2}{E(z)} d\Omega dz, \quad (1.55)$$

over survey area (Ω) and redshift grasp. This is not easy to do because cluster surveys with a set flux limit become increasingly incomplete at low masses and high redshift. Moreover,

intrinsic scatter in cluster properties with mass, combined with the steeply falling mass function, mean that significant numbers of low mass clusters that should be below the sensitivity limit are detected. By comparison, few high mass clusters are scattered below the detection threshold. In addition to intrinsic scatter, measurement errors are a major concern. These can be in the redshift estimates (see § 3.7) or in the mass proxies (see Chapter 4).

1.5 Thesis Overview

In Chapter 2 we present how XCS processes raw XMM data to create cleaned event lists and images. We then go on to show how cluster candidates are detected in XMM images. In chapter 3 we explain how cluster candidates are confirmed, and how we fit their spectral properties. In Chapter 4 the new XCS-DR2 catalogue is used to test possible sources of bias in the spectroscopic analysis of clusters. In Chapter 4 the XCS-DR1 scaling relation is revisited using the updated XCS-DR2 analysis techniques, then new scaling relations are fit using the overlap between the XCS-DR2 and the SPT cluster catalogue (Bleem et al., 2015). Finally in Chapter 6 the XCS-DR2 catalogue is exploited to find new massive, relaxed clusters that can be used to fit cosmological parameters through the f_{gas} test.

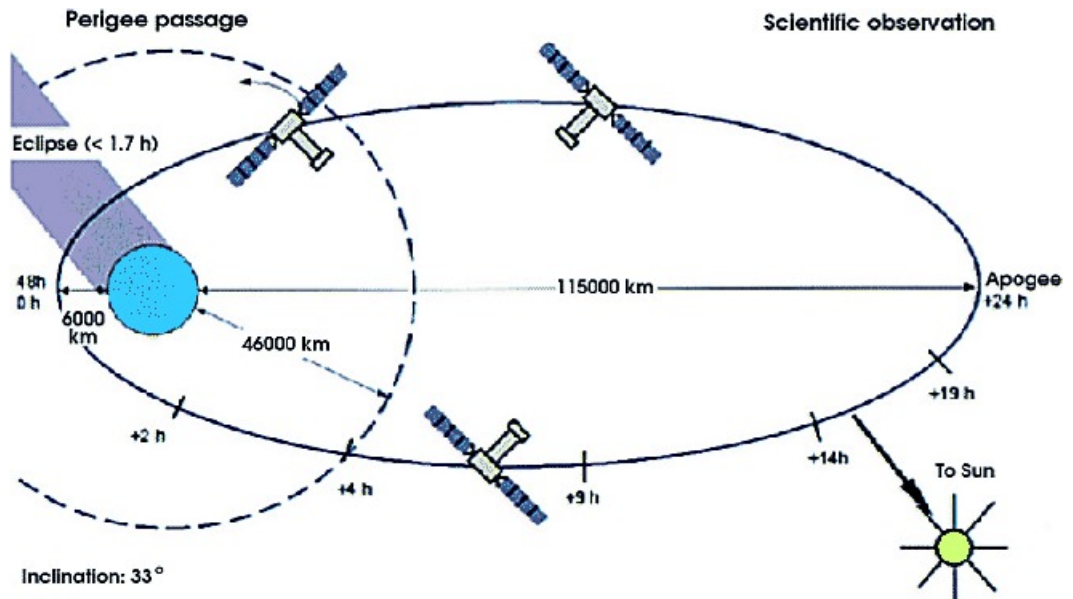


Figure 1.1: The original orbit of XMM. Since then corrections and perturbations have slightly altered this to apogee 118,000 km and perigee 8,000 km. (Figure courtesy of [Dornier Satellitensysteme GmbH, 2001](#))

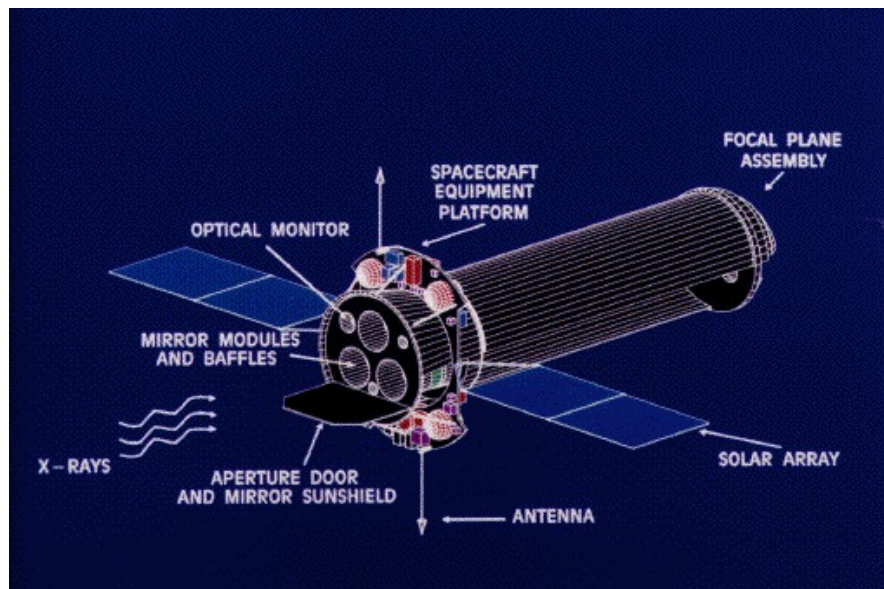


Figure 1.2: XMM-Newton layout. (Figure courtesy of the [XMM-Newton SOC VILSPA, 2001](#))



Figure 1.3: XMM mirror module. 58 Wolter I mirrors can be seen in nested arrangement. (Figure courtesy of [Dornier Satellitensysteme GmbH, 2001](#))



Figure 1.4: Left: The CCDs of one of the MOS cameras. Right: The CCDs of the PN camera. (Figures courtesy of [XMM-Newton SOC VILSPA, 2001](#))

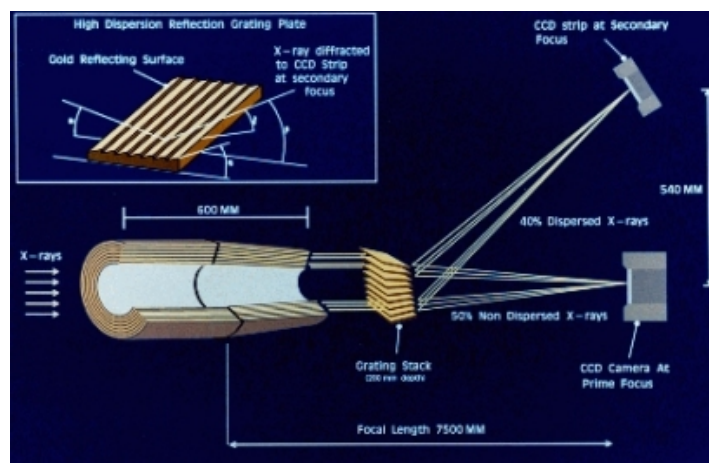


Figure 1.5: The light path to the reflection grating spectrometer can be seen. A reflection grating plate passes 40% of the light headed towards the reflection grating spectrometer at a secondary focus (Figure courtesy of [XMM-Newton SOC VILSPA, 2001](#)).

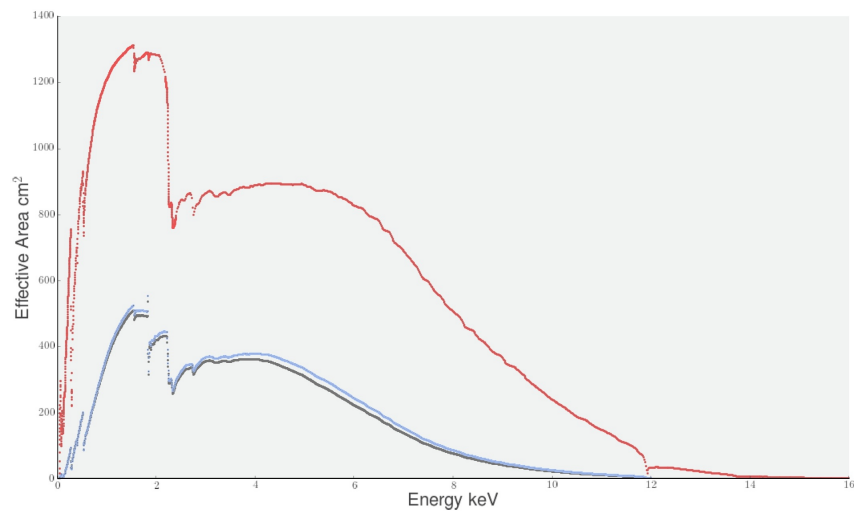


Figure 1.6: Example auxiliary response file. Red Line is PN ARF; Dark Blue Line is MOS 1 ARF; Light Blue Line is MOS 2 ARF. The PN ARF is larger as some of the light headed towards the MOS detectors is diverted to the reflection grating spectrometer.

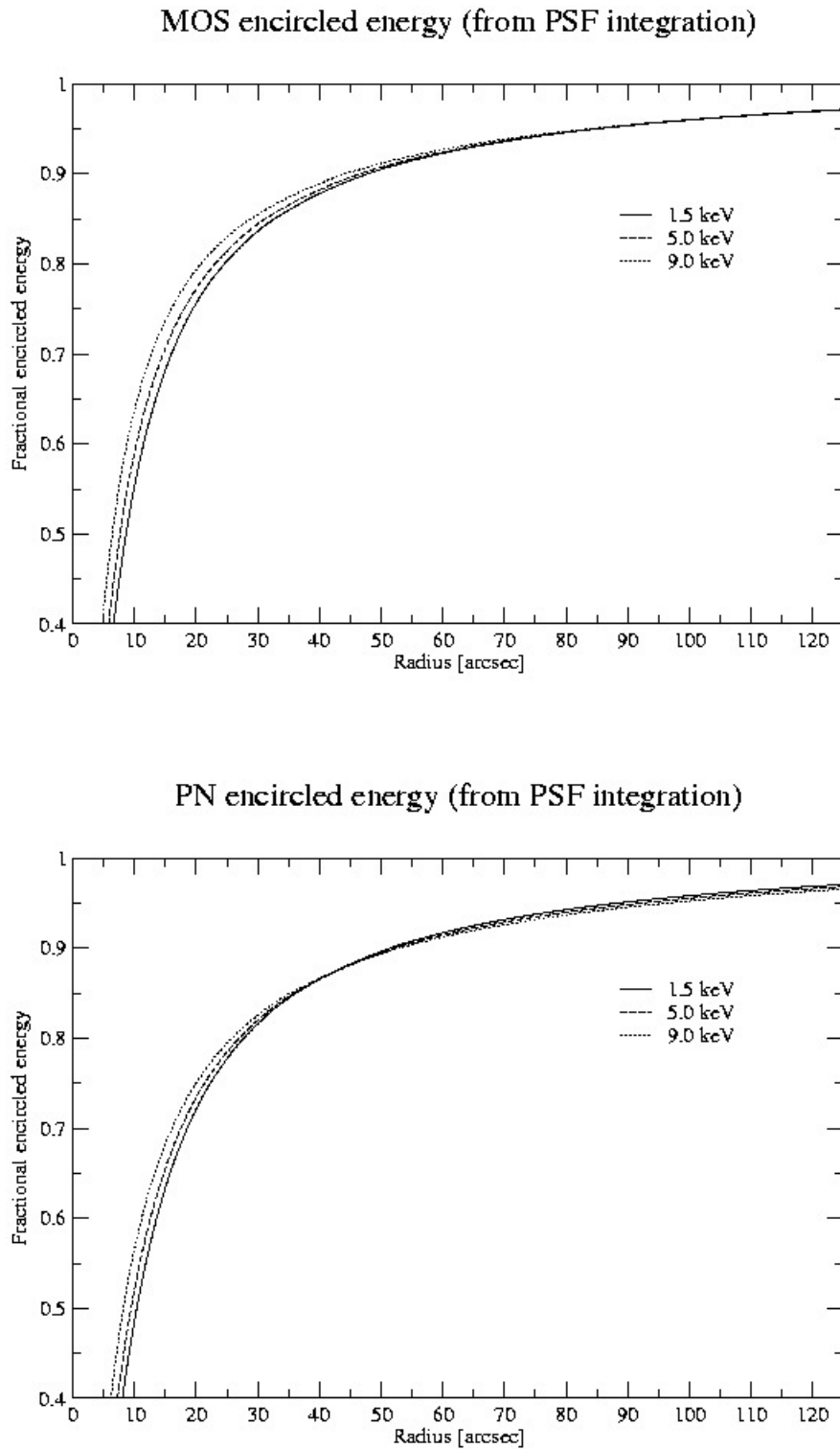


Figure 1.7: The on-axis pn encircled energy as a function of angular radius. (Figures courtesy of [XMM-Newton SOC VILSPA, 2001](#))

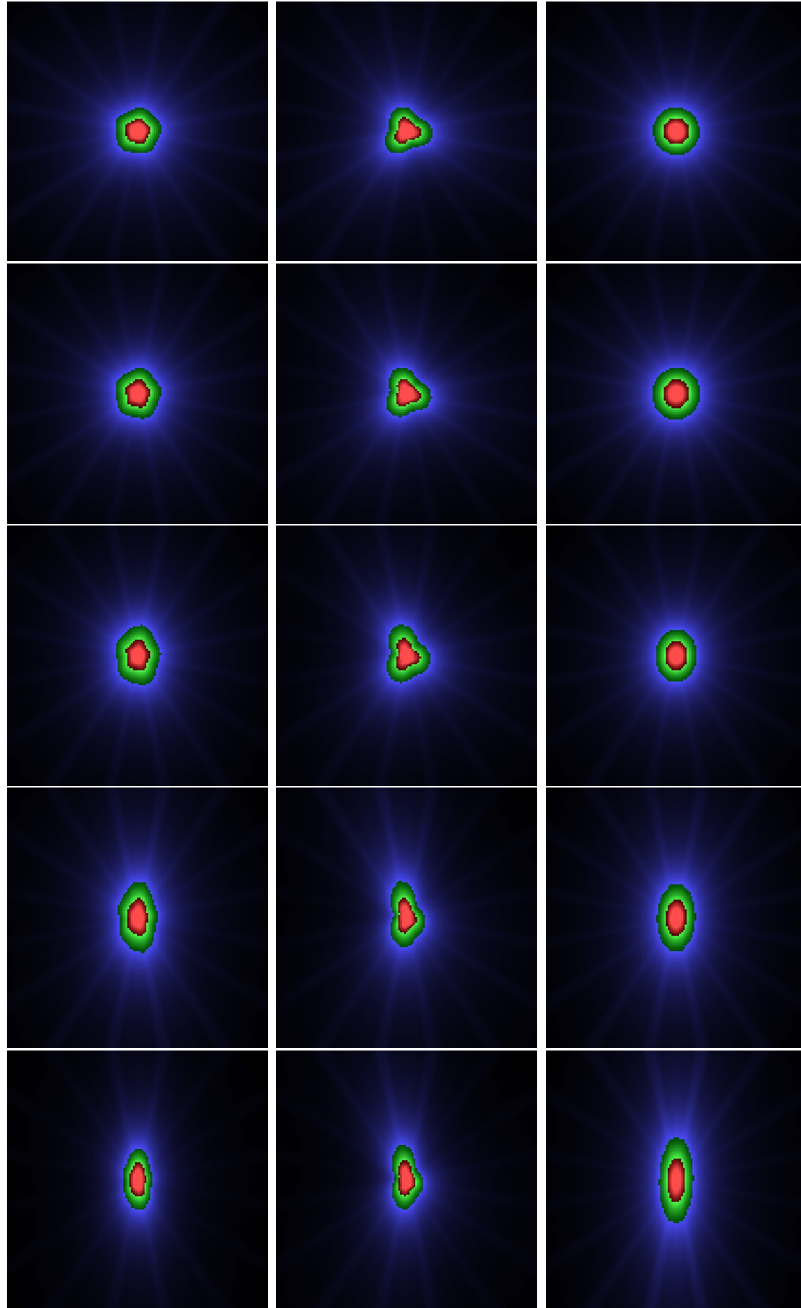


Figure 1.8: XMM PSF for 1keV photons. Left Column MOS1; Centre Column MOS2; Right Column PN. Top to bottom shows PSF at increasing off axis angle (arcminutes): 0, 2.5, 5, 7.5, 10. Images created using SAS task `psfgen` using the ellbeta model.

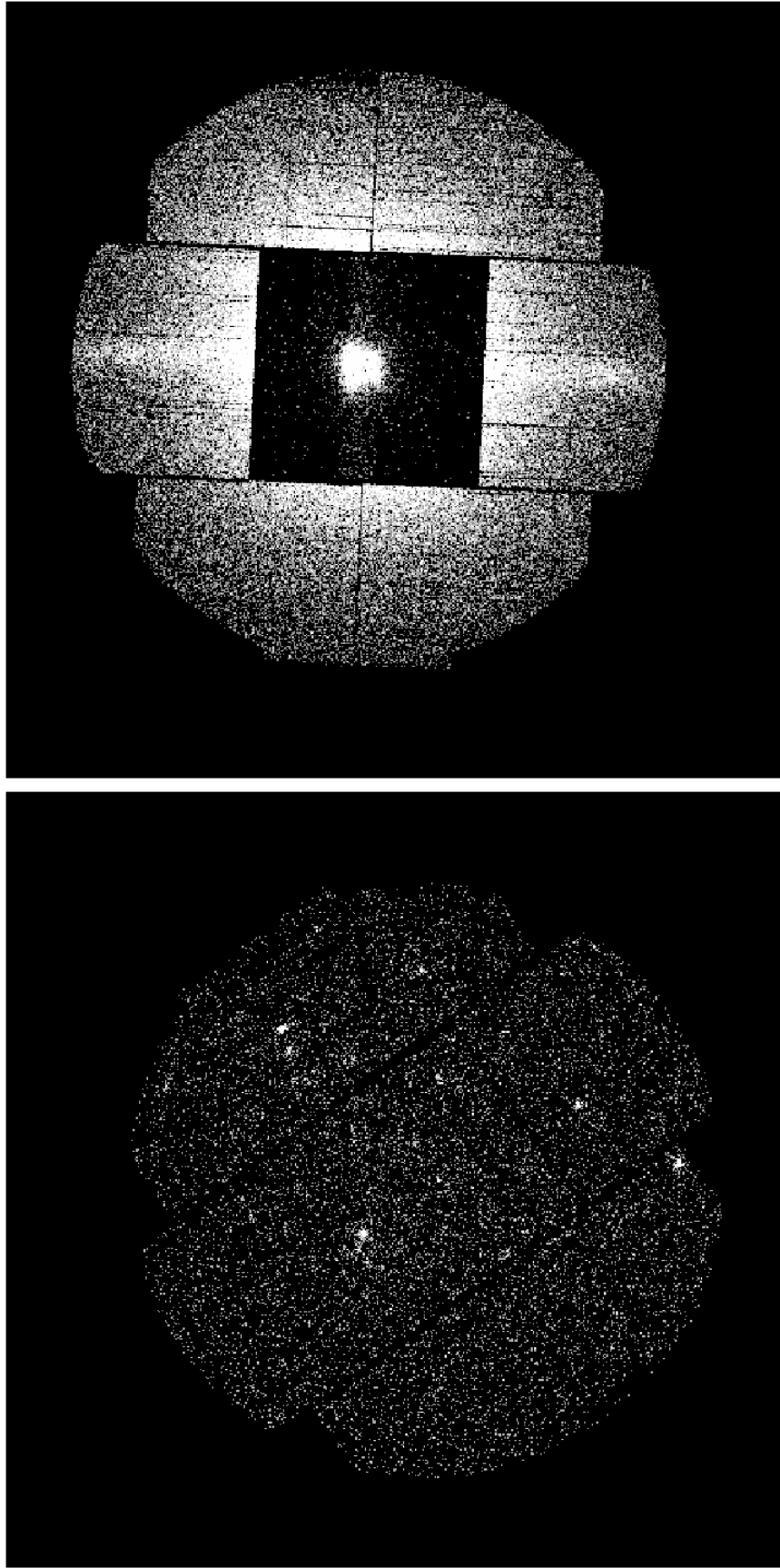


Figure 1.9: Left: An XMM MOS1 image in Full Image Mode; Right: An XMM MOS1 image in Small Image Mode 1



Figure 1.10: Left: An XMM MOSI image in Small Image Mode 2; Right: An XMM MOSI image in Small Image Mode 3

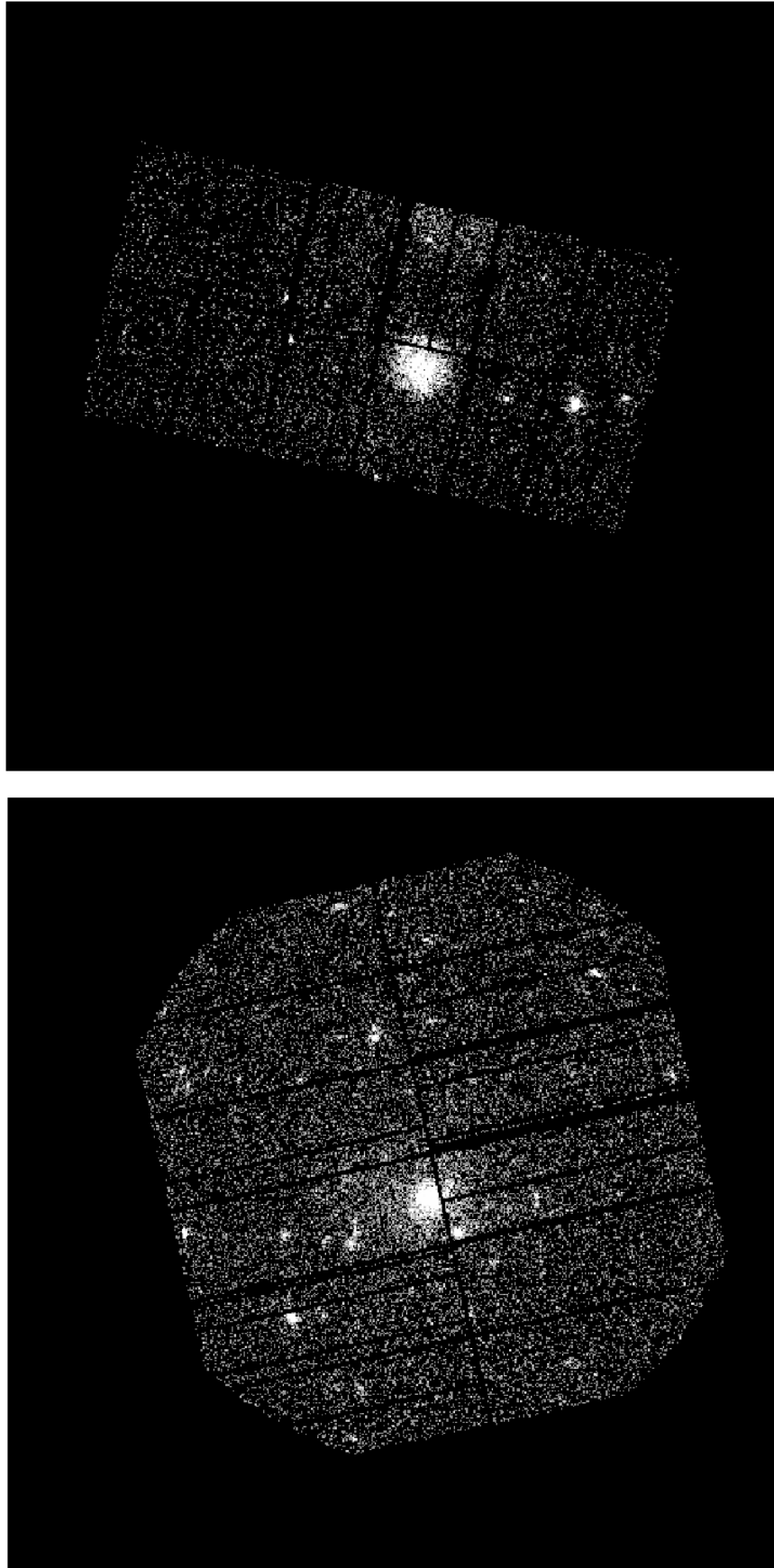


Figure 1.11: Left: An XMM PN image in Full Image Mode 1; Right: An XMM PN image in Large Image Mode 1

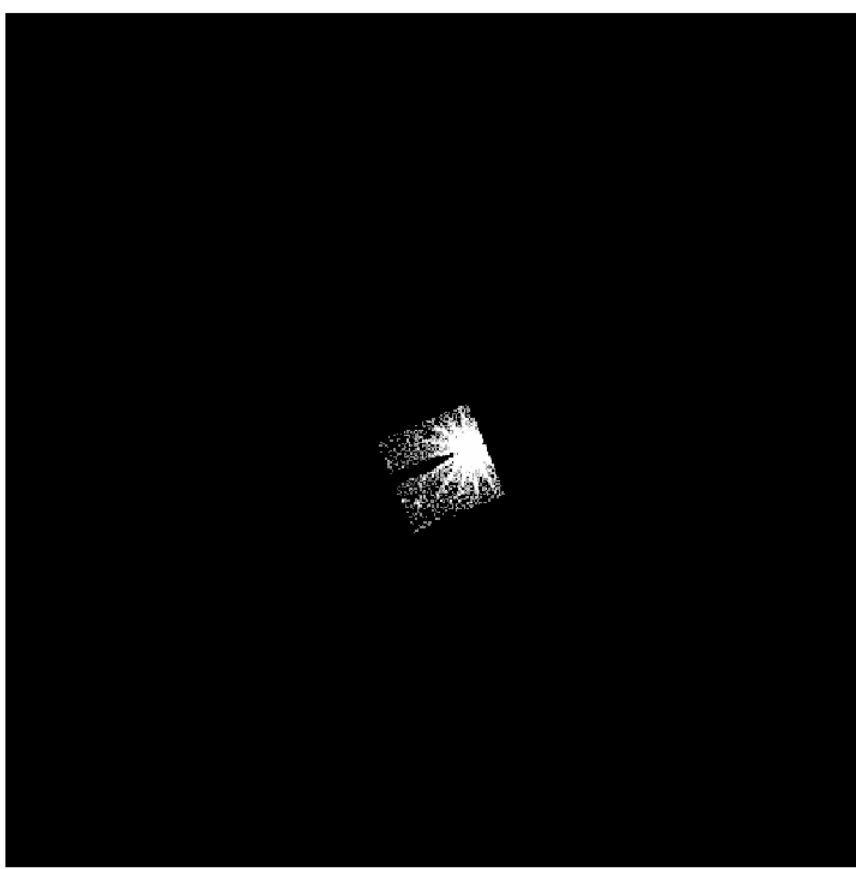


Figure 1.12: An XMM PN image in Small Window Mode 1

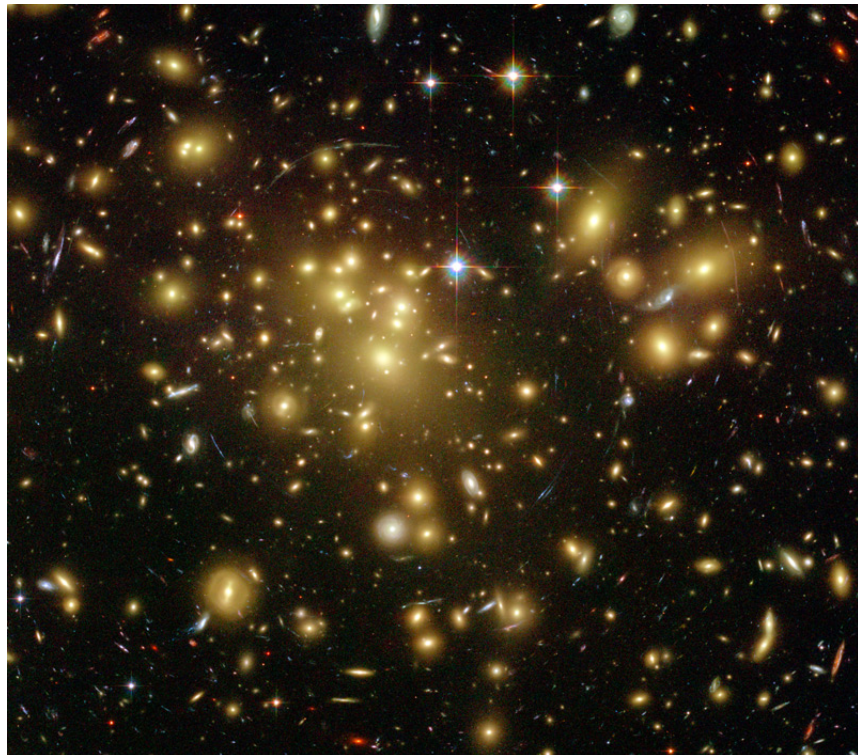


Figure 1.13: Abell 1689 taken with the Hubble Space Telescope. A galaxy cluster may contain tens, hundreds or even thousands of individual galaxies. Image credits: ESA / LFI and HFI Consortia (Planck image); MPI (ROSAT image); NASA/ESA/DSS2 (visible image). Acknowledgement: Davide De Martin (ESA/Hubble)

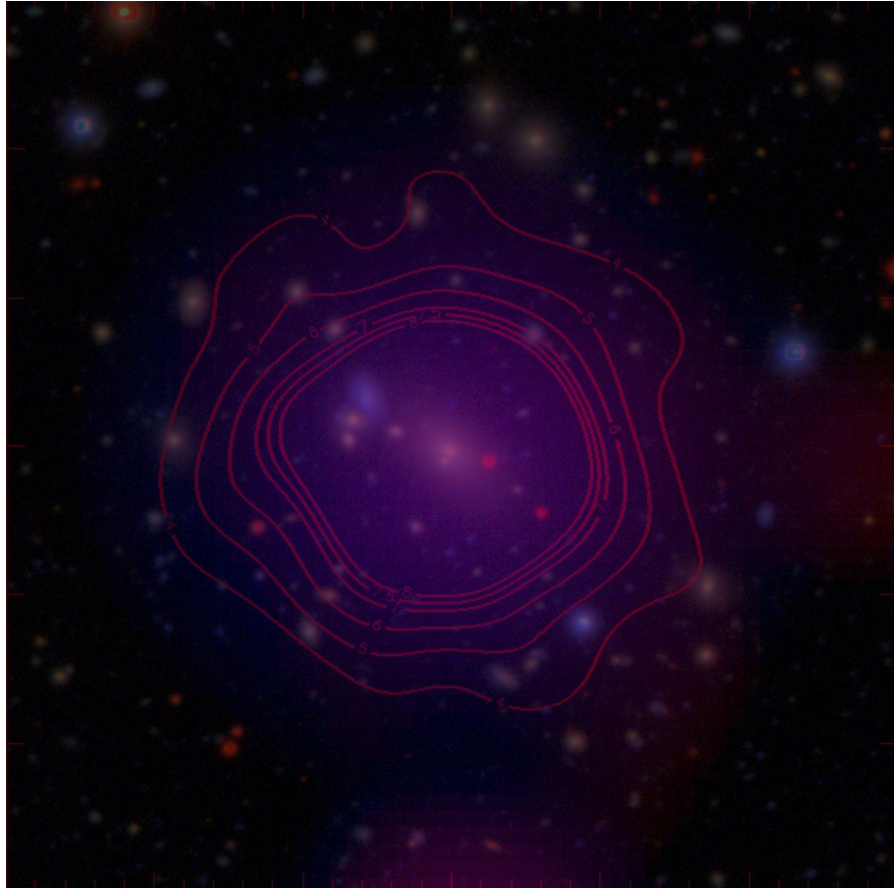


Figure 1.14: Merged X-ray and optical image of XMMXCSJ003346.3-431729.3. Galaxy data from the DES survey. X-ray data taken by XMM-Newton; soft X-rays (0.50-2.00keV) shown in blue, hard X-rays (2.00-10.00keV) shown in red. Contours show increasing X-ray surface brightness. The image is taken from Miller, Rooney et al. 2015 (in prep).

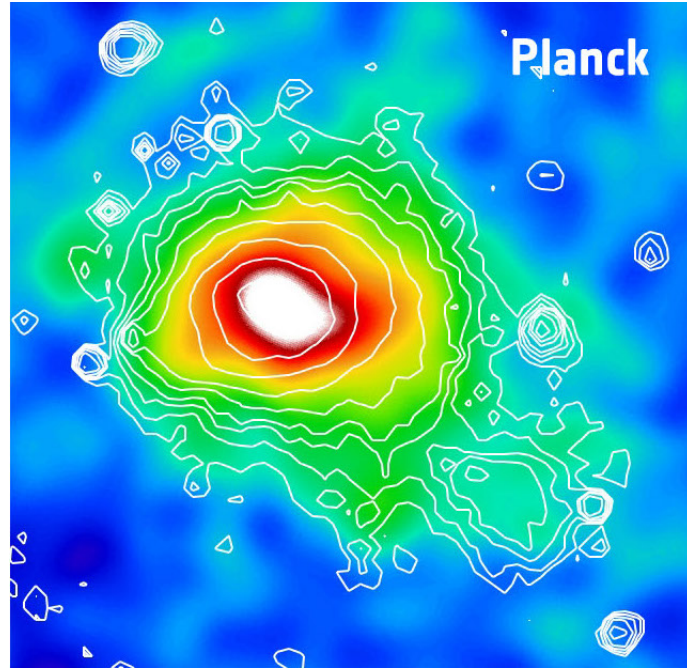


Figure 1.15: The Coma cluster observed at microwave and X-ray frequencies. The colours show the Planck satellite image of the Sunyaev-Zel'dovich Effect, and the white contours show the X-ray signal measured by the ROSAT satellite. Image credits: ESA / LFI and HFI Consortia (Planck image); MPI (ROSAT image); NASA/ESA/DSS2 (visible image). Acknowledgement: Davide De Martin (ESA/Hubble)

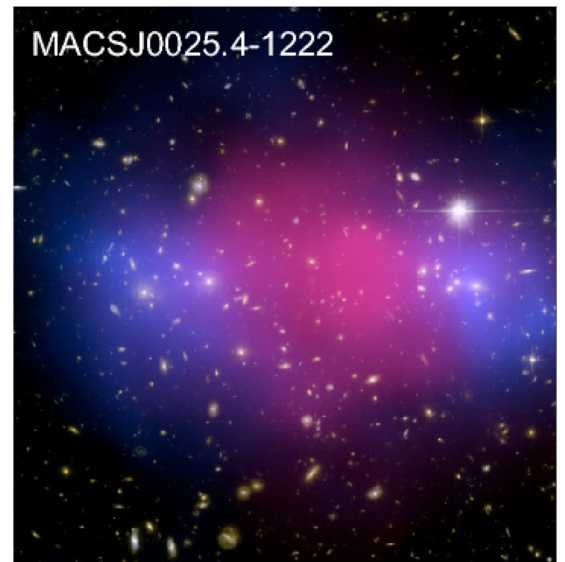
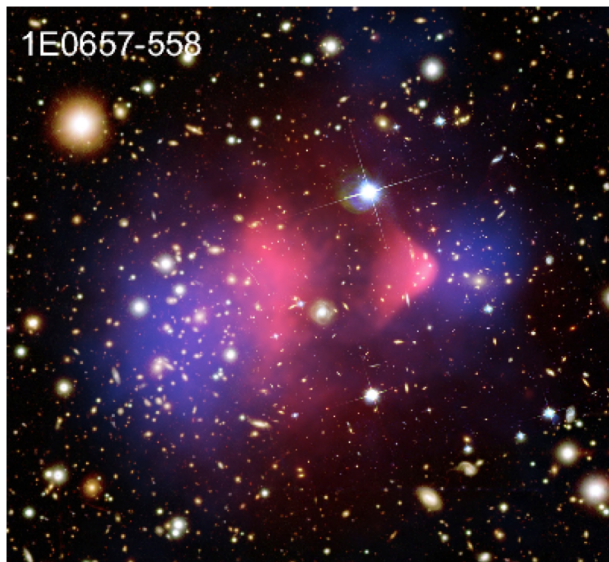


Figure 1.16: Hubble Space Telescope images of merging clusters 1E0657-558 ($z = 0.30$) and MACSJ0025.4-1222 ($z = 0.54$). X-ray emission measured with Chandra overlaid in pink and gravitational lensing reconstruction in blue. The X-ray peaks tracing the collisional gas is offset from the dark matter and collisionless galaxies. This has the implication that dark matter also behaves as a collisionless fluid. Image credits: Left: X-ray: NASA/CXC/CfA/M.Markevitch et al.; Optical: NASA/STScI; Magellan/U.Arizona/D.Clowe et al. Right: NASA, ESA, CXC, M. Bradac (University of California, Santa Barbara), and S. Allen (Stanford University).

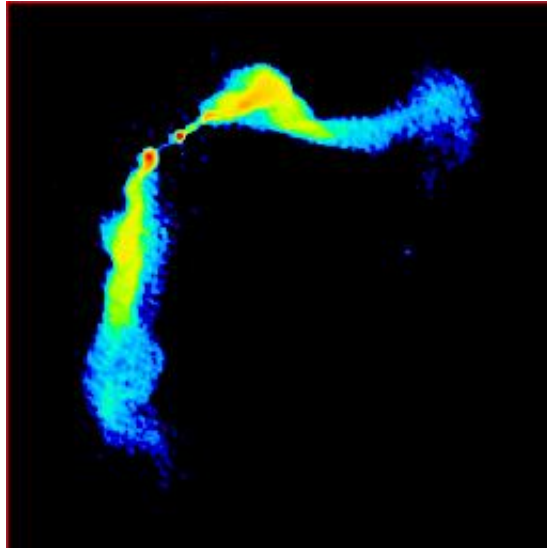


Figure 1.17: Wide angle tailed radio galaxy at the centre of the rich Abell cluster of galaxies A2634. It is thought that the high ambient density and modest speeds of the host galaxy with respect to the intra-cluster medium produce the bends. Credit: F. N. Owen



Figure 1.18: Composite Herschel (far-IR), VLT (optical) and Subaru (near-IR) image of XDCPJ0044.0-2033, a massive galaxy cluster at $z = 1.6$. Infrared emission within a 2 arcminute by 2 arcminute region centred on the galaxy cluster XDCPJ0044.0-2033. The image is constructed from K (red), J (green) and I (blue) band images. The red glow at shows far-infrared emission from galaxies located in the cluster's core. Credit: ESA/Herschel/J. Santos et al. 2015; NAOJ/Subaru; ESA/VLT/Hawk-I

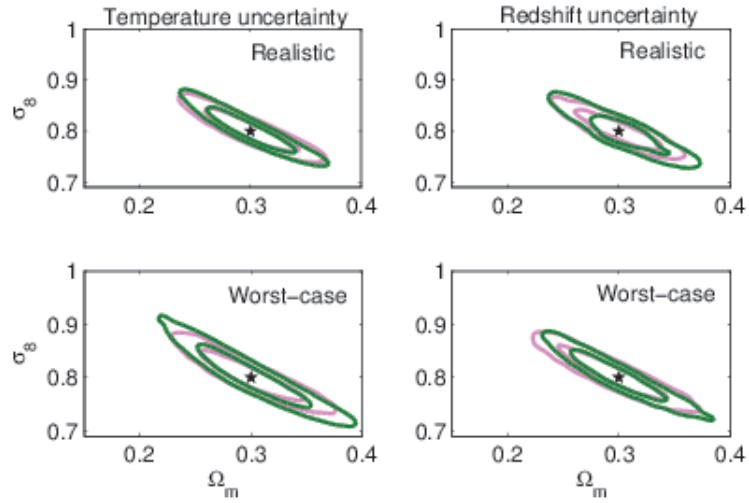


Figure 1.19: Cosmological parameter fit when uncertainty in either temperature (left) or redshift (right) exist and are accounted for.

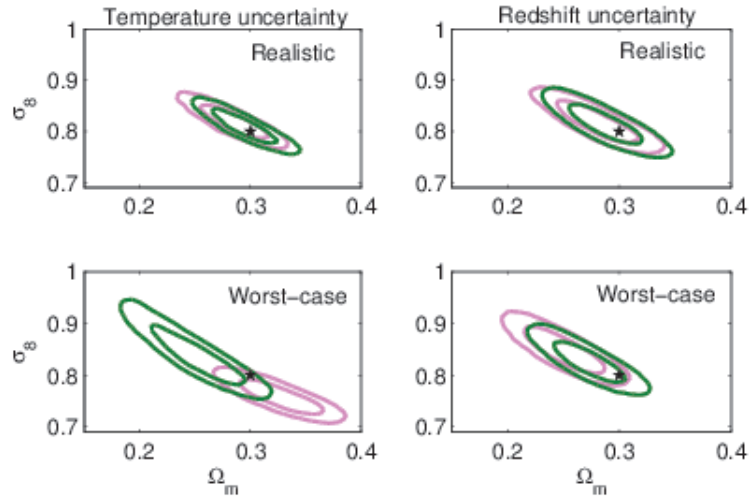


Figure 1.20: Cosmological parameter fit when uncertainty in either temperature (left) or redshift (right) exist but are not accounted for.

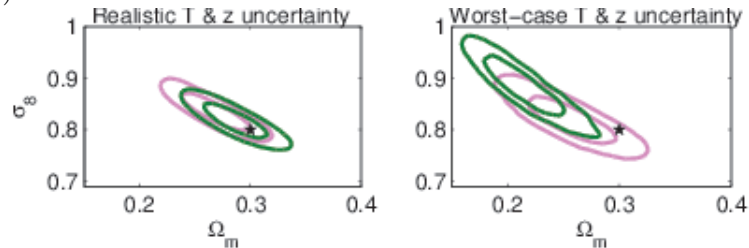


Figure 1.21: Cosmological parameter fit when there are unaccounted for uncertainties with both temperature and redshift.

Images taken from Figure 14, Sahlen et al (2009). They show the expected 68 and 95 per cent parameter constraints for XCS500 when including accounted and unaccounted for measurement errors. Stars denote the fiducial model assumed. Results are from MCMC method using self-similar evolution (green) and no L-T evolution (pink).

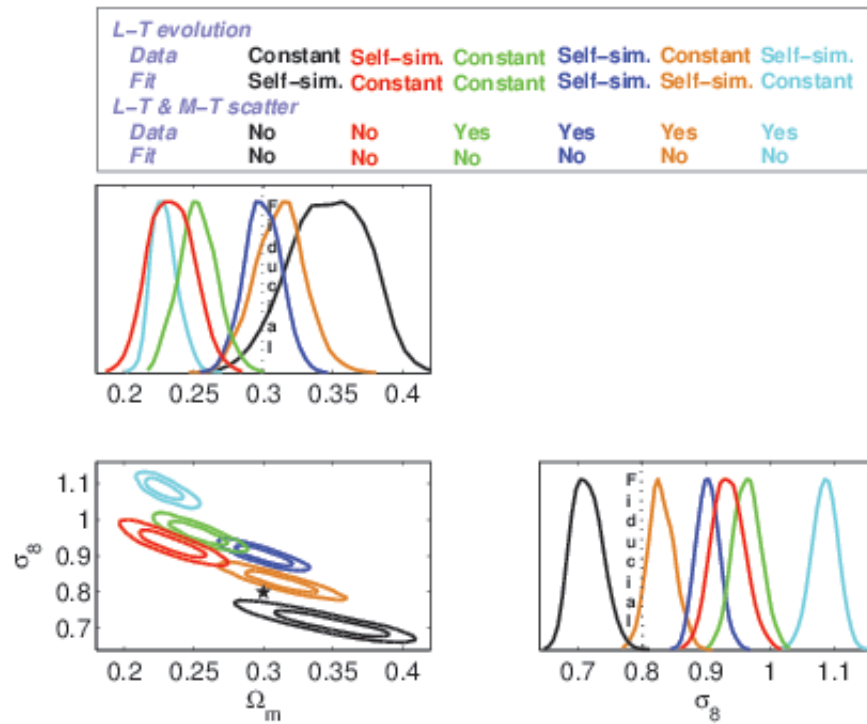


Figure 1.22: Figure 15 from Sahlen et al (2009). Expected 68 and 95 per cent parameter constraints for XCS500. Where inappropriate cluster scaling relation assumptions are made the fiducial model is not well fit. Top: Different models and fitting methods used. Middle: Confidence regions in Ω_m integrated over σ_8 . Bottom Left: Confidence regions for σ_8 and Ω_m . Bottom Right: Confidence regions in σ_8 integrated over Ω_m .

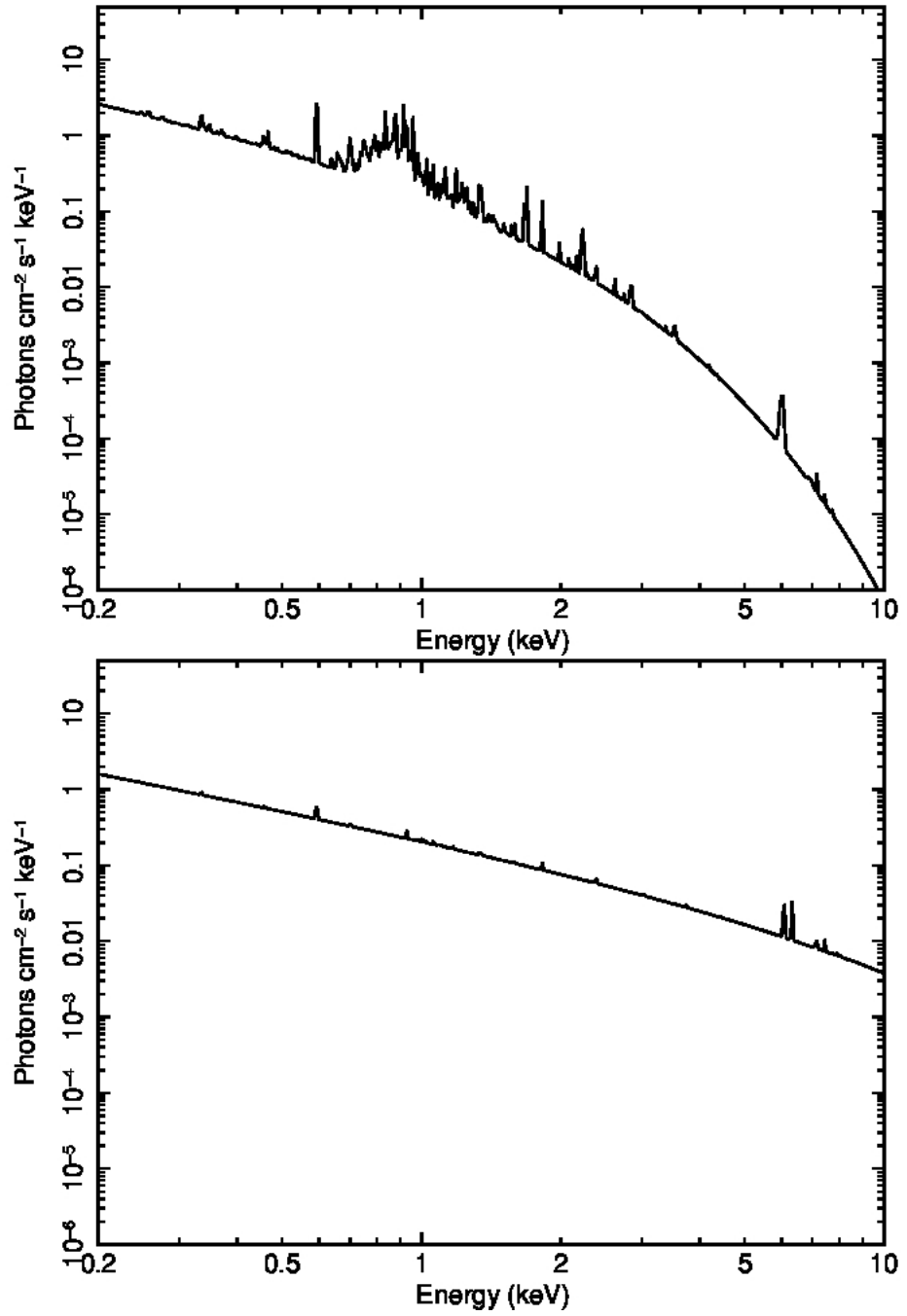


Figure 1.23: Thermal bremsstrahlung radiation for a cluster with temperature 1 keV (top) and 10 keV (below). Images made using MEKAL model with XSPEC.

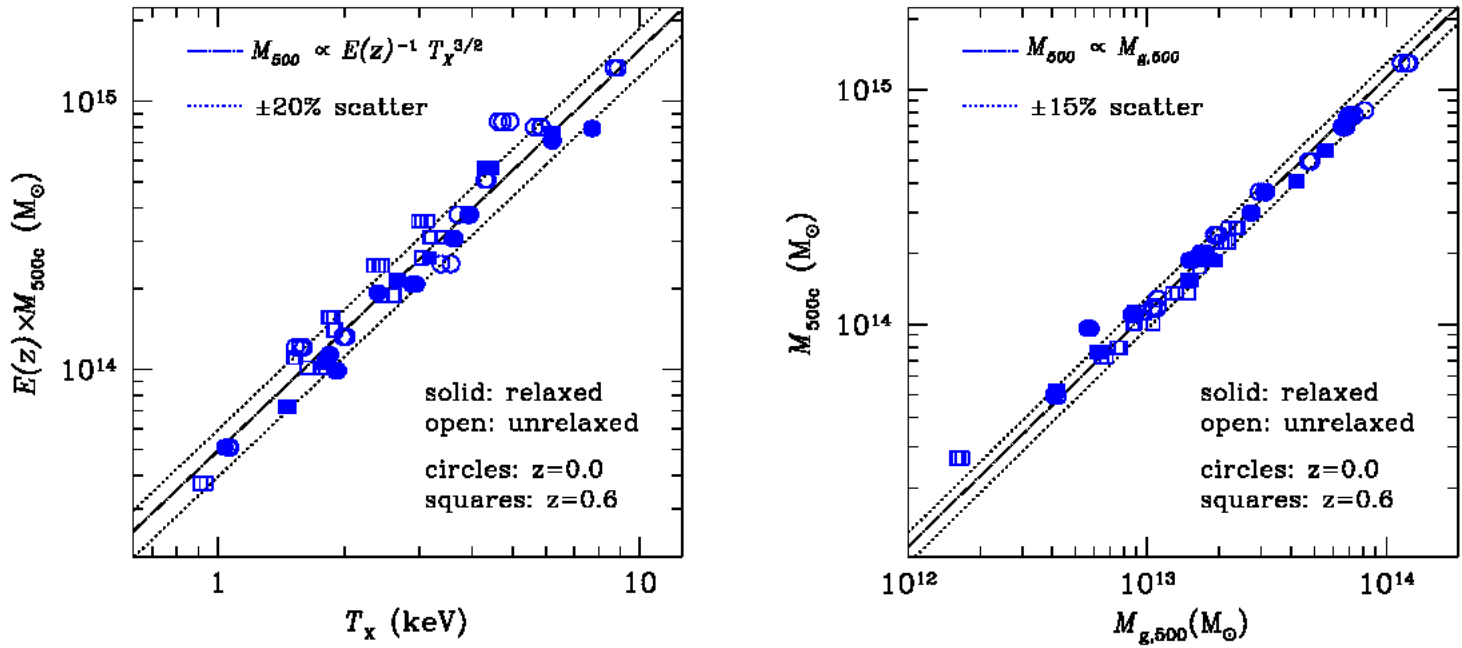


Figure 1.24: Scaling relations Mass and temperature (left) and gas mass (right). (Vikhlinin et al., 2009a)

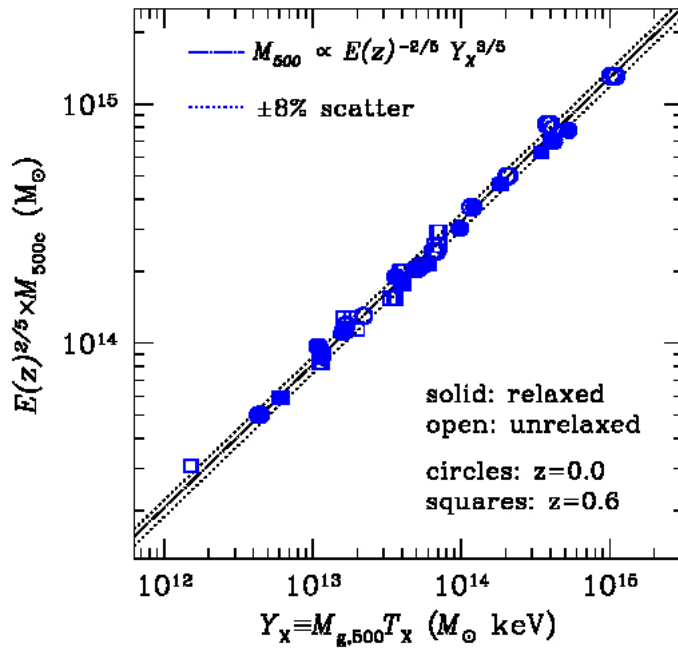


Figure 1.25: Scaling relation between cluster mass and the combination between gas mass and temperature (Vikhlinin et al., 2009a).

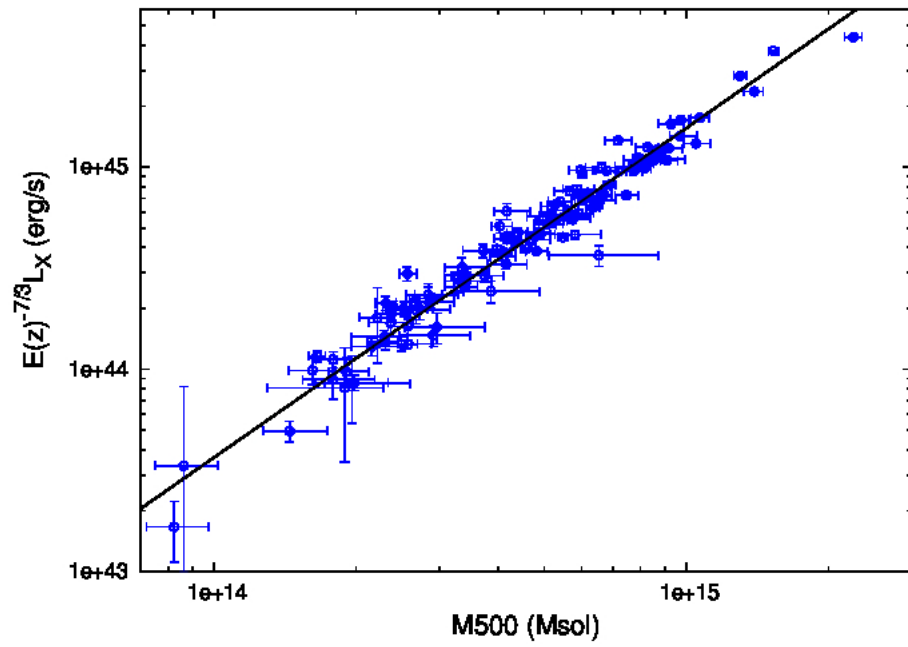


Figure 1.26: Scaling relation between cluster mass and luminosity (Maughan, 2007)

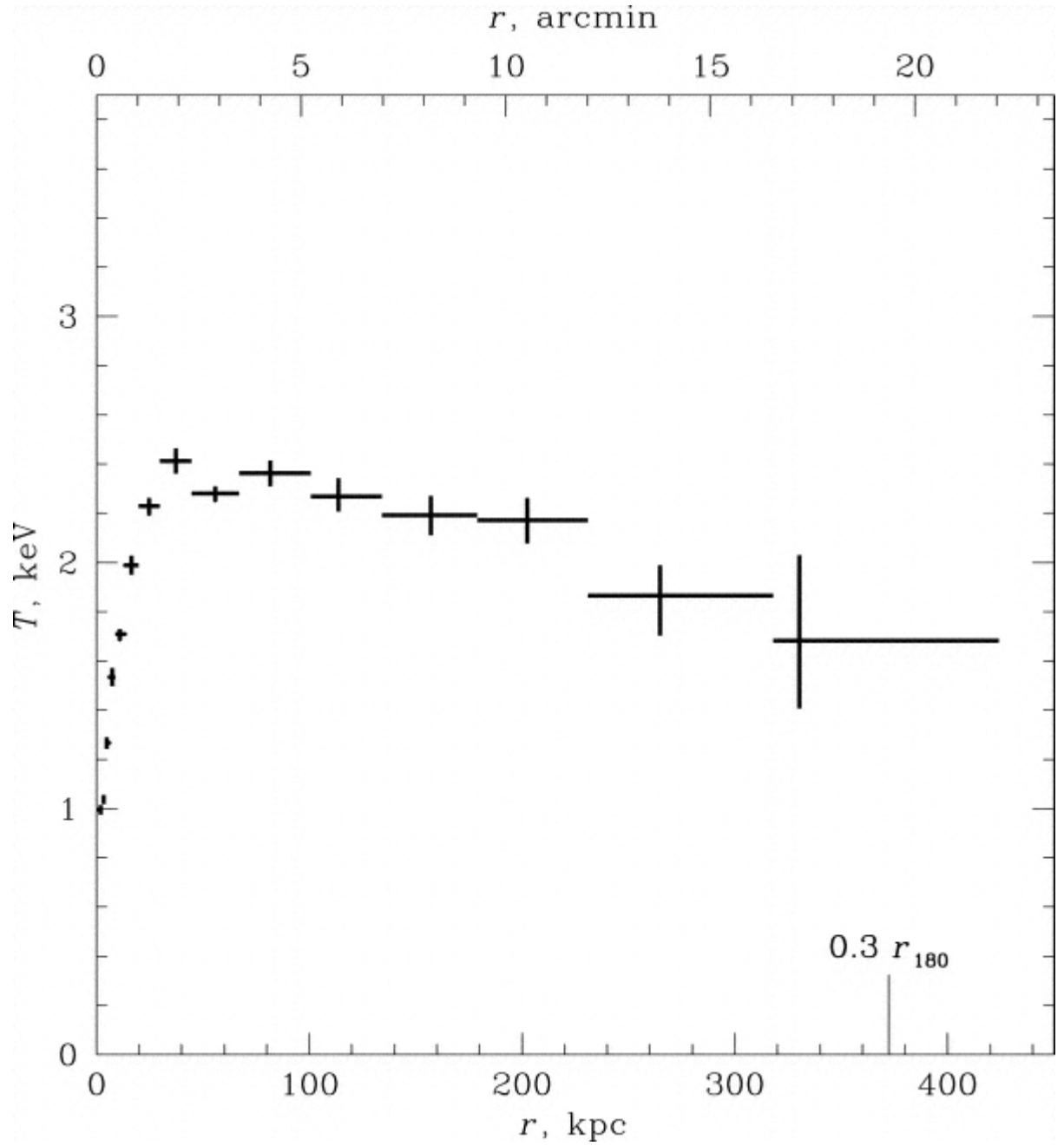


Figure 1.27: (Figure taken from Vikhlinin, 2005) An X-ray temperature profile of Abell 262

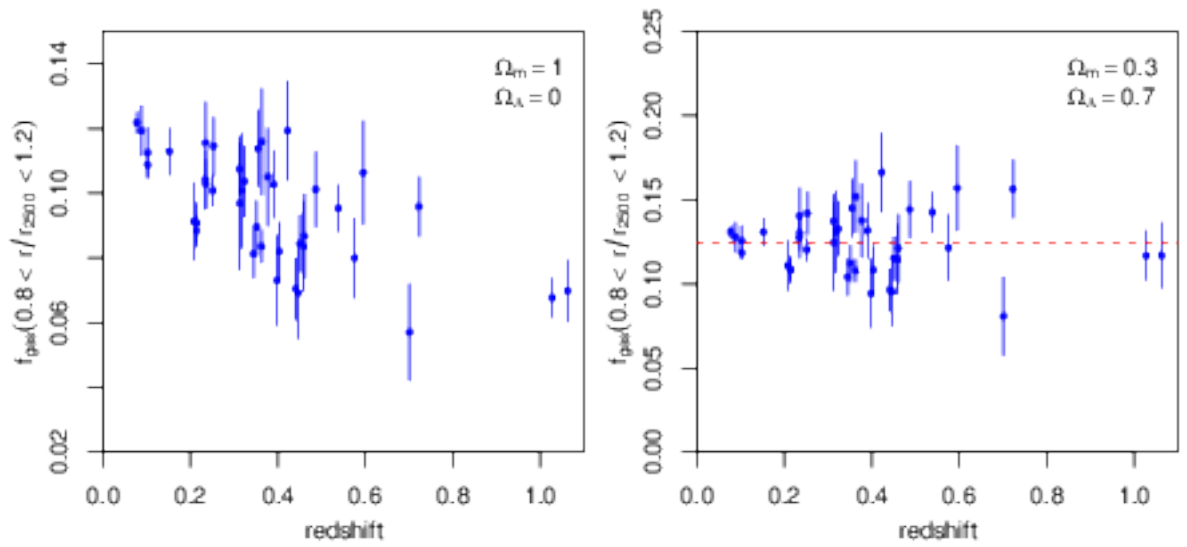


Figure 1.28: (Figure taken from M14) The ratio of gas mass and total gravitational mass in a galaxy cluster as a function of redshift for two different assumed cosmological models. Left: an open cosmology. Right: a flat cosmology.

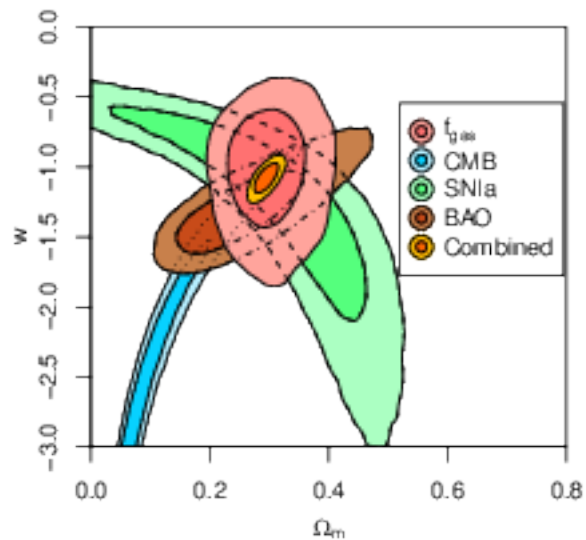


Figure 1.29: (Figure taken from Mantz et al. (2014b)) Cosmological results from f_{gas} test.

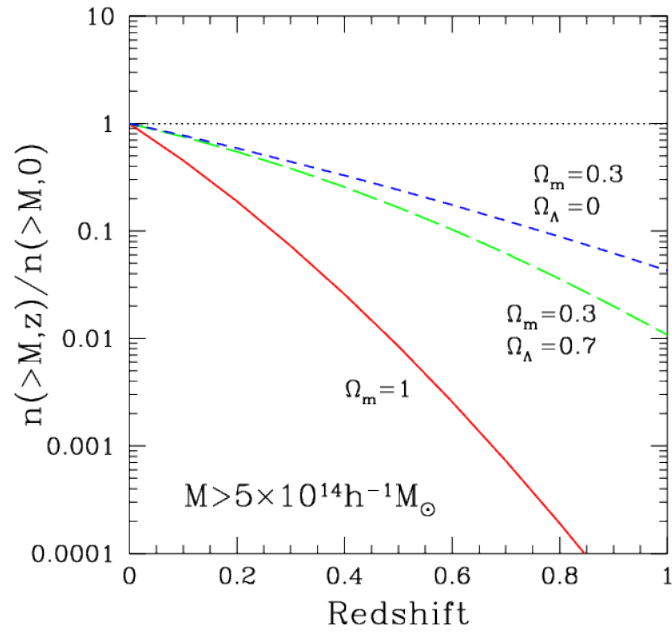


Figure 1.30: The sensitivity of the cluster mass function to cosmological models (Borgani, 2008)

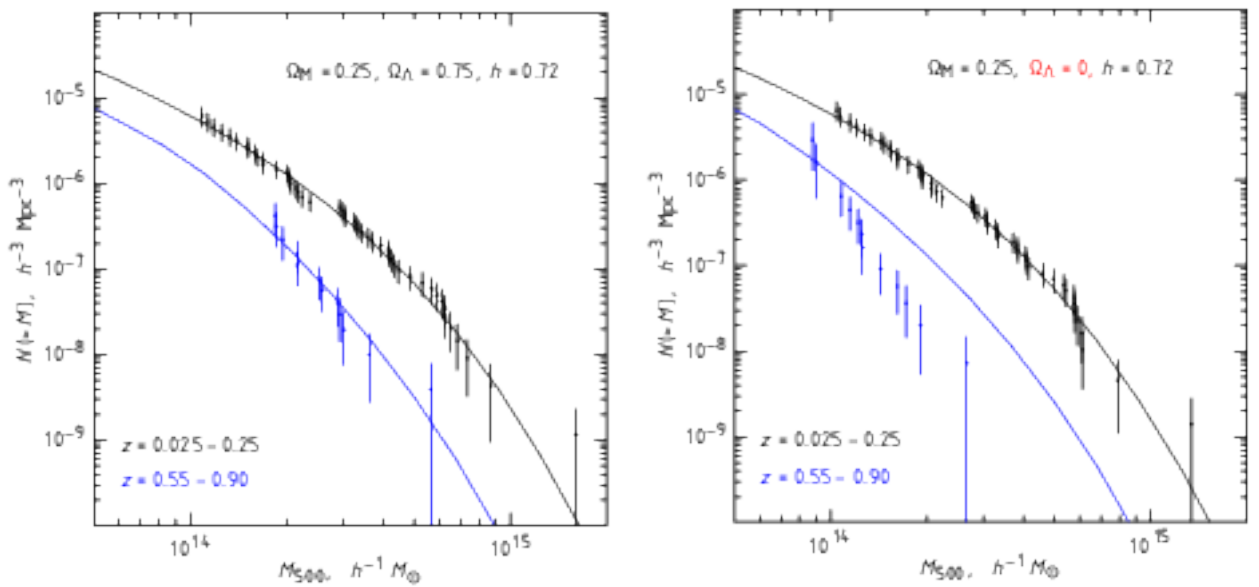


Figure 1.31: (Figure taken from (Vikhlinin et al., 2009b)) A comparison of the observed cluster mass function (data points), at two different redshifts, with theoretical predictions. Right: a flat cosmology. Left: an open cosmology.

Chapter 2

Generation of a New XCS Master Source List

2.1 Overview

Motivation There are several reasons why the XCS team decided to pursue a second data release following on from XCS-DR1 (Mehrtens et al. (2012), and § 1.2.2). For example, our cosmological and cluster scaling relation parameter forecasts (Sahlén et al., 2009) assumed a survey covering at least 500 square degrees of sky (XCS-DR1 covered significantly less area than that). Moreover, at the time XCS-DR1 was constructed, there was a paucity of deep (i.e. deeper than SDSS), contiguous, multi-colour photometry available for candidate identifications and redshift determinations. Such photometry is now available, either via public releases (CFHTLS) or proprietary access (DES), in regions with good XMM coverage.

Governing Assumptions XCS-DR1 included data from only 5,776 XMM observations (of which only 4,125 were used for X-ray source detection). The XMM archive now contains nearly 9,000 observations covering more than 1,000 square degrees. Therefore, it is safe to assume that by running XCS analysis and source detection pipelines on the latest version of the archive, we will generate roughly twice as many cluster candidates compared to XCS-DR1.

We have also assumed that the fundamental methodology of XCS-DR1 is robust, and that significant changes were not required. That said, additional fine tuning has been implemented to account for known issues with XCS-DR1, e.g. out of time events (§ 2.3.3),

mosaic observations (§ 2.3.2), mis-centered portions of an observation (§ 2.7.1), and the use of masks during source detection (§ 2.7).

Methodology The analysis methods used for XCS-DR2 are similar to those used for XCS-DR1. The XCS-DR1 versions are described in detail in (Lloyd-Davies et al., 2011) (LD11 hereafter), and so only briefly below. Where changes have been made compared to the LD11 versions, these are highlighted in the respective section.

XCS currently uses several pieces of specialist astronomy software (§ 1.1.3), including HEASOFT-6.16 and XMMSAS_20141104_1833. To make use of PYXSPEC, HEASOFT is built from source on Sussex machines rather than using precompiled versions. XMM calibration files used for the work presented in this thesis were last updated in September 2014.

Results The XCS-DR2 image archives covers more than 1,050 square degrees in total, and 688 square degrees in regions suitable for cluster finding. From a total (unique) source list of 253,667, we have constructed a cluster candidate list comprising of 15,642 extended sources detected with more than 50 background subtracted photon counts.

The quality and completeness of the new DR2 cluster candidate list has been compared to that from DR1. It has also been compared to published samples of confirmed clusters: XCS-DR1 (Mehrtens et al., 2012), XCLASS (Clerc et al., 2012b), and SPT (Bleem et al., 2015).

Conclusions and Future work The XCS-DR2 X-ray cluster candidate sample is one of the largest (if not the largest) compiled to date. It has shown to be of high quality and completeness through comparisons with other, smaller, samples.

Before these candidates can be used for scientific applications, they need to be confirmed (as clusters) and their redshifts and other properties (e.g. X-ray temperatures) measured. This work is not yet complete, but is well underway (see Chapter 3).

Looking forward to XCS-DR3, several improvements could be made to the source detection pipelines. For example, an improved treatment of the point spread function and the inclusion of larger wavelet transform kernels (§ 2.9).

2.2 Acquiring XMM Data

The aim point positions (J2000 RA & Dec), observation dates, and duration of a given XMM observation can be found in the XMM Observation Log, which is available as a table on VIZIER (Ochsenbein et al., 2000)¹. Each observation has its own ObsID, a unique ten digit identification number. One year after proprietary observations are taken, they are made publicly available (a fraction of observations, e.g. for legacy projects, are public as soon as they are made). The XMM Cluster Survey (XCS) adds batches of publicly available observations to the XCS archive, stored at Sussex University, at irregular intervals.

XMM observation data files (ODFs) are downloaded using the following command:

```
wget -O 0000000000.tar.gz "http://nxsa.esac.esa.int/nxsa-sl/servlet/data-action-aio?obsno=0000000000&level=ODF"
```

Here 0000000000 represents the observation's ten digit ObsID. These are then decompressed and are ready to process.

Changes since LD11 The XSA server was moved and upgraded 2014. This initially was problematic for XCS, because the XCS-DR1 search method no longer worked. A workaround was developed so that the XCS pipelines would operate with a box search, rather than a radial search.

2.3 The XCS Event List Cleaning and Image-Making Pipeline (XIP)

XCS data is acquired using a simple script, run by hand. The process of reducing this data and creating images is done using the IDL based 'The XCS Event List Cleaning and Image Making Pipeline'. This is referred to within the collaboration as XIP.

2.3.1 Creating Event Lists

First a list of appropriate calibration files for the observation is compiled by XIP utilizing the SAS command `cifbuild`. The command `odfingest` generates a summary file of the

¹<http://vizier.u-strasbg.fr/>

ODF. Event lists are created with the commands `epchain` and `emchain`. Event lists record where, when, and with what energy, a photon hit occurred on an XMM detector.

XIP examines each event list’s header to check if observations were taken with the filter closed², or in timing mode, or in mosaic mode. Those with the filter closed, and those in timing mode do not get processed any further by XIP. Those taken in mosaic mode require an additional step to produce event lists in the correct format (see below, § 2.3.2).

The remaining observations are passed directly to the next stage of XIP, § 2.3.3.

2.3.2 XMM Mosaic Event Lists

In mosaic mode, XMM makes multiple individual observations, taken sequentially, of neighbouring patches of sky to build up a contiguous image of a region larger than the field of view. Examples of XMM mosaic surveys are those of the XMM-XXL region (e.g. ObsID 0677700101, PI: Marguerite Pierre, 135 ks), of part of the ATLAS region (e.g. ObsID 0725290101, PI: Ioannis Georgantopoulos, 113 ks), and of part of the SDSS Stripe 82 region (e.g. ObsID 067000101, PI Megan Urry, 113 ks see Figure 2.1).

All sub-observations in the mosaics are saved into the same ODF. Although `epchain` and `emchain` will run on this ODF, they will not produce individual event lists for each sub-observation. Instead, the SAS commands `epproc` and `emproc` followed by `emosaic_prep` and `esprep_mosaic_times` are used. The de-segregated event lists are then passed to the next stage of XIP, § 2.3.3. Figure 2.2 shows an example of a sub-image generated by XIP from the full mosaic shown in Figure 2.1.

2.3.3 Out of Time Events

XMM does not have a shutter, so the CCDs remain sensitive while data are being read out. If a photon from an X-ray source strikes a CCD while it is being read out, the photon data will move along the CCD readout column until the readout finishes and then stay in that location during the next observation phase. A photon from the same X-ray source that arrives a little later will similarly be moved along the column, but won’t reach as far as the preceding one. If the source is faint, then these extra photons will not significantly impact the quality of the image, but if the source is bright then a streak will appear

²Some calibration images are made with the filter closed. The filter is also closed during periods of elevated background radiation.

(Figure 2.3, top left). These so-called ‘out of time’ events account for between 2.3% and 6.3% of EPIC-PN events (out of time events are not a concern for the MOS chips because they deliver a quicker readout time). It is possible to locate out of time events using the SAS command:

```
epchain runbackground=N keepintermediate=raw withoutoftime=Y
```

This produces a list of out of time events that are stored separately to full event list (Figure 2.3, top right). At a later a stage in XIP, the PN out of time events are subtracted from the full event list (Figure 2.3, bottom). This process lowers the effective exposure time, so the resulting PN image needs to be scaled accordingly (see § 2.5).

2.4 Data Cleaning

The XMM background varies upon where it is pointed on the sky, by the position it is located in the orbit, and by the time the observation occurs (see § 1.1.4). With regard to the latter, certain segments of an observation can be heavily contaminated by background flares. These segments need to be removed before source detection or spectral analysis takes place (Figure 2.4). For this, XIP generates light curves in 50 second time bins in both the hard (12-15 keV) and soft (0.1 - 1 keV) bands. An example hard band light curve extraction for a PN event list is: `evselect 'raw_events_pn.fits' expression="#XMMEA_EP && (PATTERN <= 4) && (FLAG .eq. 0) && (PI in [100:1000])" rateset='raw_events_pn_lc.fits' timebinsize=50 maketimecolumn=true`

The hard band light curves account for the quiescent particle background, whereas soft band light curves account for instrumental noise, solar wind charge exchange, and high energy particles interacting with the structure in and around the detectors. An iterative three sigma clipping, i.e. assuming Gaussian statistics, is then carried out on the light curves. The 50 second time bins that pass the clipping are saved as so-called ‘good time intervals’. Cleaning takes place after event list generation and before image generation.

The data cleaning method works best for observations with long exposure times and/or low background levels (Figure 2.5). For shorter exposures, especially those heavily corrupted by flares, the cleaning process is less effective (Figure 2.6). This variation in cleaning quality is not ideal for a serendipitous survey like XCS, but can be accounted for using a selection function (§ 1.2.2).

2.5 Single Camera Image Generation

For each camera, XIP extracts data from cleaned event lists in the 0.5-2.0 keV and 2.0-10.0 keV energy bands and reformats it into a two dimensional image using the **evselect** commands, e.g.

```
evselect table=eventslist.fits withinageset=yes imageset=image.fits xcolumn=X
ycolumn=Y imagebinning=binSize ximagebinsize=50 yimagebinsize=50 expression=
"#XMMEA_EM && PI in [500:2000]" writedss=yes squarepixels=yes ximagesize=512
yimagesize=512 ximagemin=3649 ximagemax=48106 withxranges=yes yimagemin=3649
yimagemax=48106 withyranges=yes imagedatatype=Real64 ,
```

where **#XMMEA_EM** selects the events that have labelled as "good" (some events can be flagged as bad during event list creation if they are unlikely to be caused by an astronomical source), "**PI in [500:2000]**" encodes the energy range to use (in this case in the 0.5-2.0keV band), "**ximagesize=512 yimagesize=512**" produces a square 512×512 pixel array (with pixel size 4.35x4.35 arcseconds²). In the case of the PN camera, the events in the out of time list are extracted from the cleaned event list before the image is generated, and an appropriate scaling applied (§ 2.6).

Corresponding exposure maps are produced with the **eexpmap** command, e.g.

```
eexpmap imageset=image.fits attitudeset=ATTHK.fits eventset=eventslist.fits
expimageset=expmap.fits pimin=500 pimax=2000
```

Exposure maps give an effective exposure time for each pixel in the image. The whole EPIC field of view is exposed for the same time, but these maps take into account instrumental effects such a chip gaps and vignetting. Examples of single camera images and their respective exposure maps are shown in Figures 2.7, 2.8, and 2.9, for PN, MOS1 and MOS2 respectively.

2.6 Merged Image Generation

XIP also produces images that merge together the individual camera images and exposure maps (Figure 2.10). For this, the MOS images/maps have to be first scaled so they

replicate the sensitivity of the PN detector. The scaling requires energy conversion factors (ECFs) that map camera count rate to energy flux.

Energy conversion factors (ECFs) can be employed to convert source counts into energy fluxes and to scale MOS images to that of the more sensitive PN image. In XIP they are generated within XSPEC using an on-axis ARF and RMF files (Sections 1.1.4 and 1.1.4) specific to the respective ObsID, and a neutral hydrogen column appropriate for the XMM aimpoint direction. The model used is an absorbed power law (with index $\alpha = 1.7$) because this is typical for AGN (the predominant type of extragalactic X-ray source in the universe). These ECFs are also used to estimate initial XCS source fluxes (§ 2.7).

For some ObsIDs not all three camera images will be available. In these cases, only the remaining two are merged.

2.6.1 XIP Batch Processing

XIP is run on the Sussex University supercomputer, *Apollo*. Parallel job submissions speed up the total processing time but need careful handling because individual SAS and HEASOFT programs temporarily store information in parameter files. In default mode, these parameter files are stored in a single location, so parallel jobs can interfere with one another when active parameter files are overwritten. This leads to XIP crashes and hangs. Therefore, to prevent pipelines interfering with one another, a new directory containing parameter files for each run was spawned for each process. The environment keywords `HEADAS_LOC_PFILES` and `PFILES` were set to point to this directory.

For XCS-DR2, XIP was run on up to 256 cores. The entire XMM archive can be re-processed within three weeks. To date a total of 8,598 observations have been processed. Their locations are plotted on an Aitoff projection of the sky in Figure 2.11, and their exposure time distribution (total and clean) in Figure 2.12. Less than 10% of the observations were gathered in mosaic mode (see § 2.3.2): 604 sub-observations were taken from 50 mosaic ODFs.

Changes since LD11 Previously, XIP was run on a 12 core machine, and the processing took several months to complete. In the past, the problem with the parameter files being overwritten by parallel jobs was not noticed, and pipeline failures were common.

2.7 Source Detection

After XIP has been run on the XMM archive, source detection is carried out using a separate package known as XAPA . XAPA is a wavelet based source detection method that takes merged detector images and exposure maps and outputs lists of detected sources and their properties.

XAPA carries out wavelet transformations at nine different scales in the merged detector image: $\sqrt{2}$, 2, $2\sqrt{2}$, 4, $4\sqrt{2}$, 8, $8\sqrt{2}$, 16, 32 pixels. The transformed images are compared to a threshold image (essentially the same image after transformation, but with sources removed) and statistically significant pixel values are then examined to determine if they are likely to have an astronomical origin. The first two scales, $\sqrt{2}$ and 2 pixels, are used to identify hot pixels (e.g. from cosmic ray hits) and very bright point sources; the latter can hamper the detection of faint sources at larger scales and need to be masked. Occasionally genuine extended sources are detected at these small scales, e.g. when a cluster has a bright core, therefore a “cuspieness” test is applied before masking takes place: genuine point sources will be cuspy whereas cool cores will not. “Cuspieness”, Q , is measured in a 5x5 array is cut-out using the following equation:

$$C = \frac{Q_{max} - Q_{min}}{Q_{max}}, \quad (2.1)$$

only if C is >0.85 , is the respective pixel removed.

XAPA then proceeds with the wavelet transformations at the other 7 wavelet sizes ($\geq 2\sqrt{2}$ pixels). XAPA uses a bespoke version of `wrecon`³, called `md_recon`, that has been optimised for extended source detection. `wrecon` is used to group collections of significant pixels together into sources and is executed at each wavelet scale. After the pixels have been grouped, an ellipse is fit around them.

It is common for a given source to be detected in several different transformed images. It is also common for two or more distinct sources, detected separately in a small scale transformed image, to lie close enough together on the sky that they are merged together in the larger scale transformed images. Therefore, XAPA uses a decision tree to distinguish between these two scenarios. Sources in small scale images are compared to those in

³`wrecon` is part of the `wavdetect` package (Freeman et al., 2002).

progressively larger scale images. When sources are deemed to be detected more than once, only the ellipse in the largest scale of detection is recorded (see Figure 2.13, and LD11 for more detail).

XAPA then calculates the sum number of background and source photon counts in an annulus around the source in each of their individual non-scaled photon images. The background annulus uses the same ellipse shape and orientation as the respective source, but the axes are 3 (2) times larger for extended (point-like) sources. If any other detected sources lie in the background annulus they are masked before the background rate is determined. A Poisson distribution is used to calculate the probability that the number of counts in the source ellipse occurred by chance from the background. If the probability of the source occurring by chance is greater than 0.00032 then the source is discarded. This is equivalent of a 4σ threshold in a Gaussian distribution. For each source, XAPA calculates a flux estimate. This is done by multiplying the background subtracted count rate by the respective energy conversion factor (see Section 2.6).

The merged MOS1, MOS2 and PN images with MOS counts scaled to the PN ECF is used to detect sources, but their statistical significance is then assessed using the real count data. MOS1 and MOS2 images are scaled so that during source detection, regions of an observation with only MOS exposure will not be penalised relative to areas with PN coverage. This will have the effect of creating spurious sources on MOS chips where the signal to noise will be artificially boosted, but the test of statistical significance, which is done using the unboosted images, will reject these sources.

The next stage is to determine which of the sources are extended (clusters dominate the extended extragalactic source population in X-rays). A Kolmogorov-Smirnov test is used to determine whether the measured enclosed energy fraction within the XAPA source ellipse is consistent with the enclosed energy fraction of the PSF at the source location. For this XAPA uses the XMM Extended Accuracy PSF model (Altieri et al., 2004) at the respective off-axis angle. XAPA tests 200 realisations of the PSF. The source is then classified as extended if the probability of it being a point source that has been misclassified as extended is 0.005 or less. Extended sources in a sub-category known within XCS as ‘PSF-sized’ are flagged. ‘PSF-sized’ sources are only slightly larger than the PSF. Experience has shown that these can be misclassified point sources, although they can also be clusters with bright cool cores and so are not immediately discarded. Examples of

sources with the three types of extent classifications are shown in Figure 2.14.

Next, for each ObsID, XAPA records for each detected source the following information: the centroid position, the ellipse parameters, the background subtracted countrate, the ECF determined flux, and the extent classification. A png file is also produced showing the observation with detected source ellipses overlaid (see Figure 2.15).

The final stage of XAPA is the generation of a master source list. XAPA collates all sources into two source lists; the first contains each source detected in every observation; the second attempts to remove duplicate sources by cross matching source detections in different observations. The program matches point sources within 5 arcseconds of one another and extended sources within 30 arcseconds. When the code finds duplicates, it keeps the source with the most counts.

Changes since LD11 For XCS-DR1, masks were applied before XAPA was run. These were used to prevent extended bright regions from biasing the wavelet threshold image, e.g. from nearby clusters, from out of time streaks, or from extremely bright targets (the latter result in a characteristic cog wheel pattern, e.g. Figure 2.3). However, in practice, masking often produced false XAPA “sources” on the mask edge. After considerable testing, it was decided that a better approach is to mask after running XAPA, not before. This approach has the added advantage that XCS-DR2 includes clusters that were the intended target of the respective XMM observation. Although these “target” clusters cannot be used for certain statistical studies, they are nevertheless very useful for other studies, e.g. the f_{gas} cosmology test described in Chapter 6.

2.7.1 Mis-targeted Observations

There are occasions when XMM either begins an observation off-centre, or temporarily loses its target star. These observations can be identified by scattered bright pixels outside of the detector footprint, or by scaling the exposure map to very low values (see Figure 2.16). These stray pixels can cause XAPA to fail. A simple fix is to set pixel values to zero in regions of an observation where the exposure map value is below 5% of the on-axis value. Usually, an observation’s effective exposure value will not go below 30% of the on axis exposure at any point in the field of view, so there is little risk of cutting out any useful regions. Currently these types of observations are identified after XAPA has

been run on the default XIP image. If XAPA fails, and the cause is due to mis-targeting, then the ObsID is run through XAPA again once the errant pixels have been set to zero.

Changes since LD11 When XCS-DR1 was produced, the problem with mis-targeted observations was not diagnosed, so many XIP images failed to run through XAPA.

2.7.2 XAPA Batch Processing

The XAPA pipeline is written in IDL. Therefore, to avoid licensing issues, batch jobs were submitted to multiple processors on as few nodes as possible. For the development of XCS-DR2, we ran the XAPA pipeline on two nodes with 60 processors each. The algorithm was run successfully on 8442 ObsIDs, failing 156 times (out of 8598). An investigation determined that failures occurred at the portion of the pipeline that calculates the probability of finding the number of counts in a source. This involves the use of the IDL program `igamma`, which in the failed cases did not converge on a solution (this issue will be investigated further before XCS-DR3).

2.8 Results

2.8.1 Area Covered

The XCS image database covers 1,050 non-overlapping square degrees of sky. However, only 688 square degrees is suitable for cluster finding: 3,233 OBSid lie either at $|b| < 20$ degrees of the galactic plane or within 5 degrees (3 degrees) of the large (small) Magellanic cloud.

In regions suitable for cluster selection, XCS-DR2 is larger than other XMM serendipitous cluster surveys: more than twice the equivalent XCS-DR1 area (276 sq.deg, LD11), and 4.5 times larger than XCLASS (Clerc et al., 2012b). XCS-DR2 is also much larger than the various contiguous XMM cluster surveys, e.g. thirteen times larger than the XXL (Pierre et al., 2011) – although only half of that area has been exposed to the nominal XXL depth of 10 ks, Figure 2.17. XCS-DR2 covers much less area than those based on the ROSAT All Sky Surveys (§ 1.2.3), e.g. the MAAssive Cluster Survey (Ebeling et al., 2001) (MACS, § 1.2.3), which covers 22,735 square degrees. However, XCS is still predicted to be more sensitive to cosmological parameters than MACS, when using the halo mass function technique (§ 1.4.2), because it is so much more sensitive (Sahlén et al., 2009).

2.8.2 Source Detection

Across all 8,598 processed observations, 330,142 sources were found. After removing duplicates 253,667 sources were found. Most of these $\simeq 90\%$ are point like. The point source flux limit falls with exposure time (Figure 2.19), and has a median value 2.31×10^{-15} ergs sec^{-1} .

Of the 253,677 unique XCS-DR2 sources, 80,210 were detected in the Galactic plane or close to the Magellanic clouds, i.e. there are 173,457 unique sources in regions suitable for cluster finding. Of the 18,192 extended sources in those regions, 15,462 extended were detected with more than 50 background subtracted counts threshold.

These 15,642 extended sources constitute the XCS-DR2 cluster candidate list. Not all of these cluster candidates will turn out to be clusters. First, because some genuine extended sources have a different origin, e.g. supernova remnants, and the halos of nearby galaxies. Those non-cluster sources are easy to pull out of the list because they are easy to see in existing, shallow, all sky optical surveys. However, there are also cluster candidates that are not genuine extended sources, either because they are blends of two or more point sources, or because they are phantom objects. XAPA finds phantom objects because wavelet transforms highlight edges, in addition to genuine sources, e.g. the edge of chip gaps, the edge of bright sources etc.

2.8.3 Comparison With XCS-DR1

The most basic test for XCS-DR2 is to be better than XCS-DR1, both in terms of area covered and the number of cluster candidates identified. This test has clearly been passed: XCS-DR2 covers 688 square degrees suitable for cluster finding, whereas XCS-DR1 covered only 276 sq.deg. Likewise, XCS-DR2 includes 15,642 cluster candidates, compared to 3,675 in XCS-DR1.

A more advanced test is to compare the XCS-DR2 and XCS-DR1 cluster candidates in the OBSids common to both. Due to a major disk failure, we cannot make a direct comparison to LD11, because the relevant files no longer exist. However, we can compare to an unpublished cluster candidate list that was derived using XCS-DR1 methodology and applied to a larger number of OBSids than was featured in LD11. In the OBSids in common, the DR1 methodology delivered 7,332 candidates, compared to 8,260 from DR2.

An exact match would not be expected because different methods were used to generate the images. Moreover, for DR1 masks were used, but not for DR2 (§ 2.8.5), so one would expect the number of DR2 candidates to be higher in a given ObsID.

When the individual 7,332 DR1-style candidates were compared with the DR2 list, 5,647 matches were found within 2 arcminutes. Of the remainder, many (993) did have a DR2 counterpart, but the latter was classified as point-like (the search radius for point source matching was decreased to $9''$, i.e. 2 pixels). This leaves 692 DR1-style candidates that were not re-detected by the DR2 methodology. Of particular concern are the 106 candidates that were detected with more than 300 counts. This is because, in simulations of the XCS-DR1 selection function, > 300 count clusters had a high probability of being detected. So it is surprising, and a little worrying, that they would be detected in an earlier version and not in a later one. That said, just because the so-called XCS³⁰⁰ sample is expected to be highly complete, it is not necessary highly pure.

Therefore, all 106 locations were checked by eye on the DR2 produced images (sadly the aforementioned disk crash means that the DR1 produced images are not available). In 10 cases, XAPA did not run properly, so no source list was produced, Figure 2.20. In 38 cases, no source is visible in the DR2 image at the DR1 location, presumably due to differences in the way the images were made and/ or due to the phantom object effect associated with the use of masks, Figure 2.21. In 33 cases, there was a point source in the DR2 image that was obviously associated to the DR1 candidate, but the separation between the centroids was $> 9''$. In 9 cases, the DR1 source was found outside the DR2 field of view, again presumably due to differences in the way the images were made, Figure 2.22. This leaves just 14 cases of good XCS³⁰⁰ cluster candidates that were found in DR1 that were not found in DR2 (Figure 2.23). Although it is disappointing that we did not find these 14, and that XAPA did not run properly in 10 ObsIDs where XCS³⁰⁰ cluster candidates were previously found, the impact on the selection function is expected to be small (quantification of the impact is beyond the scope of this thesis).

2.8.4 Comparison With XCLASS

We can further test the completeness and quality of the XCS-DR2 cluster candidate list by examining a set of serendipitous candidates produced by the rival XMM-LSS team, the so-called XCLASS sample (Clerc et al., 2012b). This sample was created using different approaches to image making and source detection and so provides an independent check

of the XCS-DR2 methodology. The XCLASS sample comprises of 850 clusters/candidates, although positions have only been made public for 422 of them. Of those 422, 412 matches to XCS-DR2 extended sources (including those with < 50 counts) were found within 2 arc minutes.

Of the remaining ten, five were classified as point sources in XCS-DR2, two were in ObsIDs for which XAPA failed, one was blended with a nearby extended source (Figure 2.24). The remaining two were missed by XAPA (Figures 2.25 and 2.26)). While missing these two, plus the blended case, is disappointing, small differences between the two samples are inevitable, given the different approaches used.

2.8.5 Contamination from non-cluster sources

As shown in LD11, it is possible to define, using an X-ray selection function, a sub-sample of XCS cluster candidates with high completeness, i.e. the so-called XCS³⁰⁰ sample. However, the selection function cannot tell us the level of contamination in the candidate list. As shown in M12, contamination remains even after obvious non-cluster extended sources (such as low redshift galaxies and supernova remnants) have been removed. In XCS-DR1, phantom sources at the edge of masks was a significant problem. This has been alleviated for DR2, by running XAPA before masking. The other problem uncovered by XCS-DR1 was that XAPA will sometimes confuse a point source (or blend of 2 or more point sources) as extended. This issue will continue in XCS-DR2 because we have not changed the PSF model in XAPA.

Figure 2.27 shows that the proportion of detected sources that were classified as extended varies across the field of view. The upturn at large off axis angles suggests that the ratio of false to true classifications rises towards the edge of the field of view. If the proportion of extended sources found between 4 and 11 arcminutes (8%) is correct, this leads to a prediction that 50% of the candidates are contaminants at off-axis angles >12 arcminutes. This trend persists even after applying a 300 count threshold.

The XMM PSF model currently being used by XAPA is clearly not sophisticated enough to classify sources correctly at all off-axis angles. A better model would help reduce contamination in future XCS cluster candidate samples. Until that time, it will continue to be necessary to confirm candidates using optical follow-up.

2.9 Conclusions and Future work

2.9.1 Conclusions

- The XCS-DR2 cluster candidate list is one of the largest (if not the largest) X-ray detected cluster candidate list.
- The modifications to the XCS-DR1 pipelines have been successful (e.g including mosaiced observations and observation targets).
- There are good matches between the cluster candidate list and XCS-DR1 and XCLASS.

2.9.2 Work Required Before Publishing in a Paper

- More work is required to understand differences between XCS-DR1 and XCS-DR2 cluster candidate lists (e.g. why new reductions fail to run through XAPA, have missing detector images, show increased noise levels).
- Analyse why previously detected clusters don't appear in the cluster candidate list - particularly where they have been found previously in XMM observations.
- Process XMM observations that have become publicly available since the last large data download.
- Understand and quantify the survey selection function.

2.9.3 Future Work for XCS-DR3

- Run XAPA including a larger ellipse size.
- Integrate the latest XMM PSF model into XAPA
- Run source detection algorithm on stacked XMM observations.

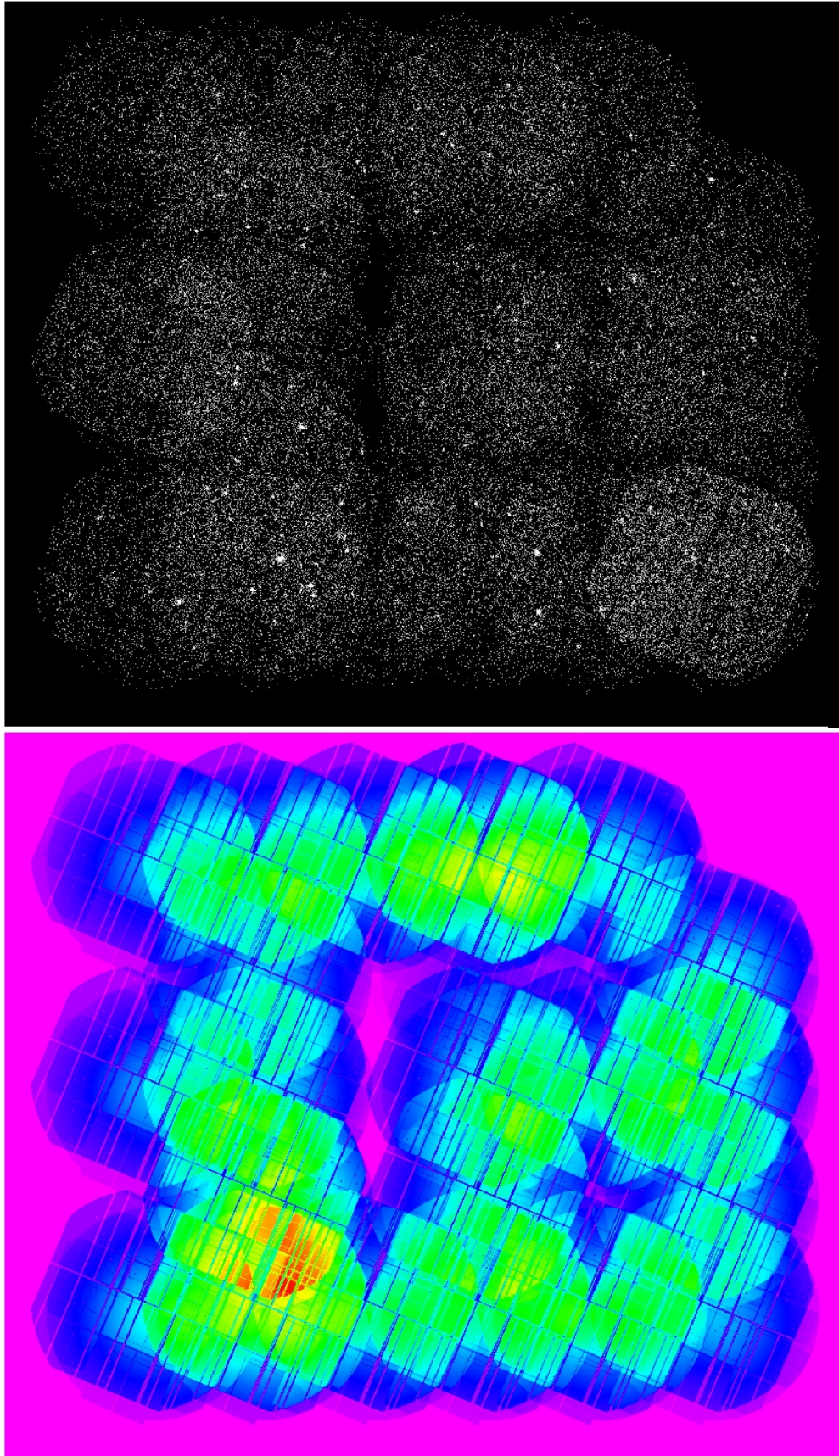


Figure 2.1: An example of an XMM mosaic mode observation, Top: mosaiced images; Bottom: mosaiced exposure maps (ObsID: 067300010, PI: Megan Urry, Total Exposure: 113 ks, Target name: *Stripe 82 X-1*).

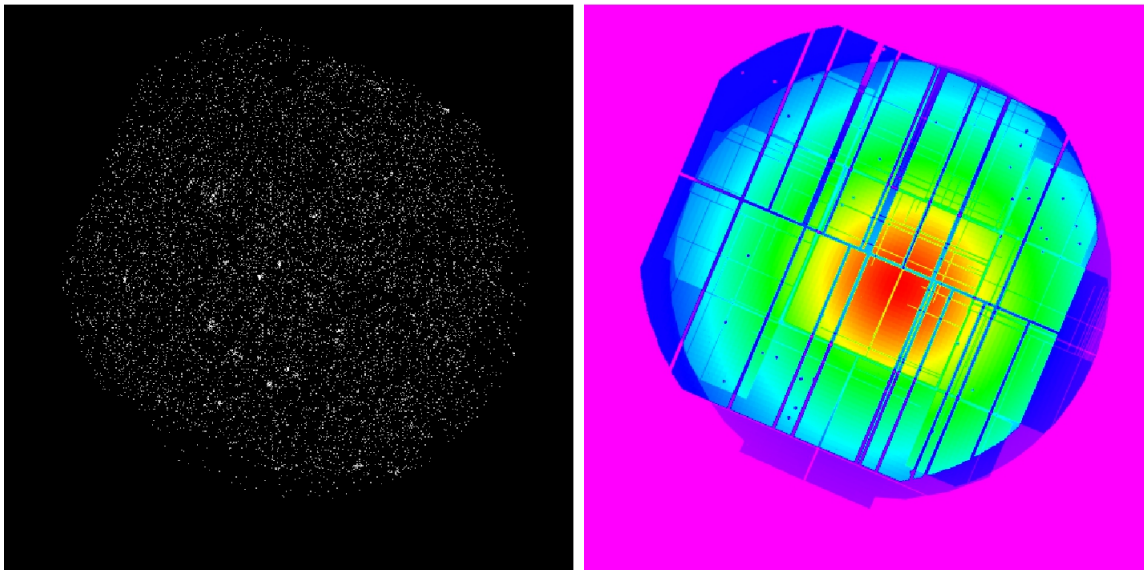


Figure 2.2: An example of a sub-observation from the mosaic observation shown in Figure 2.1. Left: The XIP produced merged (PN, MOS1, MOS2) image. Right: The XIP produced merged (PN, MOS1, MOS2) exposure map.

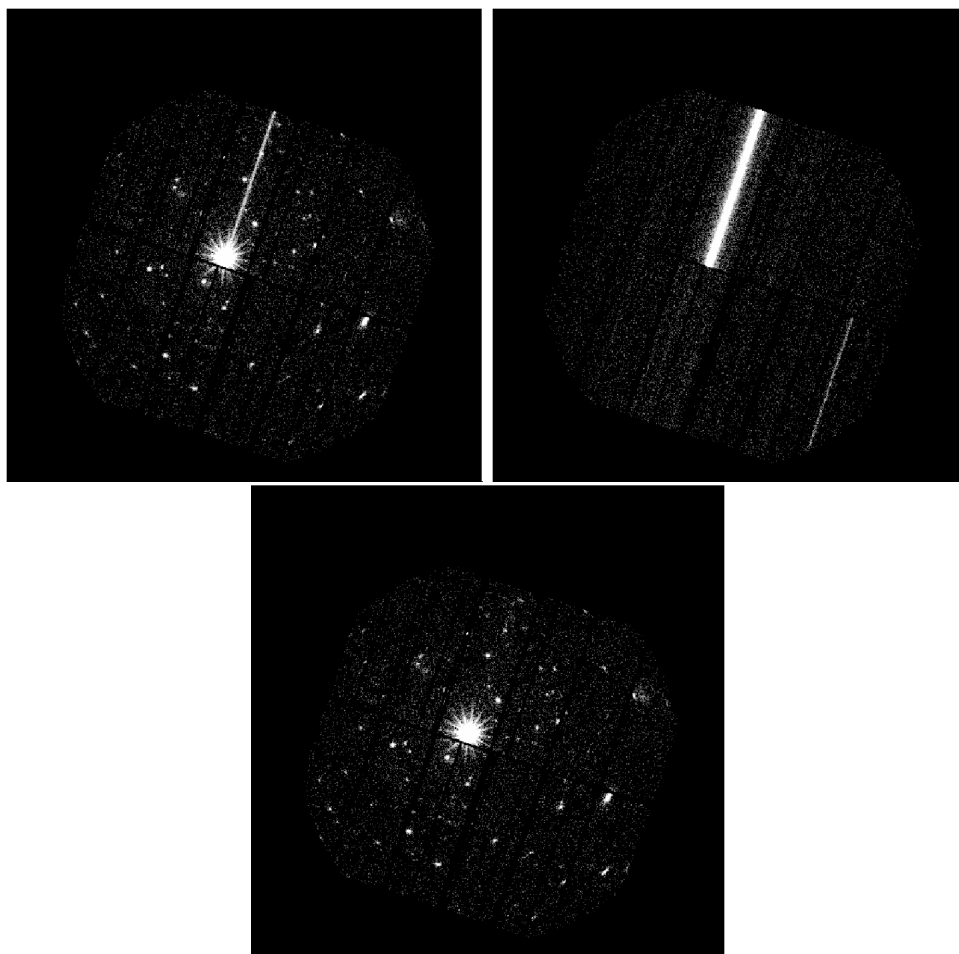


Figure 2.3: Example of an observation that has been effected by out of time events (ObsID: 0600540601). Top Left: Original XIP PN image. Top Right: The modelled out of time events. Bottom: The PN image after the modelled out of time events have been subtracted.

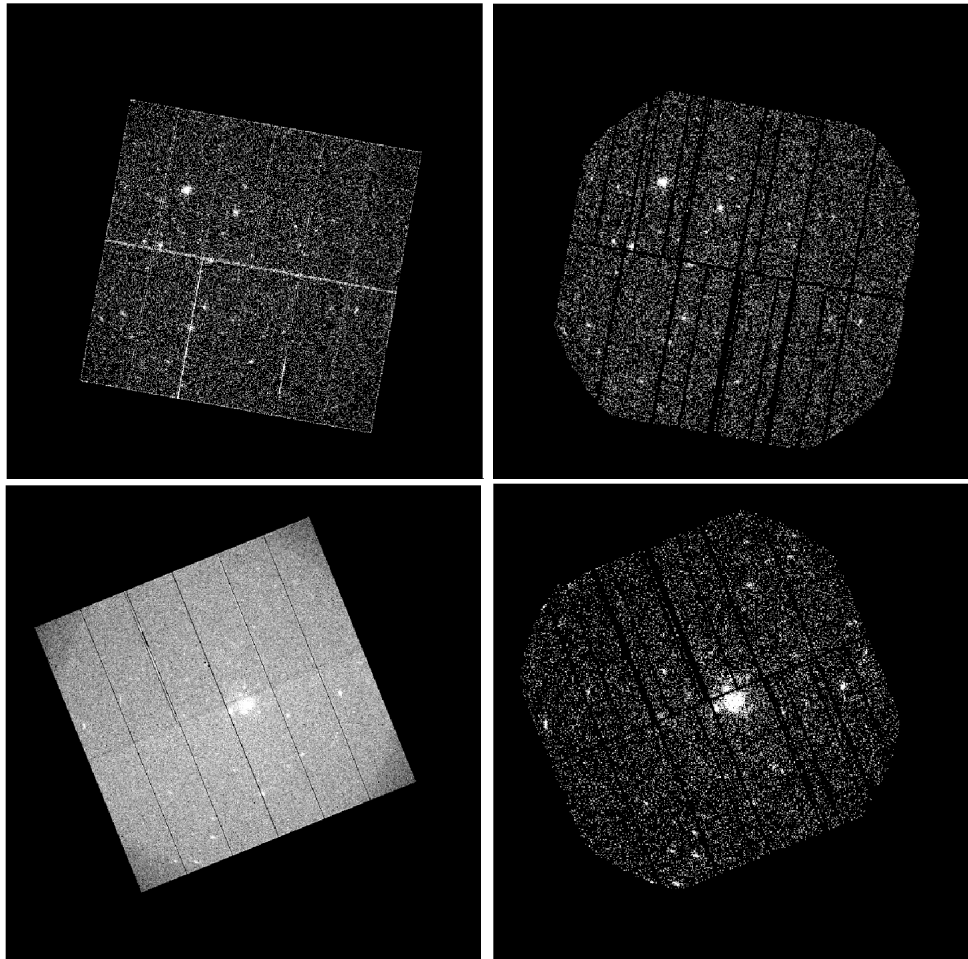


Figure 2.4: Examples of observations with different noise levels, before and after cleaning. Top row: XIP PN image of ObsID:0554700101 before and after cleaning; Bottom row: XIP PN image of ObsID:0147610101 before and after cleaning. Note that the corner of detectors are cut off in the cleaned image as they are not exposed to the sky.

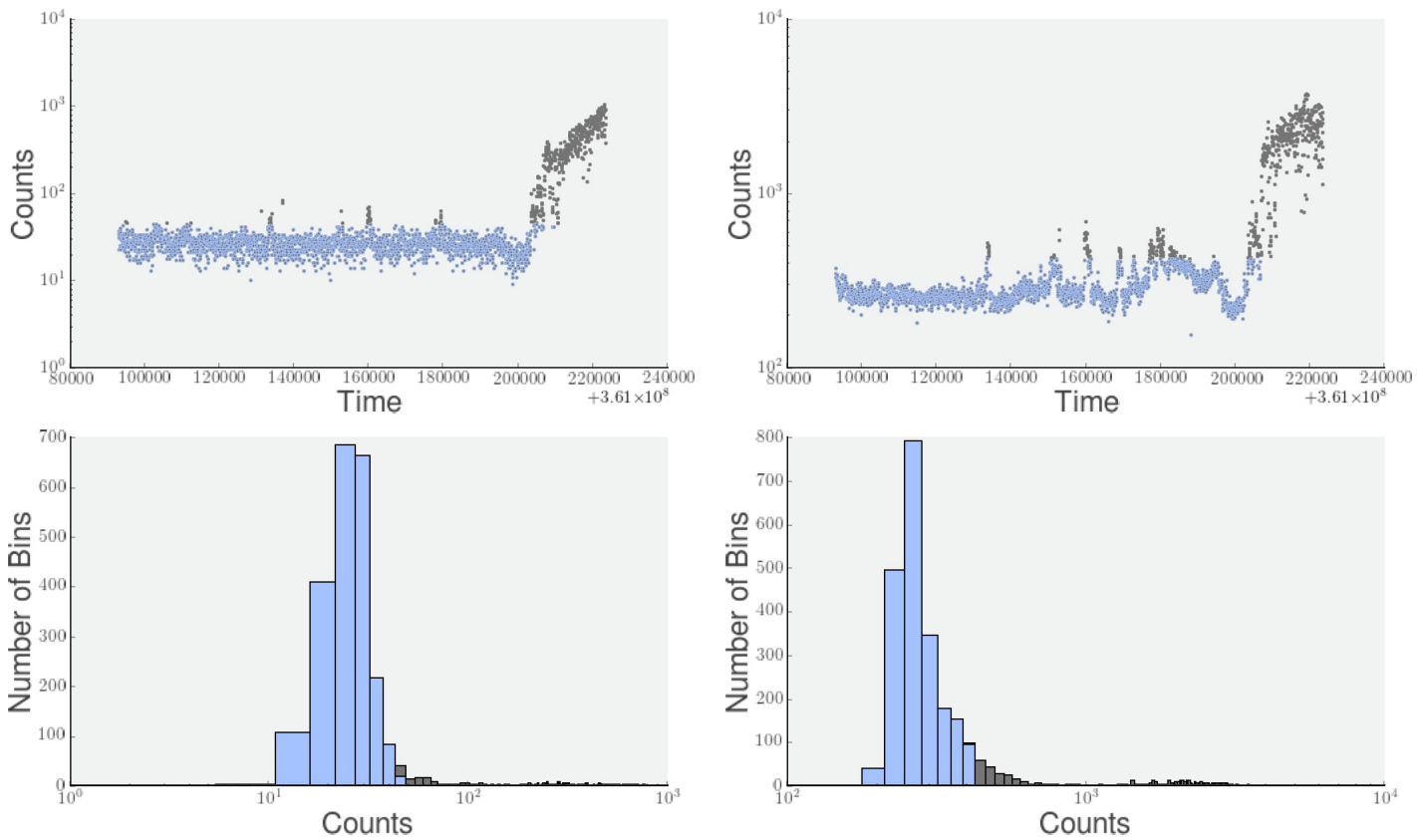


Figure 2.5: The XMM light curves for ObsID:0600540601. The left-hand plots refer to soft photon (0.1-1.0 keV) data, and the right-hand to hard photon (12-15 keV) data. The top row shows the light curve, in 50 second time bins. The bottom row shows the distribution of counts. Iterative three sigma clipping has been used to select good time intervals (blue points).

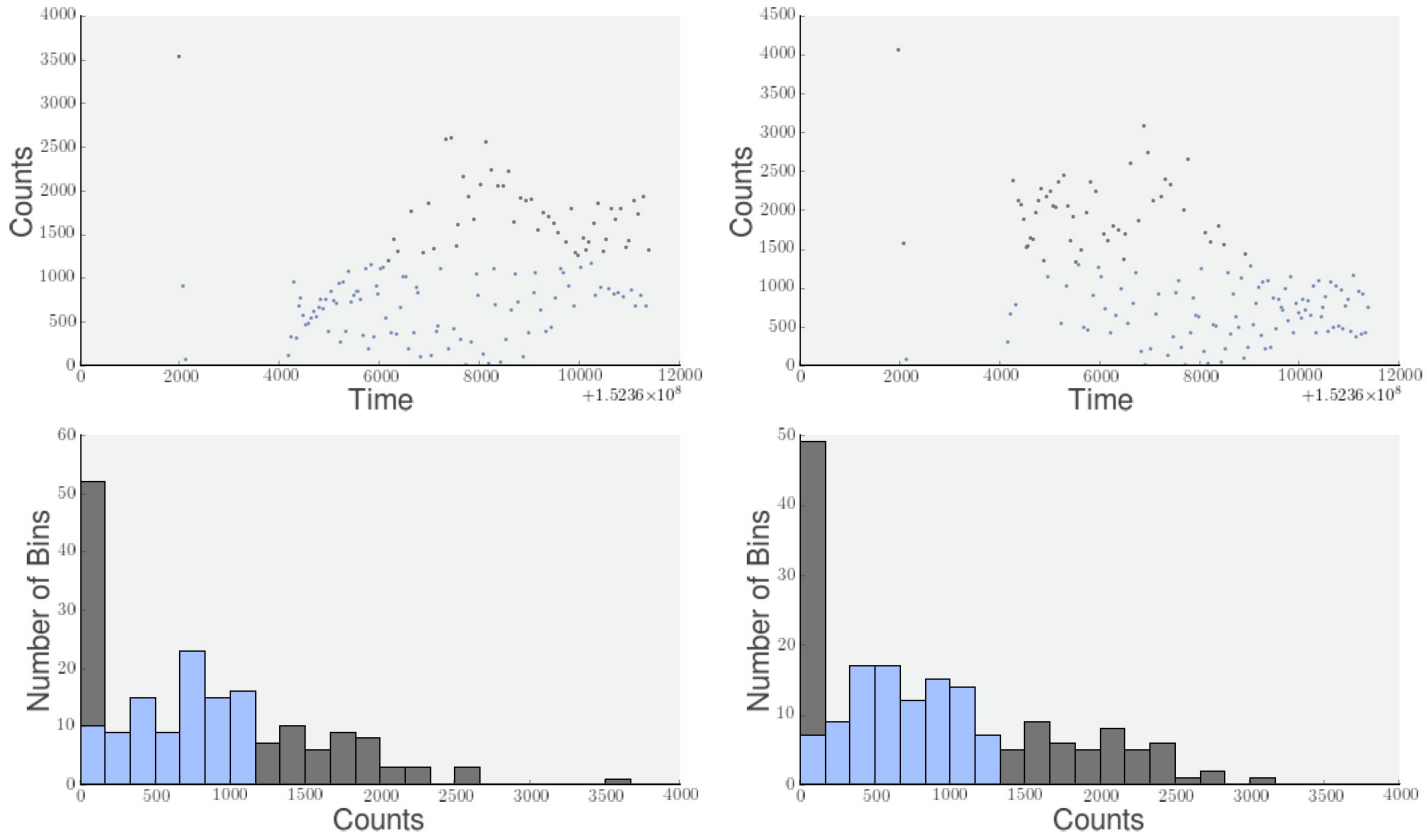


Figure 2.6: As Figure 2.5, but for ObsID:0111260501. In this case the three sigma clipping has not worked so well. (Note that the initial peak in the counts histogram reflects the fact that the filter was closed due to high background for substantial periods of the observation - hence no photons were collected during these periods.)

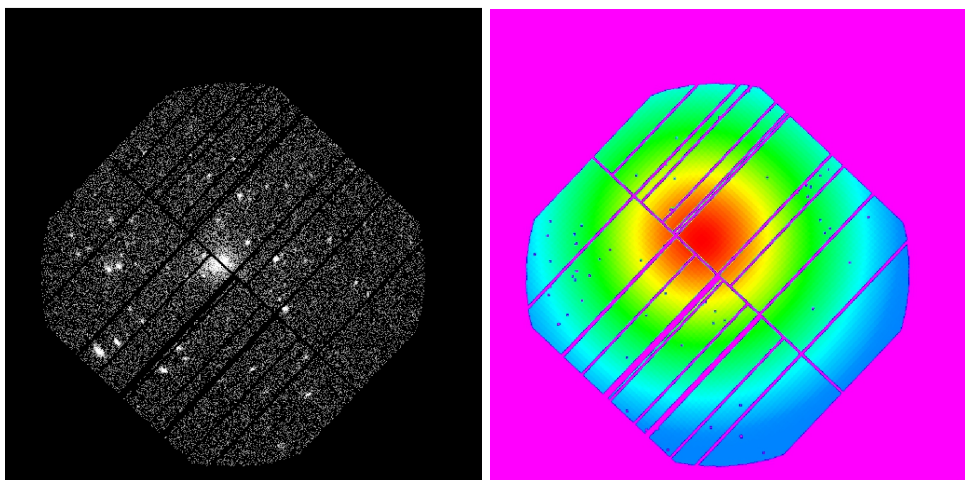


Figure 2.7: Example of a XIP PN image for ObsID:0724770501. On the left is the image and the on the right is an exposure map. The exposure map shows the effective exposure level of the observation at different points on the detector. Effective exposure is highest in the centre and then drops off due to vignetting. The dark lines represent chip gaps and bad columns.

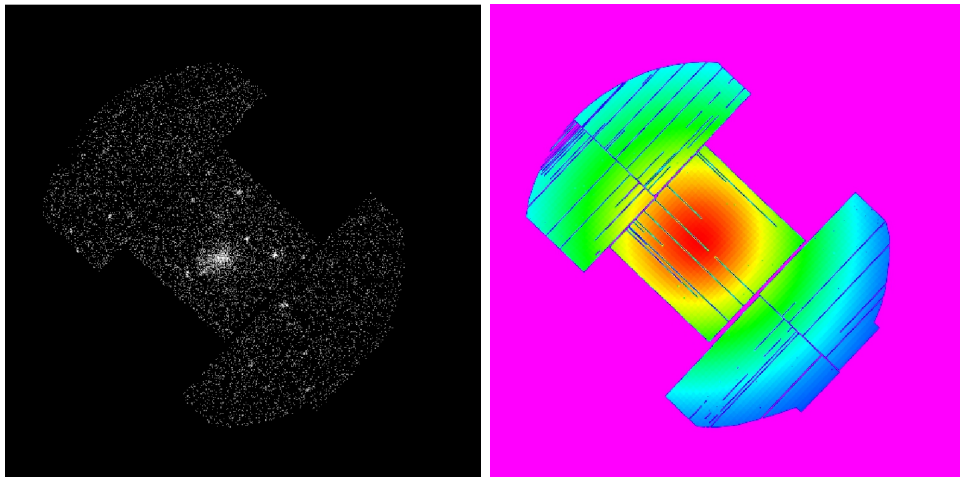


Figure 2.8: As Figure 2.7, but for the MOS1 image for ObsID:0724770501. The unusual shape is a result of the fact that two MOS1 CCDs have been damaged by micrometeorite strikes (see § 1.1.4).

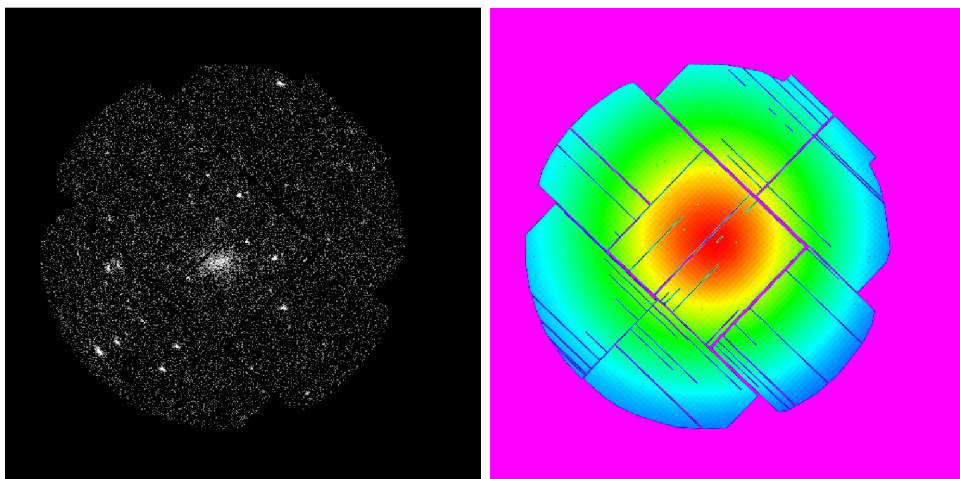


Figure 2.9: As Figure 2.7, but for the MOS2 image for ObsID:0724770501.

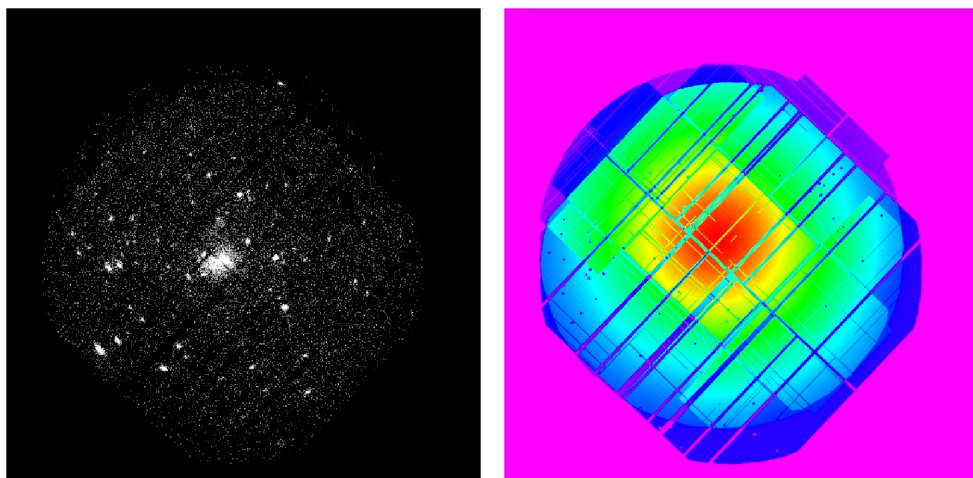


Figure 2.10: Example of a XIP merged (PN+MOS1+MOS2) image of ObsID:0724770501. This has been generated by scaling the MOS1 and MOS2 images & exposure maps (Figures 2.8 and 2.9 to the sensitivity of the PN (Figure 2.7).

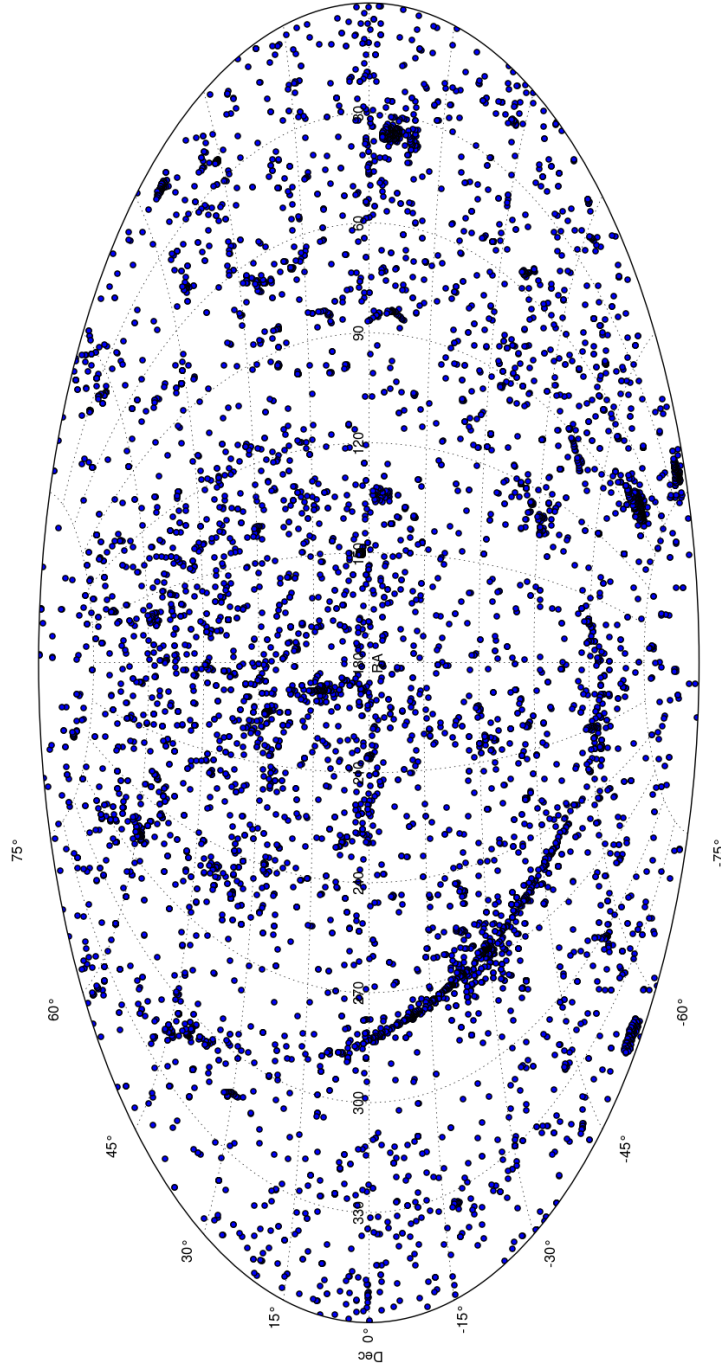


Figure 2.11: Locations of the 8,598 ObsIDs processed by XIP for XCS-DR2 (Aitoff projection in Ecliptic coordinates). The size of the dots does not represent the field of view of the EPIC camera (they are larger than the FOV). Clumps of dots indicate where surveys have taken place (including those in mosaic mode).

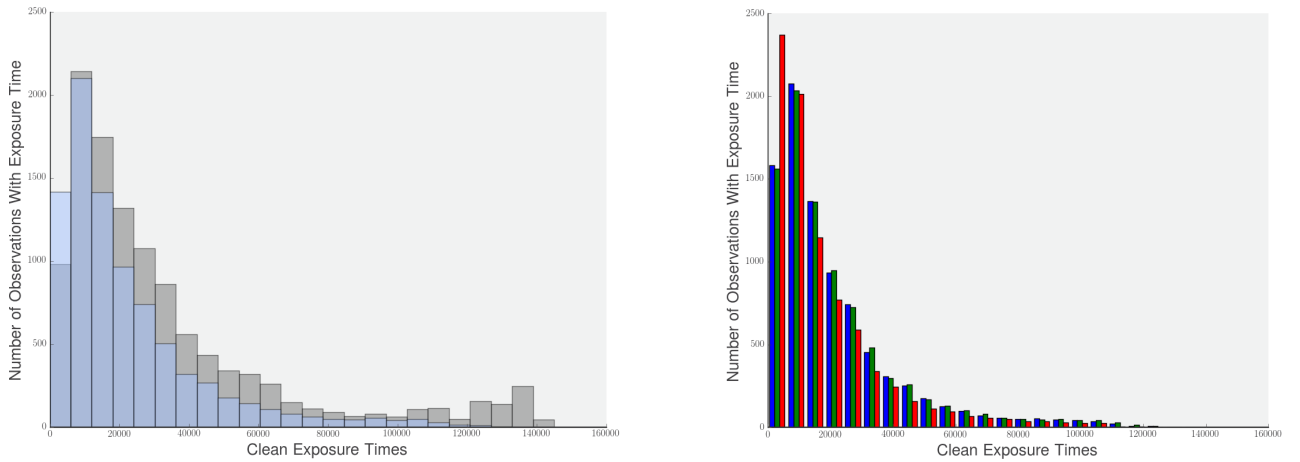


Figure 2.12: Left: The distribution of total PN observation exposure times (grey) and of clean exposure times (blue) for the 8,598 ObsIDs processed by XIP. Right: Total number of observations with clean exposure times for MOS1 (blue), MOS2 (green) and PN (red) detectors.

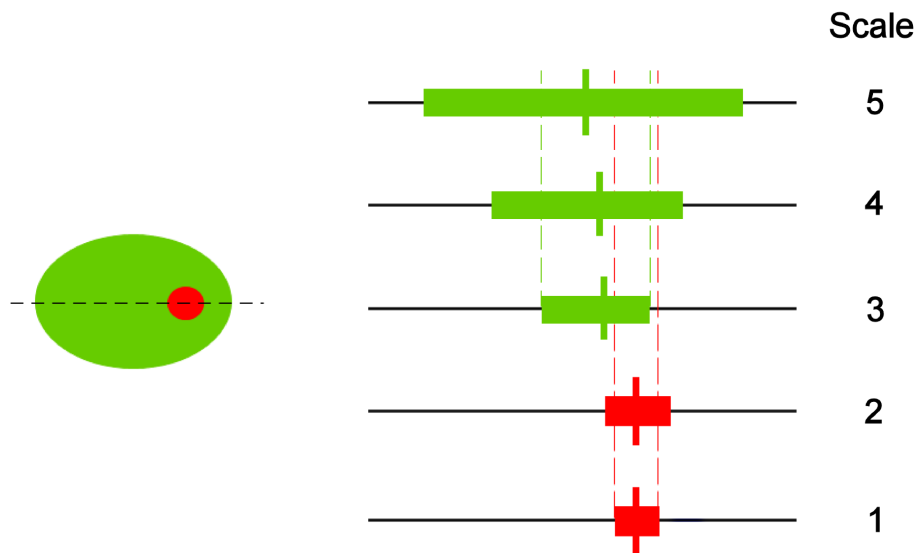


Figure 2.13: (Figure taken from LD11) A cartoon to demonstrate the decision tree used by XAPA to merge (or otherwise) sources detected at different wavelet scales. Left: An extended source and point source contaminant. Right: A 1-d slice of the source detected at five scales. The vertical bars denote the width of the source at each scale. The ellipses fit to the point source do not overlap with the centroid of the largest scale, so the point source and extended source are both detected.

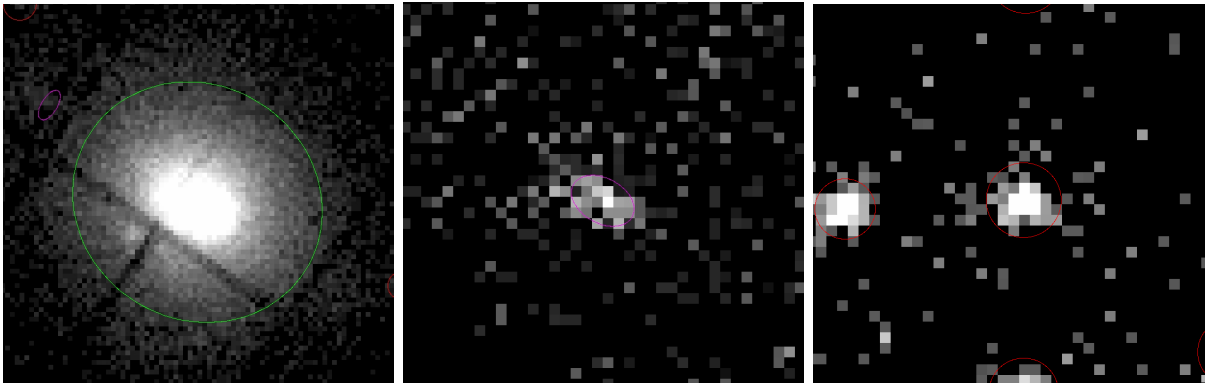


Figure 2.14: Examples of individual XAPA sources classified as extended (left), PSF-like (middle), and point-like (right). These are $3' \times 3'$ cutouts from the XIP merged image of the respective ObsID.

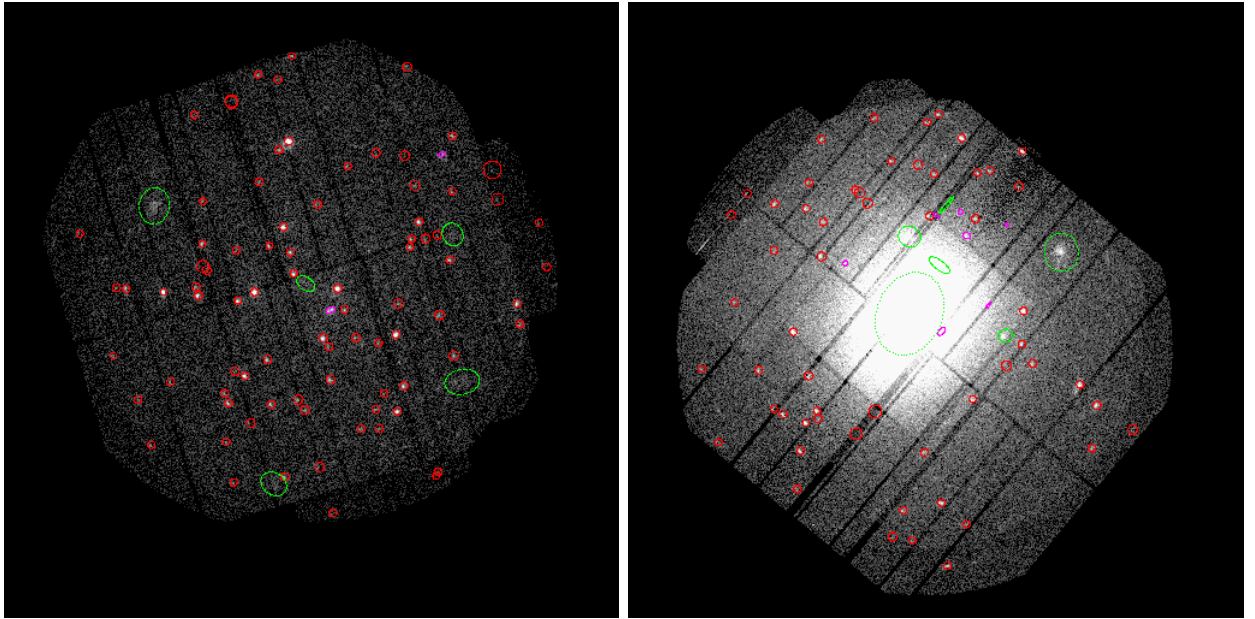


Figure 2.15: Examples of XAPA outputs for ObsID:0057560301 (left) and ObsID:0723800901 (right). The XAPA source ellipses have been overlaid on the XIP merged images. Point sources are shown by red ellipses, extended sources by green ellipses and PSF sources by magenta ellipses. Note that the target of ObsID:072380090 was Abell cluster A4059 (this is the bright extended source in the middle).

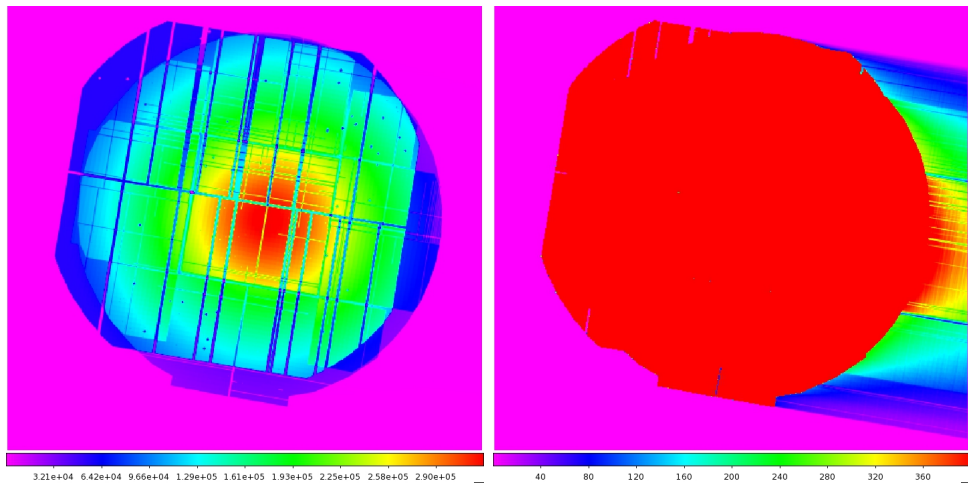


Figure 2.16: An example of an observation (ObsID:0554770101) that was mis-targeted during some of observation. Left: The exposure map with regular scaling. Right: The exposure map scaled to show very low exposure regions.

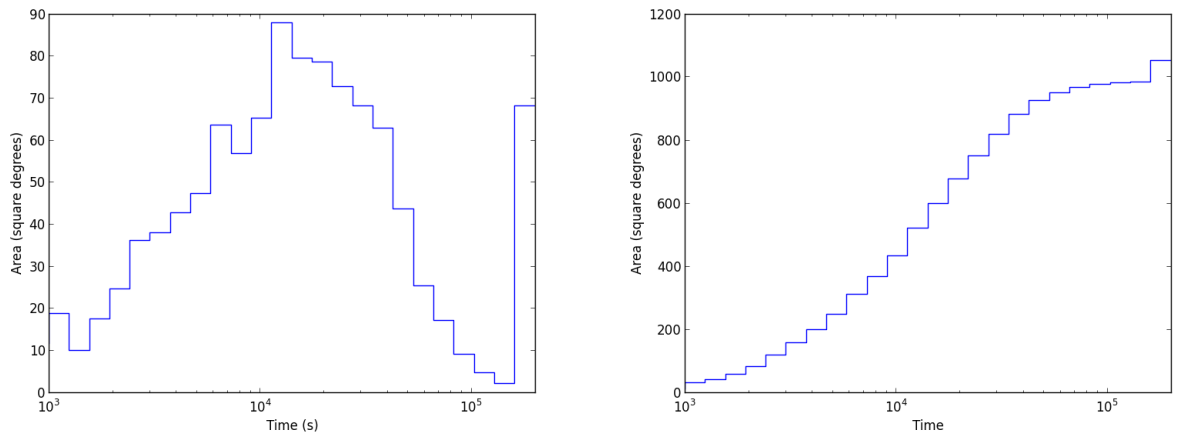


Figure 2.17: Left: Area of sky covered as a function of cleaned exposure time; Right: Cumulative plot of area of sky as function of exposure time. (These areas include the Galactic plane and Magellanic clouds.) (Image courtesy of Harry Wilcox.)

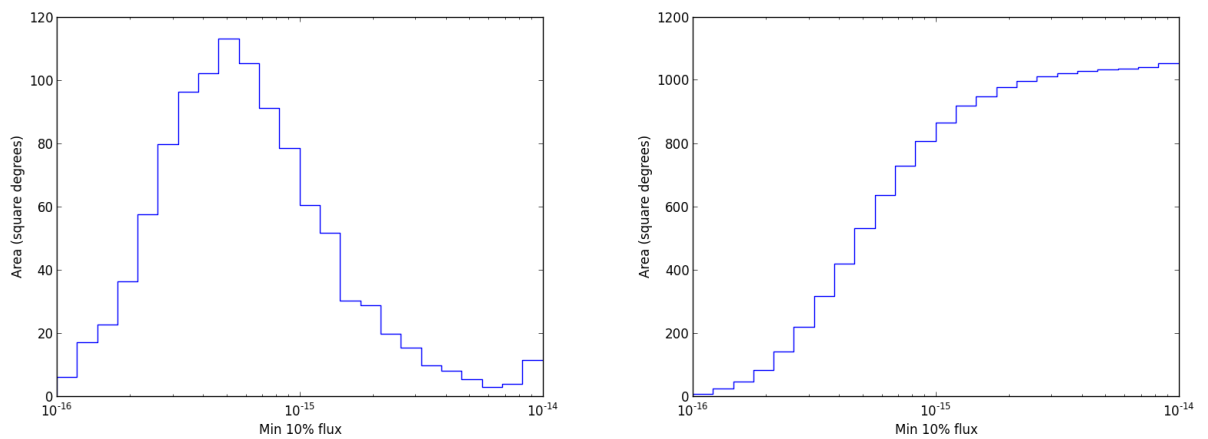


Figure 2.18: Left: Area of sky as a function of minimum flux; Right: Cumulative plot of area of sky as function of minimum.

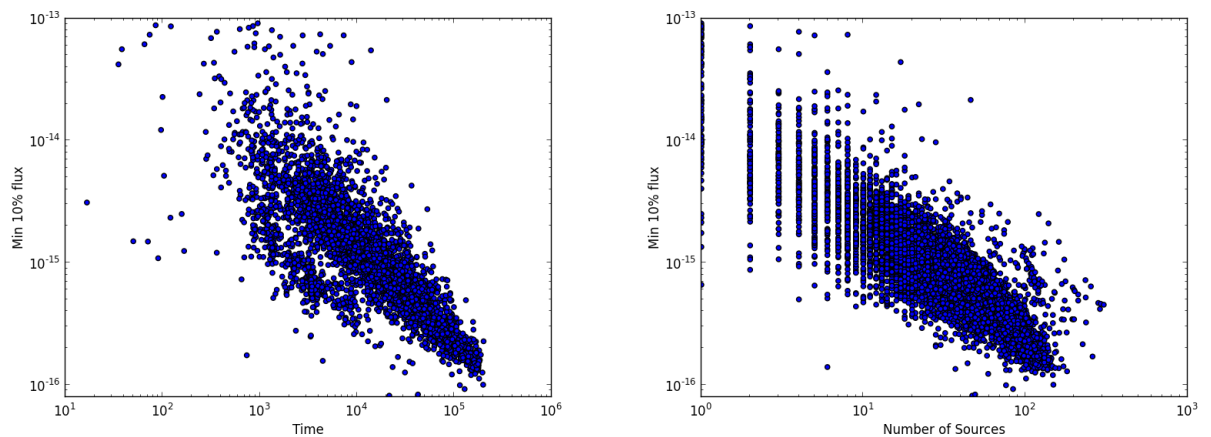


Figure 2.19: Left: Point source flux limit versus exposure time; Right: Point source flux limit versus total number of sources found by XAPA. (Image courtesy of Harry Wilcox.)

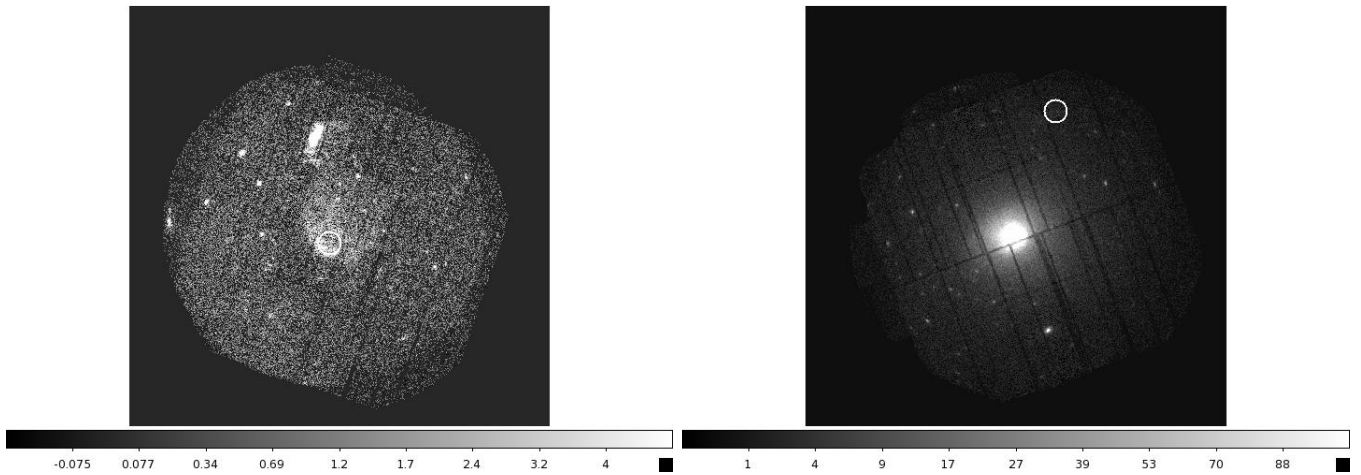


Figure 2.20: Examples of XCS³⁰⁰ candidates from the XCS-DR1 sample (shown with white circles) that were not detected by XAPA during the XCS-DR2 run. Case I: Despite the XIP images looking ‘normal’, XAPA has failed to complete successfully, so no sources have been recorded in XCS-DR2 for these ObsIds.

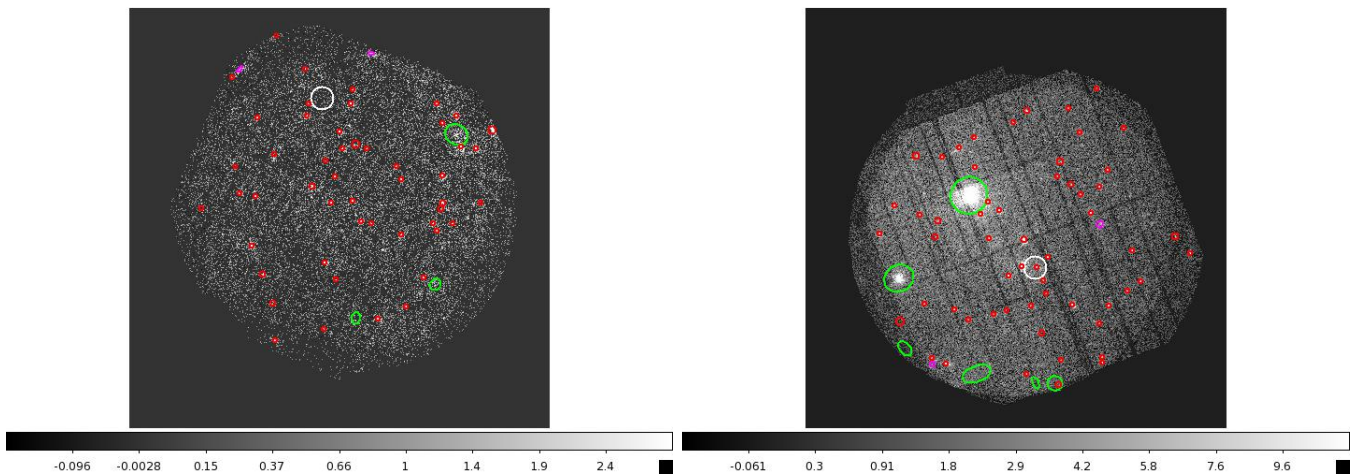


Figure 2.21: As Figure 2.20. Case II: These sources are not visible by eye in the XCS-DR2 XIP images, despite having typical exposure times and background levels (hence the XCS-DR1 sources were likely ‘phantoms’).

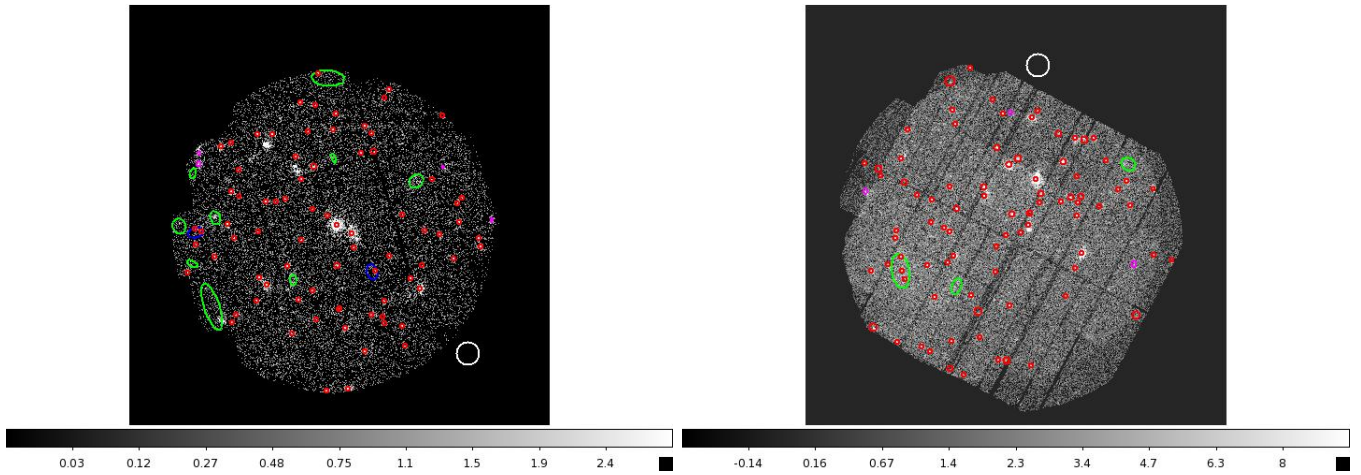


Figure 2.22: As Figure 2.20. Case III: The DR1 source lies outside the XIP merged image, because different combinations of images were used. In the left image, the PN is missing. In the right image, MOS2 is missing.

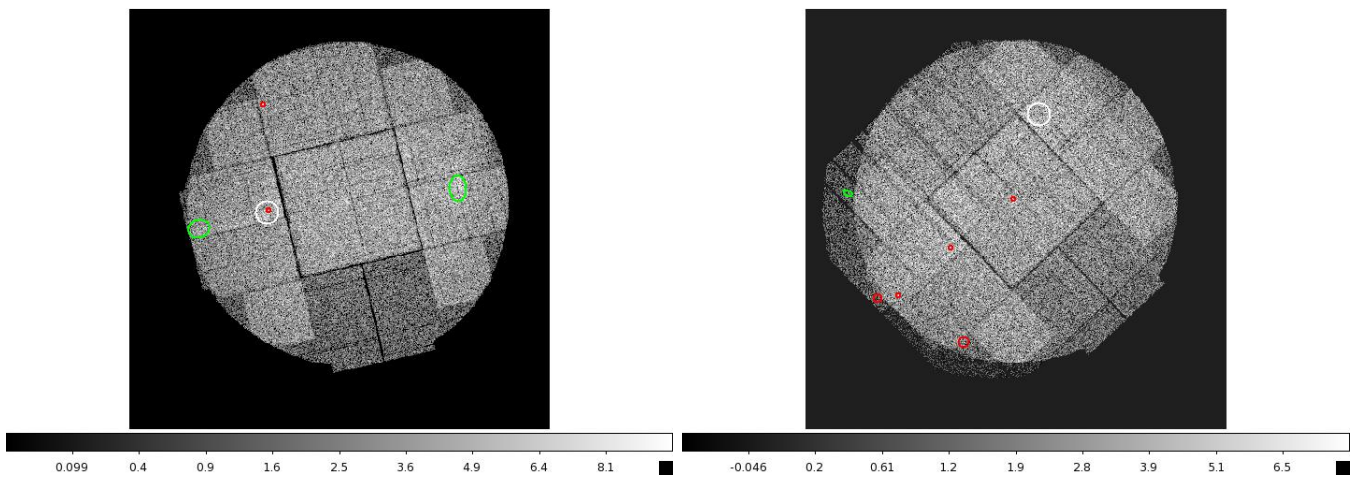


Figure 2.23: As Figure 2.20. Case IV: There is an obvious extended source at the XCS-DR1 location. We do not know why these sources were not re-directed in XCS-DR2.

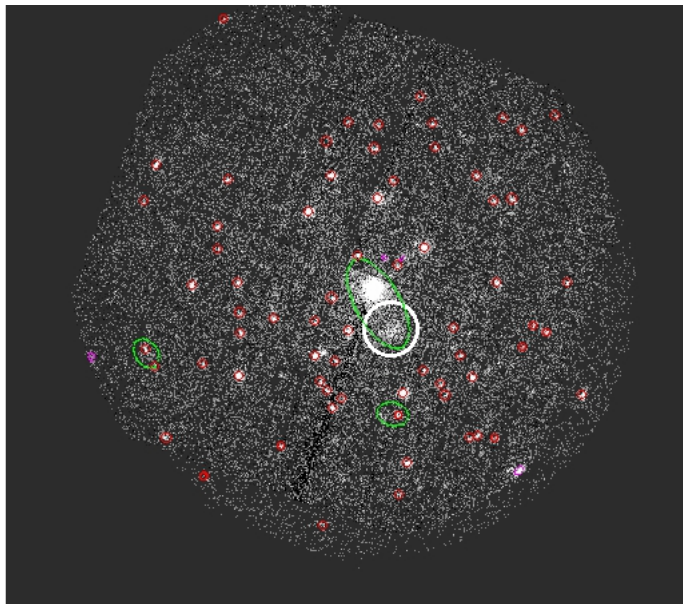


Figure 2.24: Example of an XCLASS candidate (shown with white circles) that was not detected by XAPA during the XCS-DR2 run. Case I: XClass source 1856 has been merged by XAPA with a nearby extended object.

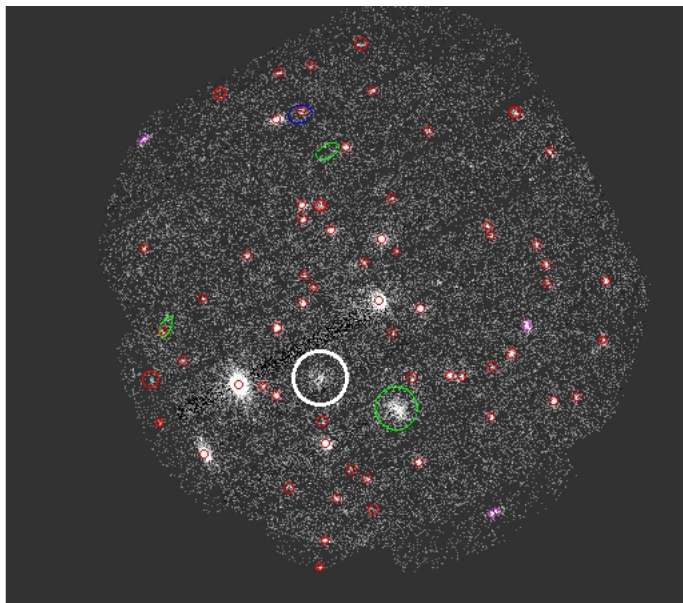


Figure 2.25: As Figure 2.24. Case II: There is an obvious extended source at the XClass source 417 location. We do not know why these sources were not re-directed in XCS-DR2.

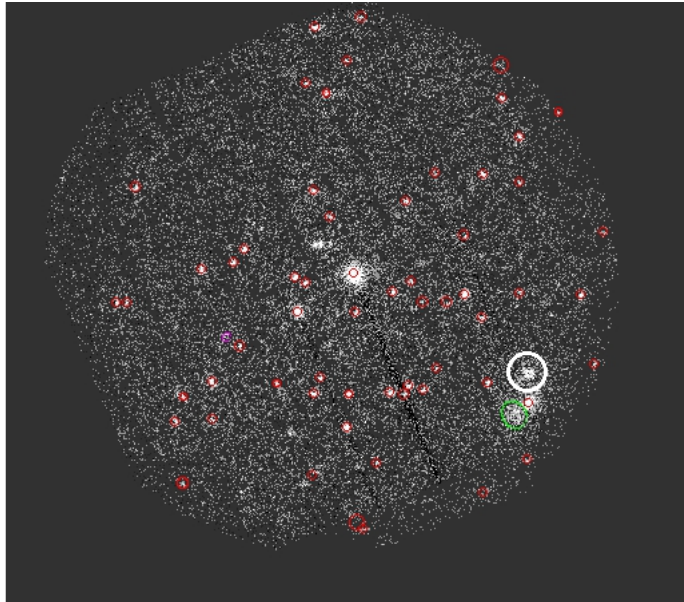


Figure 2.26: As Figure 2.24. Case III: There is an obvious extended source at the XClass source 228 location. We do not know why these sources were not re-directed in XCS-DR2.

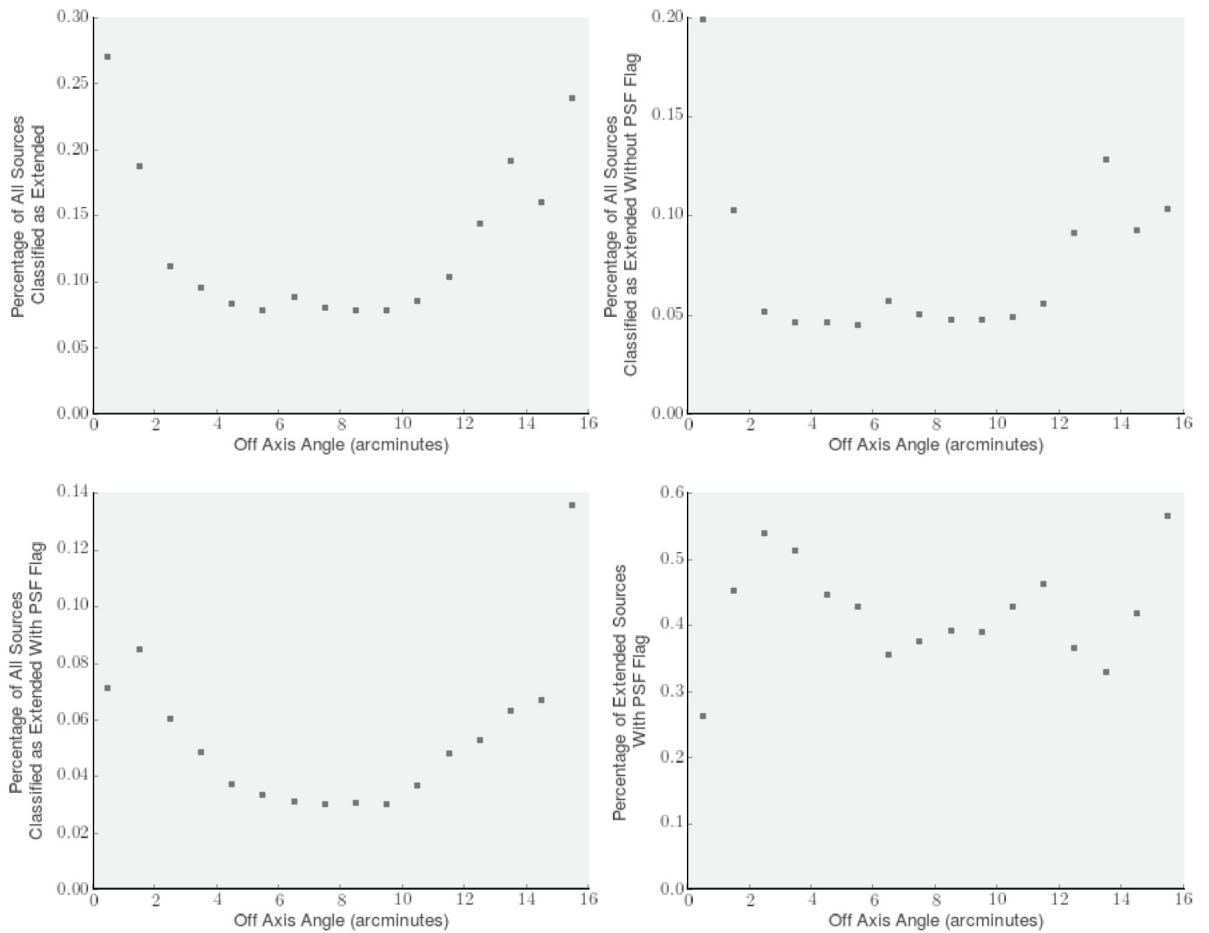


Figure 2.27: Top Left: The percentage of all sources classified as extended - including PSF flag - as a function of off-axis angle. Top Right: The percentage of all sources classified as extended - excluding PSF flag - as a function of off-axis angle. Bottom Left: The percentage of all sources both classified as extended and including PSF flag - as a function of off-axis angle. Bottom Right: The percentage of all extended sources classified with a PSF flag - as a function of off-axis angle.

Chapter 3

Generation of a New XCS Cluster Sample

3.1 Overview

Motivation The availability of 15,642 XCS-DR2 cluster candidates (Chapter 2) motivates us to confirm as many as possible as clusters. This in turn facilitates science exploitation such as the spectroscopic bias investigations (Chapter 4), scaling relation studies (Chapter 5), and rare object discovery (Chapter 6) presented in thesis. A variety of other XCS-DR2 based projects are being carried out by XCS collaborators. The work presented in this chapter is a pathfinding project with a view to a larger, more complete, release of confirmed clusters in future.

Governing Assumptions Based on our experience with XCS-DR1, we have assumed that a sizeable fraction of the candidates will be clusters, especially those detected with more than 300 counts. We have further assumed that *preliminary* identifications can be made using either a statistical approach that has been calibrated using simulations (§ 3.2), or using a literature search (§ 3.3). We have also assumed that *firm* confirmations can be made using either proximity matching with well understood cluster samples (§ 3.4) or using a “cluster-zoo” approach (i.e. eye-ball searches of high quality optical imaging (§ 3.5)).

Results Using the techniques mentioned above, and after removing duplicates between the sub-samples, the XCS-DR2 cluster sample includes 7,129 preliminary cluster identifications and 1,177 firm cluster identifications (i.e. 8,306 in total). The median redshift

is $z = 0.29$. Ninety-two clusters are at $z > 1$, with a maximum redshift of $z = 2.29$. Measurements of T_X and L_X have been made for 4,987 of the XCS-DR2 clusters.

Conclusions and Future work XCS-DR2 is the largest X-ray cluster sample to date. For example, at high redshifts, the XDCP (Fassbender et al., 2011a) sample has spectroscopically confirmed 47 galaxy clusters at $z > 0.8$, where as XCS-DR2 has 222 (although we stress that not all of these are spectroscopic redshifts). The sample has already been used for a variety of scientific studies. However, before the sample can be used for cosmology studies the optical and X-ray selection functions (§ 1.2.2) need to be properly accounted for (and that work is beyond the scope of this thesis).

3.2 Preliminary Cluster Confirmation using GMPhoRCC

Our XCS collaborators in Edinburgh (Ross Hood & Bob Mann) have developed an automated pipeline known as GMPhoRCC (for ‘Gaussian Mixture full Photometric Red Sequence Cluster Characteriser’) to measure properties of cluster candidates using multi-colour photometric surveys. The code delivers both cluster redshifts (together with associated quality flags) and a likelihood of the candidate being a cluster (calibrated using simulated galaxy catalogues). So far Hood has applied GMPhoRCC to the SDSS¹, CFHTLS², and ATLAS³ (§ 3.2.2). The GMPhoRCC algorithm has been described in detail in Hood et al. (in prep.), but for completeness we review some of its main features below (§ 3.2.1).

3.2.1 The GMPhoRCC Algorithm

The GMPhoRCC pipeline assumes that the redshift and colour distribution of the galaxies in a cluster can be modelled using Gaussian mixtures (Hao et al., 2010) assuming reliable photometric redshifts are available for every galaxy (cluster and fore/background). For every cluster (or cluster candidate), GMPhoRCC measures the over density of galaxies, inside cones of a range of radii centred on the cluster, compared to a background density. The cone size that maximises the redshift overdensity is selected as the initial cluster radius and a corresponding redshift calculated. These redshifts, together with the properties of the cluster and background galaxies within the selected cone, are used to select red

¹<http://www.sdss.org/>

²<http://www.cfht.hawaii.edu/Science/CFHTLS/>

³<http://www.h-atlas.org/survey>

sequence colour bands. GMPhoRCC then discards faint galaxies and galaxies at redshifts more than ($\Delta z = 0.25$) away from the initial redshift estimate, sets the brightest galaxy as the brightest central galaxy (BCG), and then records the BCG and the red sequence based average cluster redshift.

GMPhoRCC then grades the clusters by the cleanness of their redshift measurement: grade-4 indicates that one or both of the BCG and average redshifts were not recorded; grade-3 indicates that the two redshifts differ by more than $\Delta z = 0.1$; grade-2 indicates that one or both redshift estimates were inconsistent with the colour band; grade-1 indicates that both redshift estimates were consistent with the colour band, and with each other.

The GMPhoRCC team used mock galaxies catalogues based upon SDSS DR10 data (Ahn et al., 2014) to measure the selection function. They estimated the *purity* of cluster catalogues that rely on GMPhoRCC for confirmation to be 80%, if all redshifts grades were used, to 100% if only grade-1 was used. The corresponding *completeness* was 96% if all redshifts grades were used, and 89% if only grade-1 was used. As a compromise between completeness and purity, we have opted to use grades 1,2 and 3 in this thesis.

3.2.2 GMPhoRCC applied to XCS-DR2 Clusters Candidates

SDSS The 10th data release from Sloan Digital Sky survey (Alam et al., 2015) includes imaging data on 208,478,448 galaxies in 5 bands (*ugriz*) over 14,555 sq.deg of the Northern and Equatorial Sky. The data were collected using the SDSS telescope at the Apache Point observatory using a camera with a 3 sq.deg field of view. GMPhoRCC confirmed 5,865 XCS-DR2 cluster candidates using SDSS data (see Table 3.1). The redshift distribution peaks at $z \simeq 0.23$, see Figure 3.2.

CFHTLS The Canada France Hawaii Legacy Survey (Gwyn et al., 2012) includes photometric data on 2,597,239 galaxies in 5 bands (*ugriz*) over 410 sq.deg of the Northern and Equatorial Sky. The data were collected using the CFH telescope at the Mauna Kea observatory using a camera with a 1 sq.deg field of view. GMPhoRCC confirmed 466 XCS-DR2 cluster candidates using CFHTLS data (see Table 3.1). The redshift distribution peaks in two places ($z \simeq 0.25$ and $z \simeq 0.75$, see Figure 3.2).

Table 3.1: Detection grades of confirmed GMPHoRCC galaxy clusters.

Detection Grade	No. SDSS Clusters	No. CFHTLS Clusters	No. ATLAS Clusters
1	2311	191	185
2	1487	132	154
3	2067	141	141

ATLAS The VST ATLAS Survey (Shanks et al., 2013, 2015) includes photometric data collected in 5 bands (*ugriz*) over 4,700 sq.deg of the Northern and Equatorial Sky. The data were collected using the VLT Survey telescope at the Paranal Observatory using a camera with a 1 sq.deg field of view. GMPHoRCC confirmed 450 XCS-DR2 cluster candidates using ATLAS data (see Table 3.1). The redshift distribution peaks at $z \simeq 0.16$, see Figure 3.2.

3.3 Preliminary cluster confirmation using NED

An automated script was used to match XCS-DR2 cluster candidates with objects classified as ‘clusters’ or ‘groups’ in the NASA Extragalactic Database (NED, ⁴), and to extract redshift information. For this, a search radius of 1.5 arcminutes from the XAPA defined centroid of the candidate was used ($\simeq 500 \text{ h}^{-1}\text{kpc}$ at $z = 0.45$, assuming a flat cosmology with $\Omega_m=0.3$), resulting in 5,124 matches of which 2,562 unique objects have redshifts. There were 3,635 redshifts available for these clusters, i.e. often more than one redshift was catalogued per cluster (Figure 3.1). For the purposes of this thesis, no distinction was made between spectroscopically and photometrically confirmed redshifts.

3.4 Candidate confirmation using well understood cluster samples

The following published clusters samples have homogeneous selection methods and are claimed to have a low contamination (by non cluster sources) rate. Although many of these clusters are already included in NED, we decided to run separate matches to ensure the integrity of the sub-samples.

XCS-DR1 There are 467 clusters in common between the XCS-DR2 cluster candidate list and the M12 XCS-DR1 sample (§ 1.2.2 and § 2.8.3). The redshift distribution peaks at $z \simeq 0.1$, see Figure 3.3.

⁴The NASA/IPAC Extragalactic Database (NED) is operated by the Jet Propulsion Laboratory, California Institute of Technology, under contract with the National Aeronautics and Space Administration.

RedMaPPer There are 993 clusters in common between the XCS-DR2 cluster candidate list and the RedMaPPer sample (Rykoff et al., 2014) derived from SDSS data (§ 1.2.4). The redshift distribution peaks at $z \simeq 0.5$, see Figure 3.3. There are also 33 matches between the XCS-DR2 cluster candidate list and the preliminary RedMaPPer sample derived from Dark Energy Survey (DES) data. For these, The redshift distribution peaks at $z \simeq 0.4$, see Figure 3.3.

SPT There are 79 clusters in common between the XCS-DR2 cluster candidate list and the (Bleem et al., 2015) cluster sample derived from SPT data (§ 1.2.4). The redshift distribution peaks at $z \simeq 0.4$, see Figure 3.4.

Planck There are 342 clusters in common between the XCS-DR2 cluster candidate list and the (Planck Collaboration et al., 2015a) cluster sample derived from Planck data (§ 1.2.4). The redshift distribution peaks at $z \simeq 0.1$, see Figure 3.4.

3.5 Candidate Confirmation using DES-SV data

Several XCS members also participate in the Dark Energy Survey (DES) (Wu et al., 2010), and that has allowed us to confirm some XCS-DR2 cluster candidates using DES images. The Dark Energy Survey (DES) is a collaboration that is carrying out a deep and wide ground-based optical survey in the Southern hemisphere. DES and the National Optical Astronomy Observatory (NOAO) have deployed a new optical imager called DECam on the Blanco telescope at the Cerro-Tololo Interamerican Observatory. DECam has a three square degree focal plane covered by 62 red sensitive CCDs with ~ 0.263 arcsec/pixel resolution. The survey began in September 2013 and will be conducted during 525 nights of dark time over five years. The main goal of DES is to constrain the dark energy equation-of-state through four probes: galaxy clusters, large-scale structure, Type 1a supernovae, and weak-lensing shear maps. Ultimately, DES aims to survey 5000 square degrees in the Southern Galactic Cap in g, r, i, z and Y filters. However, in this thesis, we use only the DES science verification (SV) sky regions: ~ 250 square degrees that were taken during a period (November 2012 through February 2013) of instrument commissioning. The overlap between DES-SV and the XMM archive is shown in Figure 3.5.

For XCS-DR1, the following approach, known as XCS-Zoo, was used to carry out optical

confirmation of XCS cluster candidates (see M12 for details): Both the name and the methodology were inspired by the SDSS Galaxy Zoo project (Lintott et al., 2008), i.e. a team of volunteers use eye-ball inspection to classify XCS cluster candidates a web interface. Candidates were included in the XCS-DR1 XCS-Zoo if optical imaging was available from observations carried out by XCS members or from the SDSS public archive. Each candidate was classified at least five times. The XCS-Zoo categorisation of each source was based upon the following information: a series of (3×3 , 6×6 , 12×12 arcmin) X-ray image cutouts, highlighting X-ray contours and the region enclosed by the XAPA X-ray extent; a corresponding series of colour-composite optical images (with and without X-ray contours overdrawn). The inspected candidates were classified into one of the following categories of cluster: *gold*; *silver*; and *bronze*, or into the category *other*, see Figures 3.6 and 3.7.

For XCS-DR2, we have so far only carried out an XCS-Zoo using DES-SV imaging. The approach taken was similar, but simpler, than that in Mehrrens et al. (2012). Only three XCS members took part (Philip Rooney, Chris Miller, and Kathy Romer) and only two classification types were used: *cluster* and *other*. Colour-composite DES $3' \times 3'$ postage stamps, with X-ray contours overlaid, were generated from the DES imagery (see Figure 3.8). In total, 178 XCS-DR2 sources were confirmed as clusters this way. Of these, 123 do not match with any ‘cluster’ or ‘group’ object in NED (within a search radius of $3'$) and so have the potential⁵ to be new cluster discoveries. The catalogue will be made public together with cluster positions, DES and XMM images, photometric redshifts and T_X values (Miller, Rooney et al. 2015 in prep.).

The redshifts have been extracted from DES photometric galaxy catalogues using a model independent Bayesian redshift method, ArborZ (Gerdes et al., 2010). ArborZ uses the full $P(z)$ distribution of each galaxy in the cluster and a training set of spectroscopic redshifts (Figure 3.9). The redshift distribution peaks at $z \simeq 0.4$, see Figure 3.10.

3.6 X-ray Post Processing

3.6.1 Temperature Measurement Methodology for DR2

For XCS-DR1, the following approach to T_X measurements was taken (see LD11 for details): Spectra were generated in the 0.3-7.9 keV band using photons in the XAPA source

⁵There is usually a lag of several months before published catalogues appear on NED.

ellipse; an in-field background subtraction method was used; model fitting was performed using Cash statistics (Cash, 1979) inside XSPEC; typically⁶ all observations from the three EPIC cameras or from repeat observations) of a given cluster were used in a simultaneous fit; the model used was an absorbed MEKAL (Mewe et al., 1986) with four variations (*i*) n_{H} and Z frozen; *ii*) n_{H} and Z free; *iii*) as *ii*) but with an extra power law component; *iv*) as *ii*) but with an extra MEKAL component. When more than one of the four model variations produced an acceptable fit (defined to be $0.3 < T_{\text{X}} < 17.0$ keV, the best fitting model was adopted. XSPEC is then used to produce a bolometric luminosity (0.1-100 keV) in the spectral extraction region assuming that best fit spectral model.

For XCS-DR2, the approach taken was broadly similar. However, the following changes were made: The slowest, but best, XSPEC fitting mode was used (`'switch 0'`); only model *i* from LD11 was used, i.e. n_{H} fixed at the (Dickey & Lockman, 1990) value and Z frozen at 0.3 of the Solar abundance); and a different approach to selecting observations for a simultaneous fit was used. With respect to the latter, if more than one observation was available, a separate spectrum was extracted for each. These were then fit using XSPEC individually. The results of the individual fits govern whether the respective spectrum will be included in a simultaneous joint fit. First, the individual best fit temperature must all in the range $0.08 < T_{\text{X}} < 30.0$ keV. Second, XSPEC must have been able to define both upper and lower error bounds on the best fit value (in low signal to noise cases, it might be possible to measure a best fit value, but not one or both of the error bounds). This approach of spectral selection is very different to that used in LD11. In that work, no initial quality tests were made. All spectra were assumed to be beneficial in the joint fit unless they a) contained less than 10 counts in total or b) contained less than 10% of the counts in the individual spectrum (of the respective cluster) with the most counts. The rationale for changing the way multiple spectra were used is described in Chapter 4.

A comparison of the LD11 derived T_{X} measurements and those derived using the new methodology, for the 346 clusters in common, is shown in Figure 3.12. As expected, there is a strong correlation. However, there is a tendency for the new method to record lower temperatures than the DR11 method. A comparison of the relative error on T_{X} , $Error_{\text{rel}}$, is shown in Figure 3.13, where $Error_{\text{rel}}$ is defined as

⁶Exceptions described in the following paragraph.

$$Error_{\text{rel}} = \frac{\Delta T_{X_{\text{upp}}} + \Delta T_{X_{\text{low}}}}{T_X}, \quad (3.1)$$

and $\Delta T_{X_{\text{upp}}}$ and $\Delta T_{X_{\text{low}}}$ are the 68% upper and lower bounds on T_X measured by XSPEC. The Figure shows that the error is typically lower with the new methodology, hence justifying the changes since LD11.

3.6.2 Luminosity Measurement Methodology for DR2

For XCS-DR1, the following approach to L_X measurements was taken (see LD11 for details): New ObsID images were generated in the 0.3-7.9 keV (those already available from XIP are in the 0.5-2.0 keV band, § 2.5); a spherically symmetric β -model was fit to the cluster (using the same source and background regions used for the T_X fitting) using the MINUIT package (James & Roos, 1975); the best fit model was used to scale the bolometric luminosity obtained from the spectral fitting to R_{500} . R_{500} is chosen as it is the largest radius that XMM can reliably measure temperature and gas masses.

For XCS-DR2, the approach taken was quite different. No spatial fitting was carried out. Instead, the XSPEC derived bolometric luminosity is scaled to an approximate R_{500} using the relation given in (Arnaud et al., 2005) that is based on high signal to noise observations of 10 clusters with XMM-Newton:

$$E(z)R_{500} = 1.104 \times (kT/5 \text{ keV})^{0.57} \quad (3.2)$$

where $E(z)$ is the dimensionless Hubble parameter defined in 1.6. The XAPA defined source ellipse is typically smaller than the R_{500} value, e.g. see Figures 3.14 and 3.15. A new spectrum is extracted from an $r < R_{500}$ circular region (with XAPA ellipses of any other sources therein masked). XSPEC is then used to calculate the aperture corrected bolometric luminosity, while keeping the temperature fixed at the value previously measured from the XAPA ellipse region. Both the DR1 and DR2 measure the projected luminosity in a cylinder with R_{500} .

A comparison of the LD11 derived L_X measurements and those derived using the new methodology, for the 347 clusters in common, is shown in Figure 3.16. As expected, there is a strong correlation. However, there is a tendency for the new method to record lower

luminosities than the DR11 method. This is to be expected because L_X increases with R_{500} , which in turn scales with T_X (and these are typically lower for XCS-DR2 than for XCS-DR1, Figure 3.12).

We stress that the methods used to confirm XCS-DR2 candidates have introduced artificial biases into the resulting cluster catalogue. These are in addition to the expected bias that results from a heterogenous sensitivity limit (higher redshift and/or lower mass clusters will be detected in longer observations). For example, Planck and SPT SZ selected clusters will be hotter than the typical X-ray selected cluster, whereas clusters confirmed using SDSS will tend to have lower redshifts than those confirmed by DES. These biases can be seen in Figures 3.2, 3.3, 3.4, and 3.18. The XCS team aims to select statistically robust sub-samples of clusters for scaling relation and cosmology studies using XCS-ZOO combined with SDSS and with the full (rather than SV) DES survey, however that work is beyond the scope of this thesis.

3.7 The XCS-DR2 Cluster Catalogue

Following the confirmation and redshift measurement exercises described above (§ 3.2 to 3.5), we were able to compile a list of 8,306 clusters with redshift information once duplicate entries were removed (based on 1,177 firm and 7,129 preliminary identifications). It was not uncommon for a given cluster to have multiple redshift estimates, so redshift information is stored in separate columns depending on the source (Table 3.2). The redshift distribution for the sample is shown in Figure 3.17. It peaks at $z \simeq 0.1$, has a maximum value of $z = 1.47$, and a median value of $z = 0.2815$. In this Figure, the following redshift hierarchy was used if more than one redshift measurement was available: SPT, Planck, XCS-DR1, RedMaPPer, GMPhoRCC-SDSS, GMPhoRCC-CFHTLS, GMPhoRCC-ATLAS, NED. This hierarchy was chosen by comparing the redshift from one sub-sample, e.g. SPT, to the redshifts from the other sub-samples for clusters in common (e.g. Figure 3.11). The results are summarised in Table 3.2. We note that comparisons were not made to redshifts derived from NED because some of those redshifts may well have come from the sample under test (i.e. would artificially register a zero offset).

All clusters with redshift measurements were run through the T_X and L_X fitting pipelines. When more than one redshift value was available for a given cluster, that cluster was run

Redshift Source	No. Clusters	No. T_X and L_X fits	z -quality indicator
GMPHoRCC _{SDSS}	6446	4574	75% (1368)
NED	2903	2428	n/a
RedMaPPer _{SDSS}	773	643	79% (915)
GMPHoRCC _{ATLAS}	419	293	27% (79)
XCS-DR1	434	385	72% (474)
Planck	342	262	84% (225)
GMPHoRCC _{CFHTLS}	222	114	48% (140)
DES-SV	178	135	n/a
SPT	78	71	96% (27)
RedMaPPer _{DES}	33	32	n/a

Table 3.2: For each sub-sample of clusters used during XCS-DR2 cluster candidate confirmation, the number of clusters for which redshift information is available, the number of those for which acceptable T_X and L_X fits were derived, and the percentage of redshifts for which the difference was $\delta < 10\%$ when compared to a measurements from another sub-sample. (The number of clusters in the redshift comparison is given in parentheses).

through the T_X and L_X fitting pipelines multiple times. Not all the clusters were detected with sufficient signal to noise to yield acceptable fits: of the 8,306 clusters run through the pipelines, T_X and L_X values were measured for only 4,987 of them. The T_X and L_X distributions for the sample are shown in Figures 3.17. The temperature distribution peaks at $T_X \simeq 2$ keV, has a maximum value of $T_X = 13.8\text{keV}$, and a median value of $T_X = 2.19$ keV.

3.8 Conclusions and Future Work

3.8.1 Conclusions

- The XCS-DR2 confirmed cluster sample is the largest X-ray cluster candidate to date (and is much larger when including preliminary detections).
- GMPMorph has been successfully ran on the XCS-DR2 cluster candidate list, although there may be issues with the redshifts estimated by the pipeline.
- DES-SV data has been used to confirm X-ray cluster candidates.
- There are large, useful subsamples which overlap with other cluster catalogues (e.g RedMaPPer, Planck, SPT).
- Clusters confirmed using different techniques show different redshift, luminosity and temperature distributions.
- There are 222 preliminary clusters at redshift, $z \geq 0.8$.

- There are 1,105 preliminary clusters with temperature, $T_X > 5$ keV

3.8.2 Work Required Before Publishing in a Paper

- A new XCS cluster zoo will be carried out including public data from SDSS and Megacam, as well as proprietary data from DES.
- Redshifts will be validated to ensure their quality.
- Statistically useful subsamples will be used to test the optical selection function (for instance by using areas which overlap deep and shallow optical data).
- Almost half of the XCS-DR2 preliminary cluster detections have a redshift but no spectral fit. A new pipeline will be developed to estimate luminosity when no temperature is available.

3.8.3 Future Work for XCS-DR3

- In the future more publicly available spectroscopic data for cluster galaxies will become available.
- Include new imaging from LSST and Hyper Supreme-Cam
- Include infra-red data to find higher redshift clusters.
- Include future follow up of XCS clusters taken by pointed Chandra and XMM observations.
- Create a new XMM mosaic covering deep DES fields.

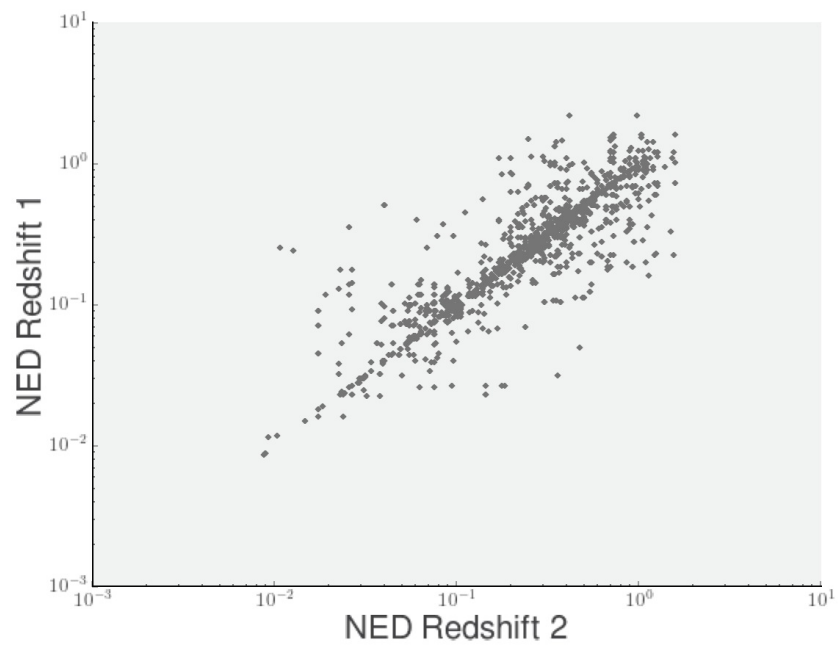


Figure 3.1: Where NED records at least two redshifts for a given XCS-DR2 cluster, the difference between those records is as shown.

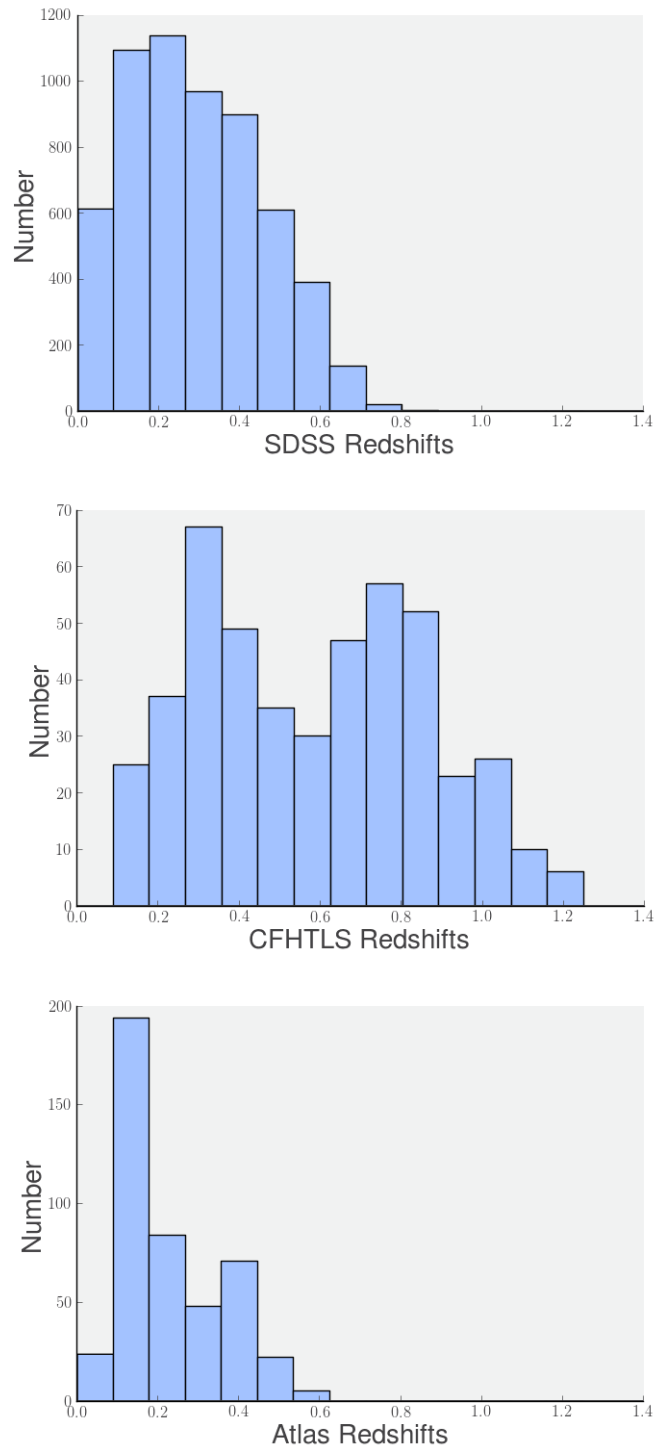


Figure 3.2: Redshift distributions for XCS-DR2 clusters. Redshifts were derived using the GMPhoRCC technique applied to photometric data from SDSS (top), CFHTLS (middle), and ATLAS (bottom)

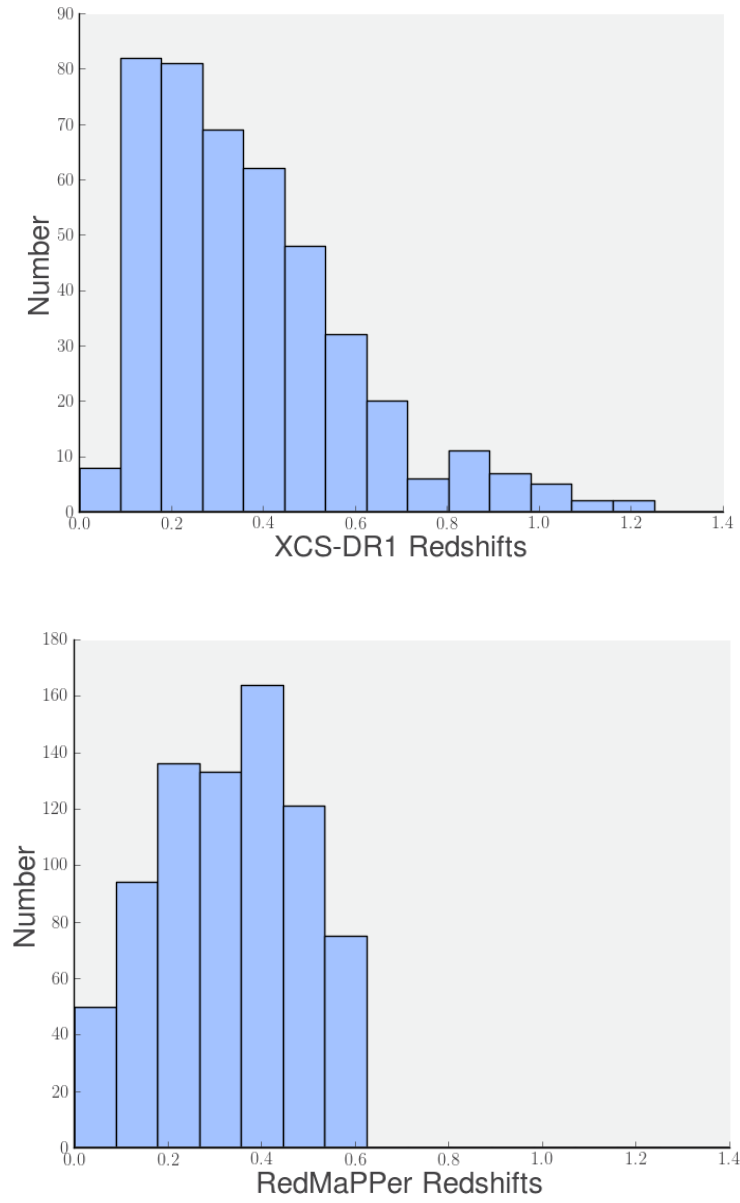


Figure 3.3: Redshift distributions for XCS-DR1 (top) and RedMaPPer (bottom) XCS-DR2 sub-samples.

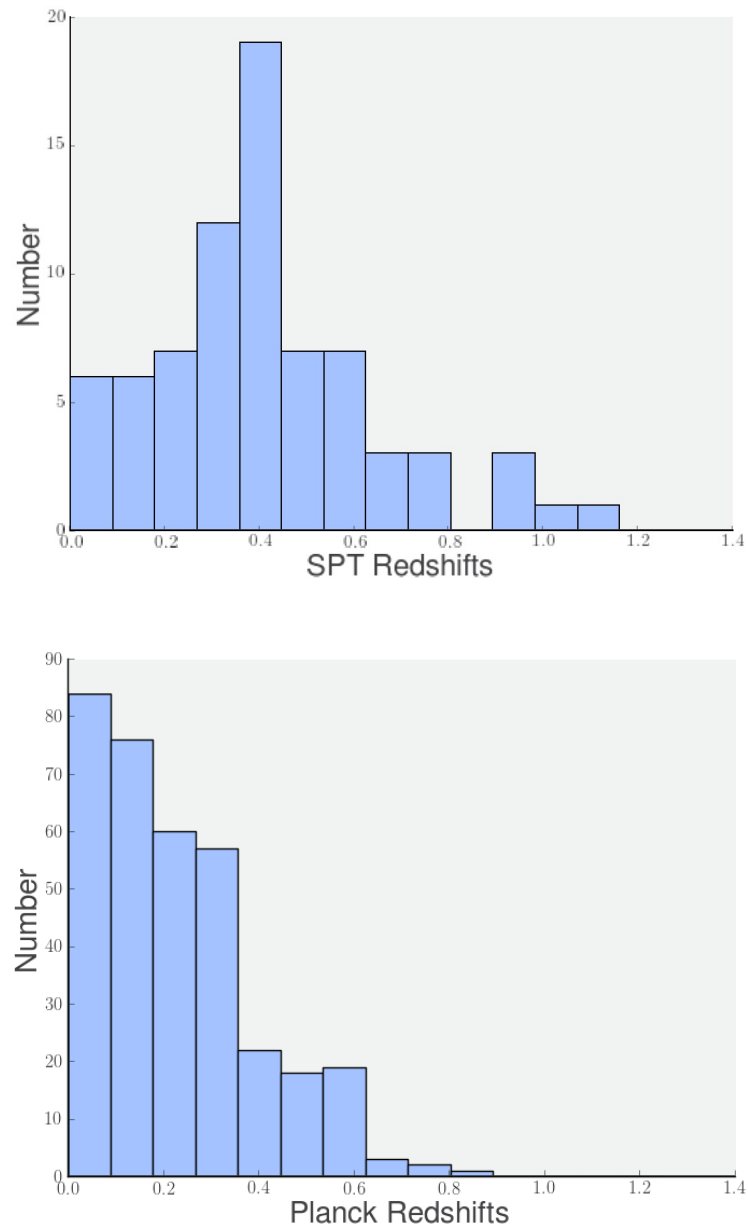


Figure 3.4: Redshift distributions for SPT (top) and Planck (bottom) XCS-DR2 sub-samples.

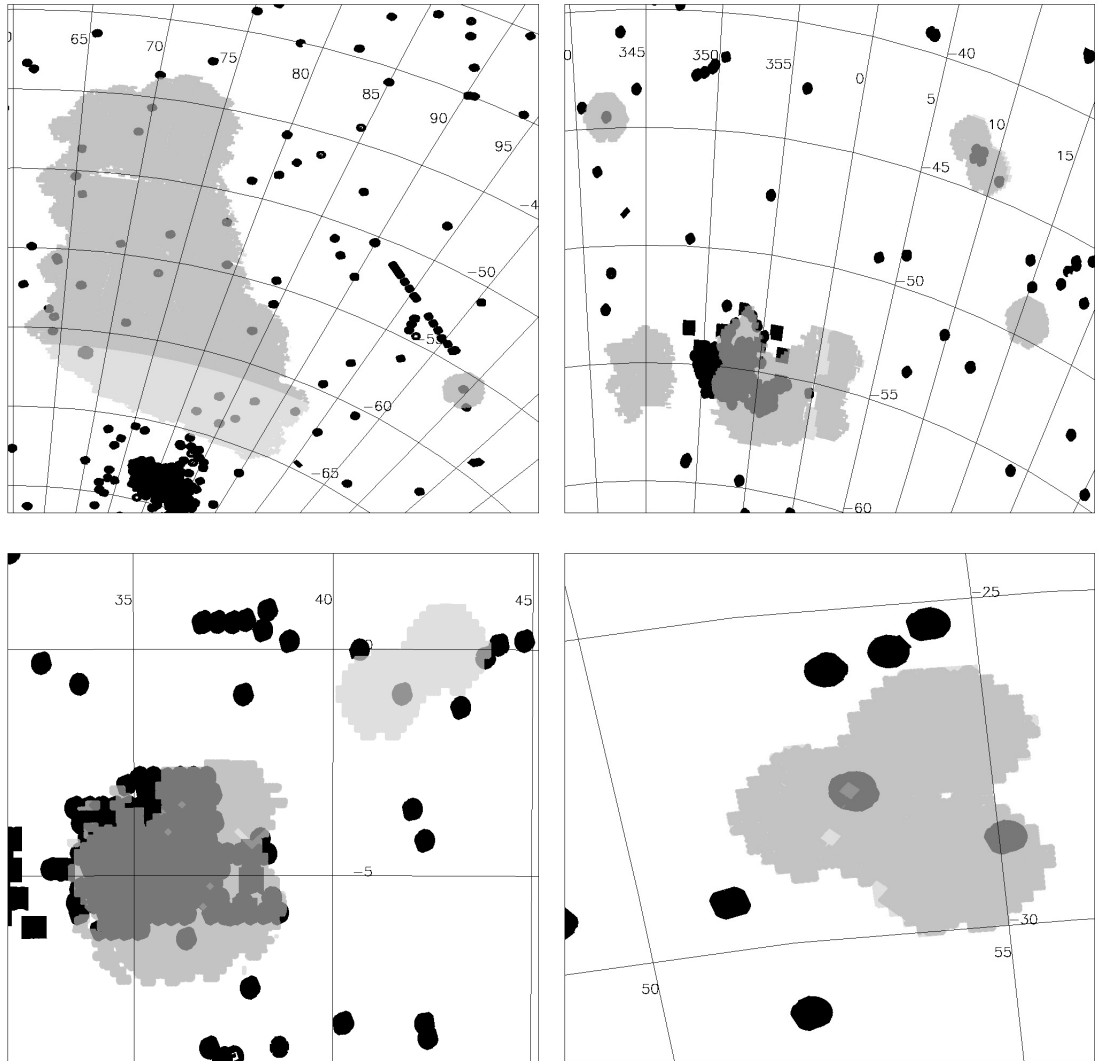


Figure 3.5: (Figures and caption wording taken from Miller, Rooney et al. in prep.) Four main regions of the footprint containing both Dark Energy Survey (DES) and the *XMM* data used in this analysis. In all panels, dark grey regions have DES g, r, i, z data as well as *XMM* coverage and define the regions used to identify and characterize the optical/X-ray cluster sample. Black regions denote other *XMM* pointings or mosaics that are without DES optical overlap. Medium-shaded gray regions denote the rest of the DES data within the “SVA” sample. Light-shaded gray regions denote other areas of the DES which have some data, but which are not included in the primary DES sample (denoted “SVAext” in the text). The **top left** panel highlights the largest contiguous region as well as the Bullet Cluster off to the right. The **top right** and **bottom left** panels show the regions with the largest contiguous X-ray coverage and include the two XXL areas (upper right is the BCS and lower left is the CFHTLS W1 region). The **lower right** highlights one of the supernovae fields.

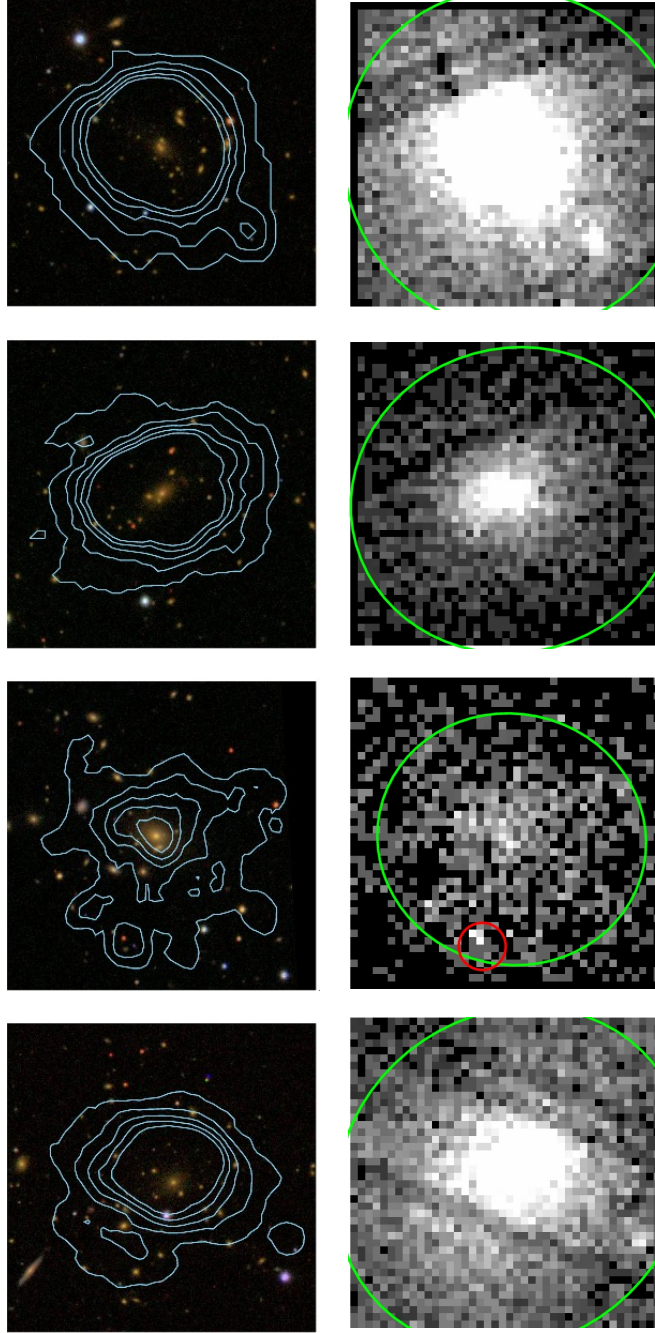


Figure 3.6: (Figures and caption wording taken from M12.) The first four clusters classified as *gold* in *Zoo*^{DR7}. False colour-composite images are 3×3 arcmin with X-ray contours overlaid in blue. Corresponding X-ray images are shown below each optical image (lighter regions show areas of increased X-ray flux). The shape of the XAPA-detected extended (point) source ellipses are highlighted in green (red). From left to right, the clusters are: XMMXCS J001737.4-005235.4 at $z = 0.21$; XMMXCS J010858.7+132557.7 at $z = 0.15$; XMMXCS J083454.8+553420.9 at $z = 0.24$; and XMMXCS J092018.9+370617.7 at $z = 0.21$.

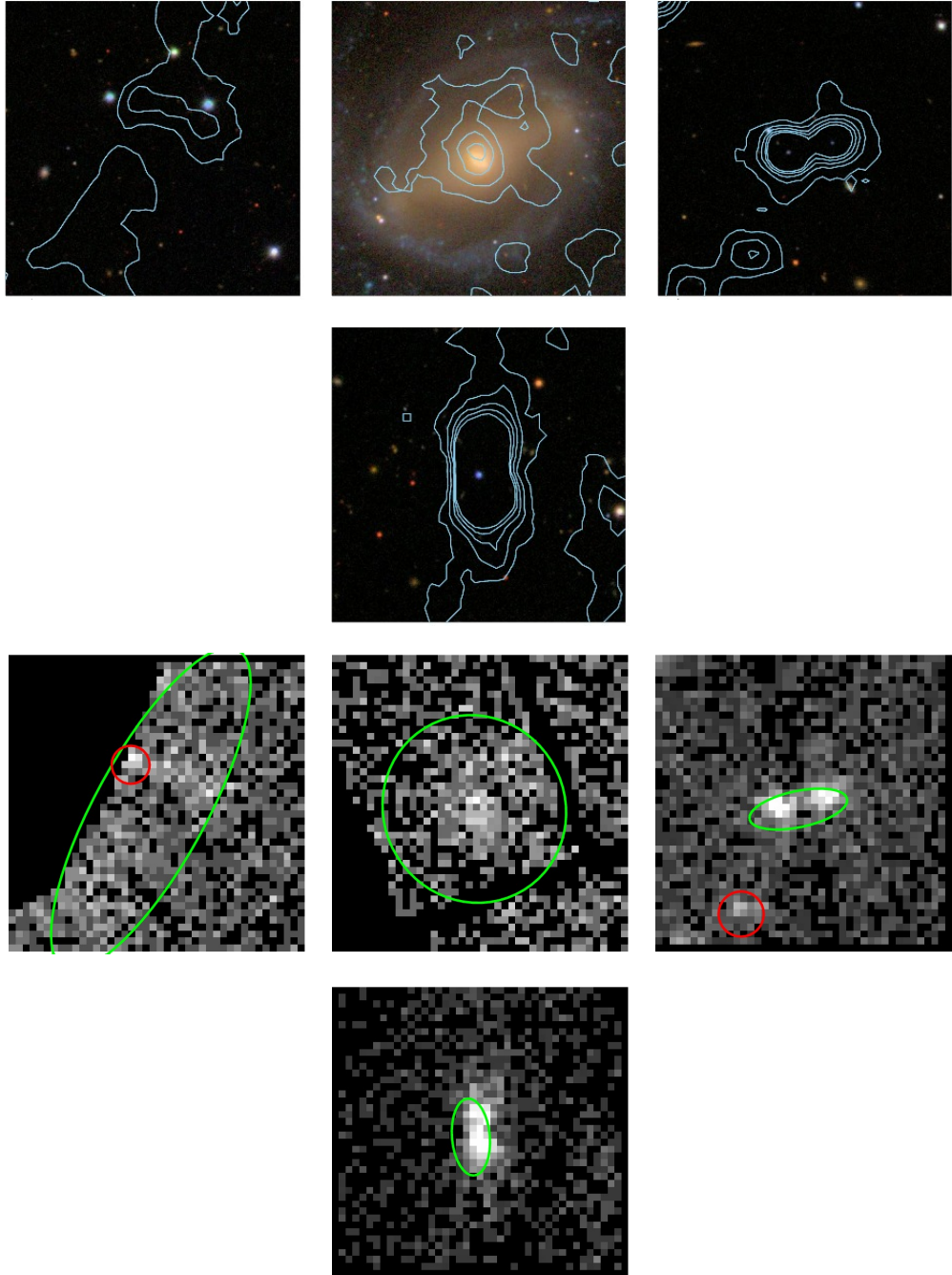


Figure 3.7: (Figure and caption wording taken from M12.) A selection of XCS sources classified as *other* in Zoo^{DR7} . None of these objects are included in XCS-DR1. False colour-composite images are 3×3 arcmin with X-ray contours overlaid in blue. Corresponding X-ray images are shown below each optical image (lighter regions show areas of increased X-ray flux). The shape of the XAPA-detected extended (point) source ellipse is highlighted in green (red). Reasons for a classification as *other* include artifacts at the edge of ObsID masks (far left); extended X-ray sources not associated with a galaxy cluster, such as a low-redshift galaxy (middle); cases where neighbouring X-ray point sources have been blended by XAPA into an erroneous extended source (mid right); and finally, cases of point sources misclassified as extended (because the point spread function model at the edge of the XMM field-of-view is inadequate;bottom).

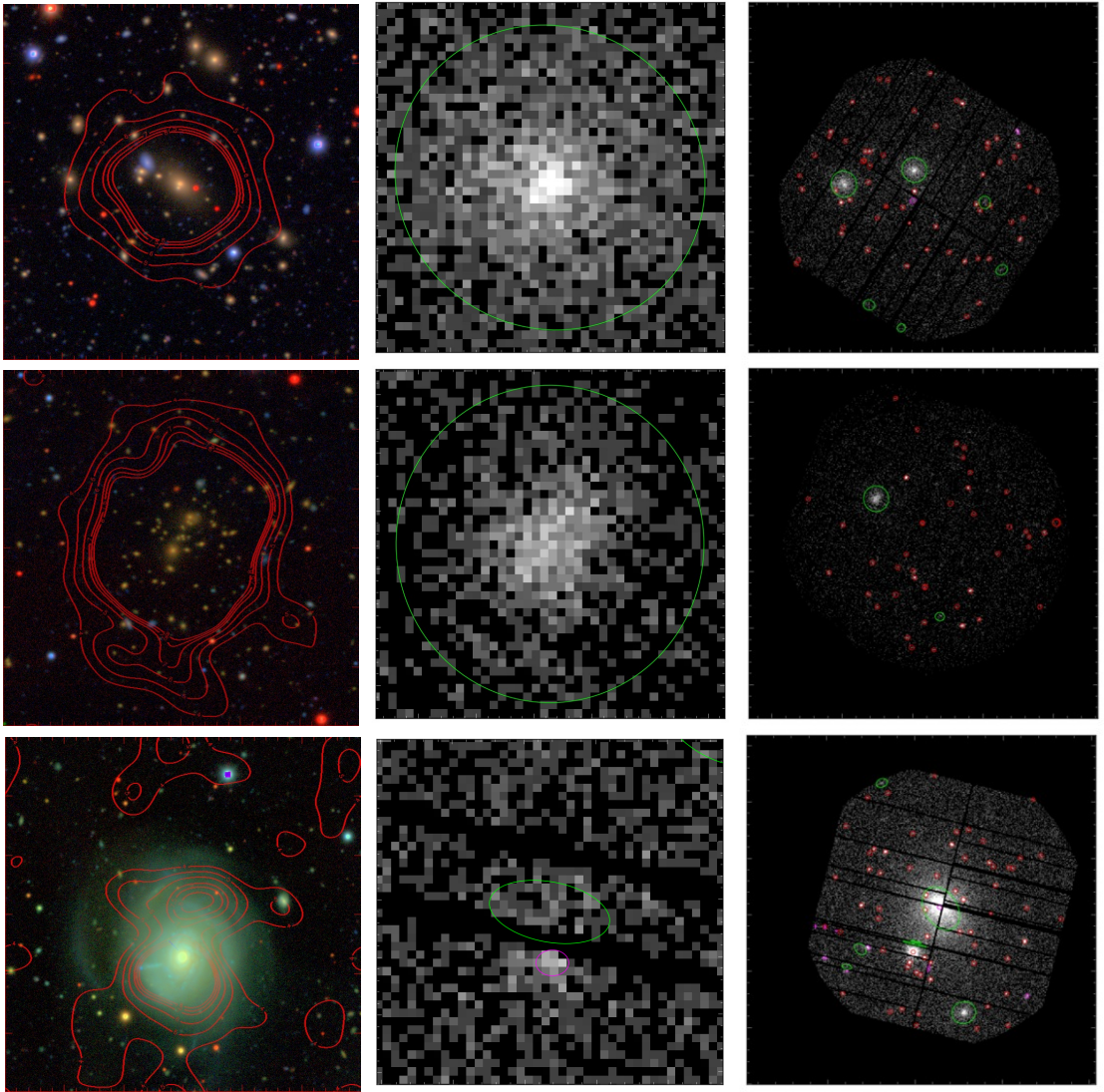


Figure 3.8: Examples of XCS-DR2 cluster candidates identified as either *clusters* (top and middle) or *other* (bottom).

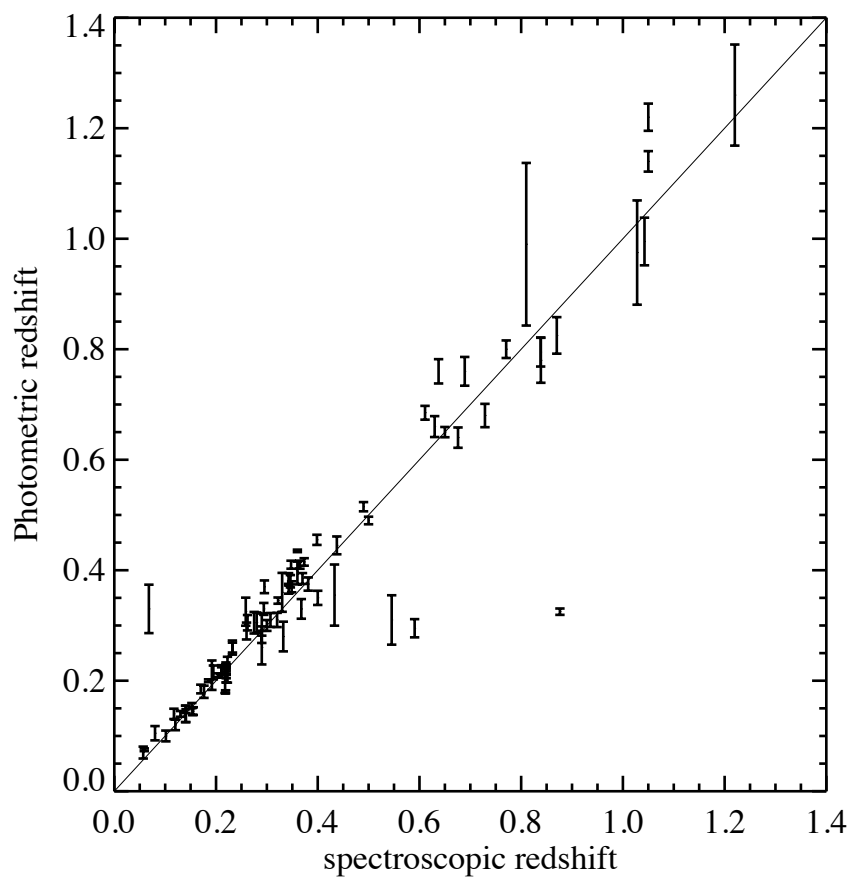


Figure 3.9: (Figure from Miller, Rooney et al. in prep) The statistical error on the DES-SV photometric redshifts of XCS-DR2 clusters.

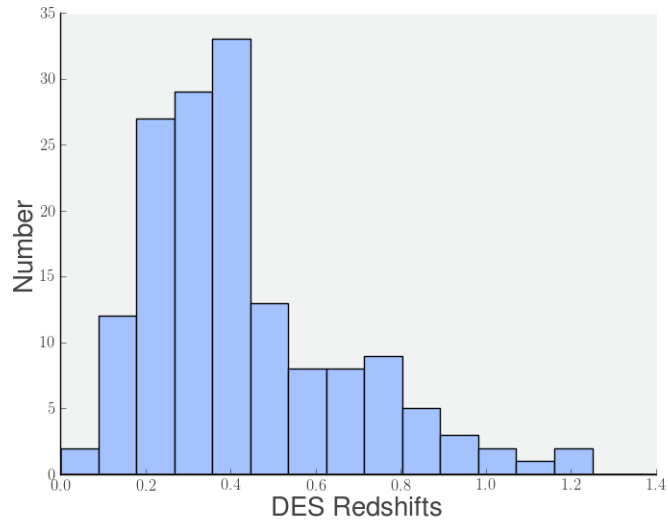


Figure 3.10: Redshift distribution of the XCS-DR2 clusters confirmed using DES-SV and XCS-Zoo.

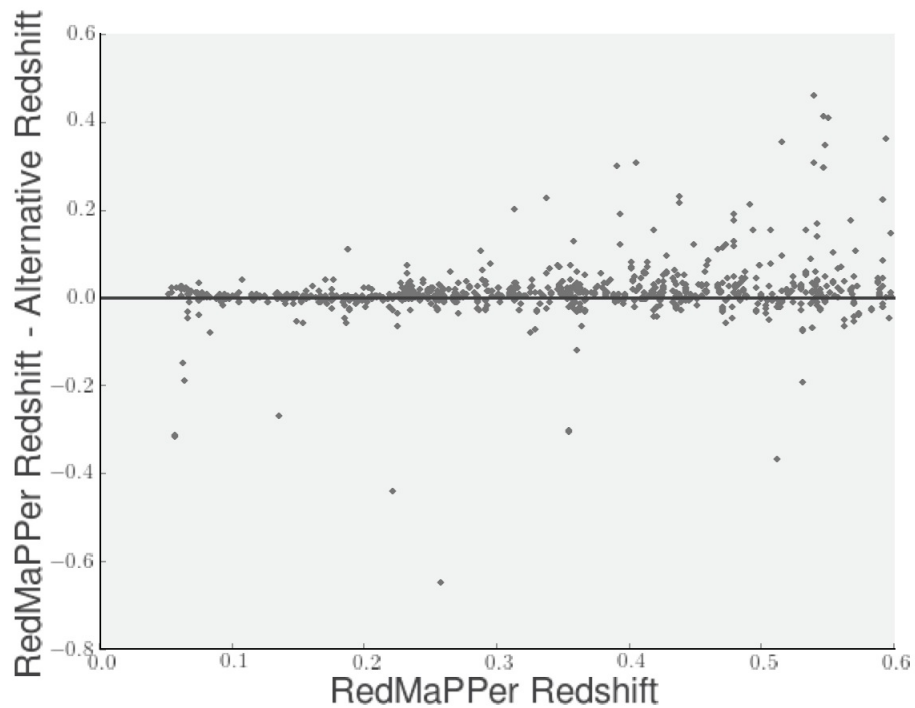


Figure 3.11: The difference in measured redshift between that catalogued by RedMaPPer and by other samples. In 719 of 915 comparisons (79%), the difference was <10%.

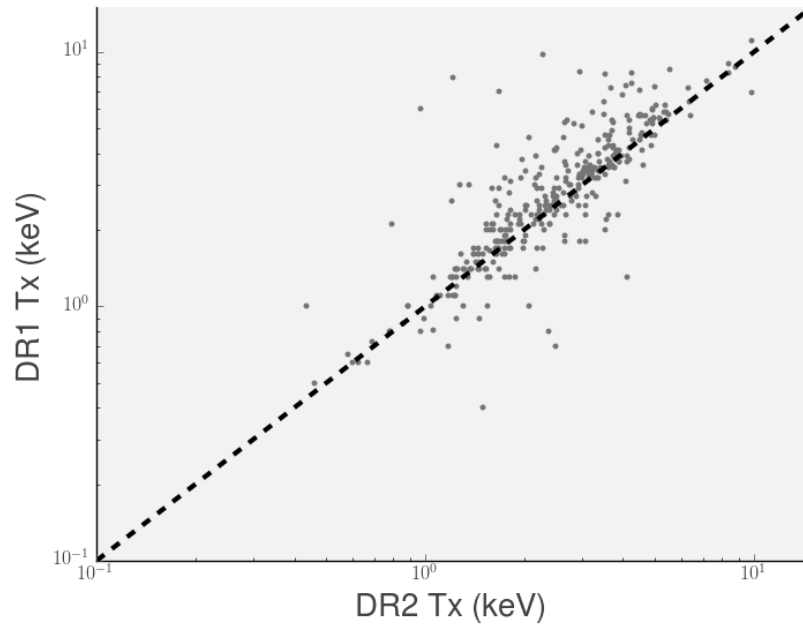


Figure 3.12: A comparison of the X-ray temperatures measured using the XCS-DR2 methodology and the XCS-DR1 (as described in LD11) methodology.

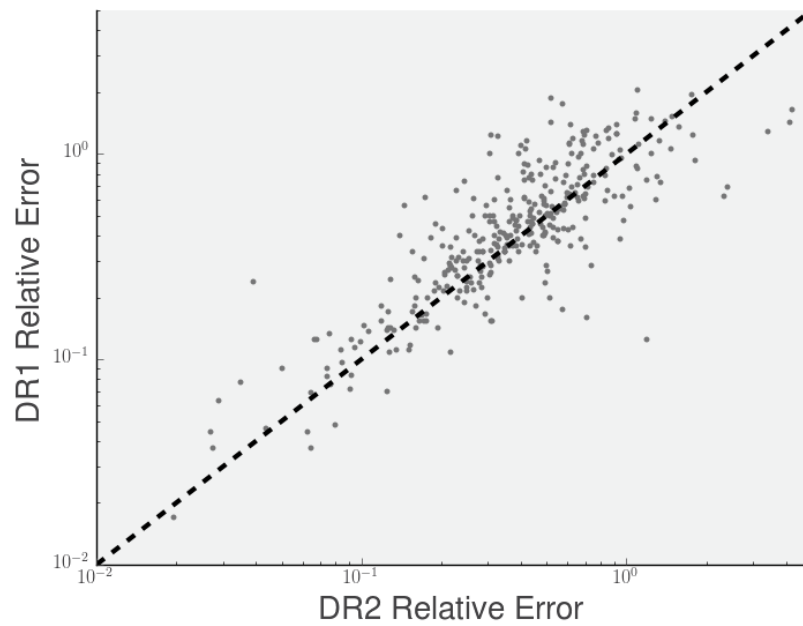


Figure 3.13: A comparison of the errors on the X-ray temperatures measured using the XCS-DR2 methodology and the XCS-DR1 (as described in LD11) methodology.

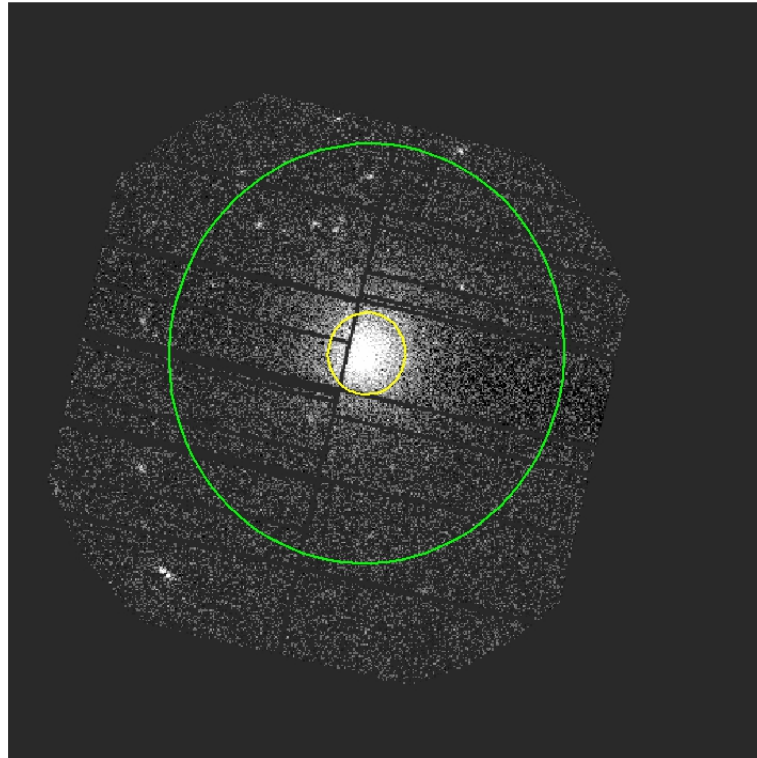


Figure 3.14: A comparison of the XAPA defined source ellipse and the R_{500} aperture (calculated using the redshift, $z=0.0844$, temperature, $T_X = 4.44$ and Equation 3.2) for XCS-DR2 cluster, XMMXCSJ032835.6-554243.2. R_{500} is shown in green and the XAPA source ellipse is shown in yellow

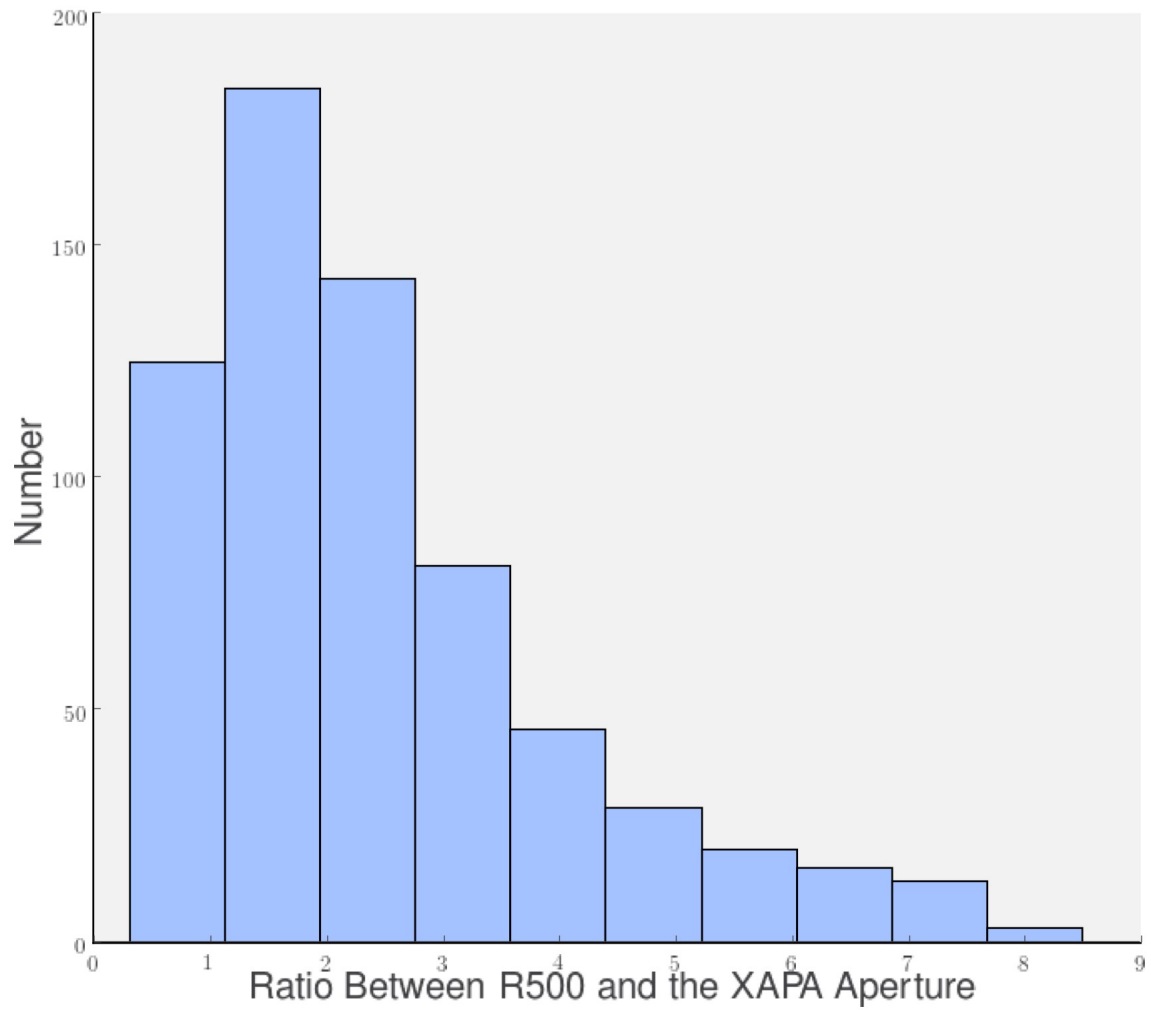


Figure 3.15: The ratio in aperture size between R_{500} and the major-axis of the XAPA source ellipse. The analysis uses 660 clusters (duplicates removed) from SPT, Planck, RedMaPPer and XCS DR1 with relative temperature errors of $\leq 15\%$

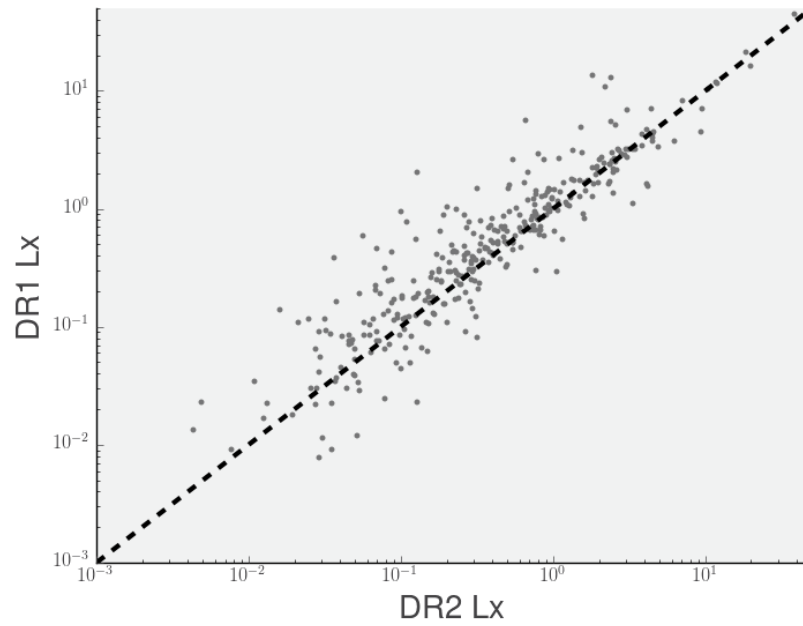


Figure 3.16: A comparison of the bolometric luminosities measured using the XCS-DR2 methodology and the XCS-DR1 (as described in LD11) methodology.

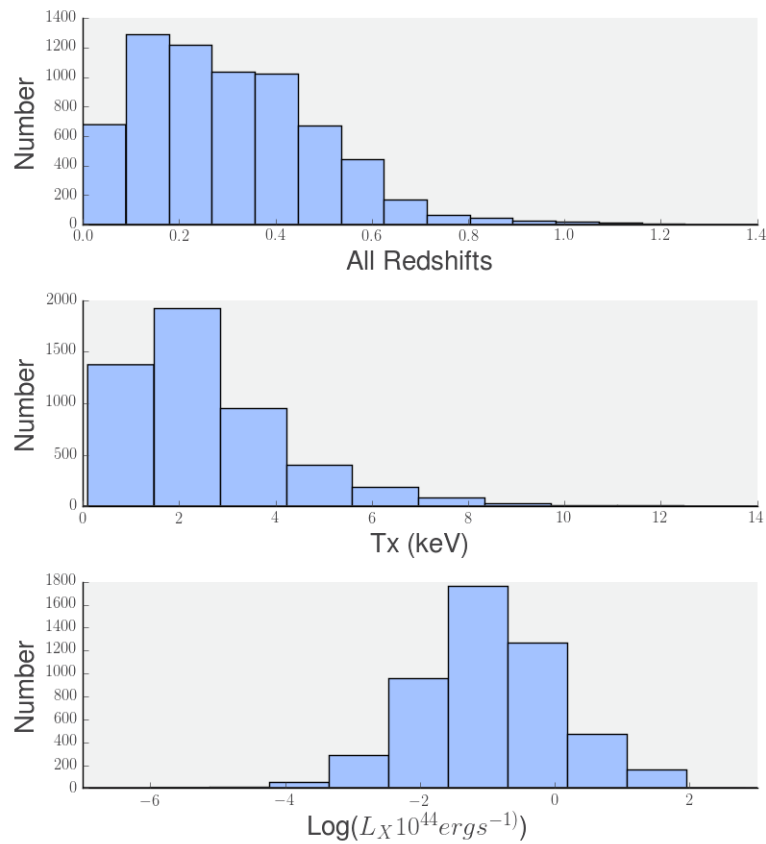


Figure 3.17: Top: Redshift distribution of all confirmed XCS-DR2 galaxy clusters. Middle: T_X distribution of all confirmed XCS-DR2 galaxy clusters. Bottom: L_X distribution of all confirmed XCS-DR2 galaxy clusters.

...

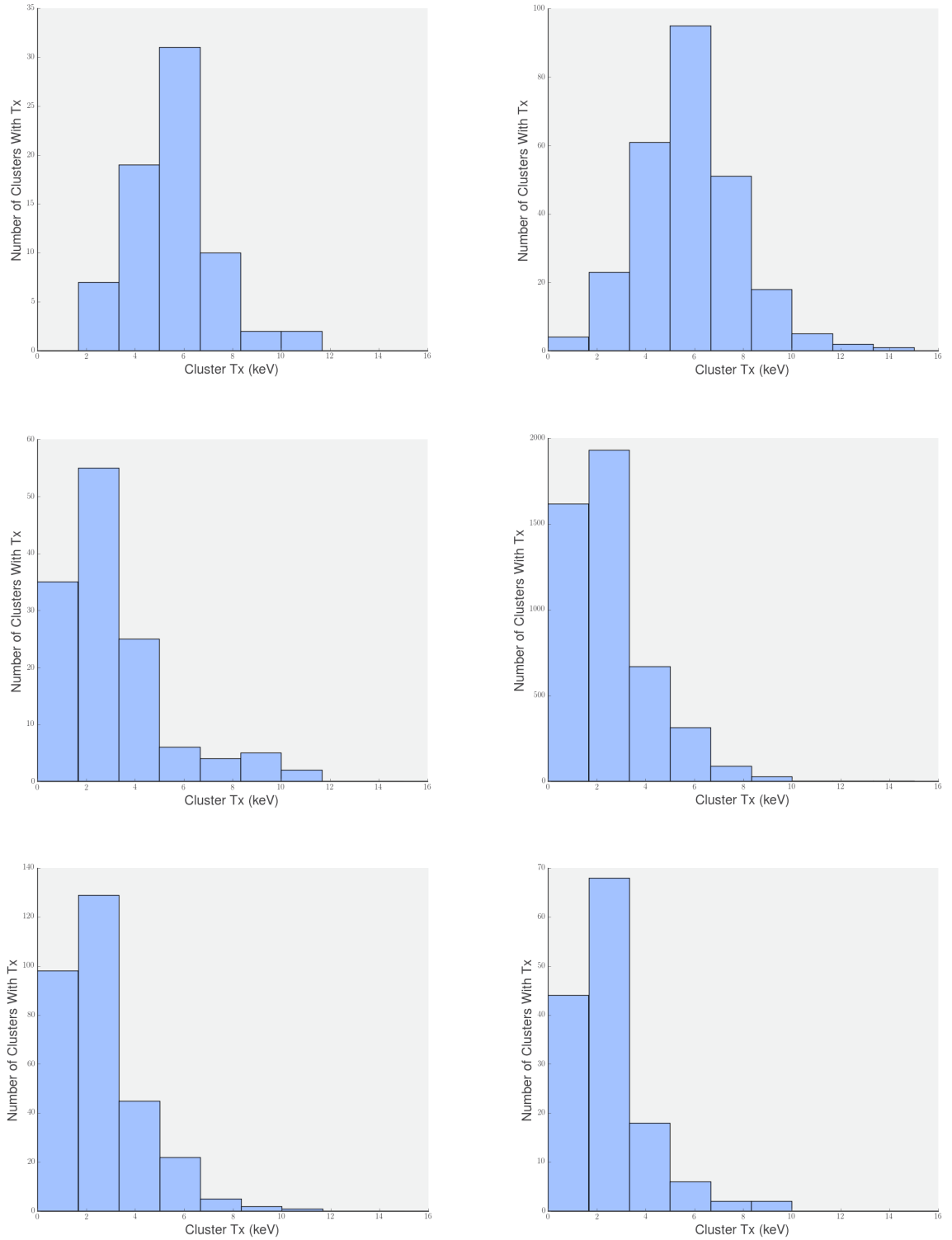


Figure 3.18: Temperature distributions for various cluster XCS-DR2 sub-samples. Top Left: SPT. Top Right: Planck. Middle Left: DES-SV. Middle Right: GMPhoRCC_{SDSS}. Bottom Left: GMPhoRCC_{ATLAS}. Bottom Right: GMPhoRCC_{CFHTLS}.

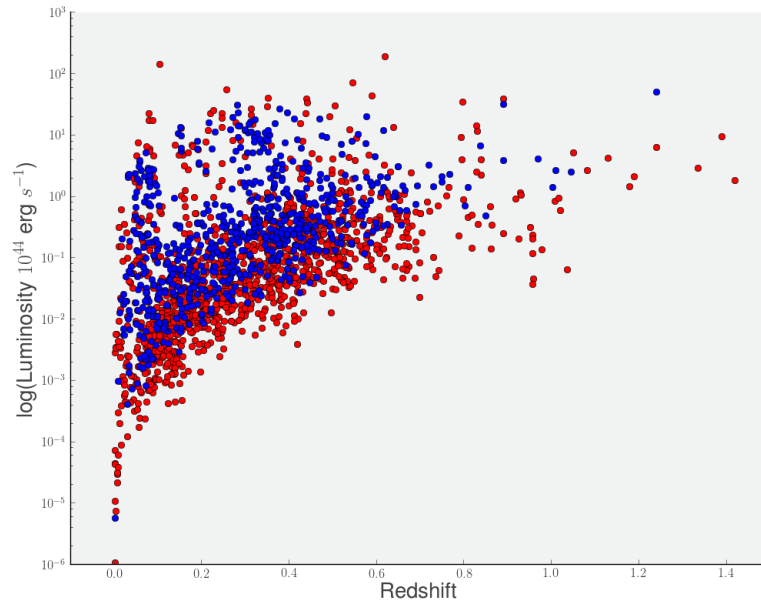


Figure 3.19: XCS-DR2 cluster luminosities as a function of redshift. Colours represent different normalised exposure time ranges (blue $< 50,000$ s, red $> 200,000$ s). Note that by ‘normalised’ we mean Mos 1 + Mos 2 + $3.5 \times$ PN, this roughly corrects for the extra sensitivity of the PN instrument.

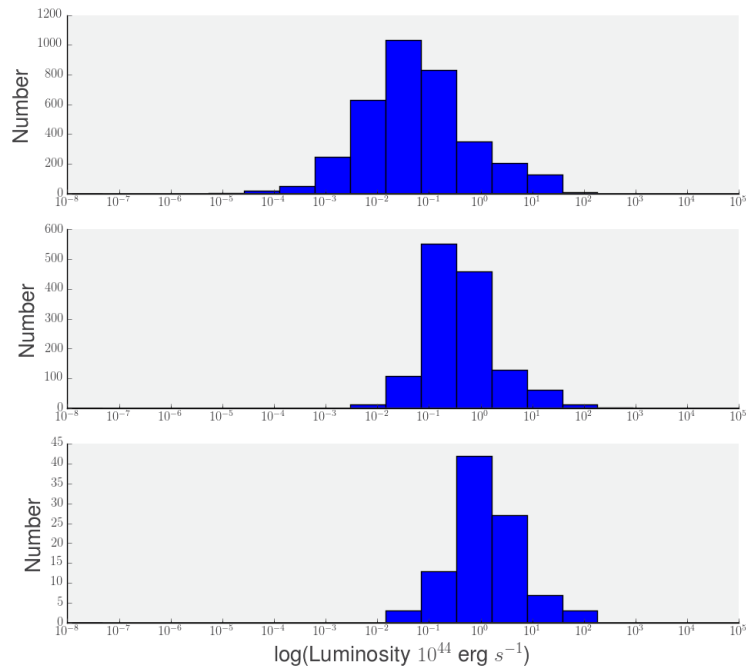


Figure 3.20: The distribution of XCS-DR2 cluster luminosities in different redshift bins. Top: $z < 0.4$. Middle: $0.4 < z < 0.8$. Bottom: $z > 0.8$.

Chapter 4

Application of XCS-DR2: An investigation of bias in the spectroscopic analysis of clusters

4.1 Overview

Motivation It has been known for a long time that X-ray temperature measurements of clusters differ when made using Chandra compared to XMM (Nevalainen et al., 2010). More recently there have been investigations into whether the so-called ‘hydrostatic’ bias in X-ray derived cluster masses compared to weak lensing derived masses has an instrumental, rather than physical, explanation (Donahue et al., 2014; Schellenberger et al., 2015). There have even been claims that part of the reason why the Planck team measured different cosmological parameters from CMB anisotropies compared to from SZ signals might be instrumental effects (Israel et al., 2015).

Governing Assumptions With such a large sample of clusters from XCS-DR2 we are in a strong position to investigate a variety of different potential biases in XMM measurements of X-ray temperatures. In particular we can take advantage of the fact that many XCS-DR2 clusters have been observed by XMM at least twice during the instrument’s lifetime. Thus we have access to spectra accumulated from the same cluster under different conditions.

Data inputs We have carried out seven different tests. Tests 1-5 are based on the 973 clusters taken from the XCS-DR2 cluster catalogue (§ 3). These 973 are drawn from the

sub-samples generated by proximity matching to the published Planck, SPT and XCS-DR1 samples (§ 3.4) and using DES-SV imaging and photometry (§ 3.5). These clusters were used because their confirmations and redshifts are the most reliable. Test 6 involves all XCS-DR2 clusters with a measured T_X value. Test 7 uses only the 113 XCS-DR2 clusters that overlap with the Planck cluster sample at redshift, $z \leq 0.2$.

Results We have shown that: the number of counts in the combined spectrum used for joint fitting is the key driver in reducing T_X errors: it is important to apply basic quality checks when adding a spectrum to a joint fit; there may be a problem with the cross-calibration of the three detectors, especially between the two MOS detectors. We have provided preliminary evidence that spectra gathered at different times, and/or through different filters, and/or from different locations of the field of view, can be successfully co-added in a joint fit. That said, certain clusters register significantly different T_X measurements from different observations (for reasons yet to be determined). Finally we have shown that it is possible to measure core excised T_X values with XMM, in an automated fashion, for low redshift clusters with high signal to noise.

4.2 Test 1: Is it beneficial to combine data from different observations?

In LD11, it was shown using XSPEC simulations that T_X errors decrease with both increasing counts and with decreasing plasma temperature (Figure 4.1). Observational support for this was also presented (Figure 4.2), by artificially reducing the exposure time of clusters detected (in the full exposure time) with over 5,000 counts. These tests were used to justify the method used in LD11, whereby T_X values were made using XSPEC fits to all but a tiny fraction of the available observations of the XCS-DR1 clusters. The only observations that were excluded were those for which the extracted spectrum contained less than 10 background subtracted counts, or for which the extracted spectrum contained less than 10% of the counts in of the counts in the spectrum (§ 3.6.1).

The tests in LD11 did not account for that fact that the instrument degrades with time or that the background level will be different in exposures taken at different times. Therefore, we have tested how the relative T_X error varies as a function of the total number of counts used for simultaneous fitting. Likewise for the total signal to noise of the composite spectrum. We note that for this test the method described in (§ 3.6.1) is used, not

the method used in LD11, i.e. the individual spectra are fit separately first and only combined into a simultaneous joint fit if their initial best fit temperature fell in the range $0.08 < T_X < 30.0$ keV *and* XSPEC was able to fit errors on that best fit value.

Figure 4.3 shows that, unlike in LD11, a sizeable fraction of individual spectra failed the quality check and were not included in the final joint fit. Despite this, the number of photon counts included in the spectral fits to XCS-DR1 clusters are typically larger using the new method (Figure 4.4). This reflects the fact that since XCS-DR1 was compiled, many more repeat observations have entered the XSA. An illustration of how simultaneous fitting is done in XSPEC is shown in Figure 4.5.

The results of test 1 are shown in Figure 4.6. The colours indicate composite spectra that were comprised of different numbers of individual spectra (grey for 3 or less, red for between 4 and 10, blue for more than 10). The lack of differentiation between the coloured dots demonstrates that, as long as the individual spectra pass a basic quality check, there is always a benefit to including them in a joint spectral fit.

This finding is not just useful for serendipitous surveys such as XCS. It is also useful to any researcher wishing to extract higher quality spectral information for a given cluster of galaxies. In order to reach the desired accuracy, they only need to re-observe the cluster for long enough to accumulate enough additional counts to make up the required total.

Summary Is it beneficial to combine data from different observations? Yes.

4.3 Test 2: What is the best way to combine data from different observations?

As mentioned previously, the T_X fitting method described in (§ 3.6.1) differs from that in LD11. In this section we justify the chosen method by comparing the XCS-DR2 T_X values to those obtained using three other methods:

- Method 1: Including all available spectra, regardless of the quality of the fits to the individual spectra;
- Method 2: Including a spectrum in the final simultaneous fitting if the best fit T_X value has a non-extrema value, i.e. $0.08 < T_X < 30$ keV, (regardless of whether

errors were also fit);

- Method 3: Including a spectrum in the final simultaneous fitting if the best fit T_X value has a non-extrema value and error bars were also fit (i.e. the method adopted for XCS-DR2);
- Method 4: Including a spectrum in the final simultaneous fitting if the best fit T_X value has a non-extrema value, error bars were also fit, and $(T_X + \Delta_T^{upper}) < 20$ keV.

The four methods are progressively more conservative. The best fit T_X can vary significantly depending on which individual spectra are included in the joint fit. The results are shown in Figure 4.7. These plots show both the best fit T_X and the relative error (Equation 3.1) for our adopted model (Model 3 above) compared to the other three models. Note that clusters only appear in this Figure (as grey dots) if the spectral selection differed between the two methods.

Compared to Model 1 (top row, no spectra ejected), it is clear that including poor quality spectra in a joint fit will often artificially boost the T_X (most points lie above the one-to-one line): a T_X boosting effect will take place when there is a high background contamination, because the background is spectrally harder than the cluster emission. Likewise the error on a given T_X fit will be typically lower when spectral selection takes place. That said there are a few dozen clusters for which the error was less when there was no spectral selection. Most likely this results from the fact that the composite spectra have fewer counts (Figure 4.6), but these should be investigated further.

The comparison with Method 2 tells a similar story (to Method 1), i.e. by being more conservative, one reduces the best fit T_X and the error on the best fit. The comparison with Method 4 is not as clear, as there were only 29 cases where the spectral selection differed between the two methods. There are a handful of cases where the best fit temperature, and relative error, is lower when Method 4 is used (suggesting that background contamination remains an issue for some composite spectra used by Method 3). Even so, we decided to stick with Method 3, rather than the more conservative Method 4. This is because Method 4 artificially excludes very hot (i.e. massive) clusters.

Summary What is the best way to combine data from different observations? Rejecting individual spectra that fail a simple initial quality check should definitely be done.

Whether an addition rejection should be made based on the one sigma upper limit T_X requires further investigation.

4.4 Test 3: Do offsets in detector calibration impact fitted cluster temperatures?

The two tests described above make the implicit assumption that the addition of spectra gathered from different EPIC cameras (PN, MOS1, MOS2) is the correct approach. In order to test this assumption we have compared individual spectral fits made for the same cluster with each of the detectors. The results are shown in Figure 4.8 for cases where both T_X values were recorded with relative errors of 15% or less. Our results show that there are small systematic offsets between the best fit T_X values measured from the individual cameras, and that these offsets are more pronounced in hotter clusters. Surprisingly, the best match is between PN and MOS2 and the greatest offset is between the MOS1 and MOS2 cameras. Although we cannot determine which camera has the *best* calibration, our study cautions us (and should caution other groups also) to take care when including T_X values derived from a single camera.

Summary Do offsets in detector calibration impact fitted cluster temperatures? Yes. In particular, T_X values measured only from MOS1 observations will be biased high compared to values measured with the other two cameras.

4.5 Test 4: Does time variation in detector calibration impact fitted cluster temperatures?

The XMM detector calibration changes with time. Not only is there is gradual general degradation of individual pixels, certain columns are now unusable. Moreover, one-off events, such as micrometeorite strikes, have destroyed entire CCDs within the MOS1 detector. The XMM ground team attempts to account for these changes with frequent updates to calibration files, and the three tests described above make the implicit assumption that the addition and/or comparison of spectra gathered at different times in the lifetime of XMM is the correct approach. In order to test this assumption we have compared individual spectral fits, made for the same cluster, with each of the detectors.

The results are shown in Figure 4.9 for cases where both T_X values were recorded with

relative errors of 15% or less. The encouraging news is that there are no trends in the temperature offsets with time. The less encouraging news is that a T_X value with a low measured error ($< 15\%$) is not always reproduced when a cluster is observed again: certain clusters have T_X values varying by several keV. An example of this is XMMXCSJ233826.6+270103.8 ($z = 0.0645$) for which temperatures were recorded to be $T_X = 3.9$ keV from one measurement and $T_X = 10.1$ keV in another. The value recorded for XCS-DR2 (using Method 3 above) temperature is $T_X = 5.0$ keV. Not all clusters have repeat observations, so more work needs to be done to try to identify another (to relative error) diagnostic that would flag up erroneous T_X values. One option would be to consider signal to noise.

Summary Does time variation in detector calibration impact fitted cluster temperatures? Not in general. However, there are cases of fitted T_X values that change significantly between repeat observations, and more work is needed to understand why.

4.6 Test 5: Does the detected position on the field of view impact fitted cluster temperatures?

In LD11, it was shown that location on the field of view did not have a systematic effect on the measured cluster temperature (Figure 4.10). For that reason, the four tests described above make the implicit assumption that the addition and/or comparison of spectra gathered from different parts of the detector is the correct approach. The LD11 study was based on only 8 clusters, so we have re-examined this assumption using clusters from XCS-DR2. In this test, spectral fits were only compared per detector, to avoid the issues seen in Figure 4.8.

The results are shown in Figure 4.11) for cases where both T_X values were recorded with relative errors of 15% or less. The encouraging news is that there are no systematic trends in the temperature offsets when the difference in the centroid location (as defined by distance from the aim point, or ‘off-axis distance’, θ) is less than $\theta = 5'$. The less encouraging news is at larger off-axis differences, particularly with PN detectors, measured temperatures are lower at larger θ . This could indicate problems with calibration. Alternatively, it could be due to issues with background subtraction when the vignetting factor is changing rapidly. However the sample size is small (403). So, once more XCS-DR2 cluster candidates have been identified, and have reliable redshift measurements, this test will be

performed again. It might also be possible to compile a large enough list of AGN with redshifts to test whether this problem also impact points sources (if it does, that would point to an issue with calibration, rather than background subtraction).

Summary Does the detected position on the field of view impact fitted cluster temperatures? Not at $\theta < 5'$, but it might at larger off axis angles, especially for the PN detector.

4.7 Test 6: Does the type of filter used during an observation impact fitted cluster temperatures?

As described in § 1.1.1, there are three filters that can be used when a cluster is observed (as a target or serendipitously): thin, medium and thick. The calibration files provided with the respective observation should compensate for the energy dependent sensitivity of the filter used, and so the five tests described above make the implicit assumption that the addition and/or comparison of spectra gathered using different filters is the correct approach. We have attempted to test this using XCS-DR2 clusters. As it is rare for a repeat observation of a given part of the sky to be made through a different filter, we expanded the number of clusters in the test from the 973 used in previous tests to any of 4,987 cluster in XCS-DR2 with a temperature. The disadvantage of doing so is that some of the cluster confirmations are preliminary, and some of the redshift information is not reliable. In this test, spectral fits were only compared per detector, to avoid the issues seen in Figure 4.8.

The results are shown in Figure 4.12 for cases where both T_X values were recorded with relative errors of 15% or less. There were 320 clusters observed through both the thin and medium filter, 37 observed through both the thin and the thick filter, and 45 observed through both the medium and the thick filter. There is sufficient data to conclude that there no significant systematic offsets between the thin and medium filter, although it is noteworthy that some clusters register marked differences in measured T_X values. There is insufficient data to make any conclusions about the other filter combinations. Given how few of the XCS-DR2 clusters have been observed *only* through the thick filter (171), it might be best to exclude them from the sample and to remove any thick filter spectra from a joint fits. It would also be prudent to carry out this test using AGN, to see how filter choice impact points sources (and thus determine if any offsets are due to calibration

or background subtraction).

Summary Does the type of filter used during an observation impact fitted cluster temperatures? Not in general between the thin and medium filter, but there is insufficient data to conclude either way for other filter combinations.

4.8 Test 7: How does core excision impact fitted cluster temperatures?

As shown in (Maughan, 2007), using Chandra observations, the exclusion of the core region when measuring X-ray parameters can dramatically reduce the scatter in X-ray cluster scaling relations, e.g. that between temperature and luminosity. The accepted reason for this reduction in scatter is that there is complex non-gravitational physics going on in cluster cores. One indication of non-gravitational processes would be a cool core, i.e. a region where the efficiency for radiative cooling, and hence the gas density and X-ray luminosity, is higher than expected from a simple isothermal sphere.

We have looked for evidence of cool cores in the XCS-DR2 sample by carrying out an additional spectral analysis of the clusters that were also detected by Planck. We chose this sample both because the clusters are massive and hence high luminosity (so their XMM images typically have high signal to noise), and because they have a lower redshift range than, other sub-samples, especially XCS-DR1 and SPT (we can carry out a meaningful core extraction with XMM).

The additional spectral analysis proceeded as follows: Initial spectra are extracted from the XAPA ellipse from all observations of a given cluster, but excluding the inner 15%. A first T_X value is fit using the spectral selection Method 3 (see above). Using this T_X value, an R_{500} value is then estimated using the method described in § 3.6.2. This process is repeated up to six times. As the R_{500} value is generally larger than the major axis of the XAPA defined ellipse (Figure 3.14), the core excised region expands to more than the inner 15% of the XAPA ellipse. If a stable solution is found during the iterative process, then the last set of parameters are used as the core extracted T_X and L_X measurements.

The results are shown in Figure 4.13) for cases where both T_X values (i.e. before and after core excision) were recorded with relative errors of 15% or less.

Summary How does core excision impact fitted cluster temperatures? The difference between core-excised and non-core excised temperature shows no trend although when the difference is greater than 1 keV the core-excised temperature is higher. The scatter between luminosity and temperature shrinks.

4.9 Conclusions and Future Work

4.9.1 Conclusions

- It is beneficial to combine data from different observations. Rejecting individual spectra that fail a simple initial quality check should definitely be done. Whether an addition rejection should be made based on the one sigma upper limit T_X requires further investigation.
- There are offsets in detector calibration that impact fitted cluster temperatures. In particular, T_X values measured only from MOS1 observations will be biased high compared to values measured with the other two cameras.
- Time variation in detector calibration does not, in general, impact fitted cluster temperatures. However, there are cases of fitted T_X values that change significantly between repeat observations, and more work is needed to understand why.
- At $\theta < 5'$ the detected position on the field of view does not impact fitted cluster temperatures, but it might at larger off axis angles, especially for the PN detector.
- The type of filter used during an observation does not in general impact fitted cluster temperatures between the thin and medium filter. There is insufficient data to conclude either way for other filter combinations.
- The difference between core-excised and non-core excised temperature shows no trend although when the difference is greater than 1 keV the core-excised temperature is higher. The scatter between luminosity and temperature shrinks.
- There is a worry that there are occasional catastrophic errors in temperature.

4.9.2 Work Required Before Publishing in a Paper

- Examine the impact of catastrophic errors. Are the large differences, sometimes seen in alternative temperature measurements for clusters statistically significant?

- To test whether these results are consequence of Cash statistics by attempting to replicate them with high signal clusters fitted with chi squared statistics.
- Expand the XCS-DR1 analysis of the relationship between counts and error. This will compare the change in error of real XCS-DR2 clusters with different count cuts to what we find when using simulated data (using the `fakeit` package within the XAPA). This can include new techniques to add noise into clusters.
- Replicate the [Donahue et al. \(2014\)](#) result that surface brightness profiles show different shapes in XMM and Chandra.

4.9.3 Future Work for XCS-DR3

- Run similar tests on the Chandra archive.
- Reobserve and use archival clusters observed by both Chandra and XMM to test their cross calibration.
- Carry out similar tests for the future eRosita and Athena missions.

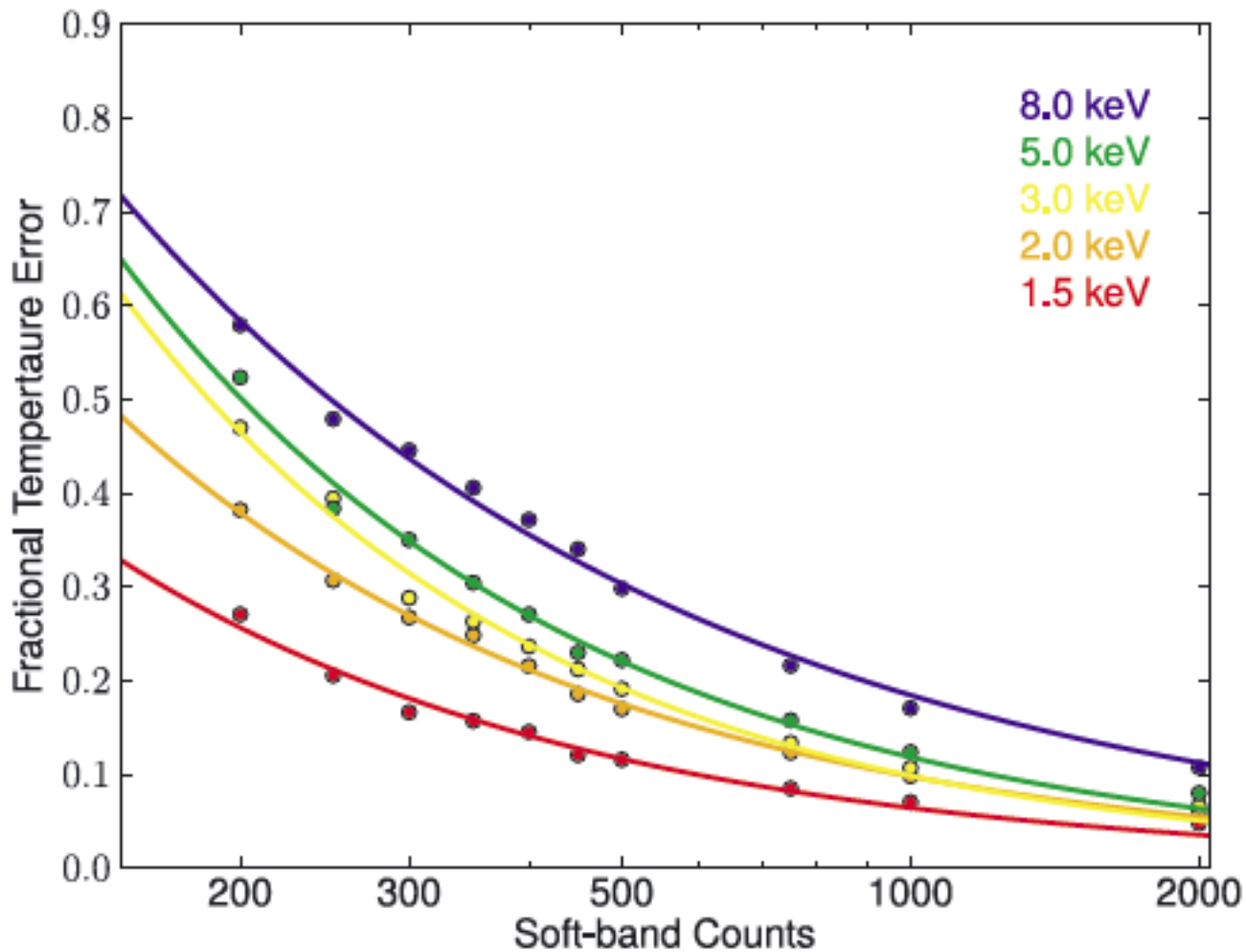


Figure 4.1: (Figure and caption wording taken from LD11.) Fractional temperature uncertainty as a function of the number of soft-band counts as a result of fitting simulated $z = 0.5$ MEKAL spectra with different temperatures, going from cool to hot clusters. The red, orange, yellow, green and blue points represent spectra of 1.5, 2, 3, 5 and 8 keV, respectively.

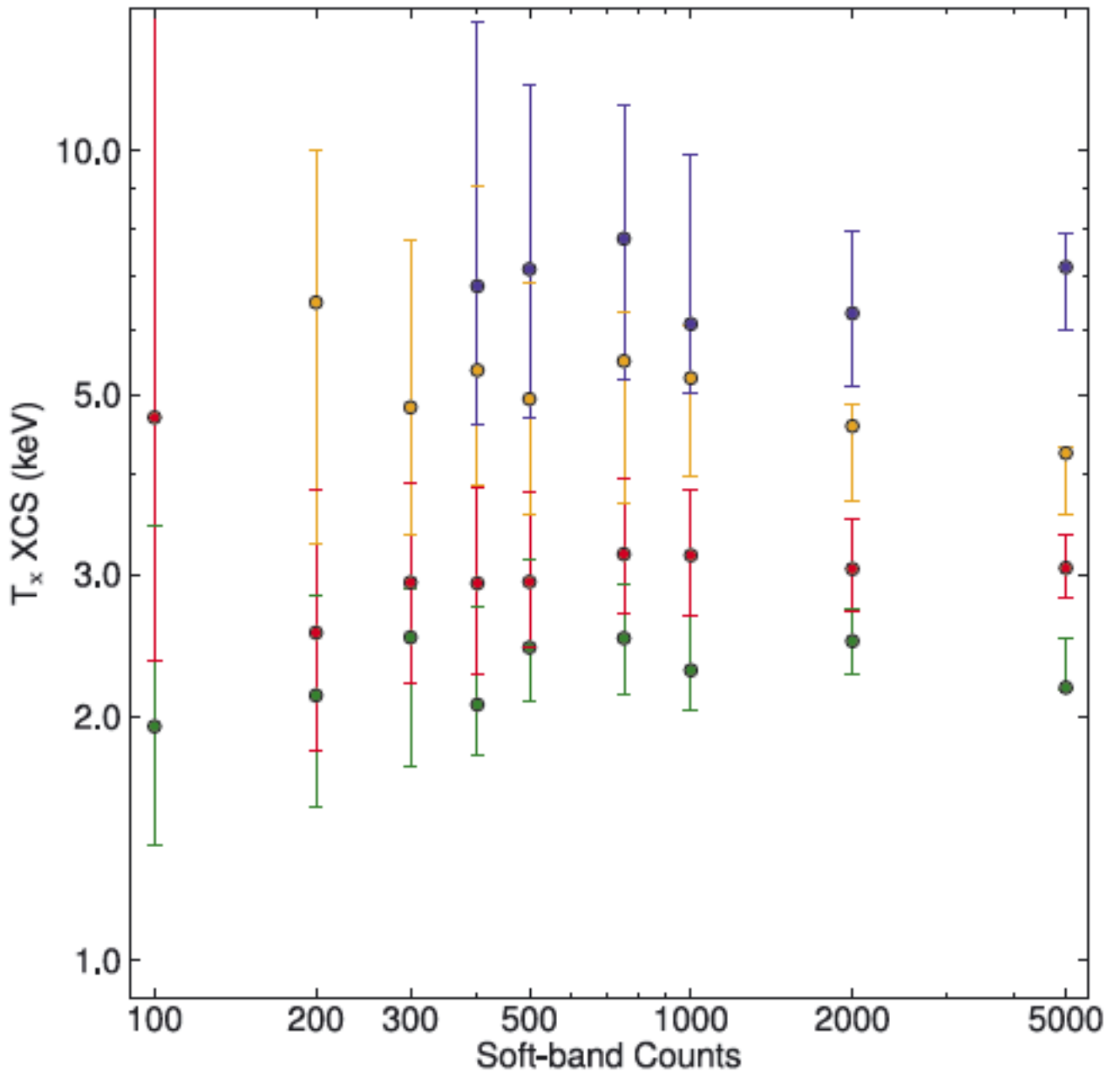


Figure 4.2: (Figure and caption wording taken from LD11.) The XCS-determined X-ray temperatures (and uncertainty) as a function of the number of counts in the fitted spectrum. Each colour represents a cluster that was detected with more than 5000 counts. For details of the four clusters used in this plot, see Table C1. The respective exposures were then subdivided to generate lower count spectra. Note that the higher temperature systems do not yield fits at the low-count end. The 1σ error bars come from the XSPEC fitting software.

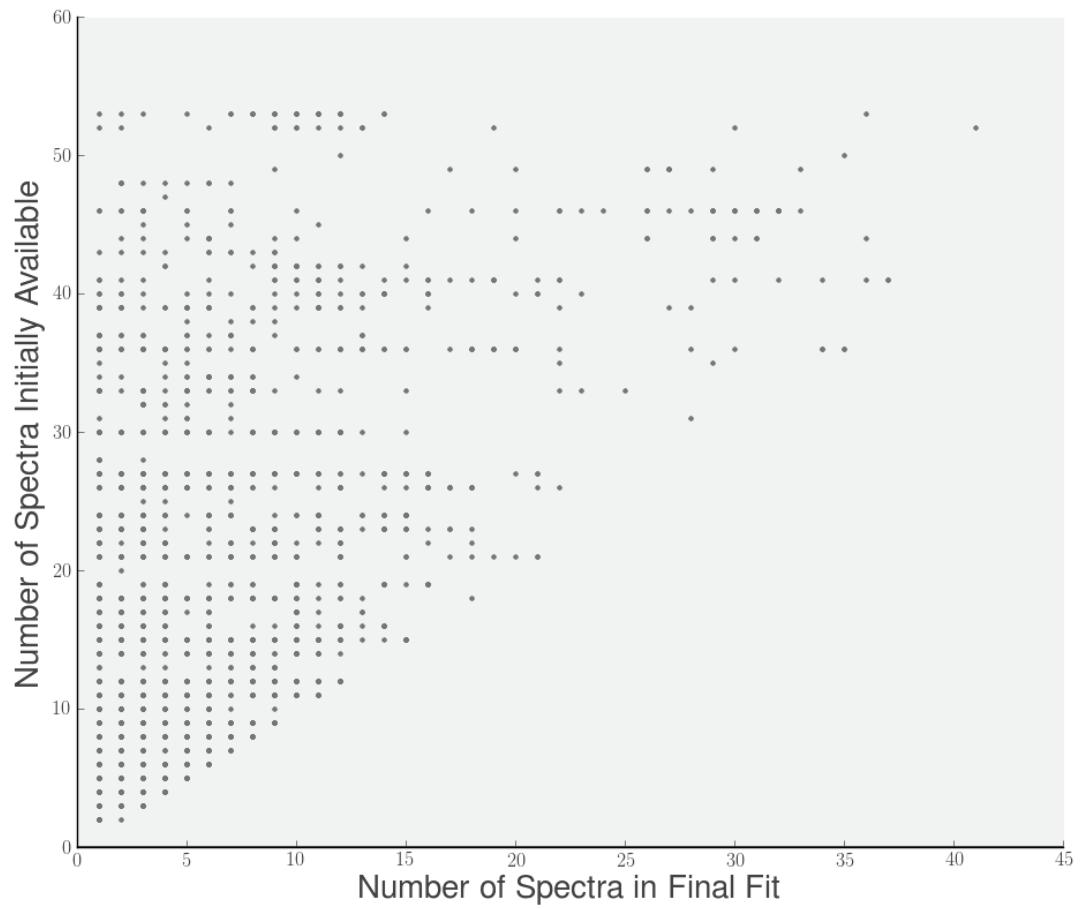


Figure 4.3: A comparison of the number of total spectra available for a given cluster compared to the number used in the XCS-DR2 joint spectral fitting (each dot represents a different cluster).

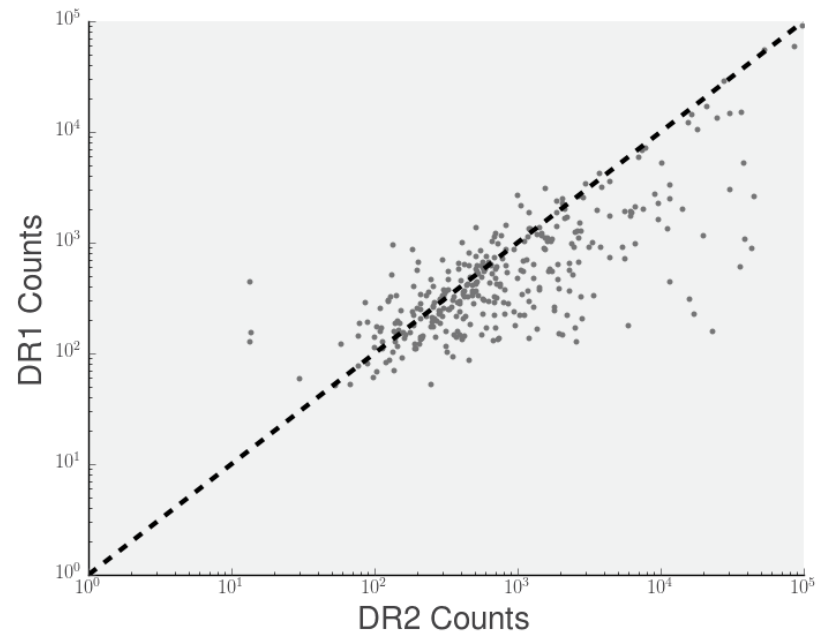
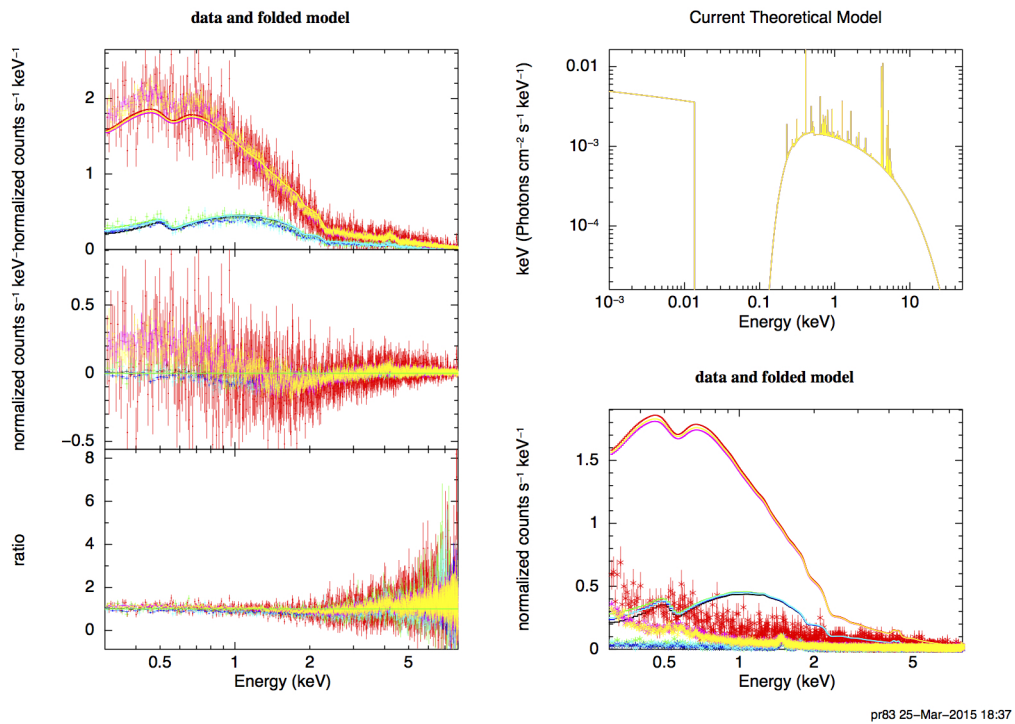


Figure 4.4: A comparison of the total counts used to fit cluster temperatures in XCS-DR1 compared to XCS-DR2, for the clusters in common between the two samples.



pr83 25-Mar-2015 18:37

Figure 4.5: An example of a joint XSPEC fit to seven spectra extracted from multiple observations of cluster XMMXCSJ234444.0-424314.2. Each colour indicates a different spectrum. Top Left: The individual spectra with the best fit model curves overlaid (solid line). Top Right: The best fit model spectrum (including energy regions not included in the observed spectrum). The low energy feature is due to the galactic absorption model. Middle left: Residuals between data and model. Bottom Left: Ratio of data to model. Bottom Right: The solid line shows the best fit model integrated through the instrument response, the data points show the number of background counts at each energy.

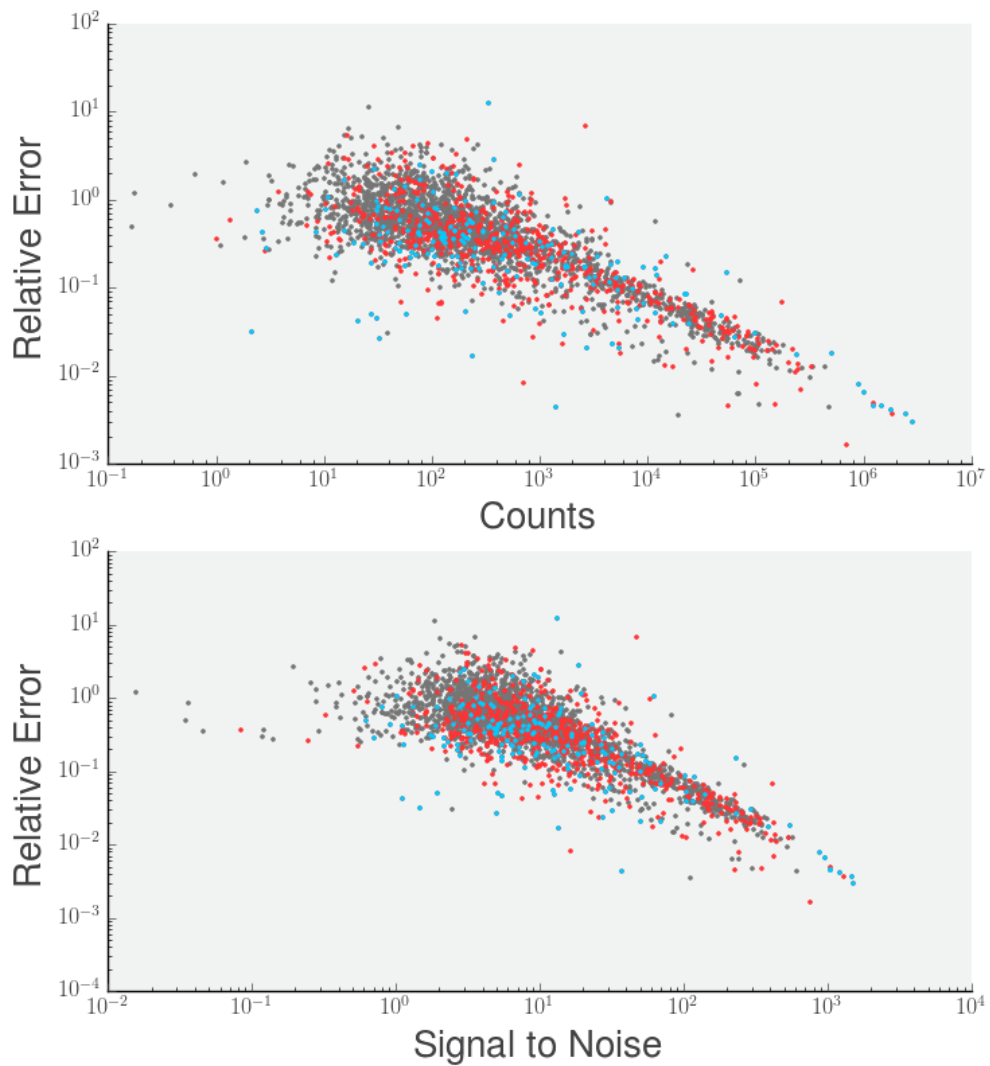


Figure 4.6: As counts increase signal to noise improves. The relative error falls with increasing counts and signal to noise. Grey points show clusters fit with 3 or less spectra - these were usually spectra from MOS1, MOS2 and PN detectors from a single observation and are shown to be the default result. Red points show clusters fit with between 4 and 10 spectra. Blue points show clusters fit with more than 10 spectra.

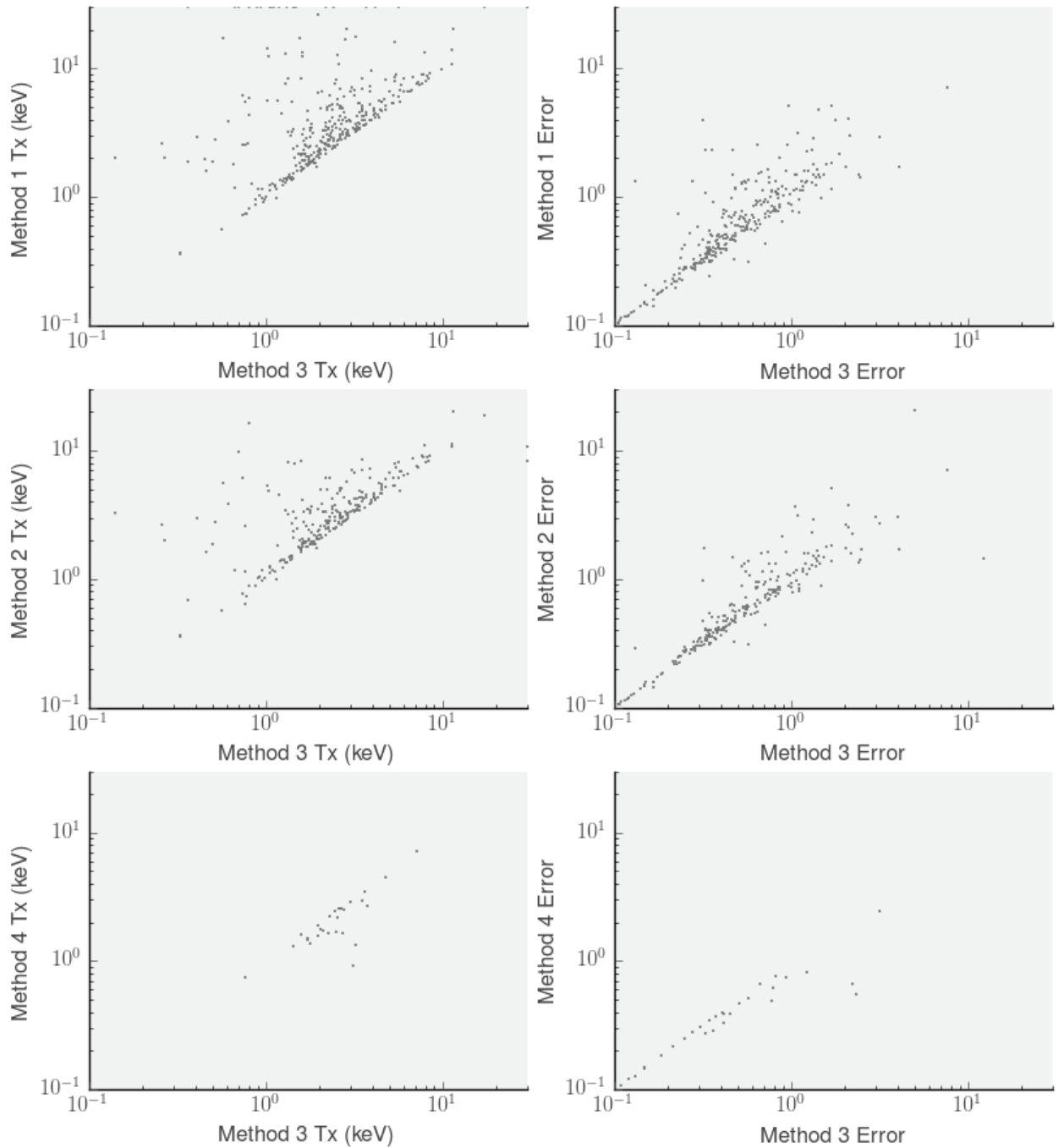


Figure 4.7: A comparison between the best fit T_X value recorded from composite spectra that met the XCS-DR2 criteria (Method 3) and other spectral selection methods (see text for details).

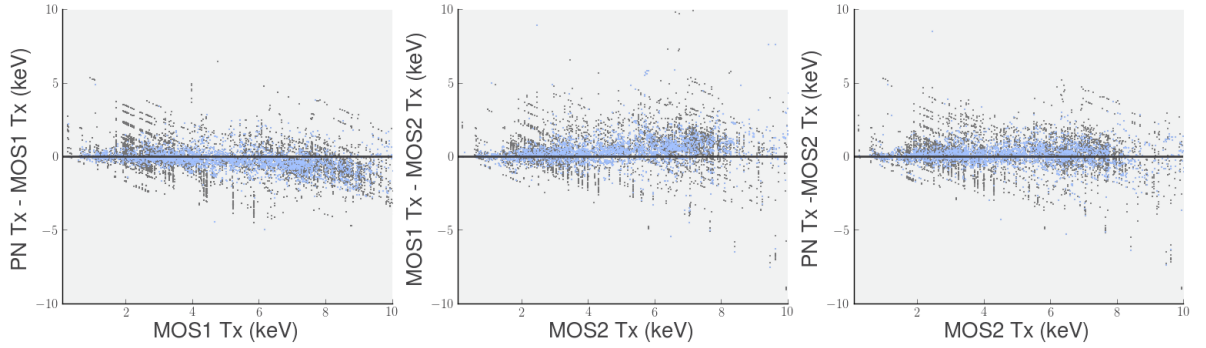


Figure 4.8: Temperature differences measured when comparing spectra accumulated in different XMM detectors. Only cases where both T_X values were recorded with relative errors of 15% or less are shown. Blue points indicate both detectors measurements were from the same observation (i.e. ObsID record), grey indicates the comparison is between detectors from different observations.

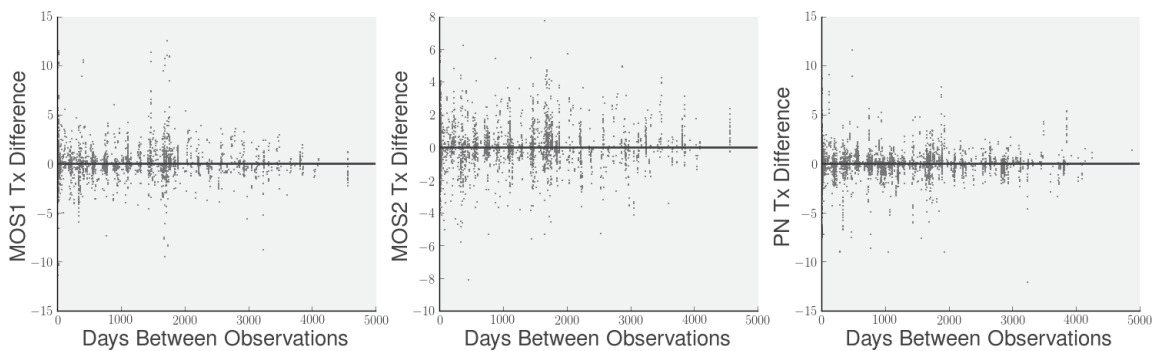


Figure 4.9: Difference in temperature measurements when two or more observations of the same cluster have been made at different times. Only cases where both T_X values were recorded with relative errors of 15% or less are shown.

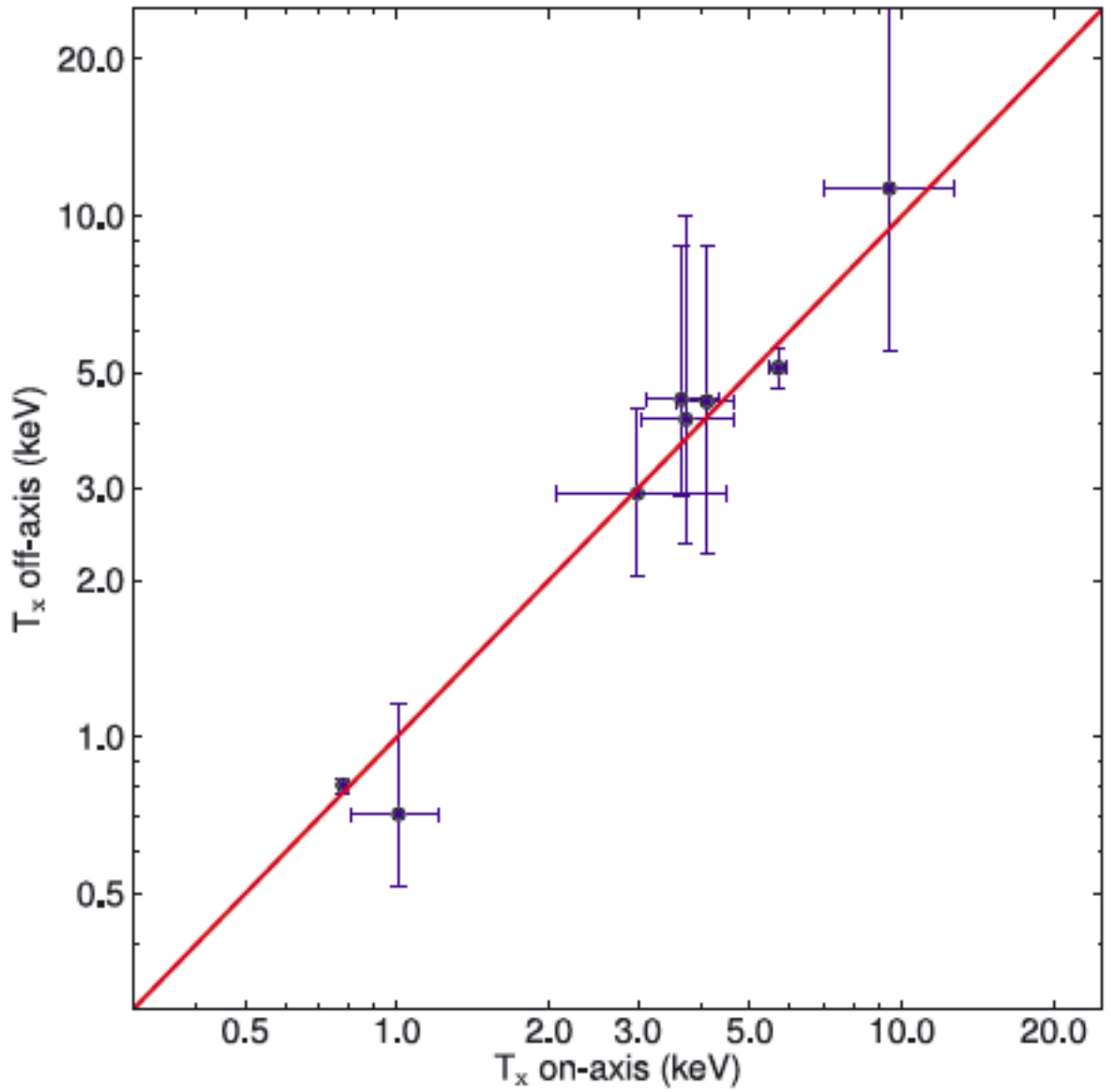


Figure 4.10: (Figure and [adapted] caption wording taken from LD11.) Comparison of XCS-determined X-ray temperatures when the cluster is observed off-axis (y-axis) or on-axis (x-axis). The solid line shows the one-to-one relationship. The error bars are 1σ . Both x- and y-errors come from XSPEC.

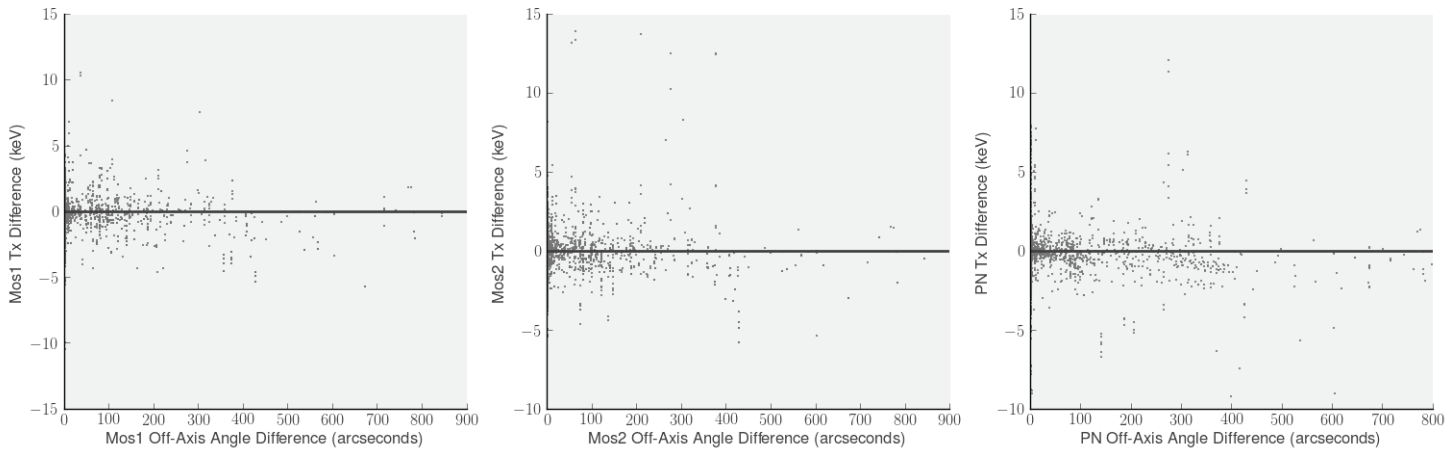


Figure 4.11: Difference in temperature measurements of clusters that have been observed at different off-axis angles. Only cases where both T_X values were recorded with relative errors of 15% or less are shown.

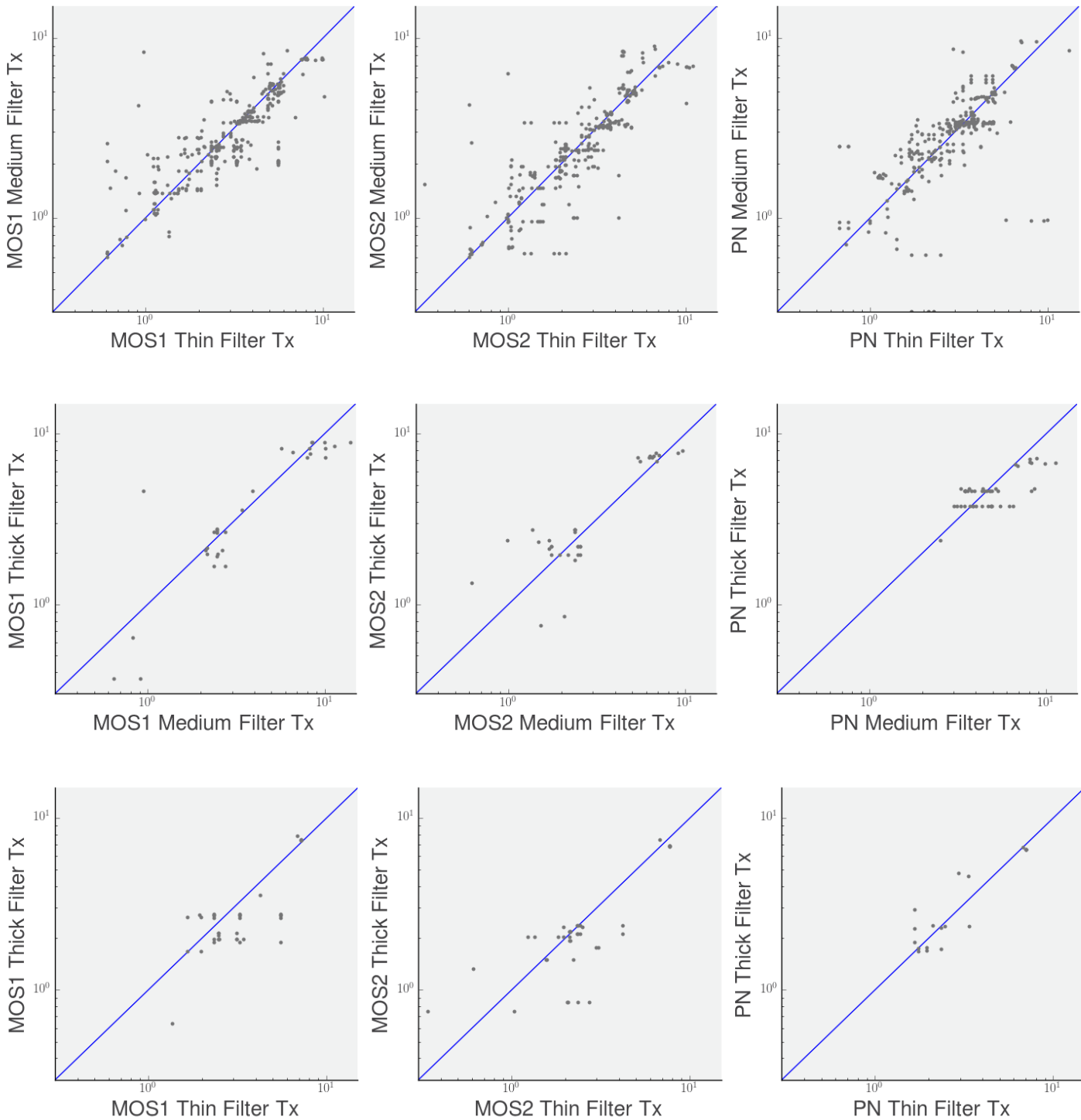


Figure 4.12: Difference in temperature measurements of clusters that have been observed through different filters. Only cases where both T_x values were recorded with relative errors of 15% or less are shown.

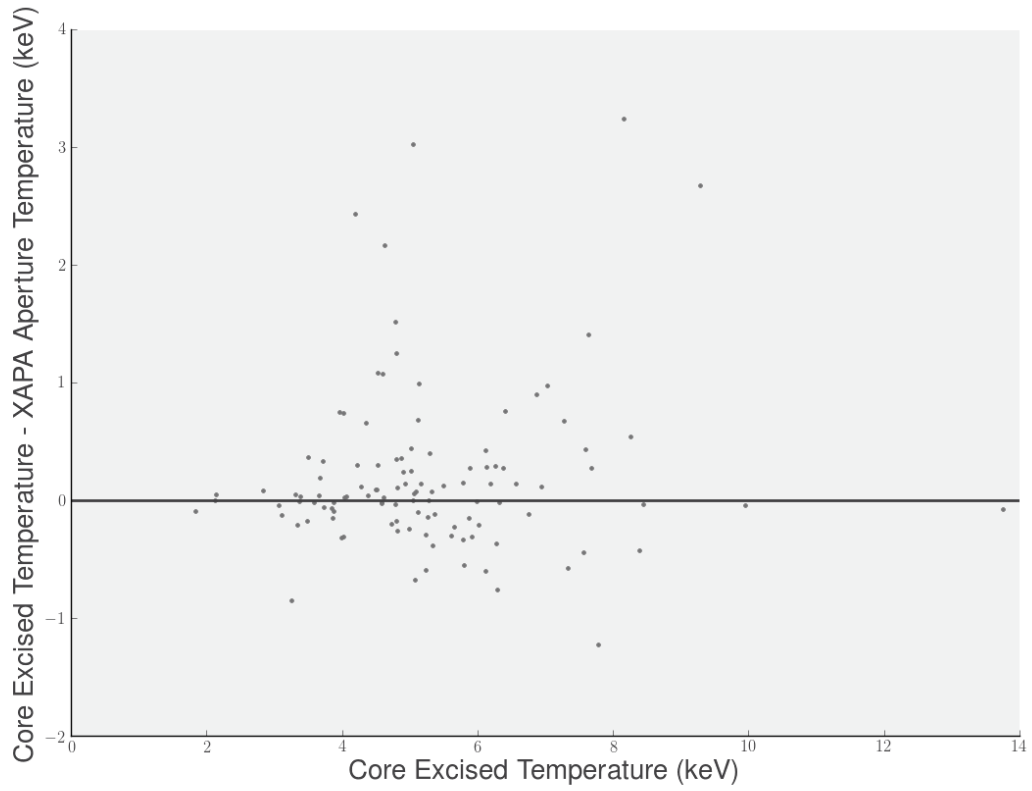


Figure 4.13: Difference in temperature measurements of Planck-XCS clusters with and without core excision before spectral fitting. Only cases where both T_X values were recorded with relative errors of 15% or less are shown.

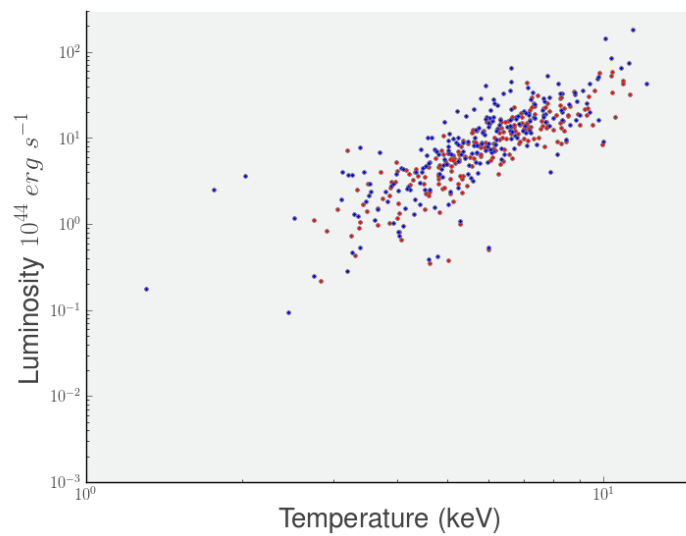


Figure 4.14: Luminosity vs temperature plot for all core excised (red) and non-core excised (blue) Planck clusters.

Chapter 5

Application of XCS-DR2: X-ray Cluster Scaling Relations

5.1 Overview

Motivation The XCS-DR1 luminosity-temperature ($L_X - T_X$) scaling relation result (Hilton et al., 2012) was controversial, because it reported a significant negative evolution in the normalisation compared to self similar predictions. The L_X and T_X values for the clusters in that study have been updated for XCS-DR2 so it is worthwhile to revisit the scaling relation to see if the negative evolution result still holds.

The considerable overlap (78 clusters) between the XCS-DR2 cluster sample and the SPT cluster sample (§ 3.4) also motivates a new study of the scaling relations between X-ray and Sunyaev-Zel'dovich (SZ) observables. This study is interesting in its own right, because it can give us insights into non gravitational physics in the ICM, but also because of its applications to cosmology studies with both SZ selected clusters (e.g. from SPT) and with optically selected clusters (e.g. from DES).

Governing Assumptions We have assumed that the Markov Chain Monte Carlo fitting method used in (Hilton et al., 2012) is robust and can be reused without alteration. We have also assumed that the XCS-DR1, and SPT cluster samples are pure, i.e. that all sources in common with XCS-DR2 are genuine clusters. We have further assumed that the SPT cluster samples is complete, and their overlap with the XMM archive is unbiased, i.e. the derived scaling relations do not need to be corrected for a selection function.

Results The XCS-DR1 and XCS-DR2 luminosity-temperature ($L_X - T_X$) scaling relations, when fit to the 211 clusters in common between the samples, have different measured normalisation evolution. The XCS-DR2 evolution is again found to be negative, but less so than with XCS-DR1. It is now within 1σ of a self-similar prediction.

The scaling relation between Y_{SZ} and T_X for the SPT subsample was also found to be consistent with self-similar predictions. The equivalent relation with L_X was found to be shallower than self-similar predictions (although as expected given the slope of the $L_X - T_X$ relation).

Conclusions and Future work The $L_X - T_X$ study demonstrates that it is essential to optimise X-ray spectral analyses (such as those reported in Chapter 4) before carrying out science investigations.

The SZ to X-ray study demonstrates the potential of XCS-DR2 to support the scientific exploitation (including cosmological parameter estimation) of other, independently constructed, cluster samples.

In future, the XCS-DR2 scaling relation work will be expanded to include many more clusters (there are 4,987 sets of $L_X - T_X$ values in the XCS-DR2 cluster catalogue, compared to the 211 used herein). However, the X-ray and optical selection functions will need to be accounted for first. We also plan to investigate, using mock catalogues, how scaling relation measurements are inhibited by the L_X and T_X precision, the sample size, and selection biases. Ultimately, comparisons will be made, as were done in (Hilton et al., 2012) between the observed and those from hydro simulations, with the aim of better understanding the non-gravitational physics at play in the ICM.

5.2 The XCS-DR1 $L_X - T_X$ scaling relation

Please note that this section contains only review (not new) material.

As shown in Equation 1.37, self-similar theory predicts that L will scale with T as a power law with a slope of 2. The luminosity-temperature scaling relation is expected to evolve with redshift by a factor of $E(z)$. However, for several decades it has been known that the observed scaling has an index of $\simeq 3$ (see below).

5.2.1 Pre-Hilton 2012 Luminosity-Temperature Scaling Relations

$L_X - T_X$ scaling relations for a sample of 31 low redshift clusters ($z \leq 0.2$) were studied in (Pratt et al., 2009) (PR09 hereafter). Luminosities and temperatures were measured for the whole cluster within R_{500} and excluding the core (0.15-1) R_{500} . Fitting was done using a "bivariate correlated errors and intrinsic scatter" (BCES) and orthogonal fitting procedure. Fits were made to the whole sample and subsamples chosen by morphology. Slopes varied between 2.5 and 3.4.

A larger sample of 238 ROSAT selected clusters ($z \leq 0.5$) - many with Chandra follow up - were investigated in Mantz et al. (2010). In this work a $L_X - T_X$ scaling relation was fit with an equivalent slope of 3.7 when including a cores and 2.6 when cores were excised. The work found that, either due to excess heating or the condensing of cold gas, temperatures were different to self similar expectations and that this process must have taken place before redshift $z = 0.5$

The 2XMMi/SDSS Galaxy Cluster Survey team find galaxy clusters in XMM data overlapping with the SDSS region (Takey et al., 2011). Their $L_X - T_X$ scaling relation, using clusters between redshift, $0 \leq z \leq 0.6$ found a slope of 3.41. Similarly to the work presented in this thesis they measured their temperatures within a detection aperture and luminosities within R_{500} .

Reichert et al. (2011) combined 14 public datasets supplemented with XDCP clusters to generate a set of 232 clusters. They find a slope of 3.12. Redshift evolution was fit up to redshift, $z = 1.5$. Self similar evolution predicts an $E(z)$ exponent of -1 whereas they measured a value of -0.23 (or -0.65 with a tentative selection bias correction).

Maughan et al. (2012) split a sample of 114 clusters into relaxed and non-relaxed samples. They find that above 3.5 keV core excised measurements of relaxed galaxy clusters do follow self-similar predictions, arguing that deviations from self similarity are due to central heating and merger shocks.

The lack of consistency in the literature regarding $L_X - T_X$ evolution, plus the availability of the XCS-DR1 cluster sample, motivated the XCS team to make a new measurement of the $L_X - T_X$ relation (Hilton et al., 2012). This work was also able to take advantage of a suite of new samples of simulated clusters that encode a variety of physical mechanisms ((Kay et al., 2004, 2007; Short & Thomas, 2009; Short et al., 2010)).

5.2.2 Data Inputs

XCS-DR1 contained 211 clusters with spectroscopically measured redshifts. The dataset is comparable in size to the largest previous sample, but with the advantage that it only includes homogeneously found and processed clusters. All clusters in the sample were measured using the same instrument, XMM. The increased sensitivity of XMM relative to ROSAT allows for the detection of lower mass clusters.

[Hilton et al. \(2012\)](#) used luminosities and temperatures values measured using the XCS-DR1 spectral fitting pipeline and published in [Mehrtens et al. \(2012\)](#). The scaling relation was fit only to the 211 galaxy clusters with spectroscopic redshifts, covering the redshift range, $0.06 \leq z \leq 1.46$ (with median redshift, $z=0.28$). The clusters have a broad range of temperatures, $0.6 \text{ keV} \leq T_X \leq 9.8 \text{ keV}$ (median temperature, $T_X = 2.9 \text{ keV}$).

5.2.3 Fitting Method

In order to measure the $L_X - T_X$ relation, the following equation was fit to the input data

$$\log(E^{-1}(z)L_X) = A + B \log(T/5 \text{ keV}) + C \log(1 + z), \quad (5.1)$$

where L_X is the bolometric luminosity, T_X is the temperature in keV, A is the normalisation, B is the slope and $C \log(1 + z)$ accounts for redshift evolution. H12 set the pivot temperature to be 5 keV for ease of comparison with other works e.g. [Pratt et al. \(2009\)](#), although this was higher than the median temperature for the sample (2.9 keV).

H12 obtained estimates of the model parameters from the posterior distributions using MCMC, implemented using the [Metropolis et al. \(1953\)](#) algorithm. Two different fitting methods were used, orthogonal and bisector (see below). They obtained estimates of the model parameters from the posterior distributions given in [Table 5.1](#). Selection effects were not accounted for in H12.

Table 5.1: Priors used when fitting XCS-DR1 luminosity-temperature relation.

Parameter	Prior
A	(41,47)
B	(1, 5)
C	(-3, 3)
S	(0.01, 0.5)

Orthogonal Line Fitting Method

An orthogonal regression technique was chosen, where the probability density that a cluster is drawn is as follows:

$$P_{model} = \frac{1}{\sqrt{2\pi(\Delta r^2 + S^2)}} \exp \left[\frac{-(r - r_{model})^2}{2(\Delta r^2 + S^2)} \right] \quad (5.2)$$

$r - r_{model}$ is the shortest distance from the cluster to the fit line, and Δr , is the error orthogonal to the fit calculated using the error on the luminosity and temperature, and S is the orthogonal intrinsic scatter. The likelihood is the product of P_{model} for all clusters:

$$\mathcal{L}(L_X, T|A, B, C, S) \propto P_{prior}(A, B, C, S) \prod_i P_{model,i}. \quad (5.3)$$

Bisector Method

For the bisector method, a model is chosen to be the product of Gaussian probabilities of the residuals of L_X and T_X . In this case instead of using r_{model} they use:

$$\begin{aligned} y_{model} &= \log(E^{-1}(z)L_X) - [A + B \log(T/5) + Cl \log(1 + z)] \\ x_{model} &= \log(T/5) - [\log(E^{-1})L_X] - A - C \log(1 + z)]/B \end{aligned} \quad (5.4)$$

and replace r with x and y and likewise with Δr). S is replaced with parameters $\sigma_{\log(L_X)}$ and $\sigma_{\log(T_X)}$. The likelihood is again the product of P_{model} for all clusters:

$$\mathcal{L}(L_X, T|A, B, C, \sigma_{\log L_X}, \sigma_{\log T_X}) \propto P_{prior}(A, B, C, \sigma_{\log L_X}, \sigma_{\log T_X}) \prod_i P_{model,i} \quad (5.5)$$

5.2.4 Results

Evolution of the slope and intrinsic scatter

[Hilton et al. \(2012\)](#) measured a similar slope at low redshift to the PR09 scaling relation (which measured 3.35) see Figures 5.1 and 5.2. The bisector method measured a slope

of 2.81, whereas the orthogonal method fit a value of 3.18. A lower normalisation was measured between the XCS and PR09 sample. This may have been because the spectral fitting methods were different (in particular XCS used a Cash rather than the Chi Squared fitting), or because XCS detected a higher proportion of cool core clusters. The bisector fit slope shows evolution in line with what is expected from Malmquist bias, whereas the orthogonal fit shows no evolution.

The intrinsic scatter appears to shrink at higher redshift. A possible explanation is that fewer cool core clusters are detected at higher redshift.

Evolution of the normalisation

An evolution parameter, $(1+z)^C$, was fit to the normalisation of the luminosity scaling relation. The normalisation of the XCS-Scaling relation is lower than that found in PR09, but consistent within 2σ .

When using an orthogonal fitting, the evolution of the normalisation was found to be strongly negative relative to self-similar predictions ($C = -1.5 \pm 0.5$). The bisector method finds a shallower evolution ($C = -0.5 \pm 0.3$). The difference can be explained by the significantly lower initial normalisation of the fit. As the slope and normalisation are degenerate, the slope was fixed to the initial fit value, to test if the negative evolution remained - which it did.

The negative evolution found using XCS-DR1 data was consistent with results found elsewhere, notably [Reichert et al. \(2011\)](#); [Fassbender et al. \(2011b\)](#); [Ettori et al. \(2004\)](#); [Clerc et al. \(2012b\)](#); [Pacaud et al. \(2007\)](#). However [Maughan et al. \(2006\)](#) found results consistent with self-similar evolutions whereas a positive evolution was found by [Vikhlinin et al. \(2002\)](#); [Lumb et al. \(2004\)](#); [Kotov & Vikhlinin \(2005\)](#). It is noteworthy that of these studies only [Reichert et al. \(2011\)](#) used a large sample of clusters out to high redshift.

Comparison with numerical simulations

The scaling relation results found in XCS-DR1 were compared to simulations. The CLEF simulation ([Kay et al., 2007](#)), included cooling and radiative feedback and reported more cool core clusters at low redshift than high redshift. The Milenium Gas project ([Short et al., 2010](#)) included a variety of models. The simplest of which was a gravity only model, other models included high redshift energy injection, radiative cooling and feedback from

AGN and supernovae. The XCS result most closely matched the CLEF and Millennium Gas simulations which include high redshift energy injection and radiative cooling. AGN feedback models appeared to be too inefficient at high redshift.

5.2.5 H12 Discussion

H12 suggests that their data set was likely to be biased by selection effects, notably Malmquist bias - leading to shallower slopes and higher normalisations. Such a bias can explain the evolution of the slope, observed when using the bisector method.

However, when [Pacaud et al. \(2007\)](#) accounted for selection effects, this drove a previously positive evolution towards self-similarity. If similar selection effects were present in XCS-DR1 this would drive the negative evolution in an even more negative direction.

H12 also notes that XCS-DR1 contained only serendipitous clusters, detected off-axis where the PSF is sub-optimal, and often with relatively low counts compared to target cluster sets. It is difficult to carry out the morphological analysis necessary to characterise the set and carry out core-excised analysis. It is possible that point source contamination of AGN occurs more often at high redshift where their density is higher. XCS observations of clusters lack the resolution to account for AGN so the effect was not quantified.

H12 did not consider cool-core clusters to have significantly biased their $L_X - T_X$ results, even though it is feasible that cool core clusters are easier than non-cool core clusters to be detected at high redshift (where their bright cores stand out against the background noise). They reference the PR09 study that found cool core samples to have a steeper $L_X - T_X$ slope than non-cool core samples. Whereas the $L_X - T_X$ slope is shallower at high redshift.

5.2.6 New Scaling Relation Results Since Hilton et al (2012)

Following the XCS-DR1 scaling relation several new results have become available. Takey et al.(2013) updated the 2XMMi/SDSS Galaxy Cluster Survey luminosity temperature scaling relation to include newly optically confirmed clusters. A systematic bias caused by not grouping and binning spectra appropriately led to cooler temperatures being recorded in this updated work. This new scaling relation was similar, but shallower to their previous result. Paper I measured a slope of 3.41 ± 0.15 , Paper II measures a slope -after a luminosity

Table 5.2: XCS-DR2 luminosity-temperature scaling relation fit without evolution

Redshift Range	A	B	σ
0-0.25	44.97 ± 0.018	3.257 ± 0.221	0.344 ± 0.043
0.25-0.5	44.82 ± 0.081	3.053 ± 0.290	0.358 ± 0.053
0.5-1.5	44.20 ± 0.052	2.417 ± 0.325	0.22 ± 0.044

cut - of 3.07 ± 0.19 . They also found that after making a luminosity cut their data shows no evolution with redshift.

Clerc et al.(2014) published a scaling relation based upon 52 galaxy clusters found in 11 square degrees, 51 of which have spectroscopic redshifts. This work finds strong negative evolution in the normalisation of the luminosity temperature scaling relation. This evolution is used as an explanation for a potential large void found in the survey. Additionally if there is an evolving AGN population in clusters could induce selection effects.

A self consistent "Physically-motivated, Internally Consistent Analysis of Cluster Scaling (PICACS)" model accounting for cluster masses and observables has been developed (Maughan, 2014). This model can simultaneously constrain scaling relations and cluster masses. The method produces similar results to conventional scaling relation fitting methods while providing additional avenues to explore the processes underlying their form. It has been hypothesised that this can be explained by the heating and depletion of gas in lower mass systems.

5.3 The XCS-DR1 $L_X - T_X$ scaling relation revisited

5.3.1 Data inputs and fitting method

The cluster sample tested was the same as that in H12, i.e. all 211 clusters from XCS-DR1 with spectroscopic redshifts. The redshift values remain unchanged from H12. However, the L_X and T_X values have been updated to the XCS-DR2 measurements. The fitting method also the same as the orthogonal method H12, i.e. the data were fit to Equation 5.1, with the priors given in Table 5.1 (the bisector method was not used in this analysis, or in any of the other scaling relation fits presented in this Chapter).

5.3.2 Results

To test the evolution of the slope we fit the luminosity-temperature scaling relation in three temperature bins ($0.0 \leq z \leq 0.25$, $0.25 \leq z \leq 0.5$, $0.5 \leq z \leq 1.5$). These bins are

consistent with the analysis done in XCS-DR1.

The normalisation found in this analysis is significantly higher than in Hilton et al.(2012) for the first two temperature bins, but comparable in the third temperature bin. The slope of the scaling relation evolves with redshift, becoming flatter for higher redshift. This is an expected effect of Malmquist bias. The normalisation, scatter and slope in the first two bins are consistent within 1σ of each other. The third redshift bin have considerably lower normalisations, slope and scatter.

The evolution of the normalisation was calculated using the whole sample fitting for the $(1+z)^C$ term in Equation 5.1. The evolution found was consistent with self similarity ($C = 0.2 \pm 0.5$). It is important to understand what brought these differences about, i.e. is it only due to the new spectral fitting pipeline used for DR2?

Fitting the luminosity temperature relation, including an evolution term, for the 166 clusters in the first two redshift bins finds consistent results for normalisation and slope for the whole set, with a larger uncertainty in evolution ($C = 0.43 \pm 0.91$). This demonstrates that the high redshift bin, while giving different results to the lower redshift bins does not do so significantly enough to drive additional evolution. However, there are only 38 clusters in the high redshift bin, which is smaller than the first two redshift bins with 96 and 77 clusters respectively. When the XCS selection function is taken into account it could give greater weight to the harder to detect high redshift clusters, driving further negative evolution.

5.4 A new measurement of X-ray to SZ scaling relations

5.4.1 Previous measurements

By using assumptions of self similarity we can derive an equation relating Y_{sz} and X-ray luminosity:

$$(Y_{sz}E(z)^{-2/3}) \propto (L_X E(z)^{-7/3})^{5/4} \quad (5.6)$$

so that the slope of a scaling relation is expected to be $5/4$. Similarly an equation relating Y_{sz} and X-ray temperature can be derived:

$$(Y_{sz}E(z)^{-2/3}) \propto (T_X E(z)^{-2/3})^{5/2} \quad (5.7)$$

so that the slope of a scaling relation is expected to be 5/2

[Bonamente et al. \(2008\)](#) explored SZ-X-ray scaling relation using 38 Chandra observed clusters between redshifts, $0.14 \leq z \leq 0.89$. SZE imaging data came from the BIMA and OVRO interferometric arrays. Values were calculated with R_{500} , excluding the central 100 kpc. They found no significant deviations from the $Y_{sz} - T_X$. Scaling relations were fit in two redshift bins, $0.14 \leq z \leq 0.3$ and $0.31 \leq z \leq 0.89$. Scaling relations in both redshift bins are consistent with self similarity within one- σ .

The SPT team have explored the X-ray properties of their SZ selected clusters using XMM and Chandra ([Andersson et al., 2011](#)). The study used 15 clusters covering a broad redshift range, $0.29 \leq z \leq 1.08$. By calculating gas mass and temperature they fit Y_X and compared this to Y_{SZ} values. They fit a Y_{SZ}/Y_X ratio of 0.82 ± 0.07 , consistent with predictions of 0.91 ± 0.01 . Using a Y_X derived mass they find a Y_{SZ} scaling relation consistent with self-similar predictions.

The Planck team have analysed the relationship between X-ray luminosity and Y_{SZ} using 1,600 clusters ([Planck Collaboration et al., 2011c](#)). They find no evidence of deviations from self-similar evolution.

Other examples of SZ-X-ray scaling relations include [Morandi et al. \(2007\)](#) and [Lancaster et al. \(2011\)](#).

The XCS-SPT scaling relation uses a larger dataset than ([Bonamente et al., 2008](#)). Unlike the Planck work, it also includes temperature data. Finally it only uses data from one X-ray instrument, avoiding any extra scatter that comes from poor cross calibration.

In this work we have access to 58 suitable clusters that been observed with the same instrument.

5.4.2 Data inputs and fitting method

There are 78 clusters in common between XCS-DR2 and the ([Bleem et al., 2015](#)) sample. The redshift and temperature distributions were presented previously in Figures 3.4 and

Table 5.3: Priors used when fitting $Y_{SZ} - L_X$ scaling relation.

Parameter	Prior
A	(-3,3)
B	(0.1, 10)
C	(-3, 3)
S	(0.01, 0.5)

Table 5.4: Priors used when fitting $Y_{SZ} - T_X$ scaling relation.

Parameter	Prior
A	(-3,3)
B	(0.1, 10)
C	(-3, 3)
S	(0.01, 0.5)

3.18. The L_X and T_X values are taken from the XCS-DR2 catalogue. The Y_{SZ} values were provided through private correspondence with members of the SPT team, rather than taken from (Bleem et al., 2015). The new estimates extrapolate the published results, which were measured within 0.75 arcminutes of the cluster centre, to the XCS determined R_{500} radius (§ 3.6.2).

The fitting method was similar to the orthogonal method used in H12, with the priors given in Table 5.3. The data were fit to the following equations:

$$(Y_{sz}E(z))^{-2/3} \propto A + B \log(L_X E(z)^{-7/3}) + C(1 + z) \quad (5.8)$$

$$(Y_{sz}E(z))^{-2/3} \propto A + B \log(T_X E(z)^{-2/3}) + C(1 + z) \quad (5.9)$$

where A is the normalisation of the line, B the slope and C measures evolution with redshift. As the SPT team indicated to us that their Y_{SZ} values are unreliable at redshifts, $z \leq 0.25$, only clusters at redshift greater than this were included. This sample contains 58 clusters. A scaling relation was fit twice, once using the full sample, and once with an additional luminosity threshold of $L_X > 10^{43.75} \text{ erg s}^{-1}$. This threshold was chosen to avoid possible selection effects where high Y_{SZ} - low T_X clusters may be contaminating our sample. This possible selection effect will be resolved by a future comparison of the XCS and SPT selection functions.

5.4.3 Results

The results of fitting to the whole sample are shown in Figures 5.6 and 5.7, and to the luminosity limited sample in Figures 5.8 and 5.9. The application of a luminosity limit does have a significant impact on the measured relations, and their evolution. The Y_{SZ} - L_X slope is shallower than self similarity predictions. The Y_{SZ} - T_X slope is steeper than self similarity predictions. After a luminosity cut is made, the evolution results are consistent with self-similar predictions.

The luminosity cut removes the highest redshift clusters from the sample. The properties of these clusters will need to be explored further to ensure that a luminosity cut is valid. For instance if they were targeted by XMM to confirm low signal high redshift clusters in the SPT sample then they may bias results. To maximise the impact of this study a joint XCS-SPT selection function may be necessary.

Comparison to previous results

The slope of the luminosity fit, 0.86, is within the broad range of values found in the literature. For instance (Morandi et al., 2007) finds a slope 0.62, Lancaster et al. (2011) finds 0.77, and Planck Collaboration et al. (2011c) finds a value of 1.087. The slope of the temperature fit is higher than those found in the literature. For instance (Morandi et al., 2007) finds a slope of 2.08 and Bonamente et al. (2008) finds a slope of 2.37.

5.5 Conclusions and Future Work

5.5.1 Conclusions

- The H12 algorithm was applied to the LT and Y_{SZ} - T/L scaling relations.
- The XCS-DR2 LT scaling relation (using the same data as in H12) has changed. The large negative evolution is no longer present. Evolution is now consistent with self similarity.
- The biggest scaling relation for SPT clusters has been produced. Currently this is assuming that the sample is complete a pure, the Y_{SZ} values are correct and that the XMM subsample is fair.

5.5.2 Work Required Before Publishing in a Paper

- Testing the scaling relation between Y_{SZ} and T/L using Planck results.
- Improve the Y_{SZ} measurements by having it recalculated within R_{500} (rather than extrapolating out using a profile).
- Further investigate the selection effect in the SPT-XCS sample.
- Fit a LT scaling relation to the whole XCS-DR2 sample, and the XCS-DR2 serendipitous sample.
- Account for selection effects (such as those pointed out in [Mantz et al. \(2008\)](#)). This will be done using both an X-ray and optical selection function.
- Simultaneously fit cosmological parameters, scaling relations and the survey selection function (c.f. [Sahlén et al. \(2009\)](#)).

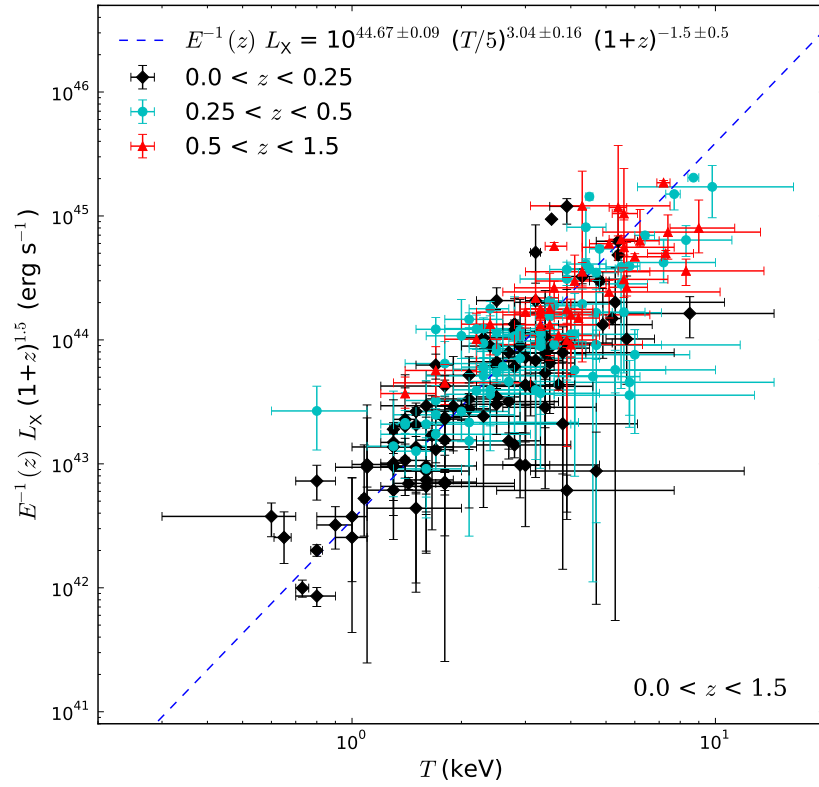


Figure 5.1: (Figure and caption wording taken from H12). The $L_X - T_X$ relation for the 211 XCS-DR1 clusters with spectroscopic redshifts. The dashed line is the best-fitting four parameter model (Equation 1), determined using the orthogonal fitting method. The luminosities have been scaled to take into account the evolution in the normalisation as a function of redshift inferred from the best-fitting model parameters, as well as the $E^{-1}(z)$ evolution expected in the self-similar case.

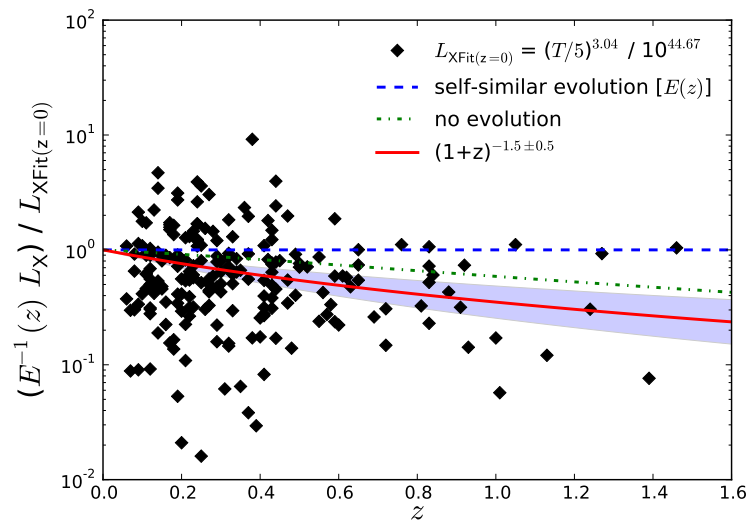


Figure 5.2: (Figure and caption wording taken from H12). Evolution of the normalisation of the $L_X - T_X$ relation relative to the self-similar case $[E(z)]$, as inferred from the best-fitting four parameter model (Equation 5.1), using the orthogonal fitting method. The shaded area shows the marginalised 68 per cent confidence region on the evolution derived using MCMC. The dot-dashed line shows the track for no redshift evolution in the normalisation of the relation. The black diamonds show individual XCS clusters (error bars are omitted for clarity).

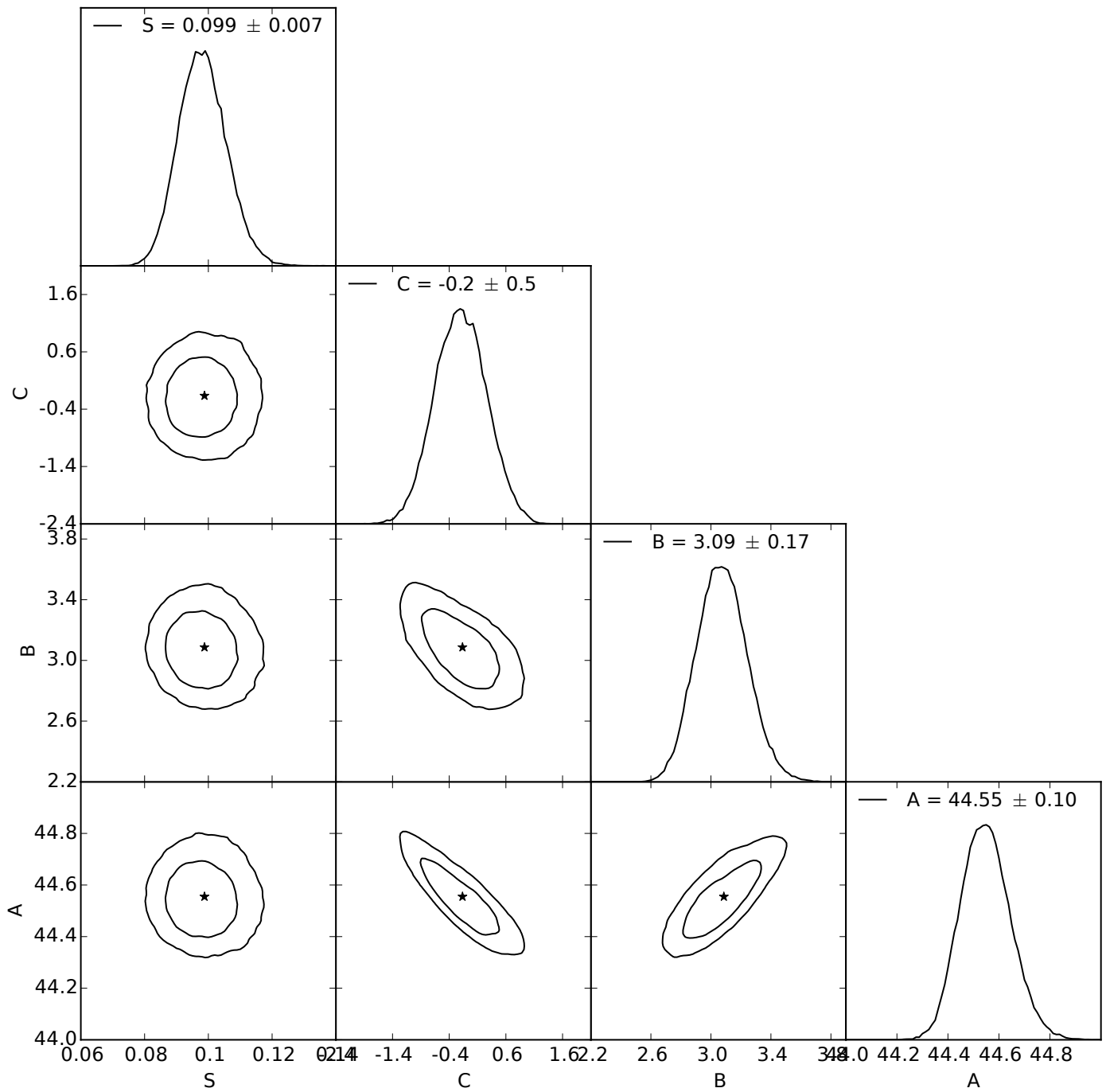


Figure 5.3: (Figure and caption wording taken from H12). One and two dimensional marginalised distributions (contours mark 68 and 95 per cent confidence limits) for each combination of parameters in the four parameter evolving $L_X - T_X$ relation model (Equation 5.1), as determined using the orthogonal fitting method. Note that the luminosities have been scaled by $E^{-1}(z)$, and so $C = 0$ corresponds to the case of self-similar evolution.

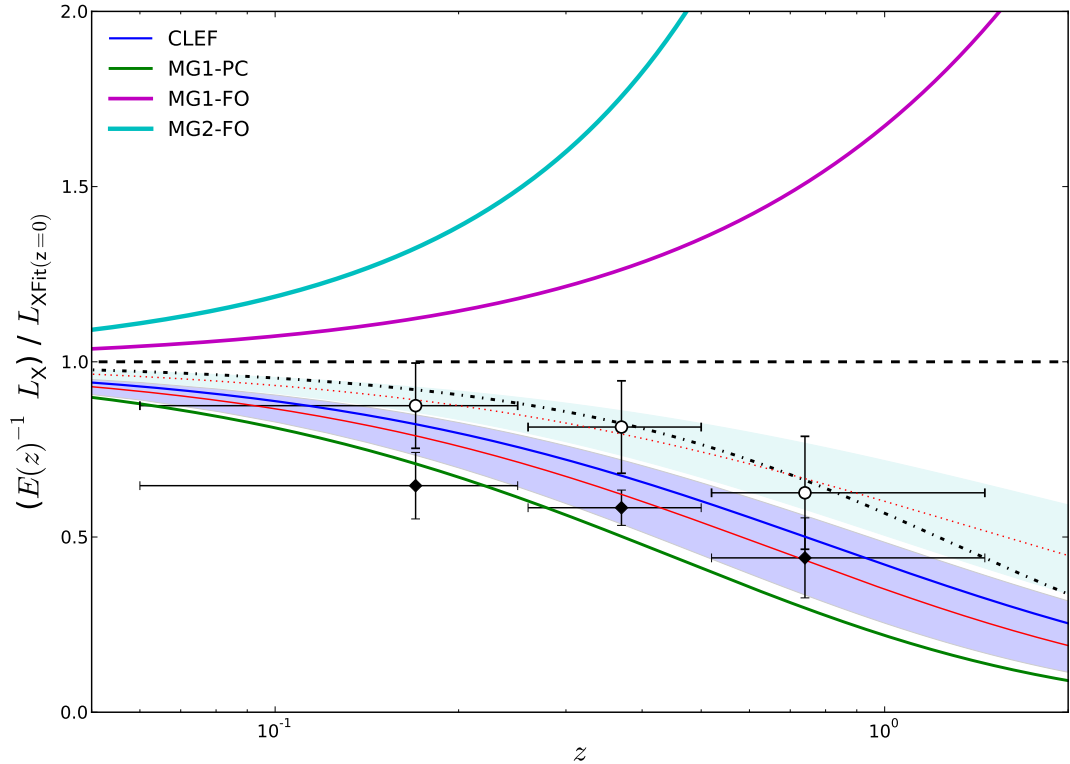


Figure 5.4: (Figure and and caption wording taken from H12) Evolution of the normalisation of the $L_X - T_X$ relation as measured from XCS-DR1, compared with numerical simulations. The solid thin red line is the best-fit obtained from XCS-DR1 using the orthogonal method, while the black diamonds show the corresponding median values for the clusters in each redshift bin (horizontal error bars indicate the redshift range of each bin, while vertical error bars indicate the 1s uncertainty in the median, estimated using bootstrap resampling). The dotted thin red line similarly represents the best-fit for XCS-DR1 obtained using the bisector method, with the slope fixed at the $z = 0$ value (2.81, see Table 3), and the open circles indicate the median values for clusters in redshift bins for this set of best-fit $L_X - T_X$ relation parameters. This latter fit is consistent with no evolution (dot-dashed line). The shaded regions mark the marginalised 68 per cent confidence regions. While the amount of evolution inferred from the XCS sample depends on the fitting technique used, there is no such dependence for the simulated data (see Table 4), and so we only show the results of the fits to the simulations using the orthogonal method. The XCS data favour negative evolution with respect to self-similar ($E(z)$; horizontal dotted line), and are clearly better described by the CLEF or MG1-PC models, rather than the models which implement AGN and supernovae feedback using a semi-analytic prescription (MG1-FO and MG2-FO).

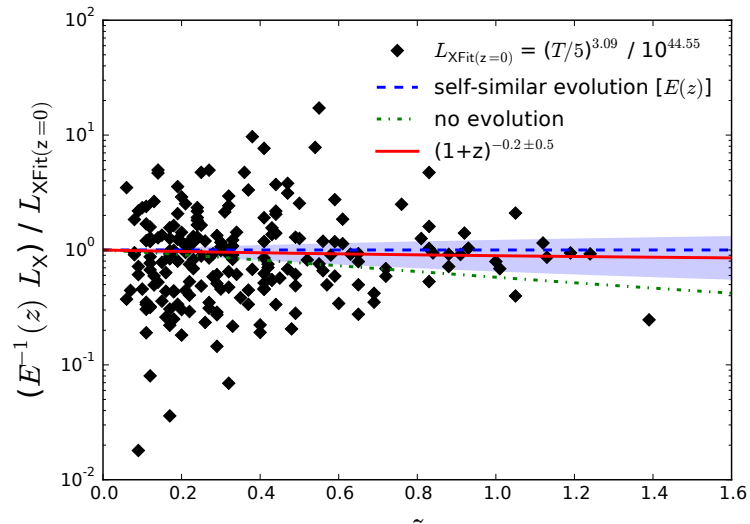
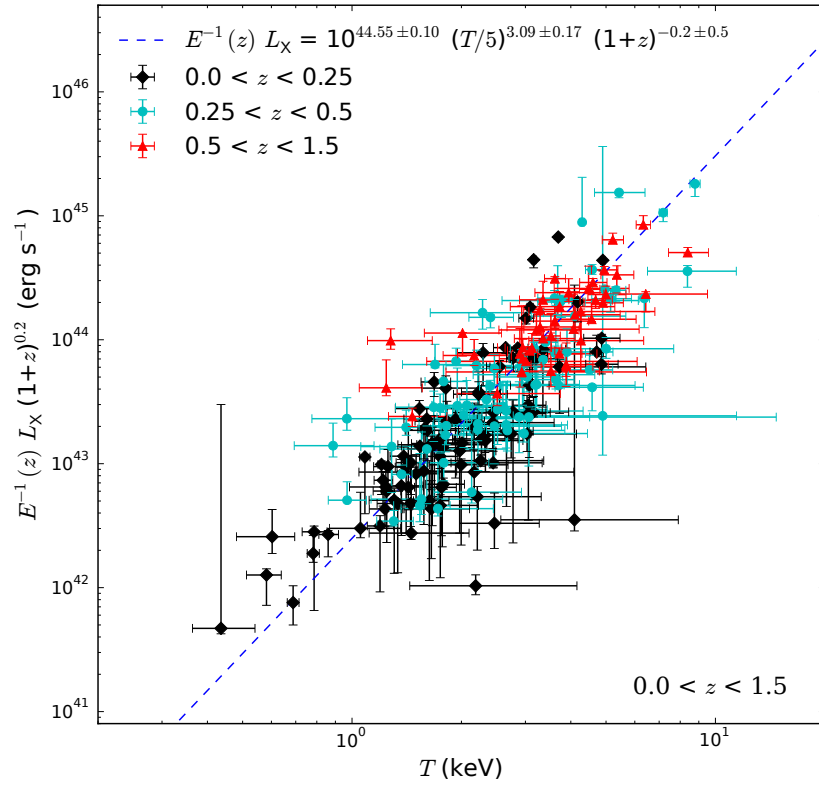


Figure 5.5: Top: as Figure 5.1, but using the XCS-DR2 derived parameters for the clusters. Bottom: as Figure 5.2, but using the XCS-DR2 derived parameters for the clusters.

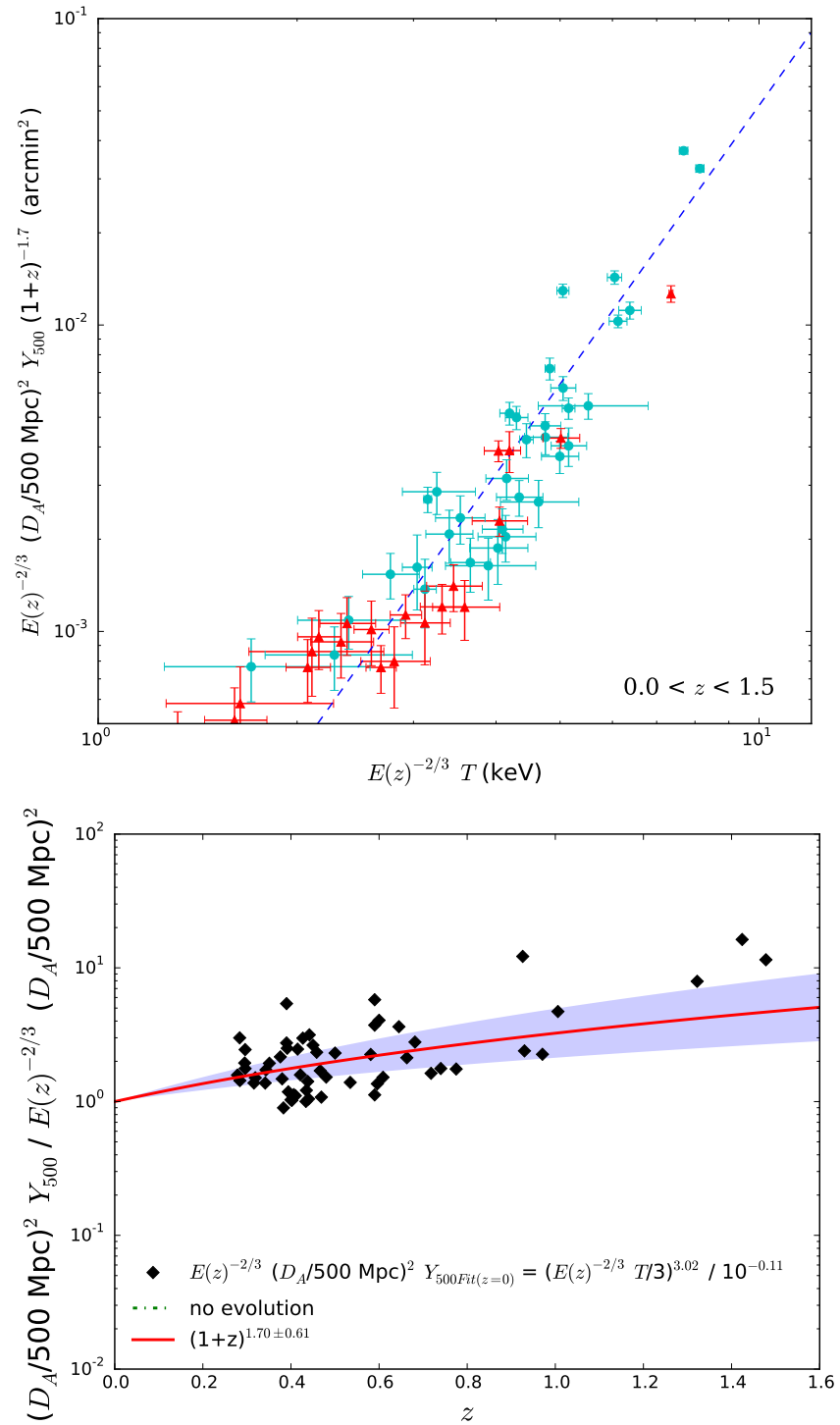


Figure 5.6: Similar to Figure 5.5, but for the SPT determined Y_{SZ} value as a function of T_X value.

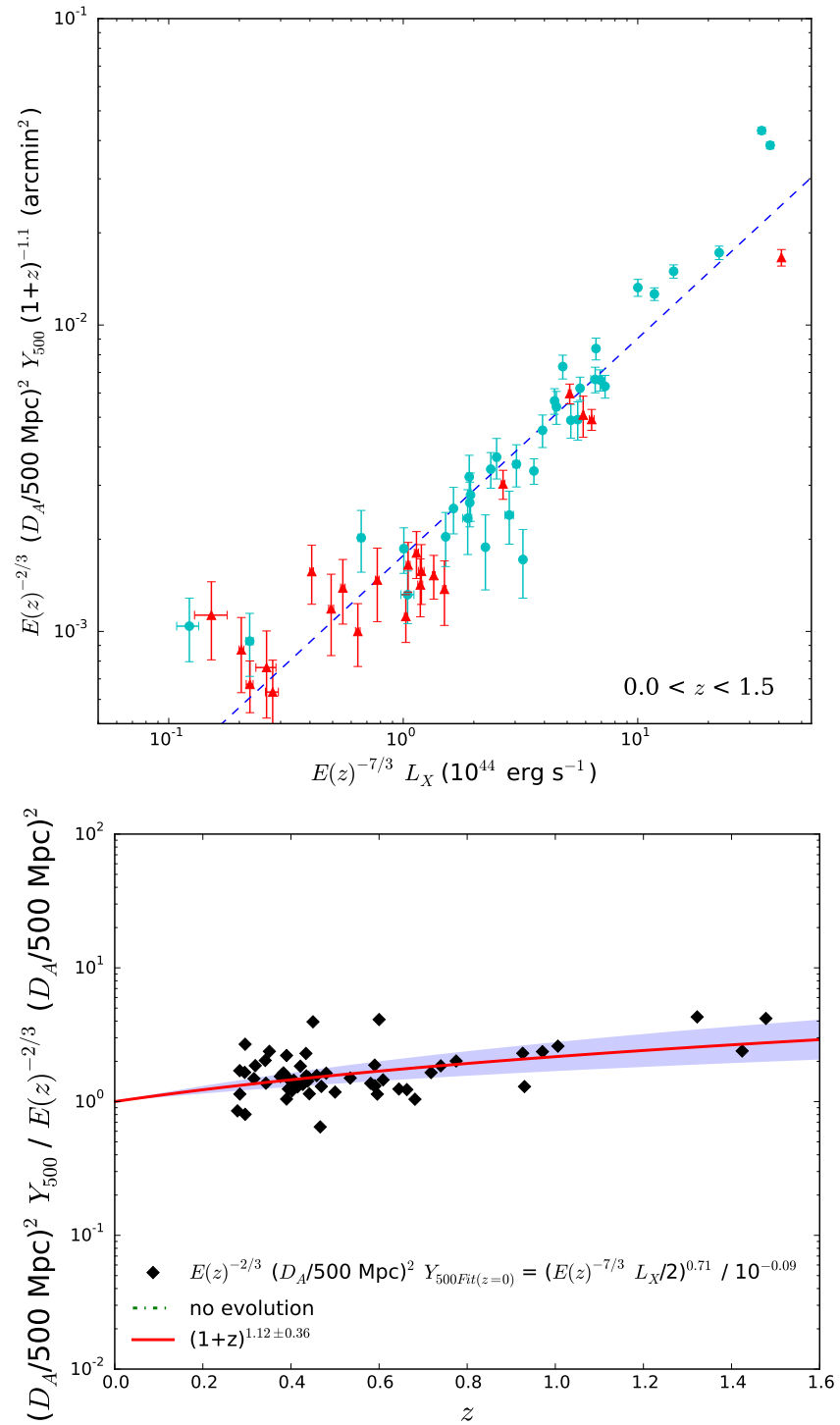


Figure 5.7: Similar to Figure 5.6, but for the SPT determined Y_{SZ} value as a function of L_X value.

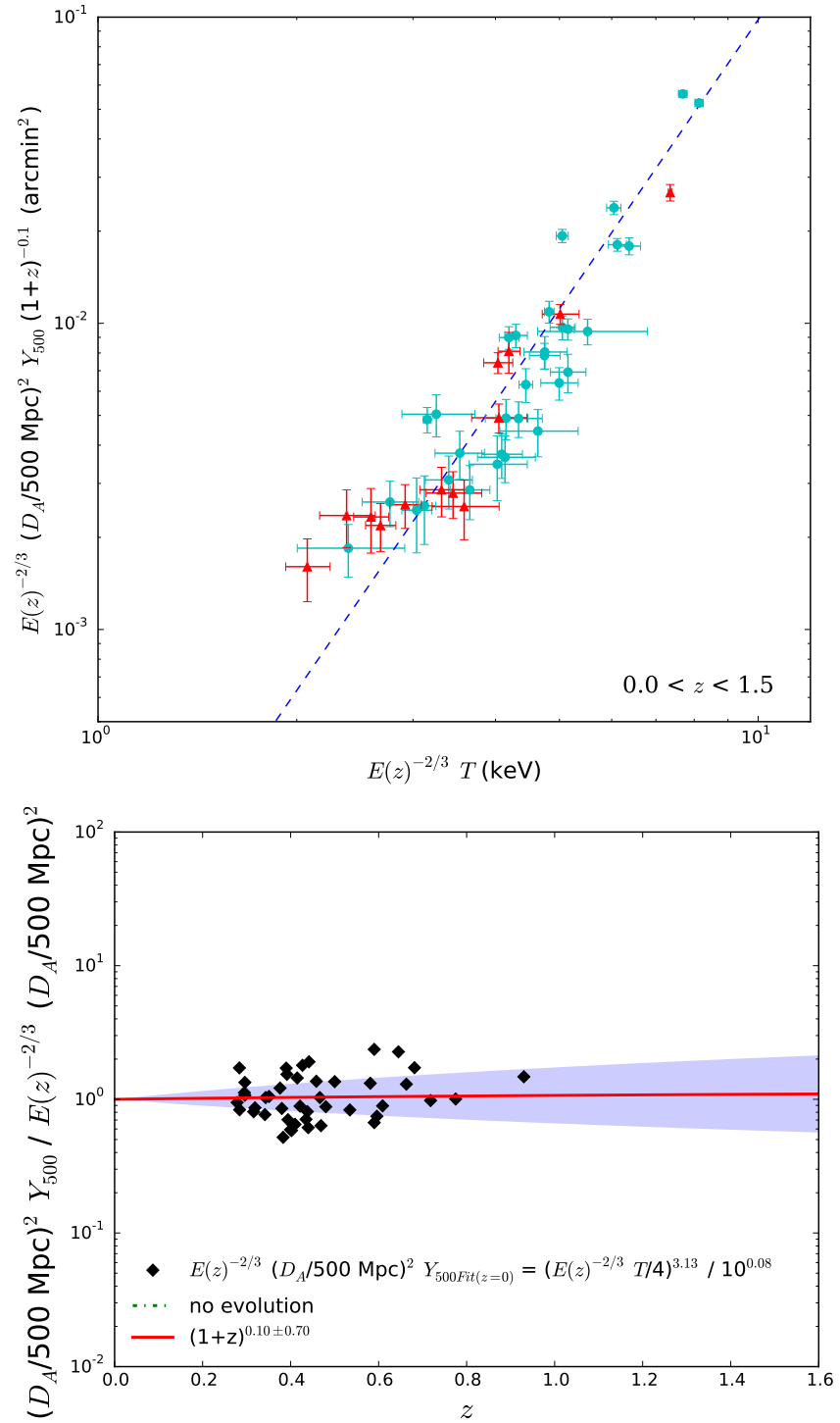


Figure 5.8: Similar to Figure 5.6, but a lower L_X threshold has been applied.

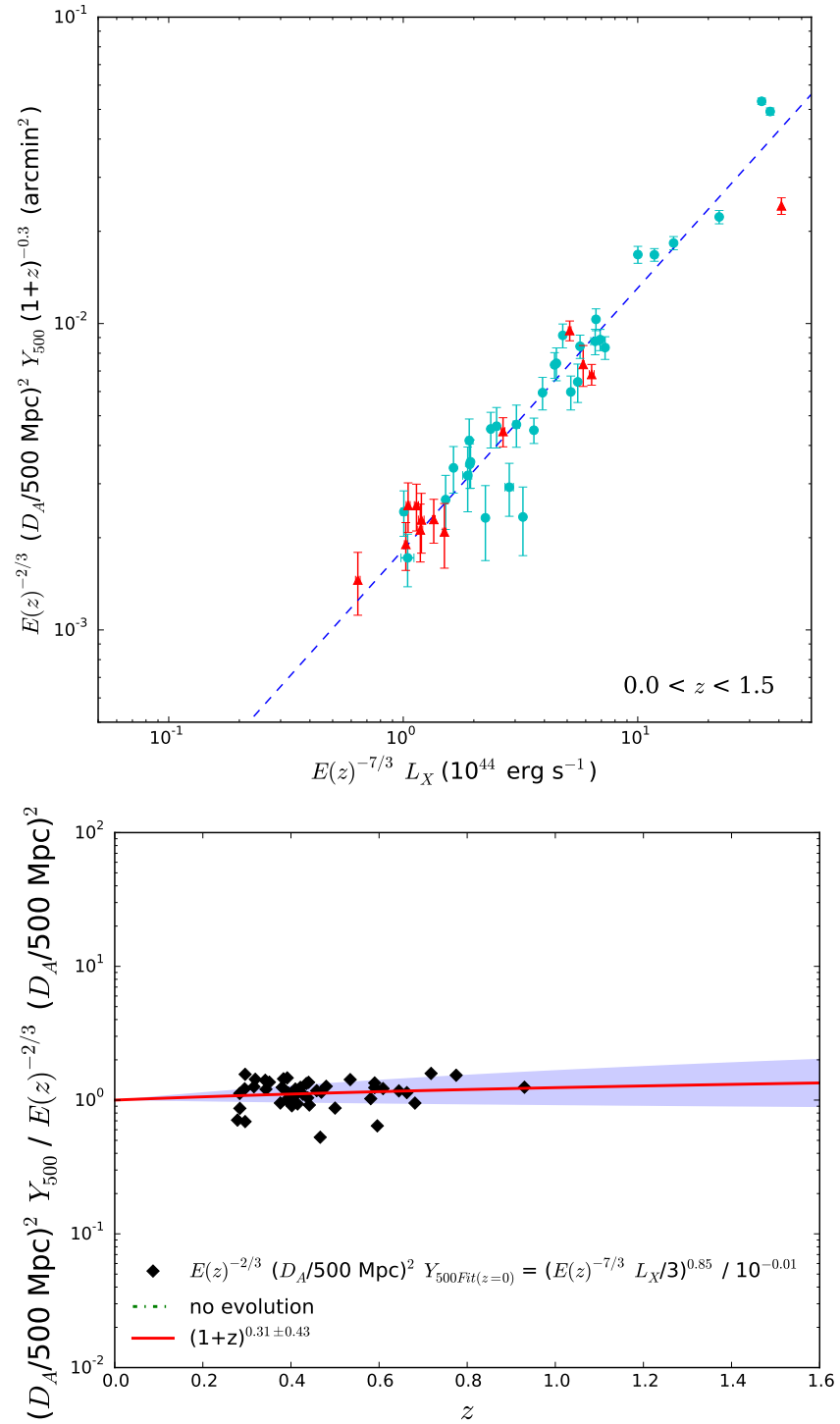


Figure 5.9: Similar to Figure 5.7, but a lower L_X threshold has been applied.

Chapter 6

Application of XCS-DR2: Selection of clusters for the f_{gas} cosmology test

6.1 Overview

Motivation The cluster baryon fraction (or f_{gas}) test has produced the strongest constraints on cosmology from clusters to date (Mantz et al. (2014b), M14 hereafter). The primary limitation on the f_{gas} test is that it requires a rare type of cluster (dynamically relaxed and Chandra measured $T_{500} > 5$ keV), and the team behind M14 (the ‘CARGC team’ hereafter) have already exhausted the suitable f_{gas} cluster candidates in the ROSAT and Chandra archives.

Underlying Assumption XCS-DR2 is one of largest sample of X-ray selected clusters to date, so it is safe to assume that catalogue will include clusters suitable for the f_{gas} test. The CARGC team created a test to identify clusters from the Chandra archive suitable for f_{gas} cosmology. By applying their technique to XMM data, we should be able to identify clusters from XCS-DR2 that are suitable for f_{gas} cosmology.

Tests We have tested the method by applying it to XMM observations of clusters that have been previously examined by the CARGC team using Chandra data. We found the same clusters to be relaxed and un-relaxed (Section 6.3).

Results So far we have identified twenty XCS-DR2 clusters with a greater than 50% chance of being relaxed (Section 6.4.2). A Chandra proposal (unsuccessful) was submitted in March 2015 to observe six of these (Section 6.5).

Conclusions and Future work We have demonstrated that XCS-DR2, in combination with the CARGC morphology test, is a useful dataset to find new clusters suitable for f_{gas} analysis. The Chandra proposal was not successful but can be further developed and resubmitted in 2016. To date, we have only run the morphology test on on-axis (i.e. XMM target) clusters. In future we apply it at larger off axis angles. Ultimately, we would like to carry out an f_{gas} cosmology test using solely XMM data, e.g. by using stacked cluster images, so that XCS can produce an independent check of the CARGC team results (Section 1.4.1).

6.2 The CARGC morphology test and its application to Chandra data

6.2.1 Principles of the CARGC Cosmology Test

As mentioned previously (Section 1.4.1), the *Cosmology and astrophysics from relaxed galaxy clusters*, or CARGC team (M15), have been able to measure, using the f_{gas} test, cosmological parameters to similar, or better, precision than other leading methods (e.g. from CMB anisotropies, Baryon Acoustic Oscillations, and Type 1 Supernovae). The CARGC approach to measuring cosmological parameters relies on the following assumptions:

- The cosmic baryon density has a predictable evolution that is governed by fundamental cosmological parameters (see Equation 1.45).
- Massive clusters have gas mass fractions, defined as

$$f_{gas}(r) = \frac{\rho_{gas}(r)}{\rho_{total}(r)}, \quad (6.1)$$

that reflect the average baryon density in the Universe (Ω_b). By contrast, baryons can be lost from the intracluster medium in less massive clusters during mergers.

- It is possible to measure the X-ray emitting gas mass in a cluster using X-ray observations and assumptions about the X-ray emission mechanisms.

- In principle, it is possible to measure the total mass of a cluster accurately using either weak lensing or X-ray observations.
- In practice, it is not possible to measure the total mass of a cluster *exactly* using observations because no cluster is completely isolated, spherical and relaxed. However, it is possible to model the measurement uncertainty using a redshift dependent ‘fudge’ parameter, K , that can be marginalised over when fitting cosmological parameters.
- The X-ray emitting gas mass in massive clusters is not exactly the same as the cosmic baryon density, because baryons are locked into stars or into diffuse gas that is too cool to emit X-rays. The so-called baryon depletion parameter, or $\Upsilon(r, z)$, is predicted to have small scatter and mild redshift evolution and to be related to the

$$\Upsilon(z) = f_{\text{gas}}\Omega_m/\Omega_b \quad (6.2)$$

- The fraction of X-ray emitting gas to total baryon content in a cluster is predictable from simulations ((Battaglia et al., 2013), (Planelles et al., 2013)), and is best measured in a spherical shell that avoids both the cluster core and unvirialised outer regions (i.e. for $0.8 < r < 1.2 \times R_{2500}$).
- Massive clusters inhabit the peaks of the initial matter density distribution. They therefore collapsed and began to form earlier and so subsequent mergers are likely to involve smaller halos that inject relatively little energy compared to the energy already in the cluster. Massive clusters are therefore more likely to be relaxed than less massive clusters.
- Clusters with cool cores are more likely to be relaxed than those without, because cool cores are easily disrupted during mergers.
- Known differences in calibration and spatial resolution between the XMM and Chandra instruments mean that an f_{gas} test should only rely on data from one or the other, but not both. Given the need to excise the core region, i.e. $r < 0.8R_{2500}$, Chandra is the preferred instrument because of its enhanced spatial resolution compared to XMM.

6.2.2 Principles of the CARGC Morphology Test

The CARGC cosmology test relies on there being sufficient suitable clusters over a range of redshifts. In this context, ‘suitable’ means massive and relaxed. To meet the ‘massive’ criterion, the CARGC team apply an X-ray temperature threshold of 4 keV (this is the core excised average value, see (Mantz et al., 2015), M15 hereafter, for details). To select clusters like to meet the ‘relaxed’ criterion the CARGC team adopt the following principles:

- A finite PSF has the effect of smoothing the surface brightness profiles of higher redshift systems. Moreover, detector artefacts such as bad rows and chip gaps will have more impact on more angularly extended, i.e. lower redshift, clusters. The morphology test must compensate for these effects so that it is fair over the relevant range of redshifts, otherwise artificial evolution will be introduced.
- Cluster surface brightness profiles are noisy, especially as radius from the core increases. The morphology test must operate in the poisson noise limit.
- Cluster surface brightness profiles are sensitive to the underlying cosmology (through the evolution of structure and through the angular diameter diastase). The morphology test must compensate for this, otherwise artificial evolution will be introduced.
- Relaxed clusters are likely to have cool cores, and hence peaky surface brightness profiles. The morphology test can use ‘peakiness’ as a selection criterion.
- Not all relaxed clusters have cool cores, so the morphology test should include alternative selection criteria.
- Relaxed clusters will have isophote levels that have a common centre of symmetry. The morphology test can use isophote symmetry and alignment as selection criteria.
- Relaxed clusters have spherical symmetry, so the assumption of sphericity when applying the morphology test is not likely to lead to relaxed clusters being rejected (although it could lead to unrelaxed clusters being accepted).
- The surface brightness profile of relaxed clusters follows the NFW (Navarro et al., 1996) prediction.

6.2.3 Practicalities of the CARGC Morphology Test

The mechanisms by which the principles described above are put into practice are as follows (see M14 for more details).

A redshift independent fitting parameter

The morphology test needs to work fairly across as range of redshifts, so a temperature and redshift independent fitting parameter, f_S (proportional to the X-ray surface brightness, S) has been introduced by CARGC:

$$f_S|_{r_\Delta} = K(z, T, n_H) \frac{E(z)^3}{(1+z)^4} \frac{kT}{\text{keV}} \text{photons Ms}^{-1} \text{cm}^{-2} (0.984 \text{ arcsec})^{-2}, \quad (6.3)$$

where $K(z, T, N_H)$ is a redshift, temperature and galactic absorption dependent scaling from the bolometric flux to observed energy band flux, $E(z)$ is the redshift dependence of the Hubble parameter (Equation 1.6). The f_S parameter depends on the radius from the cluster core, where radius is expressed in relation to the critical density of the universe. Note that, as written in Equation 6.3, the f_S parameter is Chandra specific, because it includes the Chandra pixel size 0.984 arcsec)⁻². Note also that the count rate is in units of photons per Megasecond of exposure.

Defining the Cluster Centre

The CARGC morphology code fits the location of the cluster centre, rather than using a predefined, e.g. from NED, value (Figure 6.1). A centre is found by summing the pixels along columns and rows and picking the median value of each. The third of the image furthest from the centre is cut, and the process repeated until the code finds a stable square of at least 40×40 arcseconds. During the process, sources other than the cluster in the observation are masked out. The masking is done by hand. The median value method avoids poor centring due to Poisson noise, e.g. on a point source that was not correctly masked or on a pixel where a cosmic ray hit.

Generating Surface Brightness Profiles

Using the cluster centre defined as above, azimuthally averaged surface brightness profiles generated by adaptively creating annuli, so that the signal to noise in each is greater than

2 (Figure 6.2). Up to six isophote levels are then defined as a function of the f_S parameter described above:

$$S_j = 0.002 \times 10^{0.28j} f_S \quad (6.4)$$

for $j = 0, 1, 2, 3, 4, 5$. Note that the j decreases with radius, i.e. S_0 is the outermost surface brightness, not the inner most.

Measuring Surface Brightness Peakiness

To measure peakiness, the morphology test compares the surface brightness in the inner most annulus (usually, but not always S_5) to the average surface brightness. For this test, masked out pixels, i.e. those that contain other sources, are replaced with randomly selected pixels within the same annulus. The equation for surface brightness peakiness is:

$$p = \log \left[(1 + z) \frac{\bar{S}(\theta \leq \theta_5)}{f_S} \right] \quad (6.5)$$

According to M15, “*This quantity contains as much information as the ratio of flux in small and large apertures while being measured more precisely*”.

Isophote Fitting

Ellipses were fit to the regions enclosed by the (up to) 6 surface brightness values defined above (Figure 6.1). For this, the image were smoothed with a boxcar annulus with a maximum kernel radius of 10 pixels and a target signal to noise ratio of 2. Masked pixels remain after this process, and an additional mask is placed around $0.1 S_0$ to prevent bright non-cluster pixels from contaminating the image.

Isophotes are for the smoothed image at each of the five brightness levels. Ellipses were fitted to the isophote level minimising the sum of the distances from the ellipse to each pixel in the isophote. The distance measure used is along the line that passes through the pixel and the ellipse centre. Innermost levels were been chosen to avoid the cluster core region.

Measuring Isophote Alignment

Alignment is designed to be detect centroid shifts in the set of isophotes. It is defined as:

$$a = -\log \left[\frac{1}{N_{el} - 1} \sum_{j=1}^{N_{el}-1} \frac{\delta_{j,j+1}}{\langle b \rangle_{j,j+1}} \right] \quad (6.6)$$

where N_{el} is the number of ellipses, $\delta_{j,j+1}$ is the distance between ellipse centres and $\langle b \rangle_{j,j+1}$ is the average of the four ellipse lengths.

Measuring Isophote Symmetry

The symmetry measure analyses the agreement of isophotes with regard to the clusters global centre. It is defined as:

$$s = -\log \left[\frac{1}{N_{el}} \sum_{j=1}^{N_{el}} \frac{\delta_{j,c}}{\langle b \rangle_j} \right], \quad (6.7)$$

where the subscript c refers to the global cluster centroid.

Accounting for Poisson noise

In any given cluster observation, there can be surface fluctuation peaks or troughs due to Poisson noise. These will influence the measured values of p , a and s . So the CARGC team generate 1,000 realisations of each cluster via bootstrap resampling (with replacement). Each of these realisations is run through the morphology testing code, i.e. there are 1,000 sets of p , a and s values per cluster.

Test thresholds

The CARGC team choose thresholds in the three measured properties (Peakiness, p , Isophote Alignment, a , and Isophote Symmetry, s) as given in Table 6.1. These were subjectively chosen and designed to be conservative, i.e. to reject all non-relaxed clusters, at the expenses of occasionally rejecting relaxed ones too. To pass the morphology test at least 50% of bootstrap images of the cluster, see above, had to meet all of these cuts (Figure 6.3). The CARGC morphology test was ran on more than 300 relaxed cluster

Table 6.1: Threshold cuts for s,p,a parameters.

Parameter	Threshold
<i>s</i>	>0.87
<i>p</i>	>-0.82
<i>a</i>	>1

candidates with 40 passing the test. This exhausted their set of suitable clusters for analysis, making an XMM test of XCS clusters particularly useful.

6.3 The CARGC morphology test applied to XMM data

The CARGC code was designed to work with Chandra images and several adaptations were necessary in order to get it to work on XMM images. These are described below.

6.3.1 Choice of pixel size and detector

The Nyquist criterion specifies the minimum sampling needed to preserve resolution with an audio sine wave. In short it can be expressed as the sampling frequency should be at least twice the highest frequency contained in a signal. General solutions of this theory require the resolution to be proportional to the functions width. For a 1-D Gaussian, this requires the FWHM=2.355 pixels. In 2-D, this resolution is measured across the diagonal of square pixels requiring $\text{FWHM} = 2.355 * \sqrt{2}$ pixels or approximately 3.33 pixels.

The on-axis XMM PSF can be approximated with a Gaussian with a FWHM of 4.4'' arc seconds. This is oversampled by the intrinsic MOS detector pixel size, but not by the PN detector. Therefore, for the morphology test we only used MOS images, binned into 1.1'' image pixels. These images differ from those produced by XIP (§ 2.3), which have 4''.35 pixels, but were produced (in the 0.5-2.0 keV energy band) in a similar way using SAS (Figure 6.5):

```
evselect table=/mnt/lustre/scratch/inf/pr83/0000000000/
eclean/mos1_exp1_clean.evts.fits withimageset=yes
imageset=imagem1_1.0.fits xcolumn=X ycolumn=Y
yimagesize=2650 ximagesize=2650 expression='#XMMEA_EM
&& (PATTERN<=12) && PI in [500:2000]' writedss=yes squarepixels=true
```

The equivalent exposure maps were generated using `eexpmap` with the same pixel size.

6.3.2 Accounting for the Effective Area

The exposure maps differ between XMM and Chandra. In Chandra they account for the effective collecting area of the telescope in the respective energy band, whereas in XMM they only contain information about the effective exposure. Therefore, to adapt the morphology code to XMM, we used an extra input parameter to import the average effective area in the 0.5-2.0 keV band. For this, the XMM Auxillary Response Files (ARFs, Section 1.1.4) were used.

6.3.3 Masking point sources

Sources other than the cluster need to be masked before the morphology code is run. The CARGC team did this by hand, but we are able to semi-automate the process using the XAPA source ellipses (Section 2.7) for the respective ObsID. First these ellipses need to be converted from XIP image pixel coordinates (those images have a $4.35''$, rather than $1.1'$ pixel size). Given that XAPA ellipses can sometimes underestimate the full extent of the emission, the ellipses were expanded by 100% (50%) for point (extended) sources. The expanded ellipses are then imported using DS9¹ and checked by eye for any remaining unmasked emission. If necessary, certain ellipses were adjusted manually (Figure 6.6).

6.3.4 Gridding Over the Core Radius

The CARGC morphology code includes a β -model (Equation 1.3.5) fit to the surface brightness profile, so that a background noise level can be estimated. In the Chandra version, the core radius of this β -model is a free parameter. However, their code failed at this point when run on XMM images (presumably due to the degraded spatial resolution). Therefore, the code was adapted to work with core radius as a fixed input parameter. Core radius was adjusted using a script so that 75 different values were tested per cluster. The choice of the best core radius was then made by eye-ball inspection (Figure 6.7). In future this could be improved by making this choice with a χ^2 test.

6.4 Searching for relaxed XCS-DR2 clusters

The XCS-DR2 cluster sample (Section 3) is the ideal place to look for objects suitable for future f_{gas} analysis. It is the largest X-ray galaxy cluster sample available to date. It has

¹<http://ds9.si.edu>

been processed in a consistent way, and all its data products are ready to use. Moreover, by including target clusters in the new XCS-DR2 catalogue, we have increased the number of high signal-to-noise cluster observations compared to XCS-DR1.

6.4.1 Selection of clusters for the morphology test

The CARGC morphology test is time consuming to apply, because several parts of it require human intervention, i.e. it cannot be fully scripted. Therefore, we have not applied it to all XCS-DR2 clusters. We have only applied it to clusters with XCS determined mean temperatures of $T_X > 4.5\text{keV}$ and that have XAPA defined centroids less than four arcminutes from the centre of the respective ObsID. The first cut was applied to mimic the CARGC analysis - they only included clusters with a Chandra temperature estimate of $T_X > 5\text{keV}$. We have lowered the threshold by 20% because of the known offset between the Chandra and XMM calibration (Schellenberger et al., 2015). The second cut was made to maximise the number of cluster targets in our analysis. Not only will this increase the signal to noise, compared to typical serendipitous detections, it restricts our analysis to the part of the field of view where the PSF is narrowest and best understood.

After these cuts, 342 XCS-DR2 clusters remain, in the redshift range $0.1 < z < 1.4$ (Figure 6.8). Of these, 197 yielded at least one set of p, a and s values, although the bootstrapping step only completed for 97. A thorough investigation into these failures has not yet taken place, however low signal to noise seems to be the most common reason.

6.4.2 Results

Of the 97 clusters that ran through the whole morphology test (including bootstrapping stage), 44 had a non zero probability of being relaxed, i.e. had p, a and s values greater than the thresholds in Table 6.1 in one or more of the 1,000 bootstrap realisations (Figure 6.9). Examples of relaxed and non relaxed clusters are shown in Figures 6.10 and 6.11. Of these, 21 had a greater than 50% chance of being relaxed (the criterion set by the CARGC team for Chandra images), with 16 having a probability greater than 90%.

Not all of the 21 clusters that passed the morphology test are new examples of relaxed clusters: 12 are already in the CARGC sample and included in the M14 analysis, see below. The remaining nine clusters have a redshift range of $0.08 < z < 0.26$. If any are subsequently shown to pass the morphology test using Chandra data, then they can be

included in future f_{gas} cosmology studies. A sample of just six new clusters with weak lensing and X-ray data can improve the f_{gas} cosmology accuracy by a factor of 0.82, see § 6.5.

Comparison of Chandra vs XMM morphology test results

Of the 97 clusters for which the test completed using XMM data, 32 had already been tested using Chandra data (frequently a given X-ray source will be observed as a target by both satellites). The test results for these 32 are consistent, i.e. the same 12 (20) were classed as (non-)relaxed. A comparison of the measured p , a and s values are shown in Figure 6.3. Typically XMM measures higher symmetry and alignment values, possibly due to the smoothing effect of the larger PSF.

6.5 Chandra Cycle 17 proposal

A collaboration between the XCS and CARGC teams resulted in a well received (but ultimately rejected) Cycle 17 Chandra proposal. The proposal requested Chandra follow-up for six of the nine relaxed cluster candidates uncovered by our XMM morphology analysis, with redshifts in the range $0.31 < z < 0.56$ (the remaining three were at lower redshifts and deemed to have little added value compared to the M14 sample which has a redshift range of $0.078 < z < 1.063$, of which 25 are in below $z=0.4$).

Total exposure times were estimated so that the Chandra images would contain sufficient signal to noise to be used for the f_{gas} cosmology test (Table 6.2). Specifically, the aim was to reach a statistical precision of 17% in f_{gas} in a shall spanning $0.8 - 1.2r_{2500}$. Two of the six had already been observed by Chandra, but for insufficient time to reach that precision.

In addition to high quality X-ray data, high quality weak lensing data are crucial to the f_{gas} (so that total masses can be measured). One of the six Chandra targets already has suitable multi-band photometry from DECam, and three others are approved targets for CFHT. DECam observations for the final two were requested in the proposal through the joint facilities arrangement between NOAO and Chandra.

The proposal, written by Adam Mantz, included a prediction for the improvement in the f_{gas} cosmology result from these six clusters: Ω_m results by 18% and by 11% on w

Table 6.2: XCS-DR2 clusters included in a Cycle 17 Chandra Proposal

Name	z	Current Exposure Time	Requested Exposure Time
SPT J054962	0.32	0	15 ks
SPT J023458	0.42	9 ks	25 ks
RX J024348	0.53	0	55 ks
MACS J0326+00	0.45	9	20 ks
MACS J2213+13	0.31	0	25 ks
MS 1241+1710	0.56	0	100 ks

(Figure 6.13).

6.6 Conclusions and Future Work

6.6.1 Conclusions

- When using the CARGC morphology test, XMM can classify relaxed clusters as well as Chandra.
- XCS has delivered a new list of relaxed massive clusters.
- The new XCS relaxed clusters can improve CARGC Ω_m results by 18% and on w by 11%.

6.6.2 Future Work

- Re-submit failed Chandra proposal.
- Re-run morphology code on stacked XMM data
- Run morphology code of off-axis XCS-DR2 clusters.
- Attempt to understand why the morphology fitting code failed to run to completion on some clusters.
- Run the code on all XCS-DR2 clusters to understand selection effects (e.g. for scaling relations)
- Run the code on simulated clusters.
- Test whether peakiness is the only necessary parameter.
- Process XMM observations using the ESAS package to create background maps.
- Create pipeline to measure gas masses for XCS-DR2 clusters.

- Attempt to fit cosmological parameters using XMM data and the f_{gas} test.

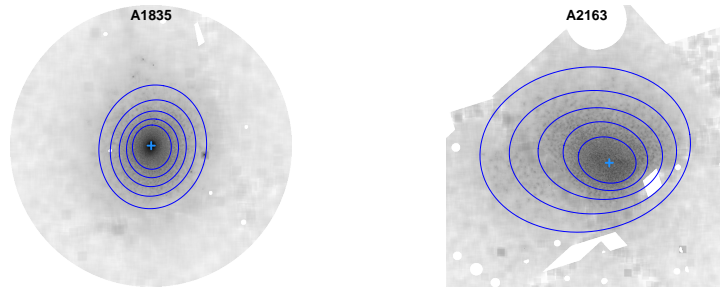


Figure 6.1: (Figures taken from M14) Chandra images clusters that have been run through the CARGC morphology test. Left: Abell 1835 (classified as relaxed). Right: Abell 2163 (classified as non-relaxed). Crosses show the global centres. Blue ellipses show the five fitted isophote levels. In the morphology test, the ‘alignment metric’ reflects how close the centres of these ellipses lie to one another, while the ‘symmetry metric’ reflects how well they agree with the global centre.

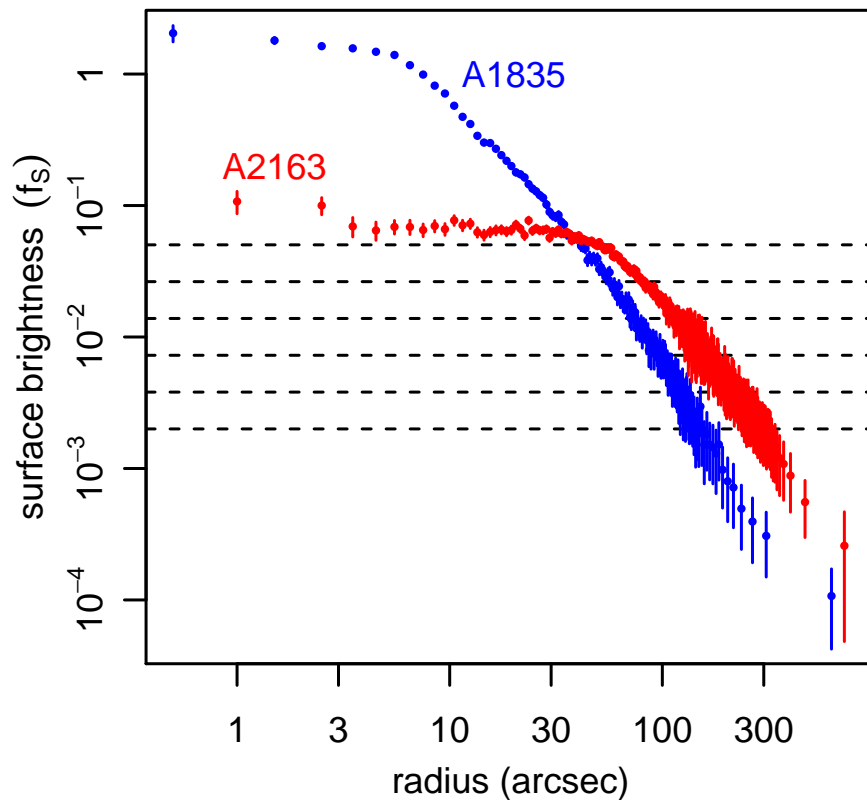


Figure 6.2: (Figure taken from M14) Surface brightness profiles for Abell 1835 and Abell 2163 (Chandra images shown in Figure 6.1), scaled according to Equation 6.3. Dashed lines correspond to the brightness levels defined in Equation 6.4 (the lowest level corresponds to $j = 0$). In the morphology test, the ‘peakiness metric’ depends on the average surface brightness in a circular aperture whose radius is given by the intersection of the observed profile with the highest level ($j = 5$).

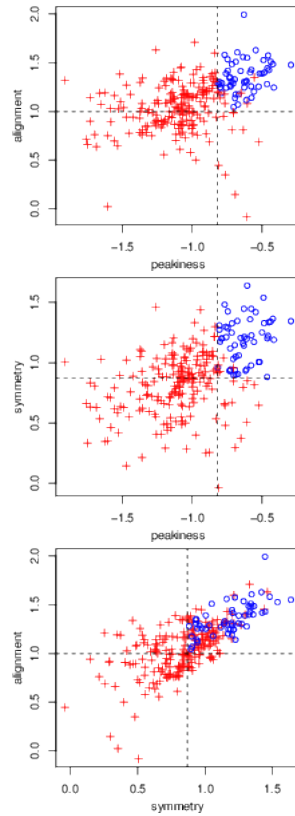


Figure 6.3: (Figure taken from M14) Results of the CARGC morphology test for all three metrics (peakiness, symmetry and alignment). Dashed lines show threshold cuts. Clusters that passed all three thresholds shown with blue points (the remainder are shown in red).

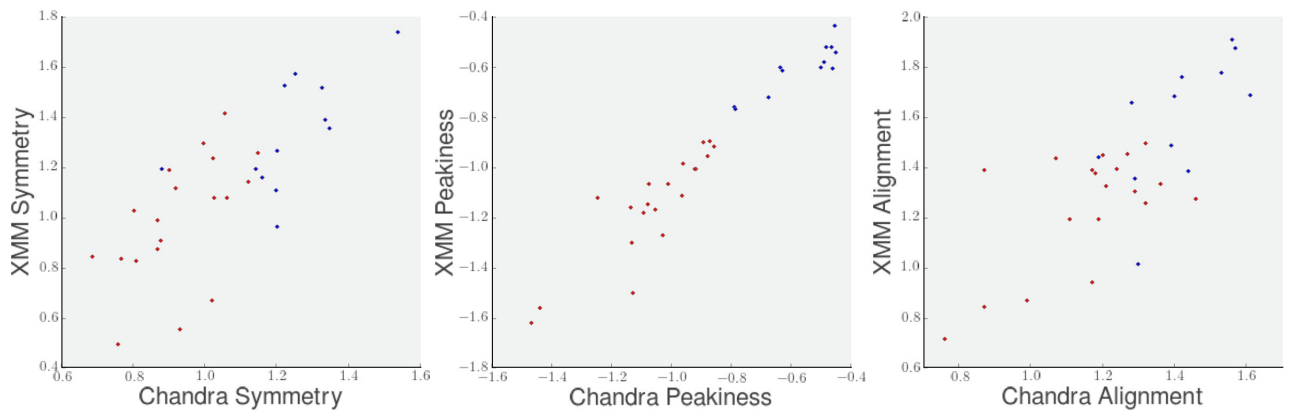


Figure 6.4: Comparison between SPA results found with Chandra and XMM. Clusters which passed morphology test shown in blue, those that failed shown in red.

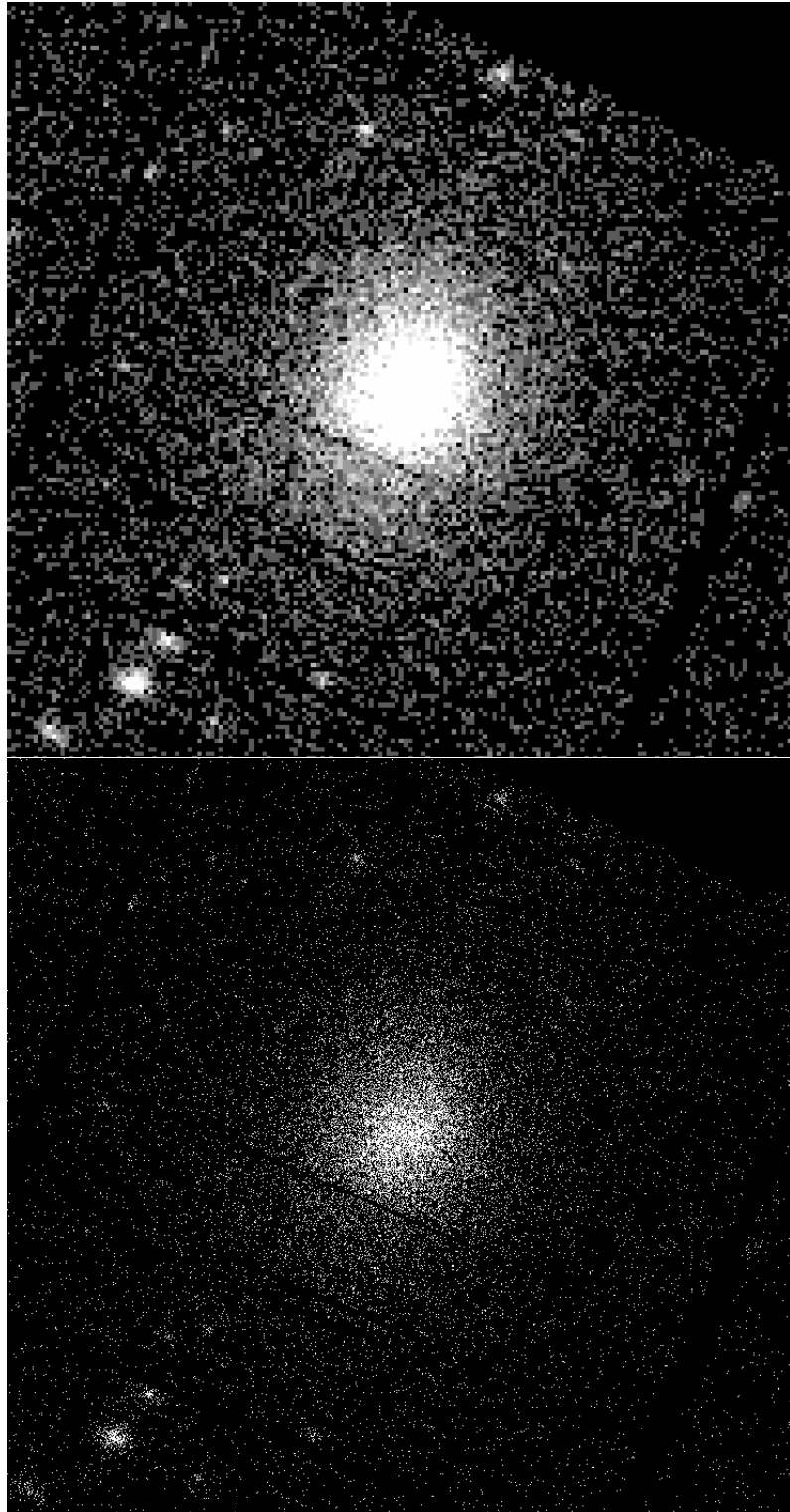


Figure 6.5: An XMM MOS image of an XCS-DR2 with two different pixel scales. Top: 4.35'' pixel scale (as used in XIP. Bottom: 1.1'' pixel scale (as used for the morphology test).

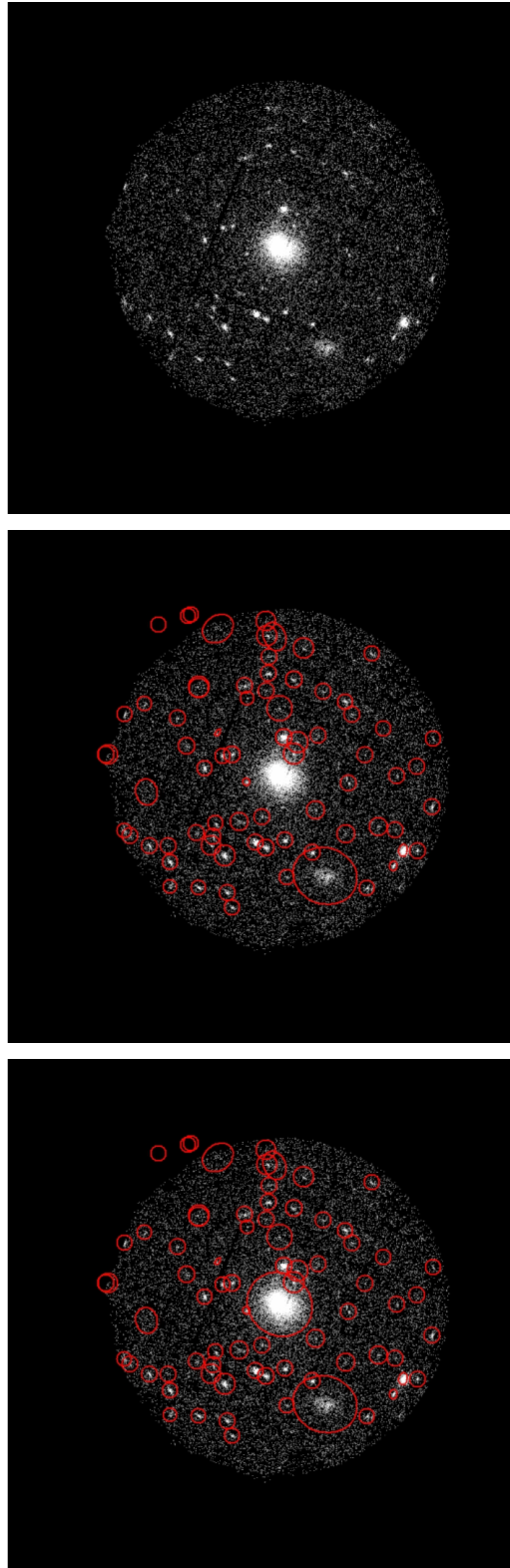


Figure 6.6: Preparation of an XMM MOS image for the morphology test. Top: MOS image of ObsID:0111000101. Middle: MOS image with XAPA source regions overlaid. Bottom: MOS image with adjusted source regions overlaid (areas inside these regions are masked during the morphology test). Note that the central cluster is not inside a ellipse (otherwise it would be itself masked during the test).

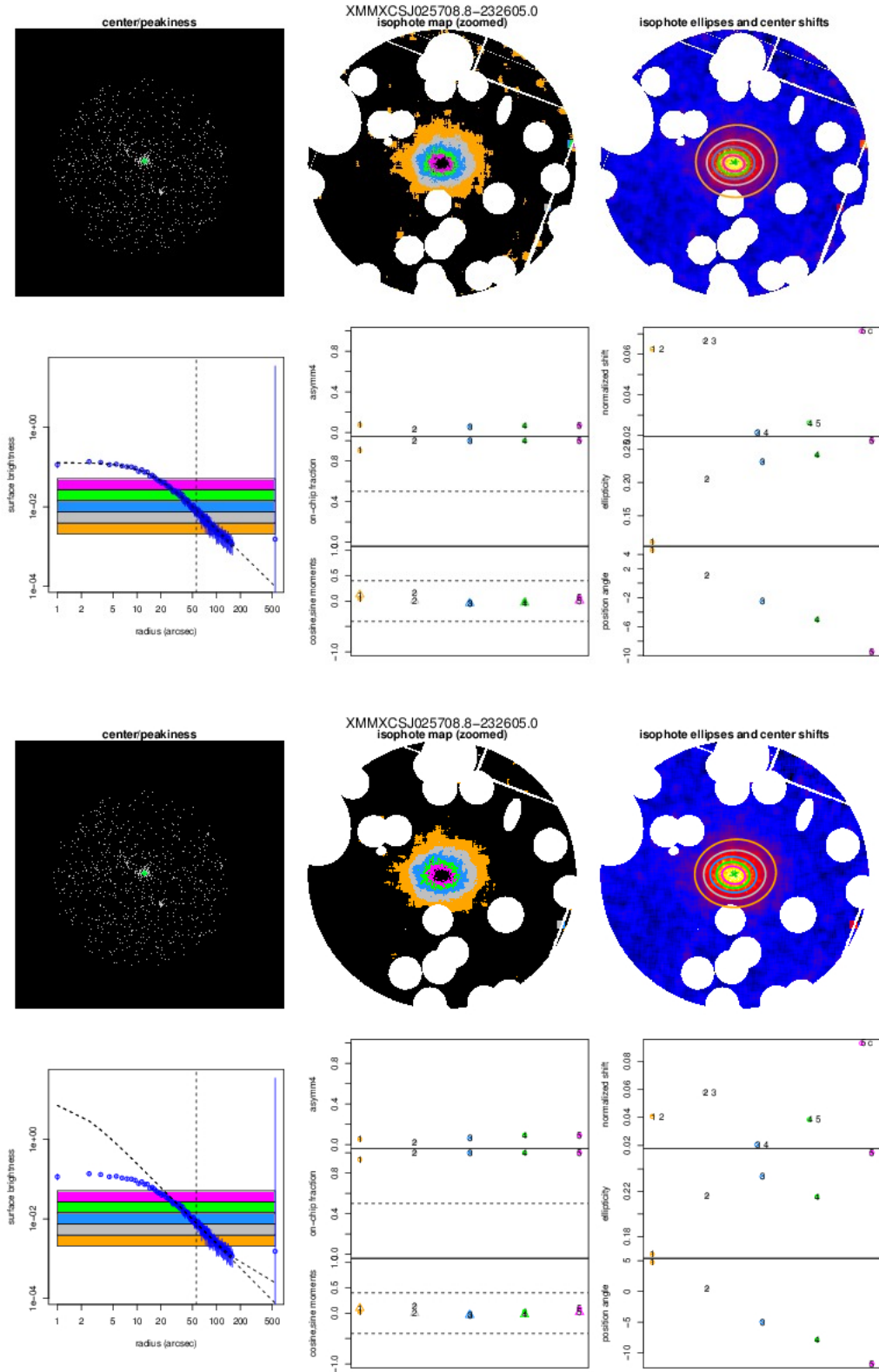


Figure 6.7: Morphology tests of a single cluster using two different core radius values as inputs. Top set (bottom left): the β -model fit (dashed line) lines up well with the surface brightness profile (blue points). Bottom set (bottom left): the β -model fit (dashed line) does not line up well with the surface brightness profile (blue points). Both sets (other figures): top left: the XMM image, top centre: the cluster region with mask applied and isophotes colour coded, top right: the cluster region with fitted isophote ellipses overlaid

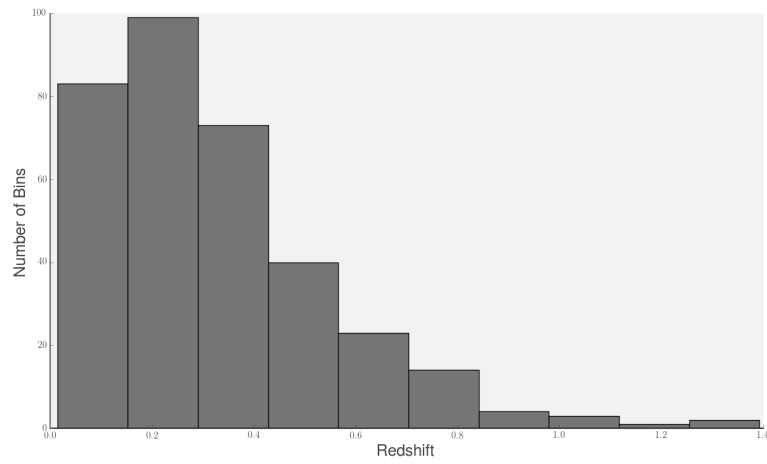
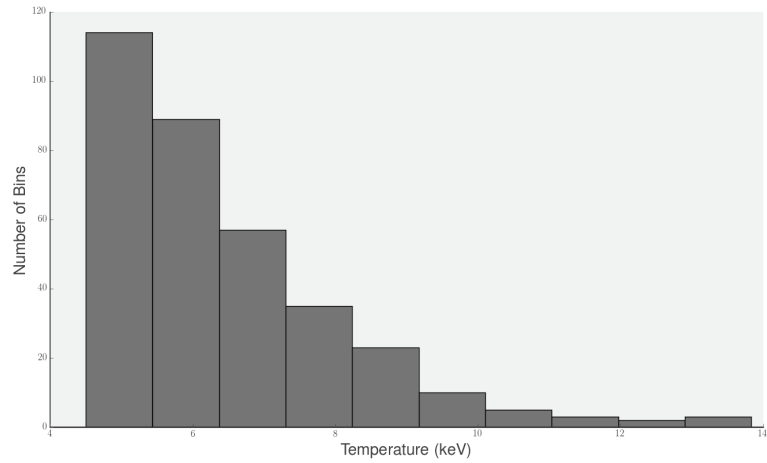


Figure 6.8: Distributions of temperature (top) and redshift (bottom) for the 342 XCS-DR2 clusters that were subjected to the morphology test.

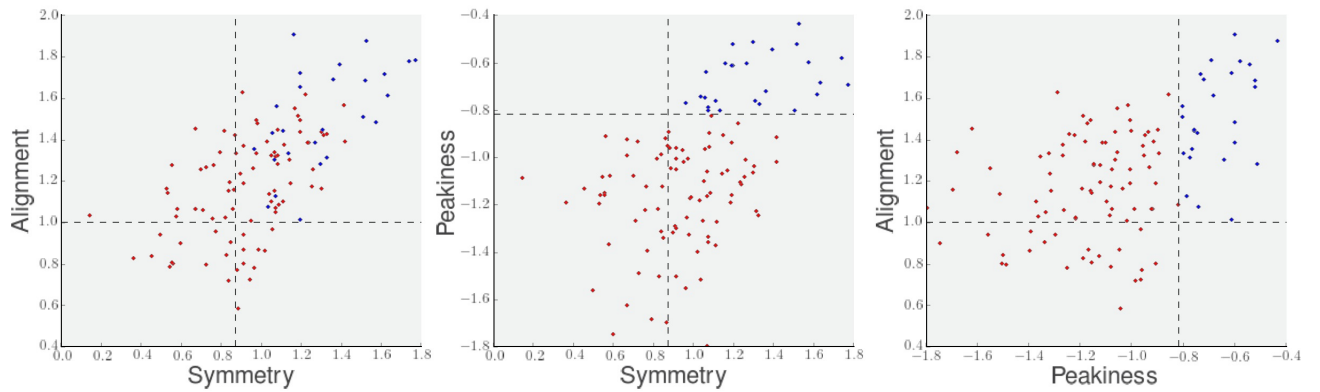


Figure 6.9: Morphology test results for 97 XCS-DR2 clusters. Objects that passed (failed) the morphology test are shown with blue (red) dots.

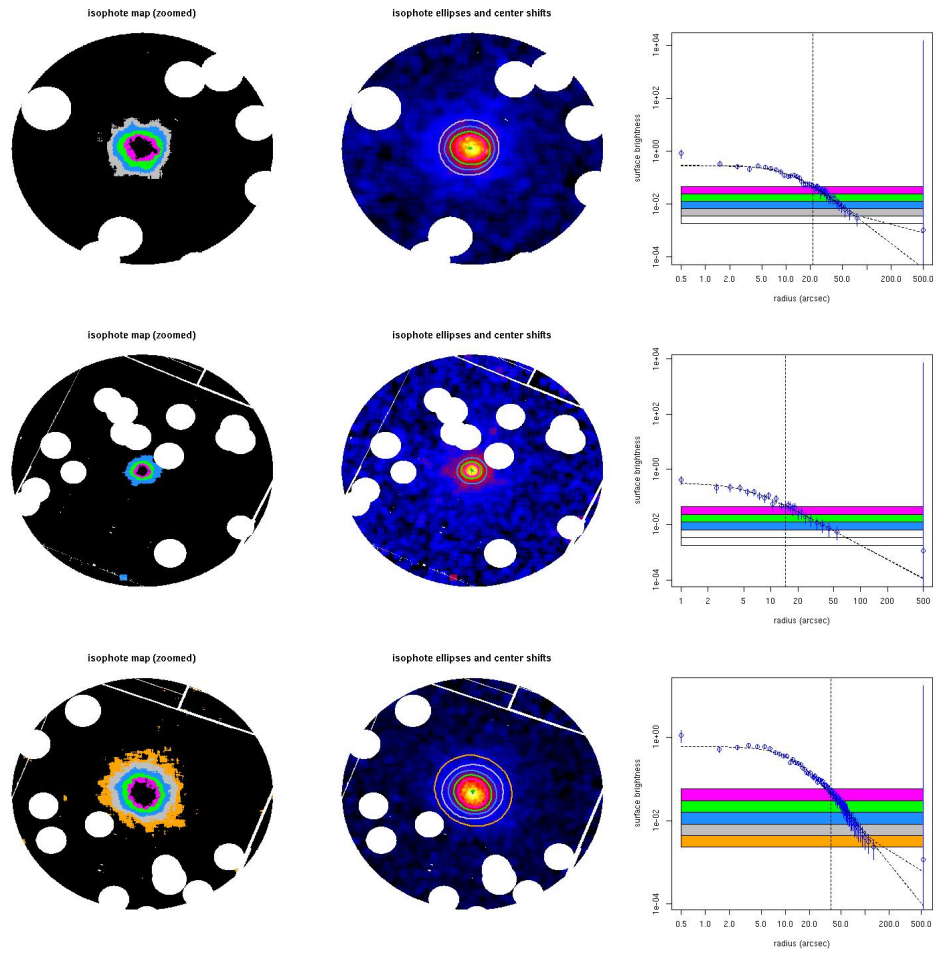


Figure 6.10: Examples of XCS-DR2 clusters classified as relaxed using the CARGC morphology test. Left: Isophote levels. Centre: Ellipses fit to isophote levels. Right: Surface brightness profile fitting.

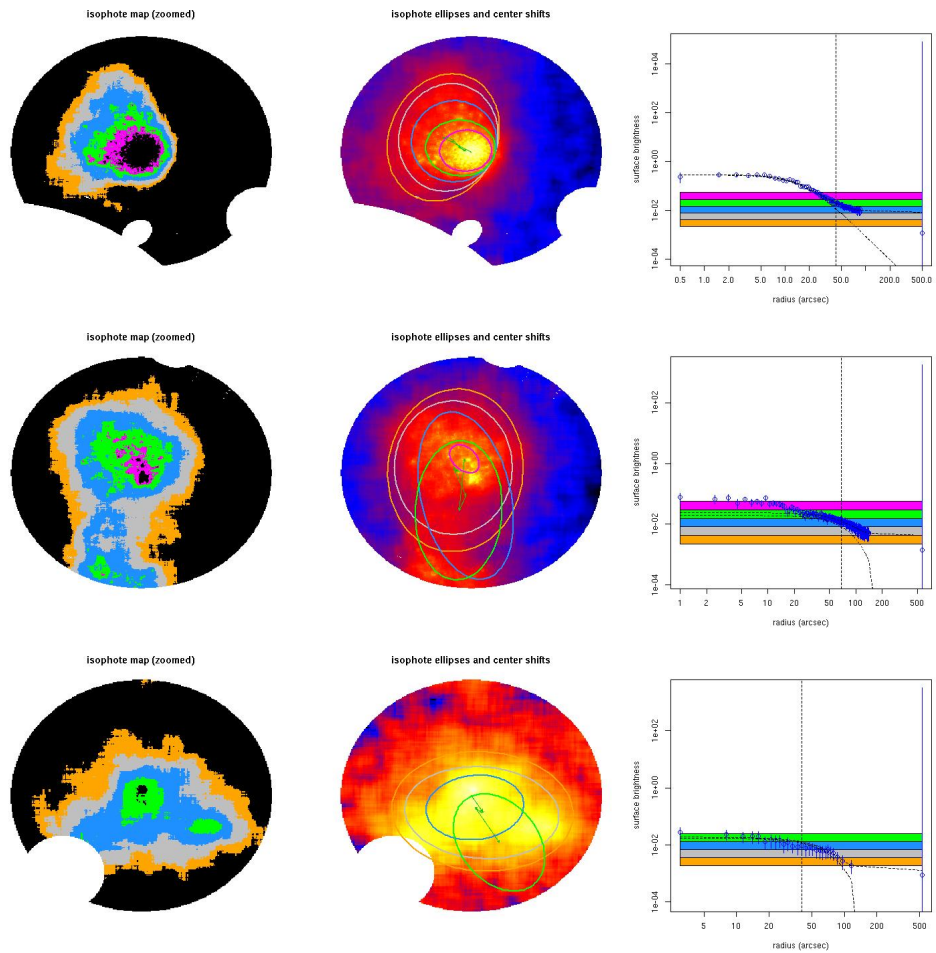


Figure 6.11: As Figure 6.10, but non-relaxed XCS-DR2 clusters.

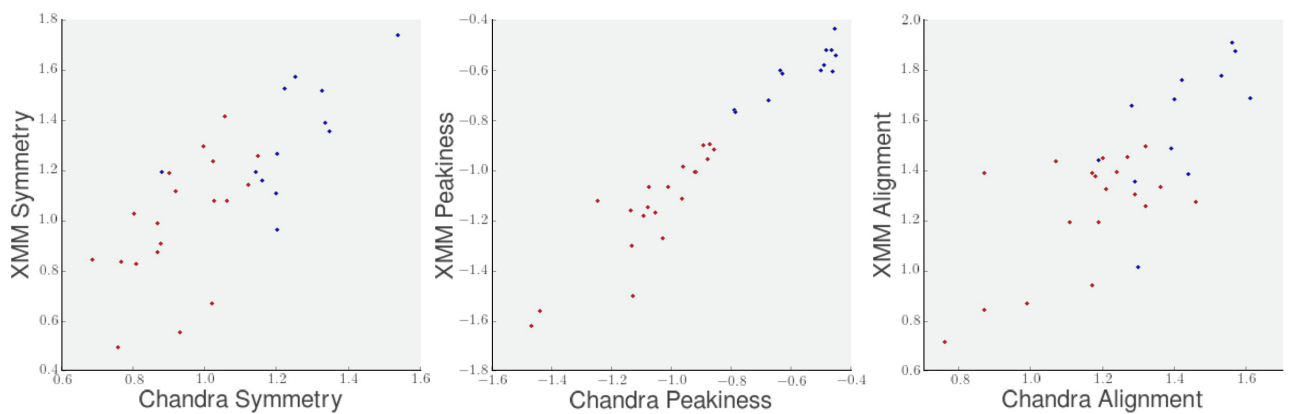


Figure 6.12: Comparison between the morphology metric values results found using Chandra (CARGC team analysis) and using XMM (our analysis) for 12 clusters in common between the sample. Clusters that passed (failed) the morphology test shown in blue (red).

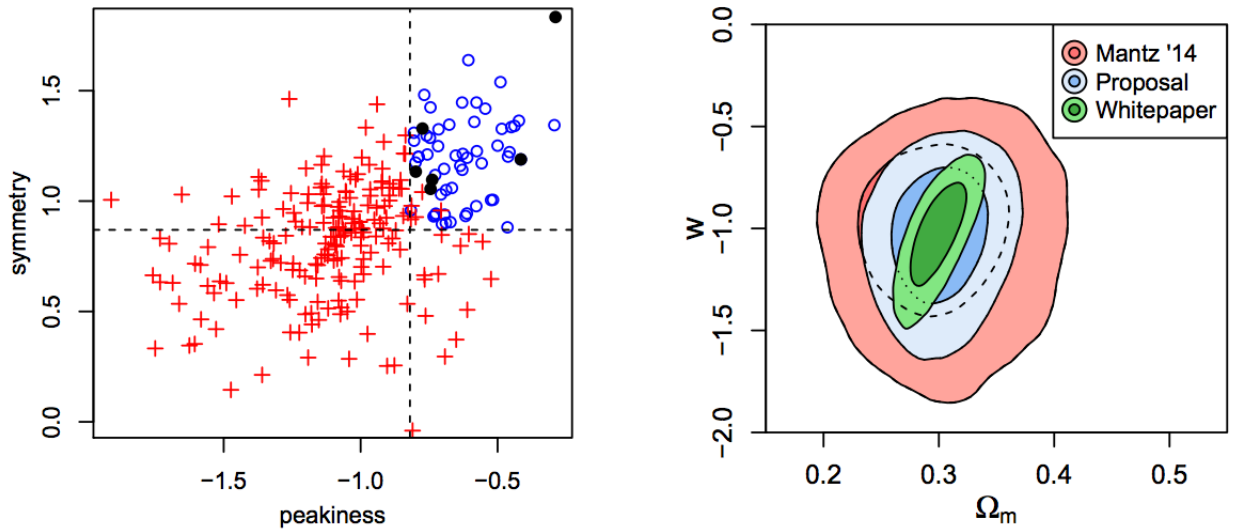


Figure 6.13: (Wording taken from the Chandra proposal) Left: Distribution of 2 of the 3 morphology statistics measured by M15 for clusters in the Chandra archive (relaxed clusters as blue circles and unrelaxed clusters as red crosses). Dashed lines indicate cuts used in the determination of relaxation. Our targets are shown as filled, black circles. We expect the XMM PSF to reduce the peakiness measurement somewhat; even without correcting for this effect, our targets pass the same morphological cuts as the Chandra-relaxed sample. Right: Constraints on flat constant- w models, showing the improvement over M14. The “Proposal” constraints are projections based on adding the 6 targets of this proposal, as well as Perseus (approved in AO16), to the M14 sample. Compared to the M14 uncertainties, the Ω_m constraint is improved by almost 20% by this proposal, while the w constraint is improved by $\sim 11\%$ by adding Perseus and an additional $\sim 11\%$ from this proposal. The “Whitepaper” contours are projections for an additional 44 clusters beyond this proposal (Allen et al., 2013), plus Perseus (which was not included in the original white paper).

Chapter 7

Conclusions

In this work we studied the X-ray properties of galaxy clusters. Galaxy clusters are astronomical laboratories that allow us to explore a plethora of baryonic, non-baryonic and cosmological processes. Clusters are the smallest objects that are large enough to contain a representative amount of the materials that make up the universe, and the largest objects small enough to be gravitationally collapsed - allowing us to use relatively simple physics to understand their masses.

Galaxy clusters undergo complex processes which can obscure information about their contents. This can be overcome by a two-pronged strategy of using the deepest observations of individual objects to find evidence of clusters diverging from theory, fitting more complex models to this data, and then testing the results against larger samples of clusters with shallower observations.

The ability to fit new models of galaxy cluster formation is hampered by inconsistent results between different X-ray satellites and between those individual satellite's instruments. Researchers must understand the tools they use to study clusters better before a clearer picture of galaxy cluster formation can emerge.

The focus of much of the work done on galaxy clusters using modern X-ray satellites (XMM and Chandra) has been to study small samples of well observed galaxy clusters and test our assumptions of cluster formation, and thereby produce more precise models. There are few X-ray cluster catalogues and none have more than 1,000 objects.

In Chapters 2-3, we showed how we produced a new catalogue of galaxy clusters, XCS-DR2. This catalogue covers the entire XMM extra-galactic footprint and contains the most

cluster detections of any X-ray cluster sample to date (1,177 firm cluster identifications and 7,129 preliminary cluster detections). XCS-DR2 contains more high- z clusters (222 clusters at $z \geq 0.8$) than any previous cluster catalogue.

Many clusters in XCS-DR2 have been observed more than once by XMM. Some of these clusters have been seen under changed conditions, e.g. they may be at different detector positions or different observations used alternative filter. Most of the XCS-DR2 clusters are observed using more than one instrument (i.e. MOS1, MOS2, and PN) at a time. Galaxy clusters evolve gradually over time, so their spectral properties should be the same in different observations. Any changes we observe that are correlated with instrument set-up, should, therefore, be a consequence of instrumental mis-calibration, a poor fitting procedure, or statistical uncertainty. The size of XCS-DR2 should help to overcome the last of these issues.

We fit the spectral properties of the XCS-DR2 catalogue, using every available spectra for each source. XCS-DR2 contains T_X and L_X measurements for 4,987 clusters. This is ten times larger than the next largest catalogue of spectral measurements. An important next step was to confirm that XMM is sufficiently well calibrated between observations to produce spectral fits with data from multiple observations.

In Chapter 4 we demonstrated that there appears to be no significant spectral differences between observations carried out at different off-axis angles, and no strong evidence that the choice of filter affects results. The single largest uncertainty found with XMM temperature measurements is the offsets between different instruments - this demonstrates the need for better instrumental calibration. XCS-DR2 shows that combining different spectra for a cluster (so long as individually they meet a minimum threshold of producing a spectral fit within sensible bounds) will produce as precise a measurement as when the same observation is done with a single long exposure.

XCS luminosity-temperature scaling relations previously showed a negative evolution relative to predictions made with self-similar assumptions. In Chapter 5 we fit new scaling relations, with data from more observations and a well tested spectral fitting method. This new scaling relation shows an evolution consistent with self-similarity. Similar results were found when comparing X-ray and SZ-mass proxies.

Finally, in Chapter 6, we demonstrated that at low redshifts ($z \leq 0.3$), XMM is as capable

of finding relaxed clusters as Chandra. A new sample of higher redshift ($z > 0.3$) clusters have been classified as relaxed using XMM. If this sample is observed by Chandra, and shown to be accurate, then the f_{gas} cosmological parameter fittings can be improved by 12%.

7.1 Future Work

Work is required to understand the differences between the XCS-DR1 and XCS-DR2 cluster candidate lists (e.g. why do some new reductions fail to run through XAPA, have missing detector images, show increased noise levels). This analysis will be expanded to examine all clusters previously detected in XMM images by any group, which don't appear in the XCS-DR2 cluster candidate list.

XCS will download and process XMM observations that have become publicly available since the last large data download. We will continue to make incremental downloads to include future observations. XCS will submit Chandra and XMM proposals to acquire deeper data on serendipitously detected clusters. A proposal will be submitted to create a new XMM mosaic covering deep DES fields.

The XAPA source detection pipeline will be run with a larger ellipse size to avoid breaking the largest sources into several smaller sources. We will integrate the latest XMM PSF model into XAPA. In future XAPA will be run on stacked XMM observations.

The most important next step for XCS is to calculate the survey selection function. The selection function describes the probability of detecting a galaxy cluster given its surface brightness profile. The selection function can be used to weight the properties of the clusters we detect so that we can represent the real underlying distribution of clusters from our biased sample.

A new XCS cluster zoo will be carried out including public data from SDSS and Megacam, as well as proprietary data from DES. Statistically useful subsamples will be used to test the optical selection function (for instance by using areas which overlap deep and shallow optical data).

In the future, additional publicly available spectroscopic data for cluster galaxies will become available. This new data will include new imaging from LSST and Hyper Supreme-

Cam. The XCS cluster sample will be expanded to higher redshifts by using infra-red data.

Almost half of the XCS-DR2 preliminary cluster detections have a redshift estimate but no spectral fit. A new pipeline will be developed to estimate luminosity when no temperature could be fit.

Cross-satellite calibration tests will be run using data from the Chandra archive. XCS can then carry out similar calibration tests for the future eRosita and Athena missions.

A key aim of XCS is to fit cosmology. For this, XCS needs to understand the scaling relations between X-ray mass proxies and the real mass of the cluster. This will be done using the previously calculated selection function and stacked weak lensing. To account for evolution, the scaling relation should be fit over as large a redshift range as possible. Once the scaling relations between mass and X-ray observables is known a cluster number function with mass and redshift can be fit. An LT scaling relation will be fit using the whole XCS-DR2 sample, and the XCS-DR2 serendipitous sample.

We will test the scaling relation between Y_{SZ} and T_X/L_X using Planck results. The Y_{SZ} measurements will be improved when SZ measurements are recalculated within R_{500} (rather than extrapolating out using a profile). X-ray-SZ selection effects will be estimated.

The XCS-DR2 catalogue can be expanded to include several other measurements, notably gas mass, Y_X , and hydrostatic mass. These additional measurements will be useful for testing baryonic physics (e.g. model selection for AGN feedback) and making comparisons between X-ray and SZ-mass proxies.

XCS will provide support to fit galaxy cluster number count cosmology with the Dark Energy Survey (DES). DES will optically detect $\sim 100,000$ galaxy clusters, and stacked weak lensing in richness bins will provide a richness-mass scaling relation. Clusters will have poor individual weak lensing mass measurements (30% error) but when stacked the total mass measurement will be precise. The scaling relation between weak-lensing mass and richness will not provide strong constraints on the scatter between richness and mass. X-ray and SZ mass estimates will have smaller errors per cluster (but may have systematic offsets and biases) so DES will be infer the scatter in the richness-mass scaling relation using X-ray and SZ-Richness scaling relations. The X-ray-richness scaling relation will be produced by XCS.

Cosmological parameters can be fit using XMM data and the f_{gas} test. The XCS relaxed cluster sample will be expanded by re-running the morphology code on stacked XMM data and including off-axis XCS-DR2 clusters.

The largest errors in X-ray measurements are due to instrumental uncertainty (e.g the offset in temperature measurements between XMM and Chandra) and uncertainty caused by poor assumptions (e.g that clusters are in hydrostatic equilibrium). A drastic retooling may be needed to solve these problems. In future X-ray astronomers could turn to Bayesian techniques and deep observations of galaxy clusters to measure the uncertainty in X-ray satellites. A strong prior should be used to force the two measured temperatures to be the same while leaving the calibration to be fit as a set of free variables (as opposed to the usual practices of leaving the calibration of clusters fixed and the temperature is fit). It should be noted that this will find consistent but not necessarily true results. Additional calibration between X-ray masses, found using the new calibration, and weak lensing masses will be needed to find the correct absolute calibration.

Once the uncertainty in calibration is understood X-ray temperatures and luminosities should also be fit in a Bayesian manner. Temperature and luminosity errors are likely to be correlated; their full joint-posterior distribution should, therefore, be used when measuring X-ray luminosity-temperature scaling relations.

Bibliography

Abell, G. O. 1958, , 3, 211

Abell, G. O. 1959, Leaflet of the Astronomical Society of the Pacific, 8, 121

Abell, G. O., Corwin, H. G., Jr., & Olowin, R. P. 1989, , 70, 1

Adami, C., Ulmer, M. P., Romer, A. K., et al. 2000, , 131, 391

Adami, C., Mazure, A., Pierre, M., et al. 2011, , 526, A18

Ahn, C. P., Alexandroff, R., Allende Prieto, C., et al. 2014, , 211, 17

Alam, S., Albareti, F. D., Allende Prieto, C., et al. 2015, , 219, 12

Allen, S. W., Schmidt, R. W., & Fabian, A. C. 2001, , 328, L37

Allen, S. W., Schmidt, R. W., & Fabian, A. C. 2002, , 334, L11

Allen, S. W., Schmidt, R. W., Ebeling, H., Fabian, A. C., & van Speybroeck, L. 2004, , 353, 457

Allen, S. W., Evrard, A. E., & Mantz, A. B. 2011, , 49, 409

Allen, S. W., Mantz, A. B., Morris, R. G., et al. 2013, arXiv:1307.8152

Allgood, B., Flores, R. A., Primack, J. R., et al. 2006, , 367, 1781

Altieri B., Chen B., Gabriel C., Gondoin P., Lammers U.,Lumb D., Kirsch. 2004, Technical Report XMM-PS-GM- 20 Issue 3.1, XMM-Newton Calibration Access and Data Handbook. ESA

Andersson, K., Benson, B. A., Ade, P. A. R., et al. 2011, , 738, 48

Applegate, D. E., von der Linden, A., Kelly, P. L., et al. 2014, , 439, 48

Arnaud, K. A. 1996, Astronomical Data Analysis Software and Systems V, 101, 17

- Arnaud, M., Pointecouteau, E., & Pratt, G. W. 2005, , 441, 893
- Bardeen, J. M., Bond, J. R., Kaiser, N., & Szalay, A. S. 1986, , 304, 15
- Barkhouse, W. A., Green, P. J., Vikhlinin, A., et al. 2006, , 645, 955
- Battaglia, N., Bond, J. R., Pfrommer, C., & Sievers, J. L. 2013, , 777, 123
- Becker, M. R., McKay, T. A., Koester, B., et al. 2007, , 669, 905
- Benson, B. A., de Haan, T., Dudley, J. P., et al. 2013, , 763, 147
- Berlind, A. A., Frieman, J., Weinberg, D. H., et al. 2006, , 167, 1
- Birkinshaw, M., Gull, S. F., & Hardebeck, H. 1984, , 309, 34
- Blackburn, J. K. 1995, *Astronomical Data Analysis Software and Systems IV*, 77, 367
- Blanton, E. L., Gregg, M. D., Helfand, D. J., Becker, R. H., & White, R. L. 2003, , 125, 1635
- Bleem, L. E., Stalder, B., de Haan, T., et al. 2015, , 216, 27
- Böhringer, H., Schuecker, P., Guzzo, L., et al. 2001, , 369, 826
- Boehringer, H., Collins, C. A., Guzzo, L., et al. 2001, arXiv:astro-ph/0106243
- Böhringer, H., Collins, C. A., Guzzo, L., et al. 2002, , 566, 93
- Böhringer, H., Schuecker, P., Guzzo, L., et al. 2004, , 425, 367
- Bonamente, M., Joy, M., LaRoque, S. J., et al. 2008, , 675, 106
- Borgani, S., Rosati, P., Tozzi, P., & Norman, C. 1999, , 517, 40
- Borgani, S., Rosati, P., Tozzi, P., et al. 2001, , 561, 13
- Borgani, S. 2008, *A Pan-Chromatic View of Clusters of Galaxies and the Large-Scale Structure*, 740, 287
- Bregman, J. N. 2007, , 45, 221
- Bremer, M. N., Valtchanov, I., Willis, J., et al. 2006, , 371, 1427
- Brinkman, A., Aarts, H., den Boggende, A., et al. 1998, *Science with XMM*, 2
- Buote, D. A., & Tsai, J. C. 1996, , 458, 27

- Burenin, R. A., Vikhlinin, A., Hornstrup, A., et al. 2007, , 172, 561
- Cavaliere, A., & Fusco-Femiano, R. 1976, , 49, 137
- Cavaliere, A., Danese, L., & de Zotti, G. 1979, , 75, 322
- Carlstrom, J. E., Holder, G. P., & Reese, E. D. 2002, , 40, 643
- Cash, W. 1979, , 228, 939
- Clerc, N., Pierre, M., Pacaud, F., & Sadibekova, T. 2012, , 423, 3545
- Clerc, N., Sadibekova, T., Pierre, M., et al. 2012, , 423, 3561
- Clerc, N., Adami, C., Lieu, M., et al. 2014, , 444, 2723
- Collier, M., Snowden, S., Moore, T., & Kuntz, K. 2004, 35th COSPAR Scientific Assembly, 35, 3575
- Collins, C. A., Guzzo, L., Böhringer, H., et al. 2000, , 319, 939
- Collins, C. A., Stott, J. P., Hilton, M., et al. 2009, , 458, 603
- Cooke, R. J., Pettini, M., Jorgenson, R. A., Murphy, M. T., & Steidel, C. C. 2014, , 781, 31
- Cowie, L. L., & Binney, J. 1977, , 215, 723
- Crawford, C. S., Allen, S. W., Ebeling, H., Edge, A. C., & Fabian, A. C. 1999, , 306, 857
- Croston, J. H., Hardcastle, M. J., & Birkinshaw, M. 2005, , 357, 279
- de Bernardis, P., Ade, P. A. R., Bock, J. J., et al. 2002, , 564, 559
- Dickey, J. M., & Lockman, F. J. 1990, , 28, 215
- Donahue, M., Voit, G. M., Mahdavi, A., et al. 2014, , 794, 136
- Dornier Satellitensysteme GmbH, http://xmm.esac.esa.int/external/xmm_user_support/documentation/uhb_2.2/img298.gif
- Dornier Satellitensysteme GmbH, http://xmm.esac.esa.int/external/xmm_user_support/documentation/technical/Mirrors/Mirrors.jpg
- Doroshkevich, A. G. 1970, *Astrofizika*, 6, 581
- Dunkley, J., Hlozek, R., Sievers, J., et al. 2011, , 739, 52

- Dunn, R. J. H., & Fabian, A. C. 2006, , 373, 959
- Dunn, R. J. H., & Fabian, A. C. 2008, , 385, 757
- Ebeling, H., Edge, A. C., Fabian, A. C., et al. 1997, , 479, L101
- Ebeling, H., Edge, A. C., Böhringer, H., et al. 1998, , 301, 881
- Ebeling, H., Edge, A. C., Allen, S. W., et al. 2000, , 318, 333
- Ebeling, H., Edge, A. C., & Henry, J. P. 2001, , 553, 668
- Eckert, D., Molendi, S., & Paltani, S. 2011, , 526, A79
- Edge, A. C., & Stewart, G. C. 1991, , 252, 414
- Ettori, S., Tozzi, P., Borgani, S., & Rosati, P. 2004, , 417, 13
- Fabian, A. C., & Nulsen, P. E. J. 1977, , 180, 479
- Fassbender, R., Böhringer, H., Lamer, G., et al. 2008, , 481, L73
- Fassbender, R., Böhringer, H., Nastasi, A., et al. 2011, *New Journal of Physics*, 13, 125014
- Fassbender, R., Nastasi, A., Böhringer, H., et al. 2011, , 527, L10
- Finoguenov, A., Tanaka, M., Cooper, M., et al. 2015, , 576, A130
- Foley, R. J., Andersson, K., Bazin, G., et al. 2011, , 731, 86
- Freeman, P. E., Kashyap, V., Rosner, R., & Lamb, D. Q. 2002, , 138, 185
- Gabriel, C., Denby, M., Fyfe, D. J., et al. 2004, *Astronomical Data Analysis Software and Systems (ADASS) XIII*, 314, 759
- Gerdes, D. W., Sypniewski, A. J., McKay, T. A., et al. 2010, , 715, 823
- Giacconi, R., Kellogg, E., Gorenstein, P., Gursky, H., and Tananbaum, H. 1971, *ApJ*, 165, L27
- Gioia, I. M., Maccacaro, T., Schild, R. E., et al. 1990, , 72, 567
- Gioia, I. M., & Luppino, G. A. 1994, , 94, 583
- Gladders, M. D., & Yee, H. K. C. 2000, , 120, 2148
- Guzzo, L., Schuecker, P., Böhringer, H., et al. 2009, , 499, 357

- Gwyn, S. D. J. 2012, , 143, 38
- Henry, J. P., Gioia, I. M., Maccacaro, T., et al. 1992, , 386, 408
- Hallman, E. J., & Jeltema, T. E. 2011, , 418, 2467
- Hansen, S. M., McKay, T. A., Wechsler, R. H., et al. 2005, , 633, 122
- Hansen, S. M., Sheldon, E. S., Wechsler, R. H., & Koester, B. P. 2009, , 699, 1333
- Hao, J., McKay, T. A., Koester, B. P., et al. 2010, , 191, 254
- Harrison, C. D., Miller, C. J., Richards, J. W., et al. 2012, , 752, 12
- Herschel, W, 1811. Philosophical Transactions of the Royal Society of London, Vol. CI (101)
- Hickox, R. C., & Markevitch, M. 2007, , 661, L117
- Hilton, M., Collins, C. A., Stanford, S. A., et al. 2007, , 670, 1000
- Hilton, M., Stanford, S. A., Stott, J. P., et al. 2009, , 697, 436
- Hilton, M., Lloyd-Davies, E., Stanford, S. A., et al. 2010, , 718, 133
- Hilton, M., Romer, A. K., Kay, S. T., et al. 2012, , 424, 2086
- Hood, R 2014, PhD Thesis
- Hood,R, Mann, B
- Hoyle, B., Jimenez, R., & Verde, L. 2011, , 83, 103502
- Hsu, L.-Y., Ebeling, H., & Richard, J. 2013, , 429, 833
- Israel, H., Erben, T., Reiprich, T. H., et al. 2010, , 520, A58
- Israel, H., Erben, T., Reiprich, T. H., et al. 2012, , 546, A79
- Israel, H., Reiprich, T. H., Erben, T., et al. 2014, , 564, A129
- Israel, H., Schellenberger, G., Nevalainen, J., Massey, R., & Reiprich, T. H. 2015, , 448, 814
- James, F., & Roos, M. 1975, Computer Physics Communications, 10, 343
- Johnston, D. E., Sheldon, E. S., Tasitsiomi, A., et al. 2007, , 656, 27

- Johnston, D. E., Sheldon, E. S., Wechsler, R. H., et al. 2007, arXiv:0709.1159
- Jones, C., & Forman, W. 1992, NATO Advanced Science Institutes (ASI) Series C, 366, 49
- Kay, S. T., Thomas, P. A., Jenkins, A., & Pearce, F. R. 2004, , 355, 1091
- Kay, S. T., da Silva, A. C., Aghanim, N., et al. 2007, , 377, 317
- Kelly, P. L., von der Linden, A., Applegate, D. E., et al. 2014, , 439, 28
- Kessler, R., Becker, A. C., Cinabro, D., et al. 2009, , 185, 32
- King, I. 1962, , 67, 274
- Koester, B. P., McKay, T. A., Annis, J., et al. 2007, , 660, 239
- Koester, B. P., McKay, T. A., Annis, J., et al. 2007, , 660, 221
- Kotov, O., & Vikhlinin, A. 2005, , 633, 781
- Kravtsov, A. V., Vikhlinin, A., & Nagai, D. 2006, , 650, 128
- Kuntz, K. D., & Snowden, S. L. 2001, , 554, 684
- Lancaster, K., Birkinshaw, M., Gawroński, M. P., et al. 2011, , 418, 1441
- Larson, D., Dunkley, J., Hinshaw, G., et al. 2011, , 192, 16
- LaRoque, S. J., Joy, M., Carlstrom, J. E., et al. 2003, , 583, 559
- Lee, J., Springel, V., Pen, U.-L., & Lemson, G. 2008, , 389, 1266
- Liddle, A. R., Viana, P. T. P., Romer, A. K., & Mann, R. G. 2001, , 325, 875
- Lintott, C. J., Schawinski, K., Slosar, A., et al. 2008, , 389, 1179
- Liu, T., Tozzi, P., Tundo, E., et al. 2015, , 216, 28
- Lloyd-Davies, E. J., Romer, A. K., Mehrrens, N., et al. 2011, , 418, 14
- Lumb, D. H., Bartlett, J. G., Romer, A. K., et al. 2004, , 420, 853
- Mantz, A., Allen, S. W., Ebeling, H., & Rapetti, D. 2008, , 387, 1179
- Mantz, A., Allen, S. W., Ebeling, H., Rapetti, D., & Drlica-Wagner, A. 2010, , 406, 1773
- Mantz, A. B., Abdulla, Z., Carlstrom, J. E., et al. 2014, , 794, 157

- Mantz, A. B., Allen, S. W., Morris, R. G., et al. 2014, , 440, 2077
- Mantz, A. B., Allen, S. W., Morris, R. G., et al. 2015, , 449, 199
- Markevitch, M., & Vikhlinin, A. 2007, , 443, 1
- Marriage, T. A., Acquaviva, V., Ade, P. A. R., et al. 2011, , 737, 61
- Mason, K. O., Breeveld, A., Much, R., et al. 2001, , 365, L36
- Mathews, W. G., Faltenbacher, A., & Brighenti, F. 2006, , 638, 659
- Maughan, B. J., Jones, L. R., Ebeling, H., & Scharf, C. 2006, , 365, 509
- Maughan, B. J. 2007, , 668, 772
- Maughan, B. J., Giles, P. A., Randall, S. W., Jones, C., & Forman, W. R. 2012, , 421, 1583
- Maughan, B. J. 2014, , 437, 1171
- McNamara, B. R., Wise, M., Nulsen, P. E. J., et al. 2000, , 534, L135
- Mehrtens, N., Romer, A. K., Hilton, M., et al. 2012, , 423, 1024
- Menanteau, F., González, J., Juin, J.-B., et al. 2010, , 723, 1523
- Messier, C, 1784, *Connaissance des Temps*, Paris
- Metropolis, N., Rosenbluth, A. W., Rosenbluth, M. N., Teller, A. H., & Teller, E. 1953, , 21, 1087
- Mewe, R., Lemen, J. R., & van den Oord, G. H. J. 1986, , 65, 511
- Miller, C. J., Nichol, R. C., Reichart, D., et al. 2005, , 130, 968
- Mitchell, R. J., Ives, J. C., & Culhane, J. L. 1977, , 181, 25P
- Mohr, J. J., Evrard, A. E., Fabricant, D. G., & Geller, M. J. 1995, , 447, 8
- Morandi, A., Ettori, S., & Moscardini, L. 2007, , 379, 518
- Mullis, C. R., Rosati, P., Lamer, G., et al. 2005, , 623, L85
- Navarro, J. F., Frenk, C. S., & White, S. D. M. 1996, , 462, 563
- Nevalainen, J., David, L., & Guainazzi, M. 2010, , 523, A22

- Nichol, R. C., Romer, A. K., Holden, B. P., et al. 1999, , 521, L21
- Ochsenbein, F., Bauer, P., & Marcout, J. 2000, , 143, 23
- Pacaud, F., Pierre, M., Adami, C., et al. 2007, , 382, 1289
- Page, M. J., Brindle, C., Talavera, A., et al. 2012, , 426, 903
- Peterson, J. R., Paerels, F. B. S., Kaastra, J. S., et al. 2001, , 365, L104
- Pierre, M., Pacaud, F., Duc, P.-A., et al. 2006, , 372, 591
- Pierre, M., Pacaud, F., Juin, J. B., et al. 2011, , 414, 1732
- Planck Collaboration, Ade, P. A. R., Aghanim, N., et al. 2011, , 536, A8
- Planck Collaboration, Aghanim, N., Arnaud, M., et al. 2011, , 536, A9
- Planck Collaboration, Aghanim, N., Arnaud, M., et al. 2011, , 536, A10
- Planck Collaboration, Ade, P. A. R., Aghanim, N., et al. 2011, , 536, A11
- Planck Collaboration, Aghanim, N., Arnaud, M., et al. 2011, , 536, A12
- Planck Collaboration, Aghanim, N., Arnaud, M., et al. 2011, , 536, A26
- Planck Collaboration, Ade, P. A. R., Aghanim, N., et al. 2013, , 550, A129
- Planck Collaboration, Ade, P. A. R., Aghanim, N., et al. 2013, , 550, A131
- Planck Collaboration, Ade, P. A. R., Aghanim, N., et al. 2014, arXiv:1407.6663
- Planck Collaboration, Ade, P. A. R., Aghanim, N., et al. 2014, , 571, A20
- Planck Collaboration, Ade, P. A. R., Aghanim, N., et al. 2014, , 571, A29
- Planck Collaboration, Ade, P. A. R., Aghanim, N., et al. 2015, arXiv:1502.01598
- Planck Collaboration, Ade, P. A. R., Aghanim, N., et al. 2015, arXiv:1502.01597
- Planelles, S., Borgani, S., Dolag, K., et al. 2013, , 431, 1487
- Plionis, M., & Basilakos, S. 2002, *Tracing Cosmic Evolution with Galaxy Clusters*, 268,
81
- Ponman, T. J., Cannon, D. B., & Navarro, J. F. 1999, , 397, 135
- Poole, G. B., Fardal, M. A., Babul, A., et al. 2006, , 373, 881

- Pratt, G. W., Croston, J. H., Arnaud, M., Boumlhringer, H. 2009, , 498, 361
- Press, W. H., & Schechter, P. 1974, , 187, 425
- Rapetti, D., Allen, S. W., Mantz, A., & Ebeling, H. 2010, , 406, 1796
- Read, A. M., Rosen, S. R., Saxton, R. D., & Ramirez, J. 2011, , 534, A34
- Reichert, A., Böhringer, H., Fassbender, R., Muumlhlegger, M. 2011, , 535, A4
- Reichardt, C. L., Stalder, B., Bleem, L. E., et al. 2013, , 763, 127
- Riess, A. G., Macri, L., Casertano, S., et al. 2011, , 730, 119
- Roediger, E., Lovisari, L., Dupke, R., et al. 2012, , 420, 3632
- z, A. K., Viana, P. T. P., Liddle, A. R., & Mann, R. G. 1999, arXiv:astro-ph/9911499
- Romer, A. K., Nichol, R. C., Holden, B. P., et al. 2000, , 126, 209
- Romer, A. K., Viana, P. T. P., Liddle, A. R., & Mann, R. G. 2001, , 547, 594
- Rosati, P., Della Ceca, R., Norman, C., & Giacconi, R. 1998, , 492, L21
- Rosati, P., Tozzi, P., Gobat, R., et al. 2009, , 508, 583
- Rosen, S. R., Webb, N. A., Watson, M. G., et al. 2015, arXiv:1504.07051
- Rowley, D. R., Thomas, P. A., & Kay, S. T. 2004, , 352, 508
- Rozo, E., Wechsler, R. H., Koester, B. P., et al. 2007, arXiv:astro-ph/0703571
- Rozo, E., Rykoff, E. S., Evrard, A., et al. 2009, , 699, 768
- Rozo, E., Rykoff, E. S., Koester, B. P., et al. 2009, , 703, 601
- Rozo, E., Wechsler, R. H., Rykoff, E. S., et al. 2010, , 708, 645
- Rozo, E., Rykoff, E. S., Becker, M., Reddick, R. M., & Wechsler, R. H. 2015, , 453, 38
- Rozo, E., Rykoff, E. S., Bartlett, J. G., & Melin, J.-B. 2015, , 450, 592
- Rozo, E., & Rykoff, E. S. 2014, , 783, 80
- Rykoff, E. S., McKay, T. A., Becker, M. R., et al. 2008, , 675, 1106-1124
- Rykoff, E. S., Evrard, A. E., McKay, T. A., et al. 2008, , 387, L28

- Rykoff, E. S., Rozo, E., Busha, M. T., et al. 2014, , 785, 104
- Sahlén, M., Viana, P. T. P., Liddle, A. R., et al. 2009, , 397, 577
- Santos, J. S., Rosati, P., Gobat, R., et al. 2009, , 501, 49
- Sarazin, C. L. 1986, *Reviews of Modern Physics*, 58, 1
- Schellenberger, G., Reiprich, T. H., Lovisari, L., Nevalainen, J., & David, L. 2015, , 575, A30
- Schuecker, P., Böhringer, H., Guzzo, L., et al. 2001, , 368, 86
- Schuecker, P., Guzzo, L., Collins, C. A., Boumlhringer, H. 2002, , 335, 807
- Schuecker, P., Böhringer, H., Collins, C. A., & Guzzo, L. 2003, , 398, 867
- Schuster, H. E. 1980, *The Messenger*, 22, 7
- Schwöpe, A. D., Lamer, G., de Hoon, A., et al. 2010, , 513, L10
- Sehgal, N., Trac, H., Acquaviva, V., et al. 2011, , 732, 44
- Shanks, T., Belokurov, V., Chehade, B., et al. 2013, *The Messenger*, 154, 38
- Shanks, T., Metcalfe, N., Chehade, B., et al. 2015, , 451, 4238
- Sheldon, E. S., Johnston, D. E., Scranton, R., et al. 2009, , 703, 2217
- Sheldon, E. S., Johnston, D. E., Masjedi, M., et al. 2009, , 703, 2232
- Short, C. J., & Thomas, P. A. 2009, , 704, 915
- Short, C. J., Thomas, P. A., Young, O. E., et al. 2010, , 408, 2213
- Snowden, S. L., Collier, M. R., & Kuntz, K. D. 2004, , 610, 1182
- Stanford, S. A., Romer, A. K., Sabirli, K., et al. 2006, , 646, L13
- Staniszewski, Z., Ade, P. A. R., Aird, K. A., et al. 2009, , 701, 32
- Stark, A. A., Gammie, C. F., Wilson, R. W., et al. 1992, , 79, 77
- Stott, J. P., Collins, C. A., Sahlén, M., et al. 2010, , 718, 23
- Stott, J. P., Hickox, R. C., Edge, A. C., et al. 2012, , 422, 2213
- Šuhada, R., Fassbender, R., Nastasi, A., et al. 2011, , 530, A110

- Sunyaev, R. A., & Zeldovich, Y. B. 1972, *Comments on Astrophysics and Space Physics*, 4, 173
- Takey, A., Schwobe, A., & Lamer, G. 2011, , 534, A120
- Takey, A., Schwobe, A., & Lamer, G. 2013, , 558, A75
- Taylor, M. B. 2005, *Astronomical Data Analysis Software and Systems XIV*, 347, 29
- Tinker, J., Kravtsov, A. V., Klypin, A., et al. 2008, , 688, 709
- Tinker, J. L., Sheldon, E. S., Wechsler, R. H., et al. 2012, , 745, 16
- Tozzi, P., Moretti, A., Tundo, E., et al. 2014, , 567, A89
- Tundo, E., Moretti, A., Tozzi, P., et al. 2012, , 547, A57
- Vanderlinde, K., Crawford, T. M., de Haan, T., et al. 2010, , 722, 1180
- Vazza, F., Roediger, E., & Brügggen, M. 2012, , 544, A103
- Viana, P. T. P., da Silva, A., Ramos, E. P. R. G., et al. 2012, , 422, 1007
- Vikhlinin, A., van Speybroeck, L., Markevitch, M., Forman, W. R., & Grego, L. 2002, , 578, L107
- Vikhlinin, A., Burenin, R. A., Ebeling, H., et al. 2009, , 692, 1033
- Vikhlinin, A., Kravtsov, A. V., Burenin, R. A., et al. 2009, , 692, 1060
- Voevodkin, A., Borozdin, K., Heitmann, K., et al. 2010, , 708, 1376
- Voit, G. M. 2005, *Reviews of Modern Physics*, 77, 207
- von der Linden, A., Allen, M. T., Applegate, D. E., et al. 2014, , 439, 2
- Watson, M. G., Auguères, J.-L., Ballet, J., et al. 2001, , 365, L51
- Watson, M. G., Schröder, A. C., Fyfe, D., et al. 2009, , 493, 339
- Wilcox, H., Bacon, D., Nichol, R. C., et al. 2015, , 452, 1171
- Williamson, R., Benson, B. A., High, F. W., et al. 2011, , 738, 139
- Wilson, G., Muzzin, A., Yee, H. K. C., et al. 2009, , 698, 1943
- Wittman, D., Margoniner, V. E., Tyson, J. A., et al. 2003, , 597, 218

Wu, H.-Y., Rozo, E., & Wechsler, R. H. 2010, , 713, 1207

XMM-Newton SOC VILSPA, https://heasarc.gsfc.nasa.gov/Images/xmm/sc_inl.gif

XMM-Newton SOC VILSPA, http://xmm.esac.esa.int/external/xmm_user_support/documentation/uhb_2.1/img28.gif

XMM-Newton SOC VILSPA, http://xmm.esac.esa.int/external/xmm_user_support/documentation/uhb_2.1/img29.gif

XMM-Newton SOC VILSPA, http://xmm.esac.esa.int/external/xmm_user_support/documentation/technical/EPIC/mosarray.jpg

XMM-Newton SOC VILSPA, http://xmm.esac.esa.int/external/xmm_user_support/documentation/technical/EPIC/pnarray.jpg

XMM-Newton SOC VILSPA, http://sci.esa.int/science-e-media/img/98/_rgapath410.jpg

Roediger, E., & Zuhone, J. A. 2012, , 419, 1338

ZuHone, J. A., Markevitch, M., Brunetti, G., & Giacintucci, S. 2013, , 762, 78 1

Zwicky, F. 1933, *Helvetica Physica Acta*, 6, 110

Zwicky, F., Wild, P., Herzog, E., Karpowicz, M., and Kowal, C., *CATALOGUE OF GALAXIES AND CLUSTERS OF GALAXIES* (called the CAT), California Institute of Technology, six volumes, 1961 to 1968.